

## Abstract

# Stirring a Giant: Feedback in the Orion A Molecular Cloud

Jesse Robb Feddersen

2019

Stars form via gravitational collapse of cold, dark clouds of molecular gas. But stars are neither cold nor dark. This thesis concerns the balance between the star-forming power of gravity and feedback: energy and momentum imparted by newly formed stars on their host clouds. Using the unprecedented combination of angular resolution and spatial coverage provided by the CARMA-NRO Orion Survey, I investigate the impacts of feedback on the Orion A molecular cloud. First, I present a survey of expanding spherical CO shells around low- to intermediate-mass young stars in Orion A. The shells inject enough energy and momentum to maintain turbulence in the cloud. The mass-loss rates needed to power the observed shells are two to three orders of magnitude higher than predicted for main-sequence stellar winds. Next, I compare gas statistics to the impact of feedback in different parts of Orion A to test if feedback changes the structure or kinematics of the cloud as predicted by molecular cloud simulations. I characterize the cloud using the covariance matrix, spectral correlation function, and spatial power spectrum. The CO spectral correlation function steepens with greater surface density of young stars, suggesting this statistic may be sensitive to feedback. The CO covariance matrix shows peaks at 1-3 km s<sup>-1</sup> toward several regions that may be produced by feedback. Finally, I present a survey of protostellar outflows in Orion A. I identify 45 outflows, including 11 that are newly detected. I measure the mass and energetics of the outflows, including corrections for velocity-dependent opacity and low-velocity outflow emission. The total momentum and kinetic energy of the outflows is significant compared to that required to maintain tur-

bulence. I also compare the orientation of outflows with dense filamentary structure traced by C<sup>18</sup>O. Outflows in Orion A show a moderately perpendicular alignment to their host filaments, suggesting the protostellar spin is correlated to processes at much larger cloud scales.

# **Stirring a Giant: Feedback in the Orion A Molecular Cloud**

A Dissertation  
Presented to the Faculty of the Graduate School  
of  
Yale University  
in Candidacy for the Degree of  
Doctor of Philosophy

by  
Jesse Robb Feddersen

Dissertation Director: Dr. Héctor Arce

December 2019

Copyright © 2019 by Jesse Robb Feddersen

All rights reserved.

## Acknowledgments

This thesis would not have been possible without the support, belief, and most of all *patience* of my advisor, Héctor Arce. Muchas gracias.

Thank you to my thesis committee and readers, Jeff Kenney, Sarbani Basu, and Stella Offner, and to all the faculty, staff, and graduate students of the Astronomy Department at Yale for putting up with me these past six years. Thank you to all of the staff and observers at CARMA, NRO, and all of the researchers from whom I have shamelessly stolen data or ideas (mostly cited, I hope).

Thank you to Michael Faison at the Leitner Family Observatory and Planetarium for introducing me to the joys of outreach, Louise Edwards for being the greatest TA supervisor ever, and all the staff and students at the Yale Summer Program in Astrophysics for showing me how rewarding teaching can be.

Thank you to the National Science Foundation and the US taxpayers for funding my work and play for the past six years.

To my family and friends, I love you all more than you know.

Dich im unendlichen zu finden,  
must du unterscheiden und dann verbinden.

*To find yourself in the infinite,  
you must distinguish and then combine.*

---

Johann Wolfgang von Goethe

# Contents

<b>1</b>	<b>Introduction</b>	<b>1</b>
1.1	Star Formation . . . . .	1
1.2	Star Formation is Inefficient . . . . .	2
1.3	Turbulence in Molecular Clouds . . . . .	3
1.4	Types of Feedback . . . . .	4
1.4.1	Protostellar Outflows . . . . .	4
1.4.2	Expanding Shells . . . . .	8
1.4.3	Other Feedback in GMCs . . . . .	9
1.5	The Orion A Giant Molecular Cloud . . . . .	10
1.6	The CARMA-NRO Orion Survey . . . . .	12
1.7	This Thesis . . . . .	14
<b>2</b>	<b>Expanding CO Shells in the Orion A Molecular Cloud</b>	<b>15</b>
2.1	Introduction . . . . .	16
2.2	Methods . . . . .	18
2.2.1	Nobeyama Radio Observatory 45m Observations . . . . .	18
2.2.2	Infrared Data . . . . .	18
2.2.3	Source Catalogs . . . . .	19
2.2.4	Identifying shells . . . . .	19
2.2.5	Characterizing Shells . . . . .	21

2.3	Results . . . . .	22
2.3.1	A Shell Near The Herbig Ae Star T Ori . . . . .	24
2.3.2	Two Nested Shells Around V380 Ori . . . . .	28
2.3.3	A Shell Centered on LP Ori . . . . .	38
2.4	Impact of Shells on Cloud . . . . .	41
2.4.1	Measuring Mass, Momentum, and Kinetic Energy . . . . .	41
2.4.2	Mass, Momentum, and Kinetic Energy Statistics . . . . .	45
2.5	Discussion . . . . .	45
2.5.1	The Impact of Shells on the GMC . . . . .	45
2.5.2	Shell Driving Mechanisms . . . . .	54
2.6	Summary and Conclusions . . . . .	56
<b>3</b>	<b>The CARMA-NRO Orion Survey: Statistical Signatures of Feedback in the Orion A Molecular Cloud</b>	<b>70</b>
3.1	Introduction . . . . .	71
3.2	Data . . . . .	74
3.2.1	CARMA-NRO Orion CO Maps . . . . .	74
3.2.2	Subregions . . . . .	74
3.3	Quantifying Feedback . . . . .	77
3.3.1	Expanding Shells . . . . .	77
3.3.2	Protostellar Outflows . . . . .	78
3.3.3	Young Stars . . . . .	79
3.4	Statistical Methods . . . . .	81
3.4.1	Principal Component Analysis . . . . .	81
3.4.2	Spectral Correlation Function . . . . .	82
3.4.3	Spatial Power Spectrum . . . . .	83
3.5	Results . . . . .	84

3.5.1	Principal Component Analysis . . . . .	84
3.5.2	Spectral Correlation Function . . . . .	86
3.5.3	Spatial Power Spectrum . . . . .	88
3.6	Discussion . . . . .	90
3.6.1	Spectral Slopes and Feedback Impact . . . . .	90
3.6.2	Line Wing Power Spectrum . . . . .	93
3.7	Conclusions . . . . .	99
3.A	Statistics of $^{13}\text{CO}$ and $\text{C}^{18}\text{O}$ . . . . .	101
3.A.1	Covariance Matrix . . . . .	101
3.A.2	SCF . . . . .	103
3.A.3	SPS . . . . .	103
3.B	Noise Peak in $\text{C}^{18}\text{O}$ SPS . . . . .	106
3.C	SCF at Large Scales . . . . .	106
3.D	Full-Map Statistics . . . . .	109
<b>4</b>	<b>The CARMA-NRO Orion Survey: Protostellar Outflows and Filamentary Alignment</b>	<b>113</b>
4.1	Introduction . . . . .	114
4.2	Observations . . . . .	116
4.2.1	CO Maps . . . . .	116
4.2.2	Source Catalogs . . . . .	116
4.2.3	Other Outflow Studies . . . . .	117
4.3	Outflow Identification . . . . .	118
4.4	Physical Properties of Outflows . . . . .	120
4.4.1	Calculating Physical Properties . . . . .	120
4.4.2	Impact of Outflows on the Cloud . . . . .	131
4.5	Outflow-Filament Alignment . . . . .	134

4.5.1	C <sup>18</sup> O Filaments . . . . .	135
4.5.2	Projected Angle Between Outflows and Filaments . . . . .	136
4.5.3	3D Outflow-Filament Alignment . . . . .	140
4.6	Conclusions . . . . .	144
4.A	All Outflows in CARMA-NRO Orion . . . . .	154
<b>5</b>	<b>Conclusion</b>	<b>178</b>
5.1	Next Steps . . . . .	179
5.2	Final Thoughts . . . . .	180
<b>Bibliography</b>		<b>182</b>

# List of Figures

1.1	Feedback is needed to reproduce observed star formation rates . . . . .	5
1.2	Illustration of protostellar outflows . . . . .	7
1.3	CARMA-NRO Orion data combination. . . . .	13
2.1	Overview of shells in Orion A . . . . .	23
2.2	$^{12}\text{CO}$ channel maps of Shell 10 . . . . .	25
2.3	PV diagram of $^{12}\text{CO}$ toward Shell 10 . . . . .	26
2.4	Spitzer 8 $\mu\text{m}$ image and integrated $^{13}\text{CO}$ of Shell 10 . . . . .	29
2.5	$^{12}\text{CO}$ channel maps of Shell 39, the larger of the two shells around V380 Ori	30
2.6	$^{12}\text{CO}$ channel maps of Shell 40, the smaller of the two shells around V380 Ori . . . . .	31
2.7	$^{12}\text{CO}$ PV diagram of Shell 39 . . . . .	33
2.8	$^{12}\text{CO}$ PV diagram of Shell 40 . . . . .	34
2.9	Spitzer 8 $\mu\text{m}$ image and integrated $^{13}\text{CO}$ of Shell 39 . . . . .	35
2.10	<i>HST WFC2</i> image and integrated $^{13}\text{CO}$ of Shell 40 . . . . .	36
2.11	$^{12}\text{CO}$ channel maps of Shell 11 around LP Ori . . . . .	39
2.12	$^{12}\text{CO}$ PV diagram of Shell 11 . . . . .	40
2.13	Spitzer 8 $\mu\text{m}$ image and integrated $^{12}\text{CO}$ of Shell 11 . . . . .	42
2.14	Mass of shells . . . . .	46
2.15	Momentum of shells . . . . .	47

2.16	Kinetic energy of shells . . . . .	48
3.1	Overview of Orion A subregions and feedback sources . . . . .	75
3.2	$^{12}\text{CO}$ covariance matrices in Orion A subregions . . . . .	87
3.3	$^{12}\text{CO}$ spectral correlation function in Orion A subregions . . . . .	89
3.4	$^{12}\text{CO}$ spatial power spectrum in Orion A subregions . . . . .	91
3.5	SCF and SPS slopes versus the momentum injection rate surface density of shells . . . . .	94
3.6	SCF and SPS slopes versus the momentum injection rate surface density of outflows . . . . .	95
3.7	SCF and SPS slopes versus the surface density of YSOs . . . . .	96
3.8	Comparison of three feedback measures . . . . .	98
3.9	$^{13}\text{CO}$ line wing power spectra in L1641N subregion . . . . .	98
3.10	$^{13}\text{CO}$ and $\text{C}^{18}\text{O}$ covariance matrices in Orion A subregions . . . . .	102
3.11	$^{13}\text{CO}$ and $\text{C}^{18}\text{O}$ spectral correlation function and power-law fits in Orion A subregions . . . . .	104
3.12	$^{13}\text{CO}$ and $\text{C}^{18}\text{O}$ spatial power spectrum and power-law fits in Orion A subregions . . . . .	105
3.13	$\text{C}^{18}\text{O}$ noise power spectrum toward L1641N . . . . .	107
3.14	$^{12}\text{CO}$ large-scale spectral correlation function in Orion A subregions . . .	107
3.15	Covariance matrices of the full Orion A map . . . . .	110
3.16	Spectral correlation function of the full Orion A map . . . . .	110
3.17	Spatial power spectrum and power-law fits for the full Orion A map . . .	111
4.1	Overview of Orion A outflows . . . . .	121
4.2	Outflow around HOPS 68 . . . . .	122
4.3	$\text{C}^{18}\text{O}$ spectrum of the HOPS 68 outflow . . . . .	124
4.4	Excitation temperature of the HOPS 68 outflow . . . . .	124

4.5	Opacity correction of the HOPS 68 outflow . . . . .	127
4.6	Mass spectrum of the HOPS 68 outflow . . . . .	128
4.7	Maximum velocity of the HOPS 68 outflow . . . . .	132
4.8	Position angle and opening angle of HOPS 68 outflow . . . . .	132
4.9	Finding the filament orientation . . . . .	137
4.10	Distribution of projected angle between outflows and filaments . . . . .	138
4.11	3D outflow-filament alignment compared to models . . . . .	141
4.12	All outflow figures . . . . .	155

# List of Tables

2.1	Shell Parameters . . . . .	60
2.2	Shell Criteria . . . . .	63
2.3	Shell Physics . . . . .	66
2.4	Impact of Shells and Outflows . . . . .	69
3.1	Subregion Results . . . . .	112
4.1	Outflow Catalog. . . . .	146
4.2	Outflow Physical Properties . . . . .	148
4.3	Outflow Angles and Filament Comparison . . . . .	151
4.4	Anderson-Darling $p$ -values . . . . .	153

# Chapter 1

## Introduction

Stars form in the coldest, darkest pockets of the galaxy: giant molecular clouds (GMCs). Only here is gas dense enough to fall inward under its own gravity. But stars are neither cold nor dark. In this thesis, I explore the question: **what happens to a GMC when stars form?**

### 1.1 Star Formation

Our current picture of how gas turns into stars has recently been reviewed by McKee & Ostriker (2007), Bergin & Tafalla (2007), Draine (2011), and Dunham et al. (2014b). Molecular gas in the galaxy is structured hierarchically. GMCs, with typical masses of  $10^3\text{-}10^5 M_{\odot}$  and sizes of a few to tens of pc, coalesce out of diffuse neutral hydrogen from colliding flows or spiral arm overdensities. Within GMCs are pc-scale clumps, with typical masses of a few hundred  $M_{\odot}$ . Clumps are the structures out of which star clusters form. The density peaks within clumps are called cores. A core collapses into a protostar when gravity overpowers thermal pressure, magnetic fields, and turbulence.

A new protostar grows by adding mass from an accretion disk, which is replenished by the surrounding envelope of the infalling core. As the protostar accretes mass, the

disk grows and the envelope diminishes, shifting its spectral energy distribution to hotter temperatures and revealing it to near-infrared (NIR) surveys (e.g. Megeath et al., 2012). The accretion disk powers a wind which entrains molecular gas in bipolar outflows around the protostar. Once the envelope shrouding it is fully cleared, the protostar becomes a pre-main sequence star which will eventually (in 1-3 Myr for a solar mass star) reach the main sequence.

The evolution of protostars can be followed by their infrared spectral energy distribution (SED). As the protostar accretes mass and clears the cold material around it, the SED shifts to hotter bolometric temperatures and peaks at shorter wavelengths. This evolution in the SED is denoted by the protostellar classes 0-III (Dunham et al., 2014b).

## 1.2 Star Formation is Inefficient

Only about 5% of a molecular cloud is converted into stars (McKee & Ostriker, 2007). But if gravity and thermal pressure are the only forces at work, clouds should collapse in a freefall time (Krumholz et al., 2014). Potential causes of this low-star formation efficiency include magnetic fields, short cloud lifetimes, and turbulence.

Magnetic fields can support cores against collapse. In this scenario, the ions in cores are locked to the magnetic fields, while neutral particles and dust gradually diffuse inward (Mestel & Spitzer, 1956; Shu, 1983). This process, called ambipolar diffusion, can slow the collapse of a core and reduces its star formation efficiency. However, the observed magnetic fields in many clouds are not strong enough to be the only support against gravitational collapse (Crutcher, 2012).

If molecular clouds are transient structures, they may only have a chance to form a few stars before they are completely disrupted by external (e.g. shear from the galaxy's gravitational potential) or internal (e.g. supernovae) forces. Murray (2011) argue that molecular clouds only live for two to three free-fall times, and Dobbs & Pringle (2013) use

hydrodynamic simulations of a Milky Way-like galaxy to support the claim that molecular clouds are transient. If clouds are not long lived, this removes the necessity for them to be supported against gravitational collapse for long periods of time.

### 1.3 Turbulence in Molecular Clouds

Larson (1981) showed that the line-width of clouds, clumps, and cores has a power-law dependence on their physical size. The larger the structure, the higher the velocity dispersion within it. This relationship is characteristic of a turbulent medium, dominated by chaotic motions. Because of this size-dependent velocity dispersion, turbulent pressure prevents large scale collapse of a cloud, while allowing local collapse of cores into protostars (Mac Low & Klessen, 2004). Turbulent driving of simulated molecular clouds is necessary to reproduce the structure of observed clouds (e.g. Federrath, 2015).

But turbulence decays rapidly, within a cloud crossing time, and it must be maintained over the lifetime of the cloud (Mac Low et al., 1998). Cloud turbulence may be maintained by external forces, such as galactic shear or supernovae (Dobbs & Pringle, 2013) and/or internal feedback sources such as protostellar outflows (Nakamura & Li, 2007). External and internal drivers of turbulence may be important at different spatial or time scales within the cloud. At cluster scales, the simulations of Nakamura & Li (2007) showed that outflows can inject momentum to maintain turbulence and reduce the star formation efficiency to the observed values of a few percent. Figure 1.1 shows the results of a simulation by Federrath (2015) who conclude that the combination of gravity, magnetic fields, turbulence, and feedback are all necessary to reproduce realistic molecular clouds.

Simulations of feedback-driven turbulence find a unique signature of the feedback injection scale in the velocity power spectrum (Nakamura & Li, 2007; Carroll et al., 2009). In observations, an indicator of feedback-driven turbulence has long been sought in statistical measures of position-position-velocity (PPV) cubes of molecular clouds. On one

hand, Brunt et al. (2009) and Padoan et al. (2009) studied principle component analysis and power spectra of the NGC 1333 region and conclude that these statistics show feedback is unimportant in driving turbulence. On the other hand, Carroll et al. (2010) showed that these statistics may not be sensitive to the presence of feedback-driven turbulence. Boyden et al. (2016) found additional statistical signatures of feedback in simulated clouds with stellar winds. **In Chapter 3, I present a study testing for the first time this predicted correlation of feedback impact and molecular gas statistics in an observed molecular cloud.**

## 1.4 Types of Feedback

In molecular clouds, feedback is any mechanism related to star formation that can inject momentum and kinetic energy into the cloud (Krumholz et al., 2014). As discussed above, feedback can potentially maintain turbulence and reduce the star formation efficiency. Feedback has also been studied for its potential to positively “trigger” star formation (e.g. Haworth & Harries, 2012; Dale et al., 2015). I review the important feedback mechanisms in molecular clouds below.

### 1.4.1 Protostellar Outflows

Around forming protostars, high-velocity, bipolar jets and outflows are ubiquitous (Frank et al., 2014). The exact launching mechanism of these jets is still uncertain, but they almost certainly originate in interactions between magnetic fields and the accretion disk (Shu et al., 2000; Pudritz et al., 2007). Once a jet is launched, it shocks molecular gas and entrains material in a bipolar outflow which can extend over a pc away from the driving protostar. Protostellar outflows have been studied extensively in rotational transitions of carbon monoxide (CO), which are observable at 1-3 mm. The neutral and ionized components of outflows are commonly observed with optical and NIR emission lines such as H $\alpha$

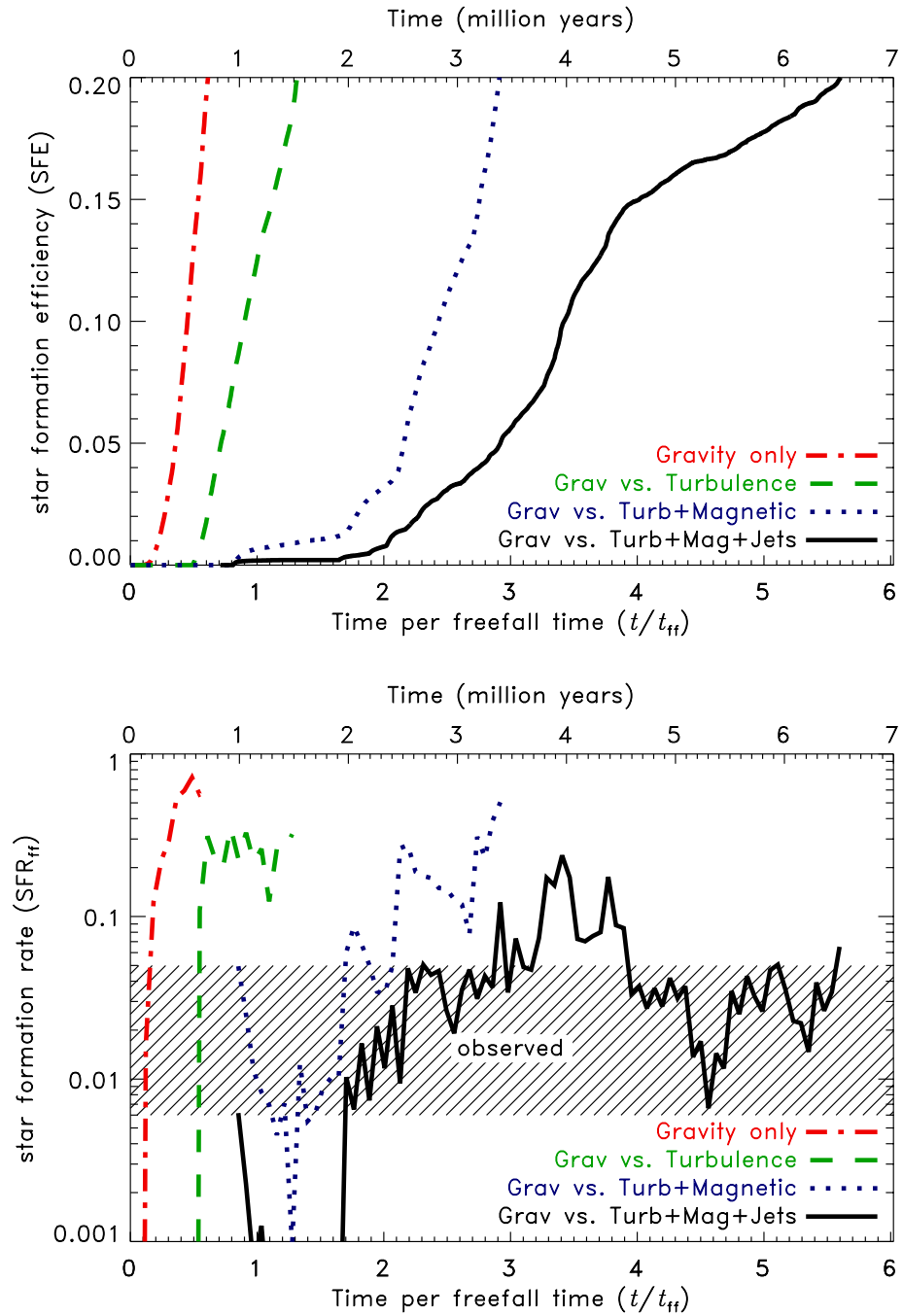


Figure 1.1 The star formation efficiency (top) and star formation rate per freefall time (bottom) in a simulated GMC. Turbulence, magnetic fields, and feedback, implemented here in the form of protostellar jets/outflows, are all needed to keep the star formation rate of simulated molecular clouds in the observed range. This figure is reproduced from Figure 2 in Federrath (2015).

and the H<sub>2</sub> rovibrational 2.12  $\mu\text{m}$  line (Bally, 2016). The structure of a typical protostellar outflow is illustrated in Figure 1.2.

Protostellar outflows can have a significant impact on their surroundings. Many studies have attempted to measure this impact using CO surveys of molecular clouds. Dunham et al. (2014a) give a thorough account of the assumptions and correction factors necessary to calculate the mass, momentum, and kinetic energy of a protostellar outflow from CO observations. In clouds such as Perseus (Arce et al., 2010),  $\rho$ -Ophiuchus (Nakamura et al., 2011), Serpens (Plunkett et al., 2015a), and Taurus (Li et al., 2015), outflows inject enough momentum and kinetic energy to significantly offset the dissipation of turbulence on pc scales. Whether or not outflows are actually responsible for driving and maintaining turbulence depends on the efficiency with which outflows couple to the cloud (Cunningham et al., 2009; Frank et al., 2014) as well as the size of outflows compared to the necessary scales of turbulent driving (Carroll et al., 2010; Offner & Liu, 2018). **In Chapter 4, I present the most complete survey of CO outflows in Orion A to date and show that outflows contain enough momentum and kinetic energy to maintain turbulence.**

Outflows have also been studied for their potential to trace the protostellar accretion process occurring at scales too small and too obscured for current observations to probe directly. For example, rotating outflows are evidence of the transport of angular momentum away from the protostellar accretion disk (Coffey et al., 2007; Larson, 2010). Clumpy, “episodic” outflows can trace the time variability of protostellar accretion over thousands of years (Plunkett et al., 2015b; Vorobyov et al., 2018). “Wiggling” S-shaped outflows can indicate precession in the protostellar system, probably from dynamical interactions between companions (e.g. Frank et al., 2014; Choi et al., 2017).

The average position angle of an outflow on the sky traces the angular momentum axis of the protostar. If the protostellar angular momentum is inherited from larger scales, outflow position angles may be correlated with larger cloud structures. It has long been known that most protostars form in narrow filaments of dense gas (Arzoumanian et al.,

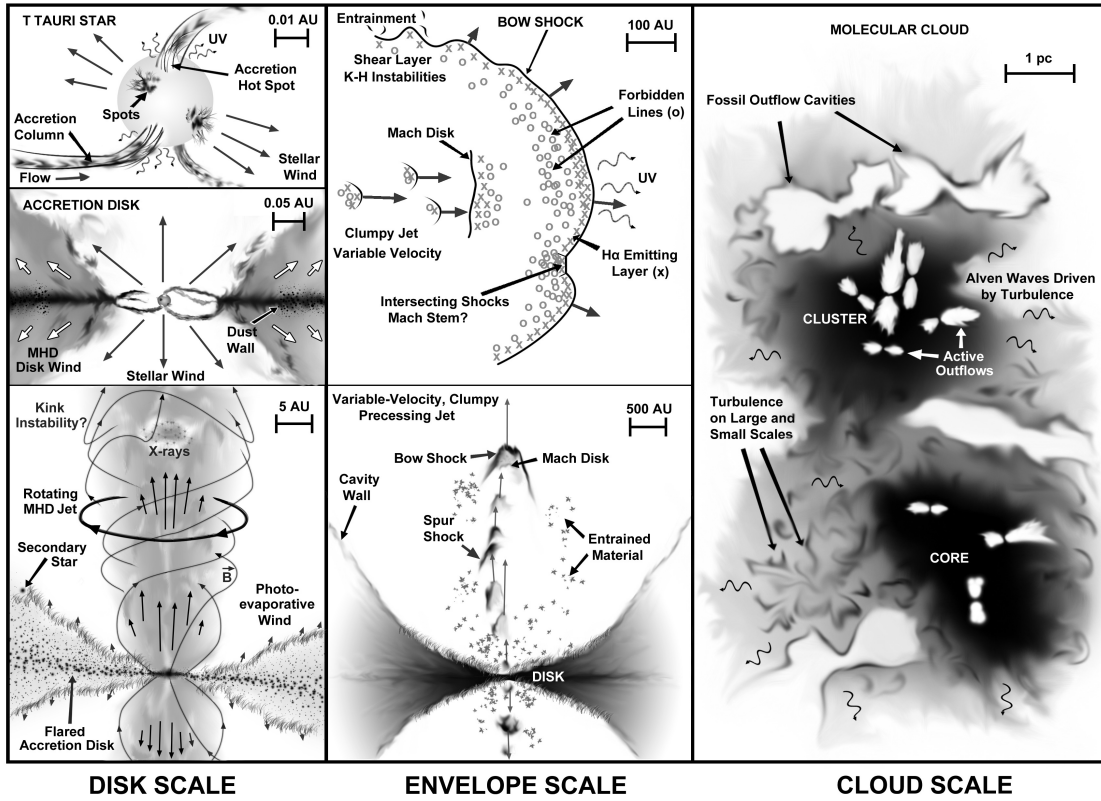


Figure 1.2 Protostellar outflows are a multi-scale process, from the sub-AU launching zone close to a forming star (left) to the momentum injected up to a pc or more away from the driving source (right). This figure is reproduced from Figure 1 in Frank et al. (2014).

2011; André et al., 2014). Recently, Stephens et al. (2017) and Kong et al. (2019a) have compared the orientation of outflows and filaments in two very different molecular clouds to test whether filaments are important in the protostellar mass accretion process. **In Chapter 4, I present the first analysis of the alignment between outflows and the complex filamentary structure in Orion A.**

### 1.4.2 Expanding Shells

Massive (OB) stars have long been known to drive expanding spherical shells into the interstellar medium. Such shells, or “bubbles”, are prominent in *Spitzer* GLIMPSE and MIPSGAL surveys of the galactic plane (Churchwell et al., 2006). Citizen scientists and machine learning classification have identified thousands of these bubbles in the Milky Way (Simpson et al., 2012; Beaumont et al., 2014). Many of these bubbles are associated with known HII regions powered by massive stars. These stars power strong stellar winds which, along with thermal overpressure and radiation pressure, are capable of sweeping up material into an expanding shell (Strömgren, 1939; Castor et al., 1975; Weaver et al., 1977). Until recently it was thought that less massive (non-ionizing) stars were incapable of generating spherical stellar winds that would affect their environment (Vink et al., 2001; Smith, 2014).

However, Arce et al. (2011) identified 12 expanding shells in CO maps of the Perseus molecular cloud. Most of these shells contain only low to intermediate-mass stars. These shells show that spherical stellar winds from less massive stars can be important inside molecular clouds. Indeed, the total momentum input of the shells in Perseus is similar to that of protostellar outflows. Thus, Arce et al. (2011) suggested that wind-blown shells may be just as dynamically important as outflows in maintaining turbulence. Since their discovery in Perseus, similar expanding shells have been found in the L1641-N region in Orion (Nakamura et al., 2012) and in Taurus (Li et al., 2015).

Aside from their impacts on GMCs, the driving mechanism of expanding shells remains a puzzle. Offner & Arce (2015) modeled spherical winds in a simulated turbulent cloud. They found that the mass loss rates needed to reproduce the observed shell properties are 2-3 orders of magnitude greater than predicted by theoretical stellar-wind models (Smith, 2014). **In Chapter 2, I present a catalogue of newly discovered expanding shells in Orion A, only the third cloud in which shells have been found, and show that they can maintain a significant fraction of turbulence in the cloud.**

### 1.4.3 Other Feedback in GMCs

I focus on shells and outflows from low to intermediate-mass stars in this thesis. Massive stars, when present, also play an important role in shaping molecular clouds. Stars more than a few solar masses emit most of their blackbody radiation in the far-ultraviolet (FUV) wavelength regime. These FUV photons can dissociate H<sub>2</sub> and eject photoelectrons from dust grains, heating the cloud and causing expansion away from the source of FUV flux (Hollenbach & Tielens, 1997; Bally et al., 2018). Places where FUV is important are called photon-dominated regions (PDRs) and include famous examples such as the Orion Bar (Goicoechea et al., 2016) and the Horsehead Nebula (Bally et al., 2018). This expansion of FUV-heated cloud surfaces may drive momentum into the cloud and help maintain turbulence (Bally, 2011).

Stars more massive than about  $8M_{\odot}$  produce enough extreme-ultraviolet (EUV) photons to ionize their surroundings, forming H II regions that expand and disrupt the molecular cloud around them. The prototypical H II region is the Orion Nebula, where intense stellar winds and EUV radiation from the Trapezium cluster of OB stars have carved out a pc-scale cavity in the Orion A molecular cloud (Pabst et al., 2019). Bally (2011) introduced the concept of a “feedback ladder” as the progression of stellar feedback from protostellar outflows to the eventual supernovae approximately 3 Myr after the most mas-

sive stars are formed. Depending on the age and masses of stars, each of these feedback mechanisms may dominate. In this thesis, I focus on regions that are not dominated by rare massive stars. As a consequence, I focus on the feedback that low to intermediate-mass stars can impart to their cloud via expanding shells and protostellar outflows.

## 1.5 The Orion A Giant Molecular Cloud

The constellation of Orion hosts one of the most active, and certainly the most famous, sites of star formation in the nearby galaxy. The most spectacular feature in optical images of Orion is the Orion Nebula. The Nebula is an H II region powered by the OB stars in the Trapezium asterism including the most luminous member, the  $50 M_{\odot}$  binary system  $\theta^1$  Ori C (Muench et al., 2008). Directly behind the Orion Nebula is the GMC at the heart of this thesis: Orion A.

The  $10^5 M_{\odot}$  Orion A GMC is the nearest cloud with both low and high-mass star formation, located about 400 pc away.<sup>1</sup> The entire GMC may be an example of “triggered” star formation, as the Orion-Eridanus superbubble has swept through the cloud from the northwest to southeast. In this direction, Orion A shows a cometary structure and a velocity gradient of about  $9 \text{ km s}^{-1}$  (Bally, 2008). The most striking feature of the molecular cloud is the dense north-south integral-shaped filament (ISF) centered on the massive star-forming core OMC-1. The ISF extends about 10 pc and is conventionally split into five parts from north to south: OMC-2/3, OMC-1, and OMC-4/5 (Bally et al., 1987; Peterson & Megeath, 2008). Directly south of the ISF are the molecular clumps L1641-N and NGC 1999 (Allen & Davis, 2008).

The stellar content of Orion A has been surveyed numerous times in optical images

---

<sup>1</sup>I adopt a distance to Orion A of 414 pc throughout this thesis, from Very Long Baseline Array (VLBA) trigonometric parallaxes to radio sources in the Orion Nebula (Menten et al., 2007). Recent parallax measurements from the *Gaia* spacecraft place Orion A slightly closer, between 380 and 400 pc (Großschedl et al., 2018; Kounkel et al., 2018; Kuhn et al., 2019).

over the last century (e.g. Brun, 1935; Parenago, 1954; Walker, 1969; Cohen & Kuhi, 1979; Herbig & Bell, 1988; McCaughrean & Stauffer, 1994; Brown et al., 1994; O'dell & Wong, 1996; Hillenbrand, 1997). Protostars and pre-main sequence stars are most commonly identified by their IR excess (from warm dust in the protostellar envelope and disk). Recent space-based surveys of Orion A in the MIR-FIR have produced catalogs of thousands of these young stellar objects (YSOs). Megeath et al. (2012) used *Spitzer Space Telescope* MIR observations to catalogue almost 3000 dusty YSOs in Orion A. The Herschel Orion Protostar Survey (HOPS Furlan et al., 2016) targeted about 300 of the reddest, most obscured YSOs in the FIR with the *Herschel Space Observatory* and in the sub-mm with the Atacama Pathfinder Experiment (APEX) to derive detailed protostellar properties from SED fitting. I use both the *Spitzer* Orion and HOPS catalogs extensively in this thesis to identify potential driving sources of feedback in Orion A. The latest YSO census in the cloud has been carried out by Großschedl et al. (2019), using sub-arcsecond resolution NIR imaging to refine the *Spitzer* and *Herschel* catalogs and reach a final count of 2980 YSOs across the cloud.

Orion A is impacted by a diverse array of stellar feedback processes. In the northern part of the ISF, also known as OMC-2/3, many protostellar outflows have been identified (e.g. Takahashi et al., 2008). OMC-1 is impacted by the expansion of the HII region and an explosive outflow from a dynamical interaction in a forming protostellar multiple system in the Orion BN-KL region (Bally et al., 2017). To the south, the OMC-4/5 region is full of cometary structures that are likely sculpted by the FUV radiation from the ONC (Bally, 2008). The L1641-N region has several clustered protostellar outflows and shells (e.g. Nakamura et al., 2012). The NGC 1999 region hosts protostellar outflows, including the famous HH 1/2 jet, and the enigmatic “Hole in the Sky” (Moro-Martín et al., 1999; Stanke et al., 2010). Despite the many targeted studies of interesting feedback features in Orion A, until this thesis no study has systematically searched for and measured the impacts of feedback throughout the cloud.

## 1.6 The CARMA-NRO Orion Survey

The key data for my thesis come from the CARMA-NRO Orion Survey (Kong et al., 2018). This survey combines data from the Combined Array for Research in Millimeter Astronomy (CARMA) with the Nobeyama Radio Observatory 45 m telescope (NRO). The survey mapped the Orion A cloud in several molecular emission lines including the CO isotopologues  $^{12}\text{CO}(1\text{-}0)$ ,  $^{13}\text{CO}(1\text{-}0)$ , and  $\text{C}^{18}\text{O}(1\text{-}0)$ , with an angular resolution of about  $8''$  (about 3300 AU at the distance of Orion A) and a velocity resolution of  $0.25 \text{ km s}^{-1}$ .

Orion A has been mapped in CO several times previously, beginning in the 1970s with the  $8'$ -resolution maps from Kutner et al. (1977). The filamentary structure of the cloud, including the famous ISF, was first resolved in  $^{13}\text{CO}$  maps from the Bell Labs 7-meter telescope (Bally et al., 1987). More recently, large single-dish telescopes such as the 15-meter James Clerk Maxwell Telescope (JCMT; Buckle et al., 2012), the 14-meter Five College Radio Astronomy Observatory (FCRAO; Ripple et al., 2013), and the 30-meter IRAM telescope (Berné et al., 2014) have been used to map the cloud with sub-arcminute resolution. CARMA-NRO Orion achieves the highest resolution of any large CO map in Orion to date (Kong et al., 2018).

The combination of interferometry (CARMA) with single-dish maps (NRO) is crucial for my study of feedback in Orion A. Both protostellar outflows and shells are multiscale phenomena, ranging in size from a tenth to a few pc. The spatial dynamic range of the CARMA-NRO Orion data spans three orders of magnitude, from 0.01 to 10 pc, making it ideal for this thesis. In fact, the survey offers the greatest spatial dynamic range of any GMC survey to date (Kong et al., 2018). In addition to my work on feedback presented in this thesis, the CARMA-NRO Orion data have been used to study the cloud's filamentary structure (Suri et al., 2019) and protostellar core kinematics (Kong et al., 2019b). Figure 1.3 shows the power of the CARMA-NRO data combination.

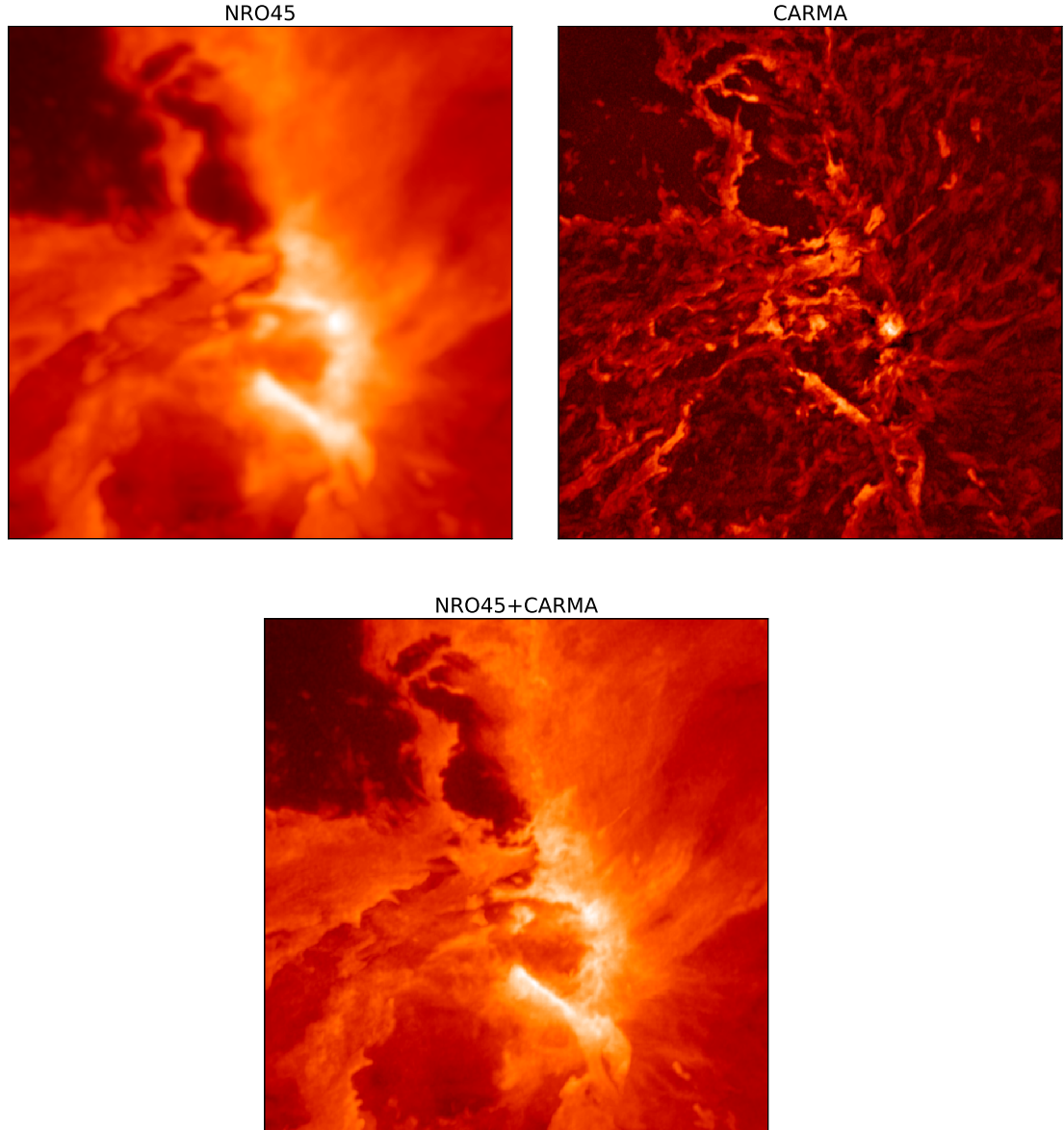


Figure 1.3 CARMA-NRO Orion data combination. Each panel shows the peak intensity of  $^{12}\text{CO}$  in the same  $2\text{ pc} \times 2\text{ pc}$  region centered on OMC-1. The bottom panel shows the remarkable spatial dynamic range achieved by combining CARMA interferometry with NRO single-dish data. This figure is adapted from Figure 2 in Kong et al. (2018).

## 1.7 This Thesis

In this thesis, I use the unmatched spatial dynamic range of the CARMA-NRO Orion Survey to shed light on several fundamental questions in star formation.

- Can feedback drive and maintain turbulence inside molecular clouds, limiting their star formation efficiency?
- How prevalent are expanding shells, and what drives them?
- Which feedback processes are most important inside molecular clouds, and how are they best quantified?
- How does filamentary structure affect the flow of mass from cloud to core?

In Chapter 2, I present a study of expanding shells in the Orion A molecular cloud and show they contain enough momentum and energy to be important in maintaining cloud turbulence. In Chapter 3, I investigate the relationship between several statistics of gas turbulence and feedback impacts in different regions of Orion A and compare to predictions from molecular cloud simulations. In Chapter 4, I show that outflows have a comparable amount of aggregate momentum and energy to the shells and I investigate the outflow-filament connection in Orion. Finally, in Chapter 5, I summarize my main findings and look to the future.

# Chapter 2

## Expanding CO Shells in the Orion A Molecular Cloud

*Originally published as Feddersen, J. R., Arce, H. G., Kong, S., Shimajiri, Y., Nakamura, F., Hara, C., Ishii, S., Sasaki, K., Kawabe, R. 2018, Astrophysical Journal, 862, 121.*

### Abstract

We present the discovery of expanding spherical shells around low to intermediate-mass young stars in the Orion A giant molecular cloud using observations of  $^{12}\text{CO}(1-0)$  and  $^{13}\text{CO}(1-0)$  from the Nobeyama Radio Observatory 45-meter telescope. The shells have radii from 0.05 to 0.85 pc and expand outward at 0.8 to 5 km s $^{-1}$ . The total energy in the expanding shells is comparable to protostellar outflows in the region. Together, shells and outflows inject enough energy and momentum to maintain the cloud turbulence. The mass-loss rates required to power the observed shells are two to three orders of magnitude higher than predicted for line-driven stellar winds from intermediate-mass stars. This discrepancy may be resolved by invoking accretion-driven wind variability. We describe in detail several shells in this paper and present the full sample in the online journal.

## 2.1 Introduction

Stars form via the gravitational collapse of molecular gas in the densest parts of giant molecular clouds (GMCs) (McKee & Ostriker, 2007; Dunham et al., 2014a). The efficiency of star formation observed in GMCs in the Milky Way is much lower than expected if gravity is the only force at work. The low star-formation efficiency has been attributed to magnetic fields (Mestel & Spitzer, 1956; Shu, 1983; Crutcher, 2012), short GMC lifetimes (Murray, 2011; Dobbs & Pringle, 2013), and turbulence (Larson, 1981; Mac Low & Klessen, 2004; Federrath, 2015).

GMCs are turbulent, characterized by a log-normal column density probability distribution function (Vazquez-Semadeni, 1994; c.f. Alves et al., 2017) and logarithmic relationship between their physical size and velocity width (Larson, 1981). However, turbulence in GMCs rapidly decays within a cloud crossing time (Mac Low et al., 1998; Stone et al., 1998; Padoan & Nordlund, 1999). If turbulence is responsible for supporting clouds, it must be maintained by some mechanism.

Mechanical and thermal feedback from forming stars can deposit significant energy and momentum into GMCs. This can help maintain cloud turbulence and support against gravitational collapse, helping to explain the low star-formation efficiencies observed in GMCs (Nakamura & Li, 2007; Federrath, 2015). It remains uncertain how these mechanisms maintain cloud turbulence. Therefore, it is important to measure how much energy and momentum are supplied by different stellar feedback mechanisms.

Young protostars launch accretion-driven collimated outflows (Arce et al., 2007; Frank et al., 2014; Bally, 2016). More evolved pre-main sequence and main sequence stars are less embedded than their younger counterparts and drive wide-angle or spherical winds (Castor et al., 1975; Vink et al., 2000; Bally, 2011).

Massive stars have long been known to drive powerful stellar winds that impact the

surrounding interstellar medium. In the last several years, *Spitzer* surveys of the galactic plane have revealed ‘bubbles’, mostly powered by massive stellar winds (Churchwell et al., 2006, 2007; Beaumont & Williams, 2010; Deharveng et al., 2010; Beaumont et al., 2014).

Arce et al. (2011) discovered expanding shells in the Perseus molecular cloud, which is not forming massive ionizing stars. They showed that these expanding shells have enough energy and momentum to drive cloud turbulence in Perseus. These shells must be driven by intermediate-mass stars or protostars. Offner & Arce (2015) found that a spherical stellar wind of sufficient strength can drive Perseus-like shells when placed in a simulated turbulent cloud. In the Taurus molecular cloud, another low-mass star forming region, Li et al. (2015) identified many expanding shells.

We identify expanding spherical structures of molecular gas in the Orion A GMC, hereafter called ‘shells’. These shells are similar to the structures first found in the Perseus Molecular Cloud by Arce et al. (2011) and later in the Taurus Molecular Cloud by Li et al. (2015). In Orion, shell-like structures have been identified by Heyer et al. (1992) and Nakamura et al. (2012). This study is the first systematic search for expanding shells in Orion.

The Orion A GMC, located behind the Trapezium OB association, is the nearest massive star forming region. Orion A has been extensively observed at all wavelengths, including CO spectral mapping by Bally et al. (1987), Wilson et al. (2005), Shimajiri et al. (2011), Ripple et al. (2013), and Berné et al. (2014). The cloud is filamentary and exhibits a North-South velocity gradient of about  $9 \text{ km s}^{-1}$  (Bally, 2008). The cloud is forming both massive stars, traced by the HII regions M42 and M43 in the north, as well as lower mass stars along the ‘integral shaped filament’ and in the NGC 1999 and L1641 clusters in the southern part of the cloud. We adopt a distance to Orion A of 414 pc (Menten et al., 2007).

In Section 3.4 we describe our data and how we find and characterize shells. In Section 3.5 we present the shells found in Orion A and discuss several shells in detail. In

Section 4.4.2, we discuss the mass, momentum, and kinetic energy of the shells. In Section 3.6 we compare the impact of the shells on the cloud to turbulence and protostellar outflows and discuss mechanisms that may drive the shells.

## 2.2 Methods

### 2.2.1 Nobeyama Radio Observatory 45m Observations

We briefly describe the observations here. For more detail, see Kong et al. (2018, Section 2.2). From 2007 to 2017, we carried out observations of  $^{12}\text{CO}(1\text{-}0, 115.271 \text{ GHz})$  and  $^{13}\text{CO}(1\text{-}0, 110.201 \text{ GHz})$  in Orion A with the Nobeyama Radio Observatory 45-meter telescope (NRO). From 2007 to 2009 and 2013 to 2014, we used the 25-beam BEARS focal plane array. With BEARS, we used 25 sets of 1024 channel auto-correlators with a 32 MHz bandwidth for a velocity resolution of  $\sim 0.1 \text{ km s}^{-1}$  at 115 GHz (Shimajiri et al., 2011; Nakamura et al., 2012; Shimajiri et al., 2014). From 2014 to 2017, we used the new 4-beam FOREST receiver with the SAM45 spectrometer for a velocity resolution of  $\sim 0.04 \text{ km s}^{-1}$  at 115 GHz.

We combine the FOREST and BEARS maps for the best sensitivity and coverage. The final NRO map has a beam FWHM of  $\sim 22''$  (0.04 pc at a distance of 414 pc) and a velocity resolution of  $\sim 0.22 \text{ km s}^{-1}$ .

### 2.2.2 Infrared Data

To assist with our search for expanding shells (see Section 2.2.4), we use archival infrared images from the Spitzer Heritage Archive. We search IRAC 3.6/8  $\mu\text{m}$  and MIPS 24  $\mu\text{m}$  for dust rings correlated with the CO shells. IRAC images are from Spitzer Programs 43 and 30641 (PI: Fazio). MIPS images are from Spitzer Programs 47 and 30641 (PI: Fazio). We also look for correlated structures in the effective dust temperature maps from Lombardi

et al. (2014) produced by fitting the spectral energy distribution (SED) of the *Herschel* and *Planck* maps.

### 2.2.3 Source Catalogs

To match expanding shells with the stars that may be driving them, we use catalogs of intermediate-mass stars and young stellar objects (YSOs) in Orion A. We queried *Simbad* for all stars with spectral type B, A, or F in the area. These intermediate-mass main sequence and pre-main sequence stars are good candidates for driving CO shells.

We also use the Spitzer Orion catalog of protostars and pre-main sequence stars produced by Megeath et al. (2012). The stars are classified as protostars or disk stars (pre-main sequence stars) by their infrared photometry. Stars with rising or flat SEDs between 4.5 and 24  $\mu\text{m}$  are classified as protostars. All other stars with infrared excess are considered to have disks and have dispersed their natal envelope. These (mostly low-mass) young stars are potential driving sources for shells, especially when clustered (see Nakamura et al., 2012).

### 2.2.4 Identifying shells

We identify shell candidates visually by searching in the CO channel maps for circular cavities that change in size with velocity - a signature of expansion. We also look in the position-velocity (PV) diagram for a  $\cup$  or  $\cap$ -shaped feature indicating expansion (see Arce et al., 2011, Figure 5).

We match the shell candidates against the source catalogs described in Section 2.2.3 to identify stars that may drive the shells. If a YSO from the Spitzer Orion catalog or an intermediate-mass BAF-type star is located inside the shell radius in projection, we consider this a potential driving source of the shell. The source need not be at the center of the shell. If the driving mechanism is not continuous, we may expect a star to

have moved from the shell center. Hartmann (2002) found an average relative velocity of  $0.2 \text{ km s}^{-1}$  between protostars and gas in the Taurus Molecular Cloud. In Orion, Tobin et al. (2009) found a similar velocity difference between stars and gas. In 1-2 Myr, a source moving at  $0.2 \text{ km s}^{-1}$  may travel 0.2-0.4 pc (100-200'') from the center of the shell. This distance is similar to the typical radius of a shell (Table 2.1).

We use infrared images of dust emission to identify dust swept up in expanding shells. Using the Spitzer IRAC and MIPS maps described in Section 2.2.2, we search for rings of dust emission that are correlated with CO shells. Using the Planck-Herschel map, we search for dust temperature correlations with the shells.

We score the reliability of each shell candidate by the number of criteria it satisfies. The criteria used to score each shell are:

1. The CO channel maps show expanding velocity structure.
2. The position-velocity diagram of the shell shows an expansion signature ( $\cup$  or  $\cap$  shape) as modeled in Section 2.2.5.
3. The shell has a circular shape in integrated CO and/or IR dust emission. To satisfy this criterion, the shell emission must be visible around at least half of the circular cavity.
4. The CO shell is correlated with infrared nebulosity in at least one band. This criterion is satisfied if any part of the observed CO shell (including a central cavity) is traced by a similar feature in an infrared band.
5. The shell contains a candidate driving source.

These criteria are subjective, and are not intended to definitively determine which shells are "real" but to give a relative measure of significance. We encourage readers to use the included figures to judge these criteria for themselves.

## 2.2.5 Characterizing Shells

We characterize each shell with four parameters: radius, thickness, expansion velocity, and central velocity. To find the most likely parameters, we use the model described below.

### A Simple Expanding Shell Model

We use a simple model for an expanding shell adapted from Arce et al. (2011). The model assumes uniform expansion, spherical symmetry and optically thin emission.

To create a model spectral cube of an expanding shell, we first randomly sample points from a spherical shell of uniform volume density with radius  $R$  and thickness  $dr$ . The number of points we sample is chosen to ensure there are several points per resolution element of the final spectral cube. We assign each sample a line-of-sight velocity  $v_z$  which scales with its displacement along the line-of-sight  $z$  and radial displacement  $r$  from shell center:

$$v_z = v_{\text{exp}} \frac{z}{r} + v_0 \quad (2.1)$$

where  $v_{\text{exp}}$  is the expansion velocity of the shell and  $v_0$  is the central velocity of the shell. We bin the sampled points by position on the sky and line-of-sight velocity to make a synthetic position-position-velocity cube with the same dimensions as the observed CO cube.<sup>1</sup>

The shell model described in Arce et al. (2011) can incorporate a turbulent cloud of uniform mean density. However, since we do not attempt to describe the underlying cloud properties, we simplify the model by removing the cloud component and only considering  $R$ ,  $dr_{\text{shell}}$ ,  $v_{\text{exp}}$ , and the central velocity of the shell  $v_0$ .

We vary these four model parameters and visually compare the model and observed integrated emission and position-velocity diagrams of each shell candidate. Table 2.1 lists

---

<sup>1</sup>The model cube is padded by 5 pixels on each side and by 5 channels blueward and redward of the most extreme shell velocities. All velocities in this paper are taken with respect to the local standard of rest (LSR).

the parameters of the model that most closely matches the observations. We vary each parameter individually while holding the others fixed to visually estimate the parameter uncertainties reported in Table 2.1. Expansion velocity is the most uncertain parameter, as most shell candidates are not detected over their entire velocity range. Therefore, the estimated expansion velocity may be considered a lower limit.

The model is meant to be a very idealized version of an expanding shell. Real shells are not symmetric; they inherit the turbulent structure of the cloud emission. Unlike the model, most observed shells are not completely contained within the cloud. Our model also assumes optically thin emission, which is unrealistic for  $^{12}\text{CO}$  (and possibly  $^{13}\text{CO}$ ) over much of the cloud. Because the model is not flexible enough to account for these complications, we do not attempt a statistical fit of the model to the CO data. The parameter ranges reported in Table 2.1 produce the range of models that most closely resemble the observed shells.

Model PV diagrams are shown in Section 3.5. These figures show that matching any one model to an observed shell is difficult and this is reflected in the uncertainties on the model parameters we report in Table 2.1.

## 2.3 Results

We identify 42 shell candidates in Orion A. Figure 2.1 shows the peak  $^{12}\text{CO}$  brightness temperature in Orion A with shell candidates overlain. Table 2.1 lists the estimated range in model parameters (radius, thickness, expansion velocity, and systemic velocity) of the shell candidates.

Table 2.2 lists the criteria (defined in Section 2.2.4) each shell candidate satisfies. We assign a confidence score of 1 to 5 to each shell equal to the number of criteria the shell satisfies. A score of 1 means the shell candidate was identified in CO channel maps but satisfies no other criteria. A score of 5 is given to the shells which satisfy all criteria. The

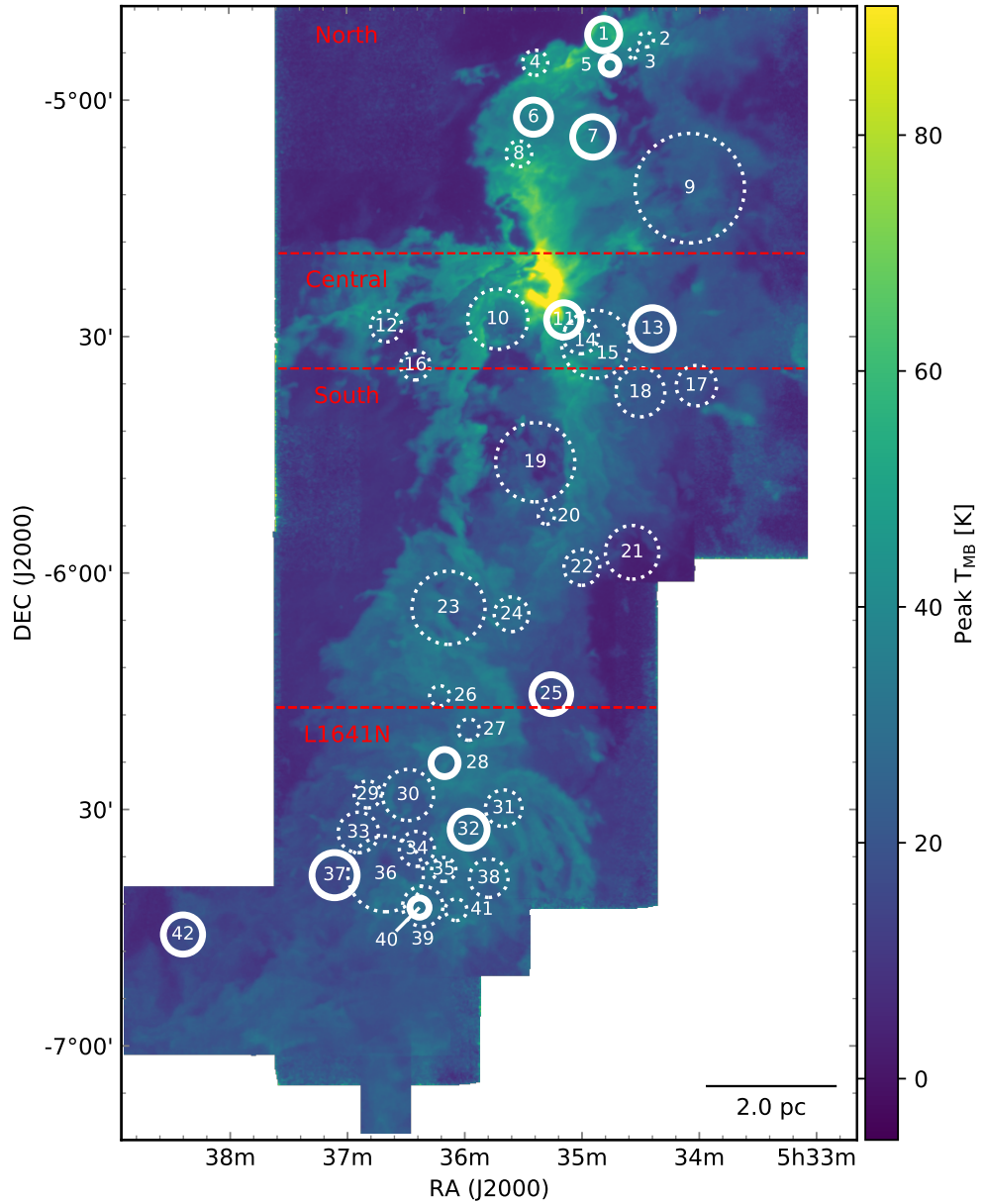


Figure 2.1 Peak  $^{12}\text{CO}$  intensity with shell candidates. Solid circles indicate 12 shells that satisfy all criteria listed in Section 2.2.4. Dashed circles show 30 less robust shell candidates.

properties of this most reliable subset of shells do not differ systematically from the full set.

We present figures detailing all 42 shell candidates in the online journal. For each shell, we show a representative infrared image with integrated CO contours, CO channel maps<sup>2</sup>, and a CO position velocity diagram. We discuss four shells in detail here. These four are not meant to be representative of the entire sample. They are chosen for their CO morphology and interesting candidate driving sources which show clear signs of intermediate-mass stellar feedback on the cloud.

### 2.3.1 A Shell Near The Herbig Ae Star T Ori

Shell 10 is about 0.16 degrees (1.2 pc) southeast of the massive molecular core OMC 1. The shell meets 4 of the criteria listed in Section 2.2.4.

**CO Channel Maps** This shell, like most in the catalog, was first discovered by inspecting the  $^{12}\text{CO}$  channel maps (Figure 2.2). The shell first appears as disconnected clumps at  $8.5 \text{ km s}^{-1}$ . At higher velocities, the shell gains prominence and is most clearly seen as the C-shaped structure at  $10.7 \text{ km s}^{-1}$ . The shell emission decreases in radius in subsequent channels as the cross section of the shell on the sky shrinks. At  $12\text{--}13.3 \text{ km s}^{-1}$ , an unrelated spur of  $^{12}\text{CO}$  appears to the southwest of the shell. This spur is part of the larger scale expansion driven into the molecular cloud by the M42 HII region. This expansion, identified by Loren (1979) and Heyer et al. (1992), can also be seen near Shell 11 in Figure 2.11.

**Position-Velocity Diagram** Figure 2.3 shows the position-velocity diagram of  $^{12}\text{CO}$  across this shell. To increase the signal to noise in the PV diagram, we compute the

---

<sup>2</sup>The figures include CO channels that show clear shell emission. Sometimes the best model central velocity listed in Table 2.1 corresponds to a channel that does not contain emission. In this case, the shell velocity range in Table 2.1 will not be the same as the velocity range shown in the channel maps.

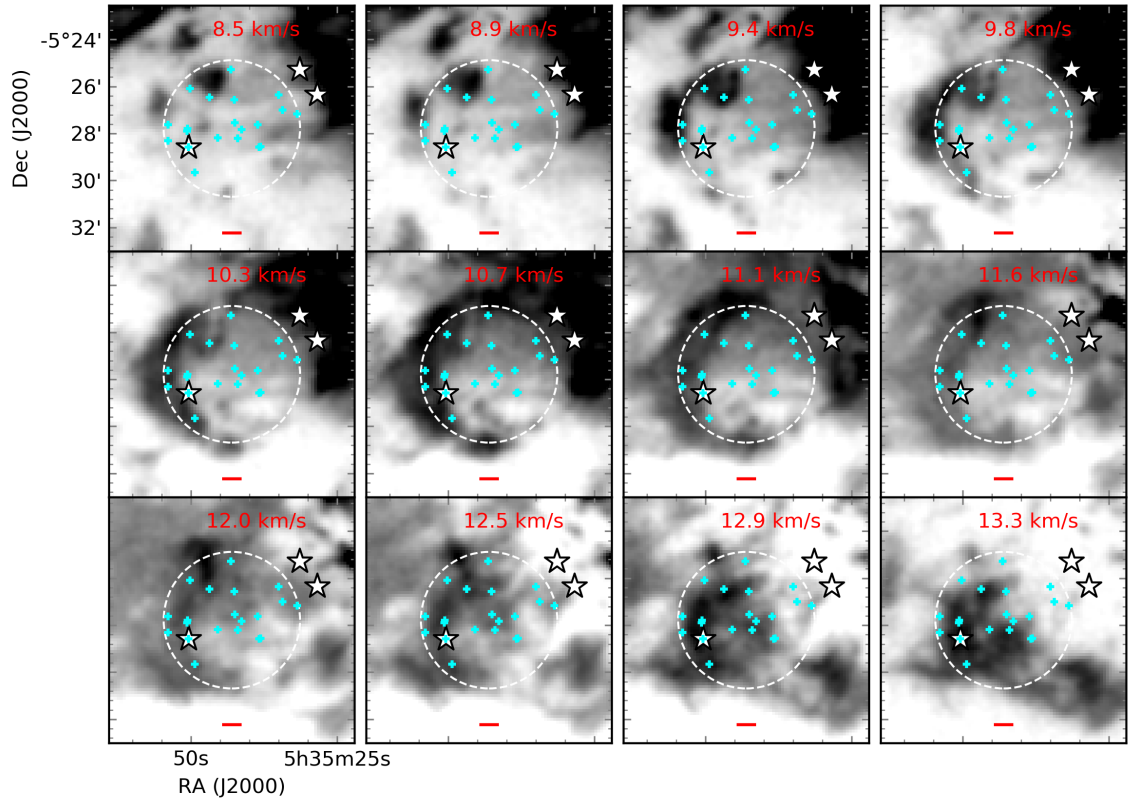


Figure 2.2  $^{12}\text{CO}$  channel maps of Shell 10, thought to be powered by T Ori. Stars indicate intermediate-mass stars of spectral type B, A, or F and are labeled in Figure 2.4. Cyan crosses indicate pre-main sequence stars from the Spitzer Orion catalog. The full best-fit radius is shown as a dashed white circle. Velocities are with respect to the local standard of rest. The red scalebar has a length of 0.1 pc. The full figure set of channel maps (42 images) is available in the online journal.

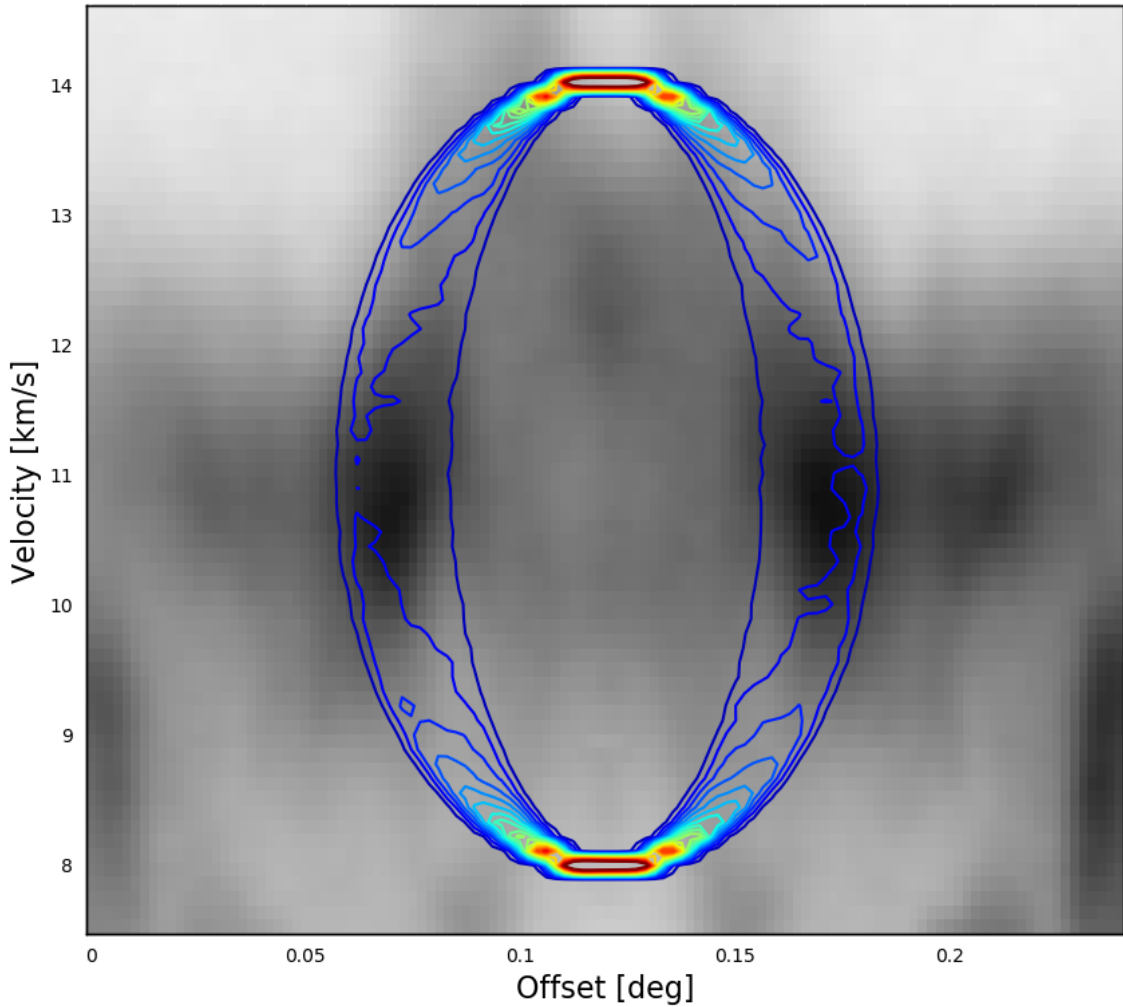


Figure 2.3 Azimuthally averaged position-velocity diagram of  $^{12}\text{CO}$  emission toward Shell 10. Darker colors indicate more intense emission. We extract emission along 4 equally spaced slices through the center of the shell and then average. The approaching and receding caps of the shell are not clearly detected. Contours show the model that best represents the shell. The model parameters are given in Table 2.1. The full figure set of PV diagrams (42 images) is available in the online journal.

azimuthally averaged PV diagram through the center of the shell at four equally spaced position angles. The PV diagram does not clearly show the  $\cup$  or  $\cap$ -shaped signature expected of an expanding structure. However, averaging across many position angles may dilute the expansion signature if the shell is not azimuthally symmetric. In the case of Shell 10, the averaged PV diagram may dilute some of the emission at  $v > 12.5 \text{ km s}^{-1}$ .

**Infrared Nebulosity** Figure 2.4 shows the  $8 \mu\text{m}$  map highlighting dust emission near the shell. The dust emission towards the west side of the shell is spatially coincident with the CO structure. An unrelated infrared-bright spur (see Shimajiri et al., 2011, 2013) projected from north to south through the center of the shell highlights the cometary structure shaped by the hard ionizing radiation field from the Trapezium OB association to the northwest.

**Potential Driving Sources** This shell contains several intermediate-mass stars and protostars. T Ori is a 5 Myr old Herbig A2-3e star (Hillenbrand et al., 1992; Liu et al., 2011) offset from the center of the shell by approximately 0.2 pc to the southeast. Fuente et al. (2002) identified a cavity in integrated  $^{13}\text{CO}$  and  $\text{C}^{18}\text{O}$  around T Ori. They argue that intermediate-mass pre-main sequence stars like T Ori excavate the molecular gas around them over time. They find the youngest stars in their sample at peaks of dense gas and more evolved pre-main sequence stars (like T Ori) in cavities, attributing this excavation to stellar winds. Liu et al. (2011) modeled the spectral energy distribution of T Ori, deriving an age of  $\approx 5 \text{ Myr}$  and an accretion rate of  $\approx 3 \times 10^{-7} M_{\odot} \text{ yr}^{-1}$ . Protostellar mass-loss rates are expected to be approximately 10-30% of their accretion rates (e.g., Pudritz et al., 2007; Mohanty & Shu, 2008). T Ori falls within the Herbig Ae/Be mass-loss rates of  $10^{-8}$  to  $10^{-7} M_{\odot} \text{ yr}^{-1}$  measured by Skinner (1994). The mass-loss rate required to power the shell around T Ori is  $\approx 10^{-6} M_{\odot} \text{ yr}^{-1}$ , an order of magnitude higher than the estimated mass-loss rate (See Table 4.2; Section 2.5.2).

$\theta^2\text{Ori C}$ , located just outside the edge of the shell, is a B4/5 star in the Orion Nebula

Cluster. Though it lacks spectral emission lines, this star has been included as a Herbig Be star by many authors based on its far-infrared excess (The et al., 1994). Manoj et al. (2002) argues that  $\theta^2$ Ori C is a young ( $\approx 1$  Myr) pre-main sequence star surrounded by dust. X-ray observations show strong flares from this star, which Stelzer et al. (2005) put forward as evidence for a low-mass T-Tauri companion to  $\theta^2$ Ori C. Megeath et al. (2012) classify  $\theta^2$ Ori C as a pre-main sequence star with a disk, based on its mid-infrared colors.

Another possibility is that this shell is shaped by the UV radiation field from the Trapezium cluster to the northwest. In this case, the shell could be seen as an extension of the cometary photon dominated region (PDR) to the south denoted the “dark lane south filament” by Shimajiri et al. (2011, 2013). However, the velocity of the PDR ranges from 5-8 km s $^{-1}$  while the shell is seen at 8-13 km s $^{-1}$ . Thus, the shell is distinct in velocity-space from these cometary pillars.

Because of its proximity to the projected center of the shell and known winds, T Ori is the most likely driving source of Shell 10.

### 2.3.2 Two Nested Shells Around V380 Ori

We identify two nested expanding shells near the young Herbig B9e star V380 Ori. Shell 39, the larger of the two, was first identified while searching the CO channel maps. The smaller Shell 40 was found upon closer inspection for shells around potential driving sources. This region also contains several Herbig-Haro (HH) objects (Stanke et al., 2010) and CO outflows (Morgan et al., 1991; Moro-Martín et al., 1999).

**CO Channel Maps** Figure 2.5 shows Shell 39 in  $^{12}\text{CO}$ . Shell 39 is most clearly defined by the arcs of emission at 9.8-10.9 km s $^{-1}$  to the north and southeast of the center. At 8.9-9.4 km s $^{-1}$ , an unrelated spur of emission appears to the north, and at 10-10.9 km s $^{-1}$ , another unrelated spur is visible to the south.

Nested inside of Shell 39, Shell 40 is shown in the  $^{12}\text{CO}$  channel maps in Figure 2.6.

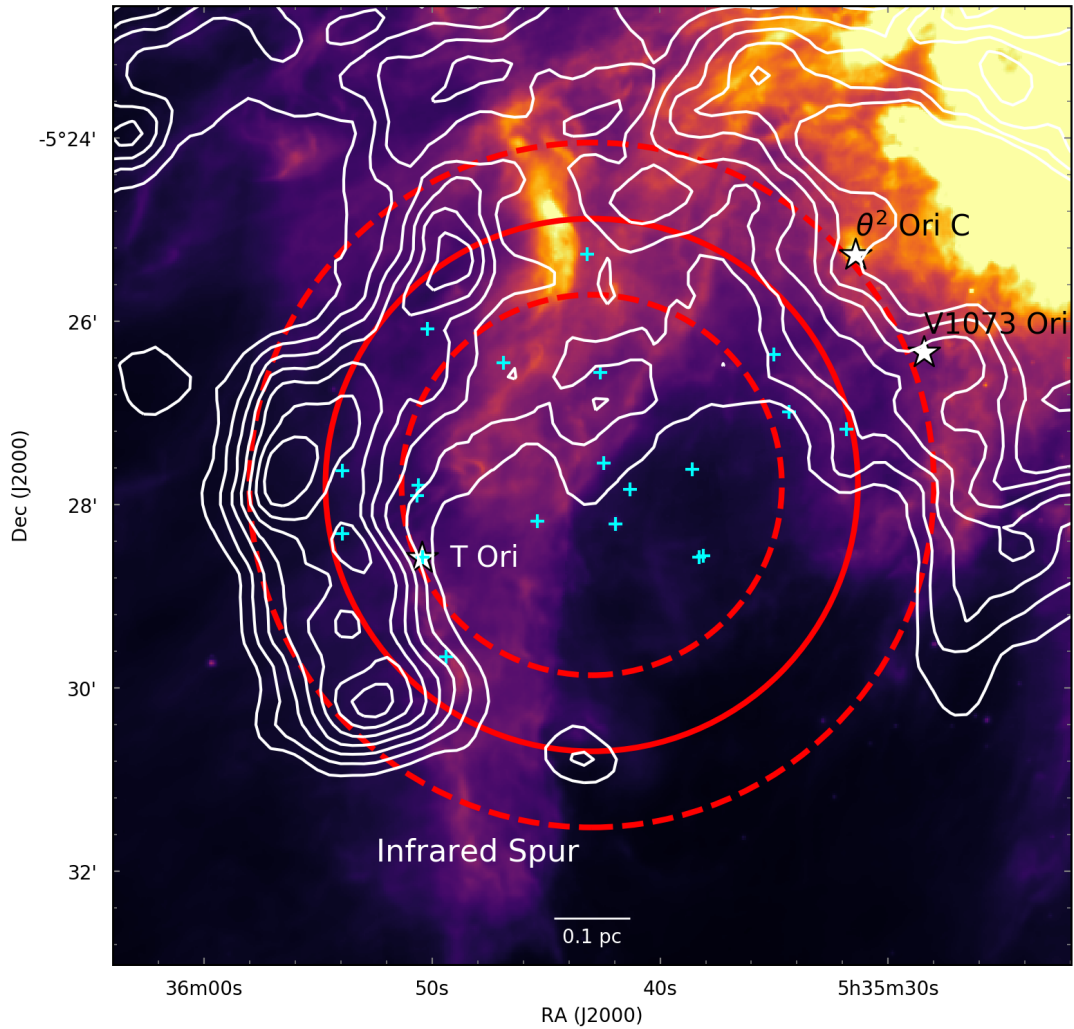


Figure 2.4 Spitzer 8  $\mu\text{m}$  map toward Shell 10. Contours show  $^{13}\text{CO}$  integrated from 8.5 to 13.5 km s $^{-1}$ . Contours are drawn from 10 to 22 $\sigma$  with steps of 2 $\sigma$ , where  $\sigma = 1.2 \text{ K km s}^{-1}$ . Symbols are the same as Figure 2.2. The large solid circle and dashed annulus indicate the best-fit radius and thickness of the CO shell, respectively. The full figure set (42 images) is available in the online journal.

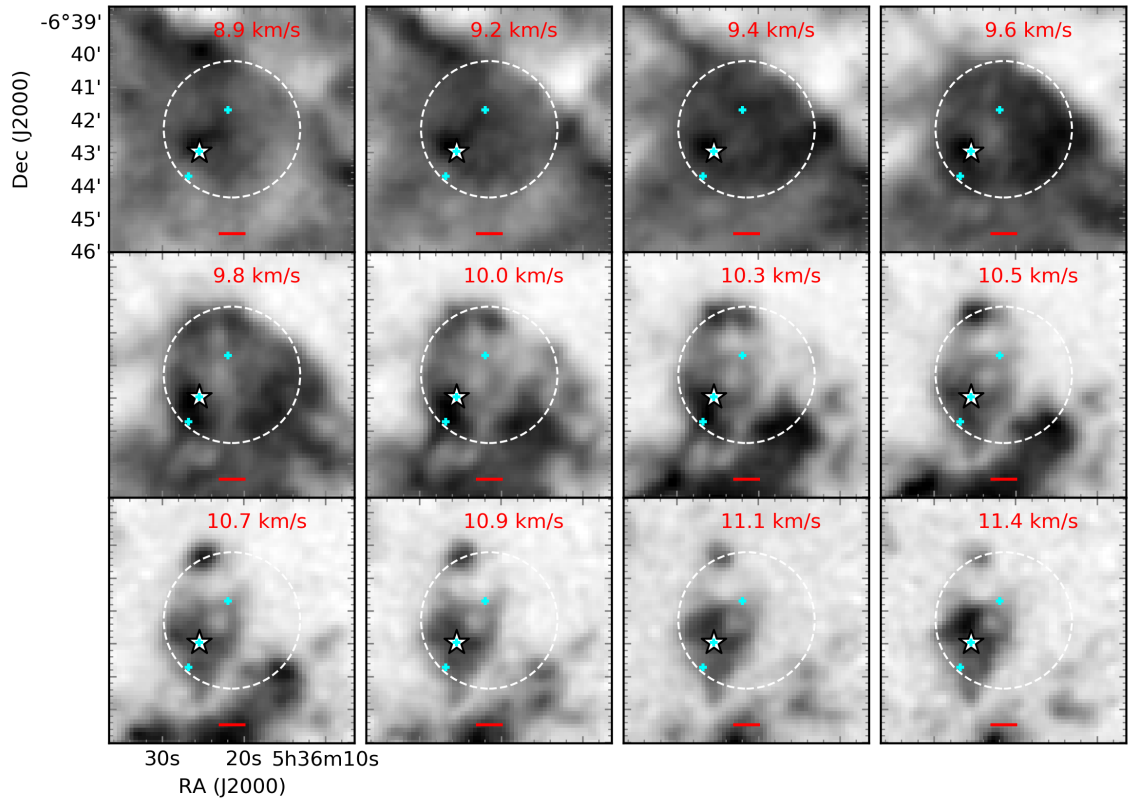


Figure 2.5  $^{12}\text{CO}$  channel maps of Shell 39, the larger of the two shells around V380 Ori. Symbols are the same as Figure 2.2. The best-fit model radius is shown as a white dashed circle. The smaller Shell 40 can be seen near V380 Ori (white star). The red scalebar has a length of 0.1 pc.

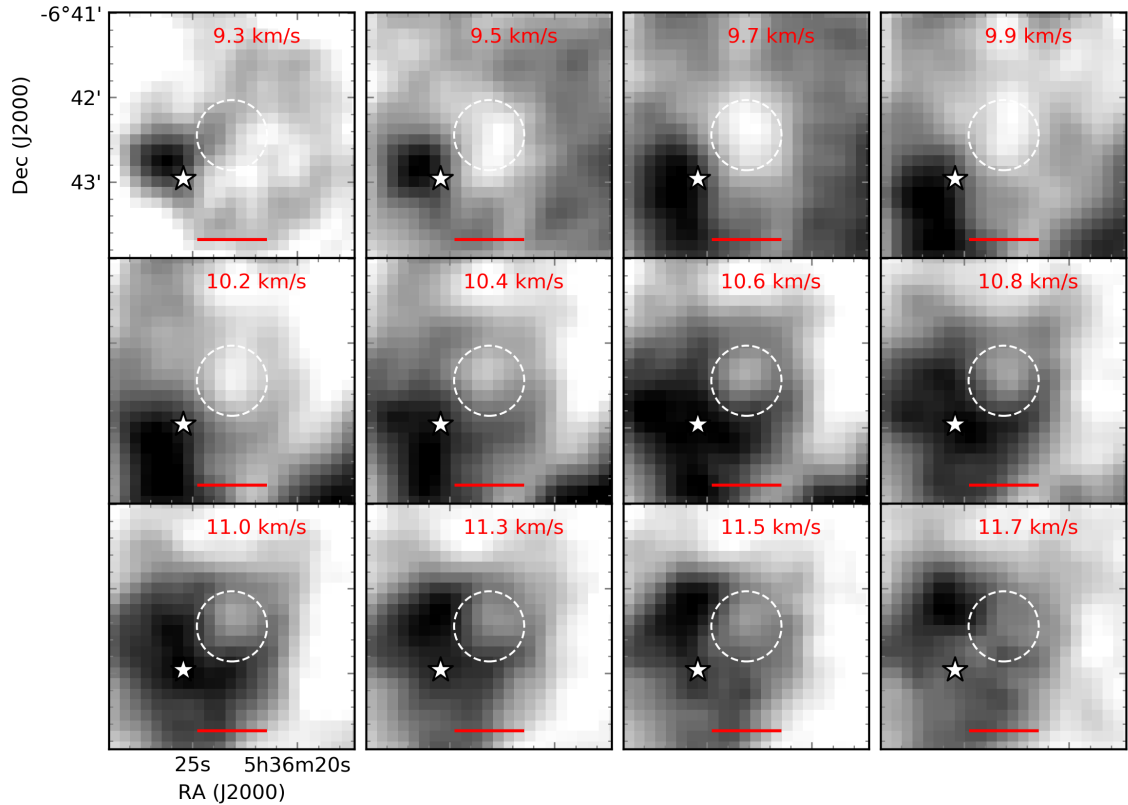


Figure 2.6  $^{12}\text{CO}$  channel maps of Shell 40, the smaller of the two shells associated with V380 Ori. Symbols are the same as Figure 2.2. The best-fit model radius is shown as a white dashed circle. The red scalebar has a length of 0.1 pc.

Shell 40 is one of the most ideally symmetric shells in the catalogue, with a circular cavity that persists at higher velocities than the larger Shell 39. In fact, Shell 40 includes some of the highest velocity CO emission in the southern half of Orion A. The “smoke-ring” structure of Shell 40 is most clearly seen in the channel maps at  $10.4\text{--}10.8 \text{ km s}^{-1}$ .

**Position-Velocity Diagram** Figure 2.7 and Figure 2.8 show azimuthally averaged position-velocity diagrams of  $^{12}\text{CO}$  towards Shell 39 and Shell 40 respectively. We only detect the side of Shell 39 approaching us, lending its PV diagram a U-shaped morphology. Because we do not detect the shell through its entire velocity range, the expansion velocity is difficult to constrain. By contrast, Shell 40 is detected over most of its velocity range and shows a mostly complete ring structure in its PV diagram. The shell is very faint compared to the cloud emission at lower velocities, but its uniquely high central velocity separates it well from the rest of the cloud.

**Infrared Nebulosity** Figure 2.9 shows  $8 \mu\text{m}$  emission along with integrated  $^{13}\text{CO}$  towards Shell 39. Much of the  $8 \mu\text{m}$  emission in this area is concentrated to the north and west of the shell. This may be dust swept up by the part of the shell where CO is not seen or could be unrelated.

Figure 2.10 shows integrated  $^{12}\text{CO}$  toward Shell 39 with a three-color optical image taken from the Hubble Legacy Archive. There is no sign of related emission in the Spitzer images, but this shell is likely related to the dark cavity excavated by V380 Ori. We discuss this cavity in more detail below.

**Potential Driving Sources** The most likely driving source for both of these shells is the V380 Ori system. V380 Ori consists of a 1-3 Myr Herbig B9e star with a luminosity of  $200 L_\odot$  (Rodríguez et al., 2016), an infrared companion identified by Leinert et al. (1997), a low-mass spectroscopic companion with a luminosity of  $3 L_\odot$  (Alecian et al., 2009), and a fourth M5/6 companion (Reipurth et al., 2013).

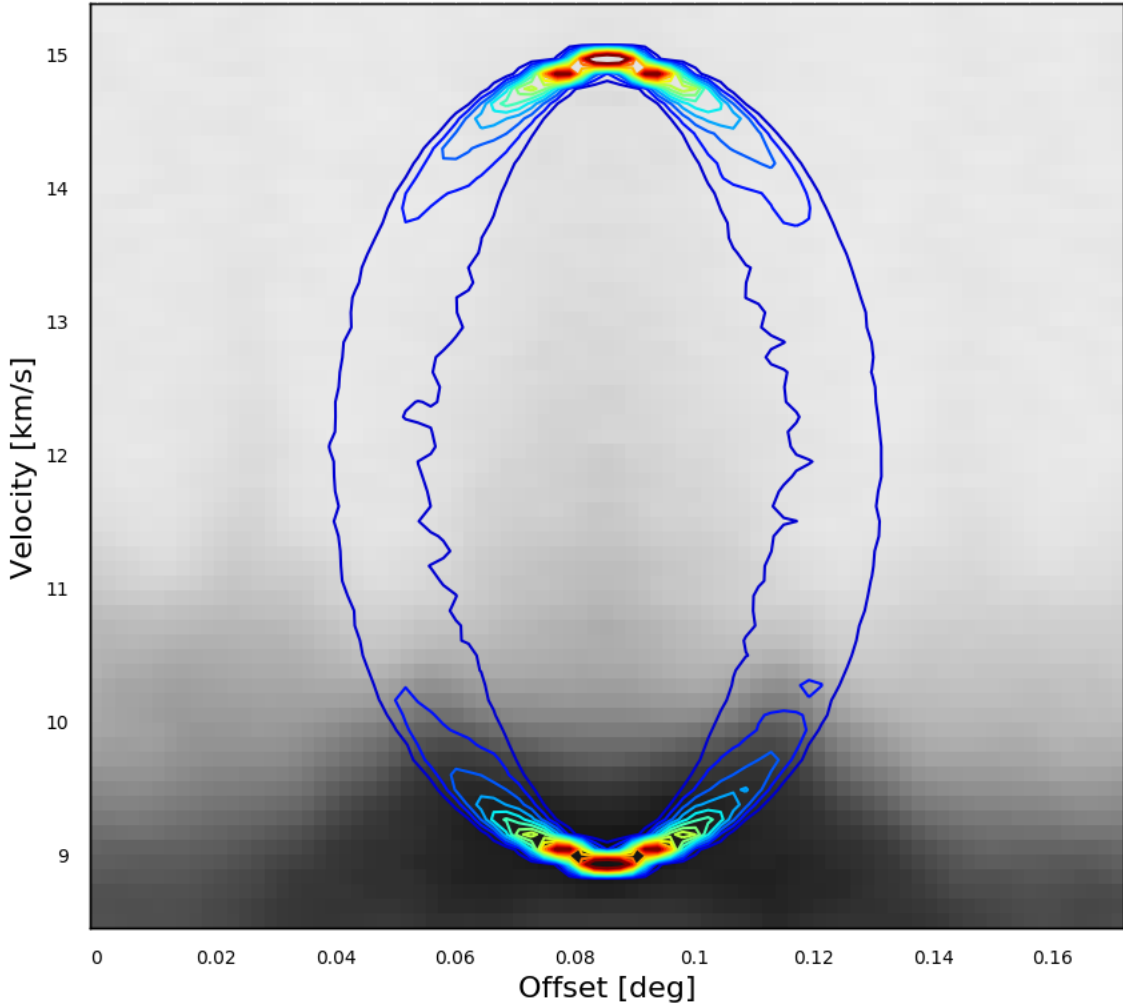


Figure 2.7 Shell 39  $^{12}\text{CO}$  position-velocity diagram. We extract emission along 4 equally spaced slices through the center of the shell and average. Contours show the model that best represents the shell. The model parameters are given in Table 2.1. Based on the U-shaped PV diagram, we only detect the near, approaching cap of the shell.

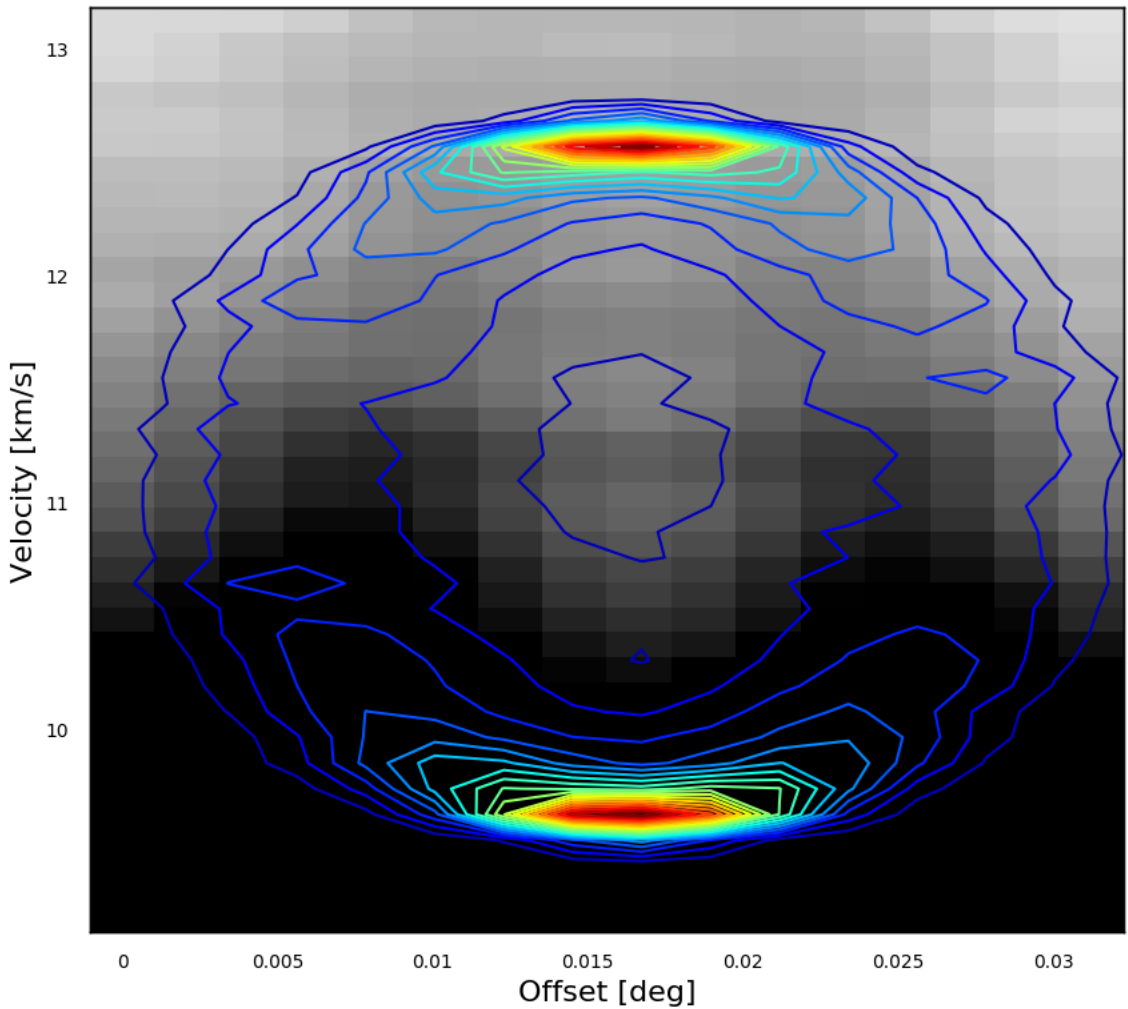


Figure 2.8 Shell 40  $^{12}\text{CO}$  position-velocity diagram. We extract emission along 4 equally spaced slices through the center of the shell and average. Contours show the model that best represents the shell. The model parameters are given in Table 2.1.

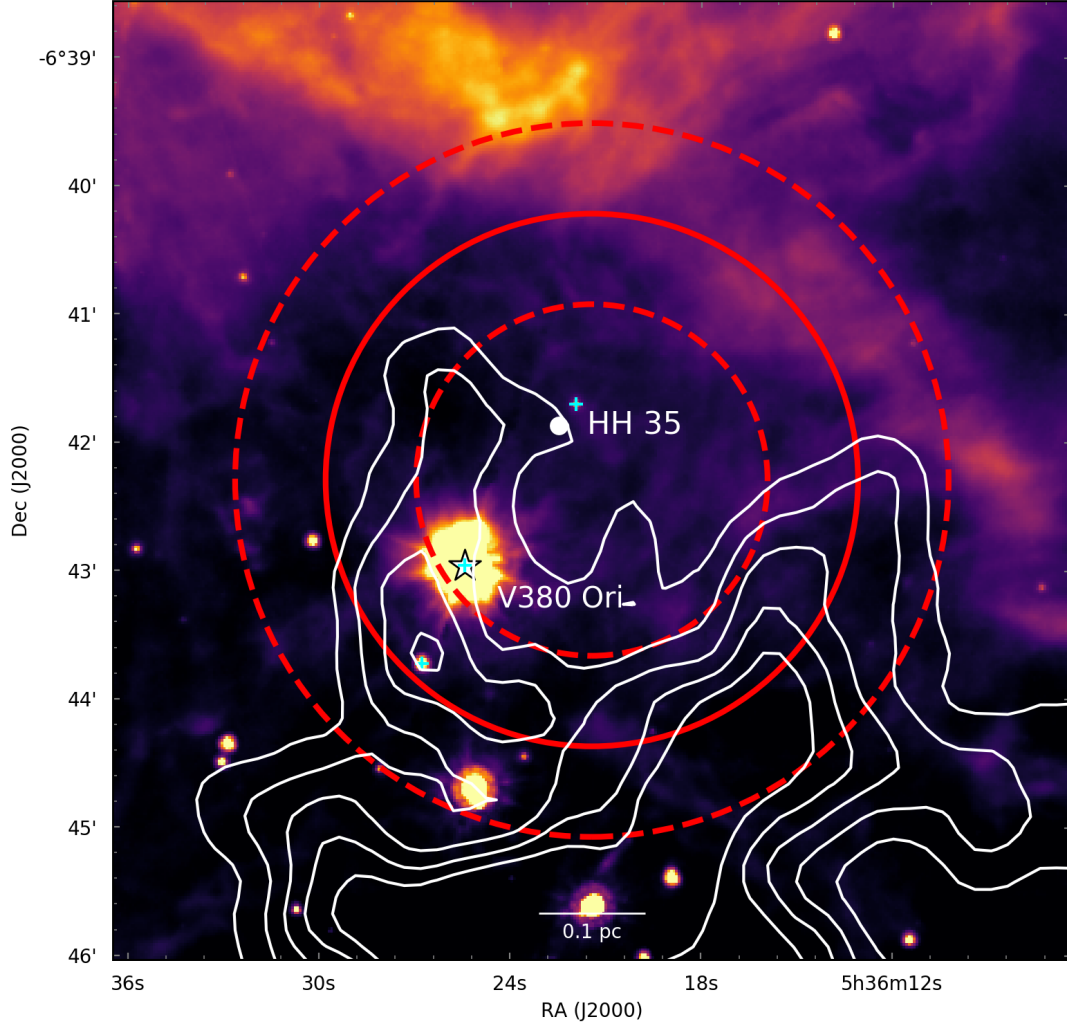


Figure 2.9 Spitzer  $8 \mu\text{m}$  map toward Shell 39. Contours show  $^{13}\text{CO}$  integrated from  $9$  to  $11 \text{ km s}^{-1}$ . Contours are drawn from  $20$  to  $40\sigma$  with steps of  $5\sigma$ , where  $\sigma = 0.5 \text{ K km s}^{-1}$ . The star indicates the Herbig B9e star V380 Ori. The cyan crosses indicate pre-main sequence stars from the Spitzer Orion catalog. The filled white circle indicates the Herbig-Haro object HH 35. The large solid circle and dashed annulus indicate the best-fit radius and thickness of the CO shell, respectively.

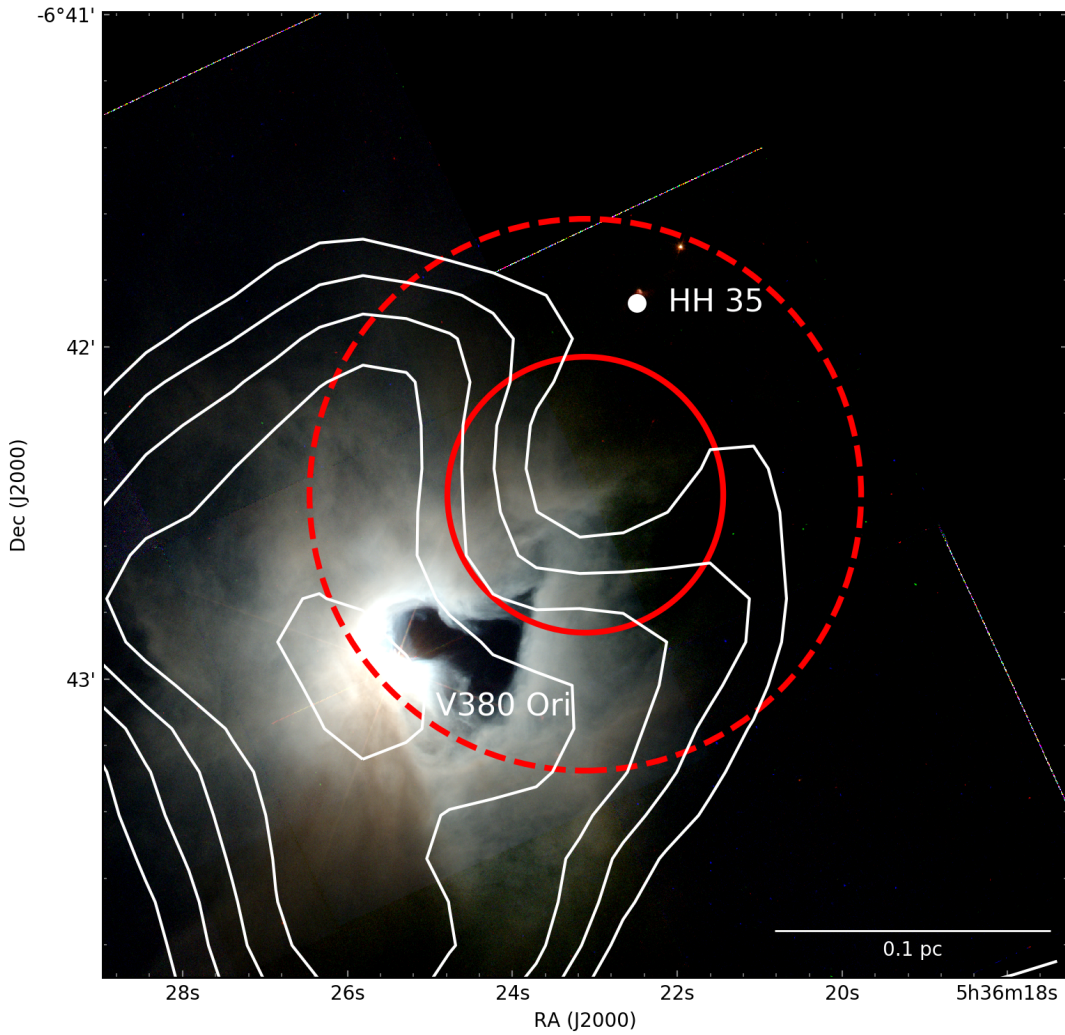


Figure 2.10 *HST WFC2* composite image toward Shell 40 with F450W/F555W/F675W filters represented by red/green/blue colors respectively (Hubble Legacy Archive - Program 8548, PI: K. S. Noll). Contours show  $^{12}\text{CO}$  integrated from  $10.2$  to  $12 \text{ km s}^{-1}$ . Contours are drawn from  $20$  to  $32\sigma$  with steps of  $3\sigma$ , where  $\sigma = 0.7 \text{ K km s}^{-1}$ . The bright nebulosity around V380 Ori is the reflection nebula NGC 1999. The dark feature is a cavity in the cloud, possibly excavated by outflows and/or winds from the Herbig B9e star V380 Ori. The Herbig-Haro object HH 35 (filled white circle) traces an outflow coming from the V380 Ori system which may help to shape the shell and cavity.

V380 Ori is responsible for several Herbig-Haro flows, including the 5.3 pc long HH 222/1041 flow identified by Reipurth et al. (2013). This flow may have originated in a massive accretion event triggered by a dynamical decay of the quadruple stellar system. Based on the proper motion of HH 222, this event occurred less than 28,000 yr ago. The expansion time of a shell assuming uniform constant expansion is  $t_{\text{exp}} = R/v_{\text{exp}}$ . For Shell 39,  $t_{\text{exp}} \approx 80,000$  yr. For Shell 40,  $t_{\text{exp}} \approx 30,000$  yr. If a shell's expansion has slowed over time it would be younger than this estimate. The same accretion-driven outburst that is responsible for the high-velocity large-scale Herbig-Haro flows may have caused an increased mass-loss rate and spherical wind that produced the expanding shells. The smaller-scale Herbig-Haro flows from V380 Ori are HH 1031/130 and HH 35, which may represent more recent dynamical interactions between the components of the V380 Ori system. Any of these interactions may have played a role in shaping the shells we see in this region.

Liu et al. (2011) fit the SED of V380 Ori to derive a current infall rate from the envelope of  $2 \times 10^{-6} M_{\odot} \text{ yr}^{-1}$  and a disk accretion rate of  $3 \times 10^{-9} M_{\odot} \text{ yr}^{-1}$ . Typically, the mass-loss rate of a protostar is expected to be about 10-30% of the accretion rate (e.g., Pudritz et al., 2007; Mohanty & Shu, 2008). This implies a mass-loss rate of  $3 \times 10^{-10}$  to  $9 \times 10^{-10} M_{\odot} \text{ yr}^{-1}$ . Shell 39 requires a wind mass-loss rate of a few  $10^{-7} M_{\odot} \text{ yr}^{-1}$  and Shell 40 requires  $10^{-8}$  to  $10^{-7} M_{\odot} \text{ yr}^{-1}$  (see Table 4.2). An accretion-driven outburst like the one discussed above could strengthen the wind enough to produce the expanding shell (see Offner & Arce, 2015, § 4.3.2). Such wind enhancements over short timescales ( $\approx 0.1$  Myr) could have powered the shells despite the much lower current mass-loss rate. We discuss this mechanism more in Section 3.6.

Adjacent to the NGC 1999 reflection nebula is a dark cavity in the cloud indicated by a deficit in far-infrared emission coupled with lower extinctions of background stars through this part of the nebula (Stanke et al., 2010). Figure 2.10 shows that the CO shell is offset from the optical cavity by about 0.1 pc. Stanke et al. (2010) speculate that that the outflow

driving HH 35 and H<sub>2</sub> 2.12 $\mu$ m shock SMZ 6-8 (Stanke et al. (2002)) is responsible for carving out the northern part of this cavity. Near this dark cavity, Corcoran & Ray (1995) found a cavity in H $\alpha$  that may also be related to the V380 outflows. In this scenario, the shell may be considered an evolved state of the wide-angle outflow cavities observed around outbursting pre-main sequence stars (Ruiz-Rodríguez et al., 2017; Principe et al., 2018).

### 2.3.3 A Shell Centered on LP Ori

Shell 11 is about 0.1 degrees (0.7 pc) southwest of OMC 1. At its center lies the pre-main sequence B2 star LP Ori.

**CO Channel Maps** Figure 2.11 shows <sup>12</sup>CO channel maps toward Shell 11. The distinctly circular shell is highlighted by emission along the rim to the northeast and west. The bright unrelated emission in the northeast corner of the channel maps is associated with the Orion Bar photodissociation region (PDR). Shell 11 is superimposed upon a larger CO expansion seen to the south and west at 13 to 13.5 km s<sup>-1</sup>. First identified by Loren (1979) and Heyer et al. (1992), this  $\approx$  2 pc CO shell traces the southern edge of the Orion Nebula HII region and is likely being driven by the expansion of the HII region into the molecular cloud behind it. The HII-driven CO expansion can also be seen in the vicinity of the T Ori shell (Section 2.3.1).

**Position-Velocity Diagram** Figure 2.12 shows the azimuthally-averaged position-velocity diagram of <sup>12</sup>CO toward Shell 11. The U-shape of the PV diagram indicates that the expanding shell is only detected at velocities blueward of the central shell velocity. Thus, we only see the emission on the near side of the shell while the far side of the shell has broken out of the cloud.

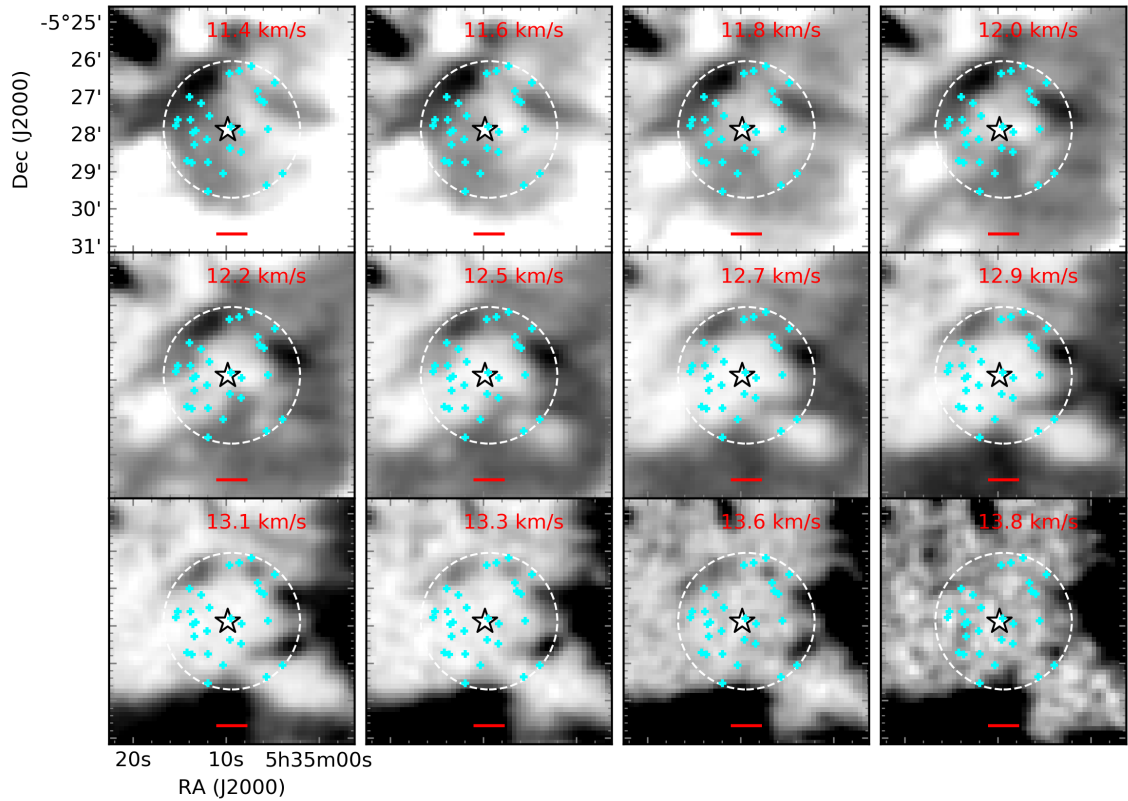


Figure 2.11  $^{12}\text{CO}$  channel maps of Shell 11, associated with LP Ori (white star). Symbols are the same as Figure 2.2. The best-fit radius is shown as a dashed white circle. The red scalebar has a length of 0.1 pc.

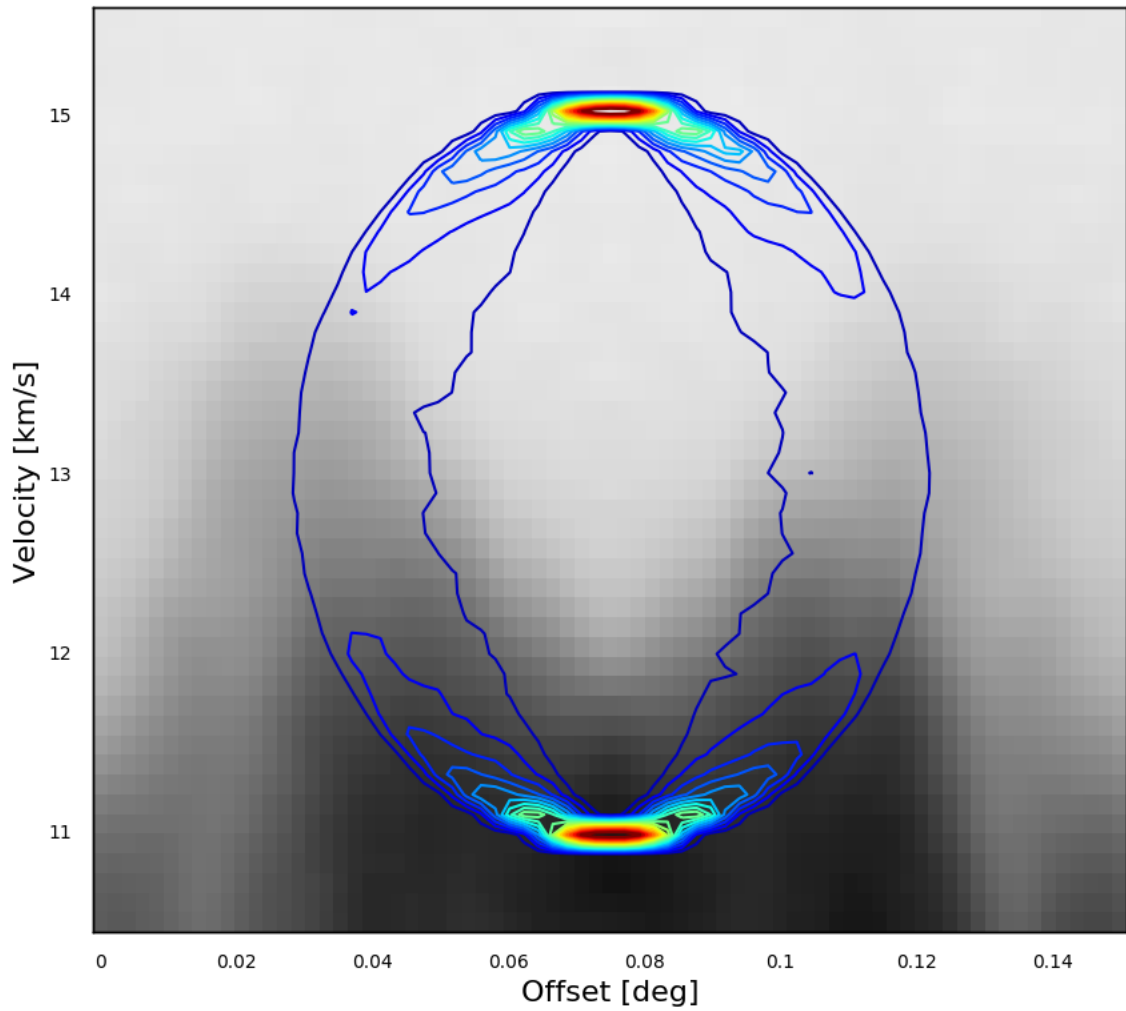


Figure 2.12 Azimuthally averaged position-velocity diagram of  $^{12}\text{CO}$  emission toward Shell 11. We extract emission along 4 equally spaced slices through the center of the shell and then average. Contours show the model that best represents the shell. The model parameters are given in Table 2.1. Based on the U-shaped PV diagram, we only detect the near, approaching cap of the shell.

**Infrared Nebulosity** Figure 2.13 shows  $8\text{ }\mu\text{m}$  emission along with integrated  $^{12}\text{CO}$  toward Shell 11. The shell is located near the bright infrared emission from the Orion Nebula in the northeastern corner of Figure 2.13). This complicates any analysis of dust emission correlated to the CO shell, but infrared nebulosity along the north and east of the shell rim may trace dust swept up by the shell. The central star LP Ori is shrouded in dust emission, a sign that it is still associated with its birth cloud.

**Potential Driving Sources** Located at the center of Shell 11, LP Ori (HD 36982) is a B2V pre-main sequence star (Hillenbrand et al., 2013). While it lacks spectral emission lines, LP Ori was classified as a Herbig Be star by Manoj et al. (2002) on the basis of its infrared excess. LP Ori is one of the  $\sim 7\%$  of Be stars with an organized magnetic field (Alecian et al., 2017), as measured by polarimetry (Petit et al., 2008; Alecian et al., 2013).

Using model stellar evolutionary tracks, Alecian et al. (2013) report a mass of  $7 M_{\odot}$  and age of 0.2 Myr. The age of LP Ori is consistent with Shell 11’s expansion time of 0.1 Myr.

Using the mass-loss recipe of Vink et al. (2000), Nazé et al. (2014) estimates LP Ori’s mass-loss rate at  $10^{-9} M_{\odot}\text{ yr}^{-1}$ , or 2-3 orders of magnitude lower than the necessary wind mass-loss rate needed to drive the observed shell (Table 4.2). In order to produce the required momentum, LP Ori may have undergone a burst of accretion-driven mass-loss.

## 2.4 Impact of Shells on Cloud

### 2.4.1 Measuring Mass, Momentum, and Kinetic Energy

We measure the mass, momentum, and kinetic energy of the shell candidates following methods laid out in Arce & Goodman (2001), Arce et al. (2010), and Arce et al. (2011). We briefly describe our method here. For more details, see Dunham et al. (2014a) and

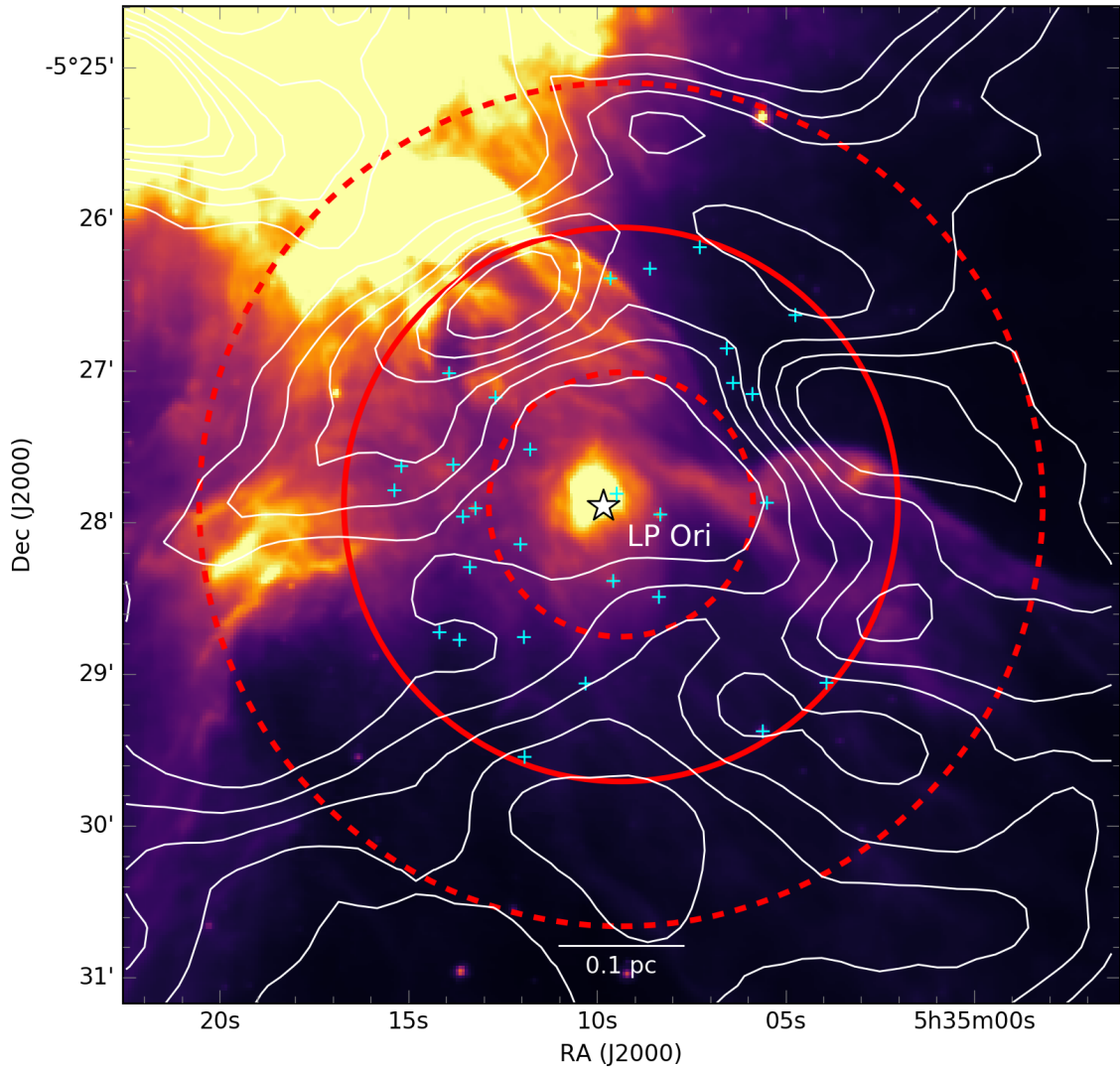


Figure 2.13 Spitzer  $8 \mu\text{m}$  map toward Shell 11. Contours show  $^{12}\text{CO}$  integrated from  $11.7$  to  $13.4 \text{ km s}^{-1}$ . Contours are drawn from  $35$  to  $75\sigma$  with steps of  $8\sigma$ , where  $\sigma = 0.7 \text{ K km s}^{-1}$ . The white star indicates the likely driving source - pre-main sequence B2V star LP Ori. Cyan crosses indicate pre-main sequence stars from the Spitzer Orion catalog. The large solid circle and dashed annulus indicate the best-fit radius and thickness of the CO shell, respectively.

Zhang et al. (2016).

To extract the shell from the spectral cube, we first construct a mask using a model cube generated from the best fit parameters as described in Section 2.2.5. We extract each shell multiple times using sets of model parameters spanning the ranges given in Table 2.1 to estimate the uncertainty on the derived physical properties.

Where  $^{13}\text{CO}$  is detected at  $5\sigma$  we assume it is optically thin and use it in the mass calculation. Where  $^{13}\text{CO}$  is not significant but  $^{12}\text{CO}$  is detected at  $5\sigma$ , we compute an opacity correction to  $^{12}\text{CO}$  using the  $^{12}\text{CO}/^{13}\text{CO}$  ratio in the vicinity of the shell. This correction is detailed below.

Assuming that  $^{12}\text{CO}$  and  $^{13}\text{CO}$  are both in LTE, have the same excitation temperature, and  $^{13}\text{CO}$  is optically thin, the ratio between the  $^{12}\text{CO}$  and  $^{13}\text{CO}$  brightness temperature is

$$\frac{T_{^{12}\text{CO}}}{T_{^{13}\text{CO}}} = \frac{[^{12}\text{CO}]}{[^{13}\text{CO}]} \frac{1 - e^{-\tau_{12}}}{\tau_{12}}. \quad (2.2)$$

$[^{12}\text{CO}]/[^{13}\text{CO}]$  is the abundance ratio, assumed to be 62 (Langer & Penzias, 1993), and  $\tau_{12}$  is the opacity of  $^{12}\text{CO}$ . We measure the velocity-dependent ratio between the  $^{12}\text{CO}$  and  $^{13}\text{CO}$  brightness temperature, averaging over an area around each shell. Using this ratio and Equation 2.2 we compute the opacity correction factor  $\tau_{12}/(1 - e^{-\tau_{12}})$  at each velocity channel for each shell. We multiply the observed  $T_{^{12}\text{CO}}$  in each shell voxel by this factor to correct for opacity.

We add the shell voxels with  $5\sigma$   $^{13}\text{CO}$  to the shell voxels without  $5\sigma$   $^{13}\text{CO}$  but having  $5\sigma$   $^{12}\text{CO}$ . Integrating each, we compute the column density of H<sub>2</sub> using equation A6 in Zhang et al. (2016):

$$\frac{dN}{dv} = \left( \frac{8\pi k \nu_{ul}^2}{hc^3 A_{ul} g_u} \right) Q_{\text{rot}}(T_{\text{ex}}) e^{E_u/kT_{\text{ex}}} \frac{T_R(v)}{f} \quad (2.3)$$

where  $\nu_{ul}$  is the frequency of the transition,  $A_{ul}$  is the Einstein A coefficient,  $E_u$  is the energy of the upper level,  $g_u$  is the degeneracy of the upper level,  $Q_{\text{rot}}$  is the partition

function (calculated to  $j = 100$ ),  $T_{\text{ex}}$  is the excitation temperature,  $T_R(v)$  is the brightness temperature of the CO line (opacity-corrected  $^{12}\text{CO}$  or  $^{13}\text{CO}$ ), and  $f$  is the abundance ratio of  $\text{H}_2/\text{CO}$ . For  $^{12}\text{CO}$ ,  $f = 1 \times 10^{-4}$ . For  $^{13}\text{CO}$ ,  $f = 1 \times 10^{-4}/62$  (Frerking et al., 1982).

An excitation temperature is calculated for each shell by assuming  $^{12}\text{CO}$  is optically thick. We estimate  $T_{\text{ex}}$  with the peak brightness temperature of the average  $^{12}\text{CO}$  spectrum in the vicinity of each shell, using the equation from Rohlfs & Wilson (1996):

$$T_{\text{ex}} = \frac{5.53}{\ln(1 + [5.53/(T_{\text{peak}} + 0.82)])} \quad (2.4)$$

The mass of molecular hydrogen in each voxel is then  $M_{\text{H}_2} = m_{\text{H}}\mu_{\text{H}_2}A_{\text{pixel}}N_{\text{H}_2}$  where  $m_{\text{H}}$  is the mass of a hydrogen atom,  $\mu_{\text{H}_2}$  is the mean molecular weight per hydrogen molecule, and  $A_{\text{pixel}}$  is the spatial area subtended by each pixel at the distance of the cloud (414 pc for Orion A, Menten et al., 2007).

We find the total mass of a shell by adding the mass in every shell voxel. We use this mass to calculate the momentum  $P = M_{\text{H}_2}v_{\text{exp}}$  and kinetic energy  $E = 0.5M_{\text{H}_2}v_{\text{exp}}^2$ , assuming that the shell is expanding uniformly at the model's expansion velocity.

For each shell, we report best-fit values as well as lower and upper limits on mass, momentum, and kinetic energy in Table 4.2. The lower limits are found by using the lower limits on the model radius, thickness, and expansion velocity reported in Table 2.1 to extract the voxels in the shell. We compute multiple models with these lower limits at central velocities ( $v_0$ ) spanning the range reported in Table 2.1. The median of this set of models is the lower limit reported in Table 4.2. We compute the best-fit values and upper limits in the same way except with the best-fit values and upper limits on model radius, thickness, and expansion velocity from Table 2.1.

Unrelated emission overlaps the shells in many of the channel maps. This may contaminate the derived masses of the extracted shells. We use models instead of extracting shell voxels by hand, accepting some contamination from extraneous cloud emission in order to

report consistent and reproducible masses. As described in Section 2.2.5, the uncertainties on the model parameters (Table 2.1) are large and reflect the most extreme models that resemble the observed shells, so any contamination in shell mass (and all values derived from shell mass) should fall within the uncertainties reported in Table 4.2.

### 2.4.2 Mass, Momentum, and Kinetic Energy Statistics

Figures 2.14, 2.15, and 2.16 show the distribution of mass, momentum, and energy for the full shell sample and the 12 most robust shells which meet all criteria in Table 2.2. We show the range of physical parameters derived for each shell using the lower limit, best-fit, and upper limits on the model parameters.

Table 2.4 reports the total kinetic energy of the shells in Orion A. The total mass, momentum, and energy contained within shells in Orion A are similar to the cumulative totals of the Perseus cloud shells reported by Arce et al. (2011).

## 2.5 Discussion

### 2.5.1 The Impact of Shells on the GMC

To compare the impact of the shells on the cloud with protostellar outflows and cloud turbulence, we split Orion A into several subregions, shown in Figure 2.1. The North subregion covers the OMC 2 and OMC 3 areas of the molecular cloud, as well as the southern portion of the HII region NGC 1977 (Peterson & Megeath, 2008; Davis et al., 2009). The Central subregion includes the Orion Bar (Goicoechea et al., 2016), Orion KL and the OMC 1 explosive outflow (Bally et al., 2017). The South subregion covers OMC 4 and OMC 5 (Johnstone & Bally, 2006; Buckle et al., 2012; Davis et al., 2009). The L1641N subregion covers the L1641 North cluster and the reflection nebula NGC 1999 powered by Herbig Be9 star V380 (Davis et al., 2009; Nakamura et al., 2012). Shells are

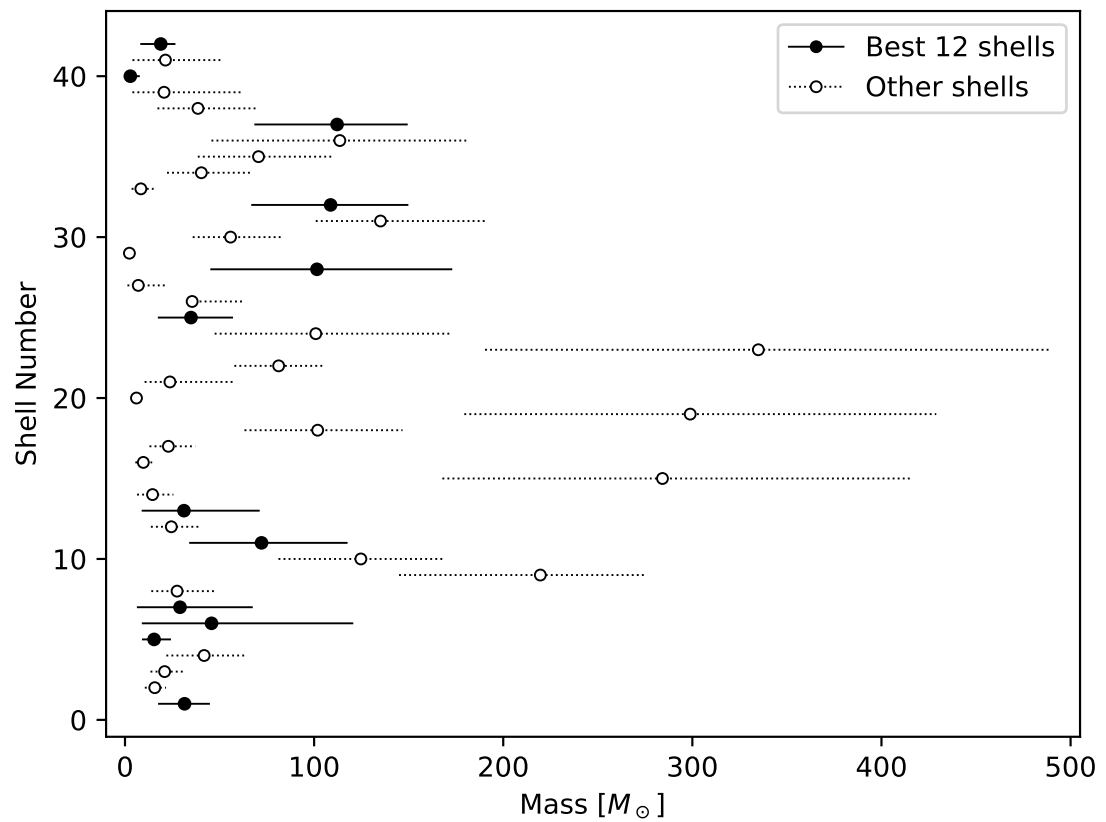


Figure 2.14 Range in mass of each shell candidate. The points represent masses derived from best-fit model parameters. Upper and lower limits are calculated using the upper and lower limits on the model parameters (see Section 2.4.2). The 12 most robust shells are shown as filled circles.

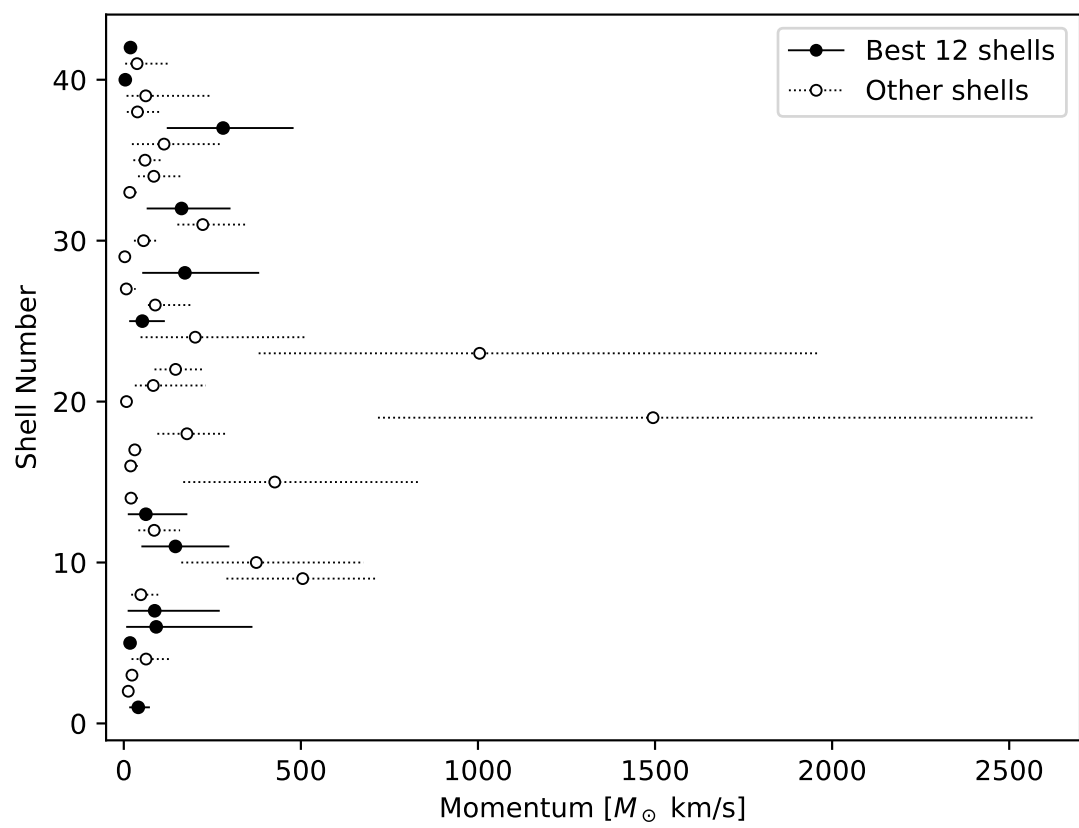


Figure 2.15 Same as Figure 2.14 except plotting the range in momentum of each shell.

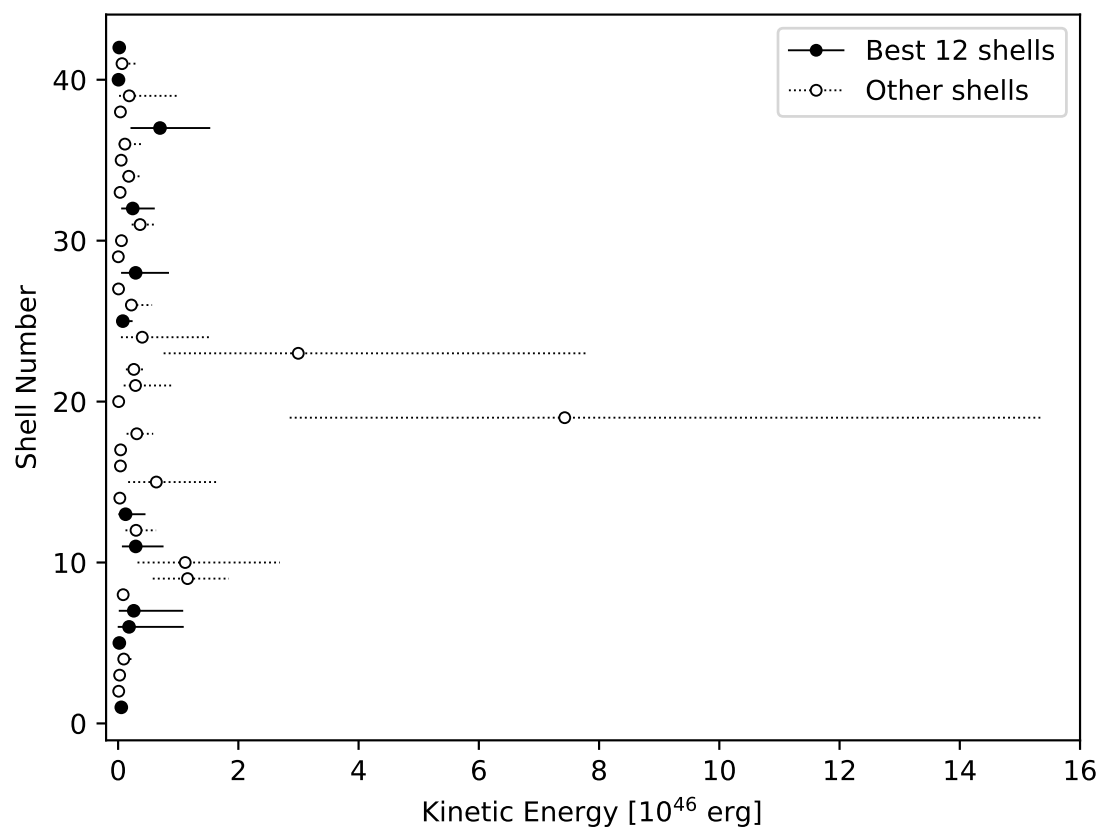


Figure 2.16 Same as Figure 2.14 except plotting the range in kinetic energy of each shell.

assigned to the subregion containing their center.

### Comparing Shells and Protostellar Outflows

To assess the relative importance of feedback mechanisms, we compare the kinetic energy and momentum injected by the shells and by protostellar outflows gathered from the literature. Table 2.4 summarizes the impact of protostellar outflows in Orion A. We detail below the outflows considered in each subregion.

**North** In the North, outflows in OMC 2 and OMC 3 were observed by Williams et al. (2003) and later expanded by Takahashi et al. (2008). We estimate the kinetic energy and mechanical luminosity of these outflows using the velocities, masses, and dynamical times reported in Takahashi et al. (2008) Table 3. The 15 outflows in OMC 2/3 contain a total kinetic energy of  $6.8 \times 10^{45}$  erg, mechanical luminosity of  $2 \times 10^{34}$  erg s $^{-1}$ , and momentum injection rate of  $2 \times 10^{-3} M_{\odot}$  km s $^{-1}$  yr $^{-1}$ .

**Central** In the Central region, the OMC 1 explosive outflow dominates. Bally et al. (2017) made detailed measurements of the outflowing gas using ALMA. The energy [momentum] of this outflow has been estimated at  $4 \times 10^{46}$  erg [ $160 M_{\odot}$  km s $^{-1}$ ] (Snell et al., 1984) to  $4 \times 10^{47}$  erg [ $1257 M_{\odot}$  km s $^{-1}$ ] (Kwan & Scoville, 1976). We adopt an average of  $10^{47}$  erg [ $730 M_{\odot}$  km s $^{-1}$ ]. Snell et al. (1984) found a dynamical time of 1500 yr, corresponding to a mechanical luminosity of  $2.1 \times 10^{36}$  erg s $^{-1}$  and a momentum injection rate of  $0.47 M_{\odot}$  km s $^{-1}$  yr $^{-1}$ .

About 100'' south, another high-velocity outflow was identified by Rodríguez-Franco et al. (1999) in the OMC1-South region. Zapata et al. (2005) measured a total energy of  $4.6 \times 10^{46}$  erg, mechanical luminosity of  $2.3 \times 10^{36}$  erg s $^{-1}$ , and momentum injection rate of  $9.3 \times 10^{-2} M_{\odot}$  km s $^{-1}$  yr $^{-1}$ . These two high velocity outflows dominate the Central subregion.

**South** In the South, we could not find any systematic study of outflows. As part of the Gould’s Belt survey, Buckle et al. (2012) identify three outflows in their  $^{13}\text{CO}$  map of the OMC4 region, but do not measure the energetics of these outflows. Berné et al. (2014) include the OMC1-South outflow discussed above in their assessment of the energetics of this region, but it is clearly contained in our Central subregion.

**L1641N** In L1641-N, Stanke & Williams (2007) detected a sample of outflows which was expanded on by Nakamura et al. (2012). Nakamura et al. (2012) measure five outflows in L1641N with a total mass, momentum, and energy of  $13 M_{\odot}$ ,  $80 M_{\odot} \text{ km s}^{-1}$ , and  $5.46 \times 10^{45} \text{ erg}$ . Assuming an outflow dynamical time of a few  $\times 10^4 \text{ yr}$  (Nakamura et al., 2012), the mechanical luminosity of these outflows is  $10^{34} \text{ erg s}^{-1}$  and the momentum injection rate is  $2 \times 10^{-3} M_{\odot} \text{ km s}^{-1} \text{ yr}^{-1}$ .

Morgan et al. (1991) measured three other outflows south of the L1641N cluster but within our L1641N subregion. Two of these outflows are apparently associated with the Herbig Haro objects HH 1/2 and V380. Morgan et al. (1991) calculate upper and lower limits on the energy of these outflows. The lower limit only accounts for emission in the high-velocity wings of the outflow spectrum. The upper limit attempts to account for the outflow emission at very low velocities (presumably buried under the line core) by assuming that the molecular outflow emission at each velocity channel in the line core is equal to the emission of the lowest velocity channel in the wing. For these three outflows, we adopt an average of the lower and upper limits for a total energy of  $7.4 \times 10^{45} \text{ erg}$ , mechanical luminosity of  $6.9 \times 10^{33} \text{ erg s}^{-1}$ , and momentum injection rate of  $2.6 \times 10^{-3} M_{\odot} \text{ km s}^{-1} \text{ yr}^{-1}$ .

## Cloud Kinetic Energy

We measure the kinetic energy in the molecular cloud in each of the subregions described above. We follow the method in Section 2.4.1 to calculate the  $\text{H}_2$  mass in each pixel using  $^{13}\text{CO}$  (when present) and opacity-corrected  $^{12}\text{CO}$ . We estimate the velocity dispersion of

the molecular gas following the method of Li et al. (2015). The one-dimensional velocity dispersion  $\sigma_{\text{los}}$  is computed from the second-moment map of  $^{13}\text{CO}$ . The three-dimensional velocity dispersion  $\sigma_{\text{3D}}$ , assuming an isotropic turbulent velocity field, is equal to  $\sqrt{3}\sigma_{\text{los}}$ . The kinetic energy in each pixel is  $(1/2)M_{\text{H}_2}\sigma_{\text{3D}}^2$ . The total kinetic energy of a subregion is a sum of the kinetic energy in each of the subregion’s pixels. Table 2.4 compares the kinetic energy of the cloud to the energy injected by the shells in each subregion.

## Shells and Turbulence

**Energy Injection and Dissipation** In the previous section we showed that the total energy contained within expanding shells is a significant fraction of the turbulent energy in the Orion A cloud. But in order to maintain this turbulence, the shells must provide this energy at a rate greater than or equal to the turbulent energy dissipation rate.

The turbulent energy dissipation rate  $\dot{E}_{\text{turb}}$  is given by the total turbulent energy  $E_{\text{turb}} = 5.8 \times 10^{47} \text{ erg}$  divided by the dissipation timescale  $t_{\text{diss}}$ . Arce et al. (2011) estimates  $t_{\text{diss}} = 5 \text{ Myr}$  in Perseus using the method of Mac Low (1999).

Alternatively, McKee & Ostriker (2007) show that the dissipation time of a homogeneous isotropic turbulent cloud with diameter  $d$  and one-dimensional velocity dispersion  $\sigma_{\text{los}}$  is:

$$t_{\text{diss}} = 0.5 \frac{d}{\sigma_{\text{los}}} \quad (2.5)$$

We use the geometric average of the cloud length and width in the plane of the sky to estimate  $d \approx 12 \text{ pc}$ . The median  $\sigma_{\text{los}}$  of  $^{13}\text{CO}$  is  $1.7 \text{ km s}^{-1}$ . Using Equation 2.5, we estimate  $t_{\text{diss}} \approx 3.5 \text{ Myr}$  in Orion A. With these assumptions, the turbulent energy dissipation rate is  $10^{34} \text{ erg s}^{-1}$ , a factor of a few higher than that found in the Perseus (Arce et al., 2011) and Taurus (Li et al., 2015) molecular clouds. We repeat this procedure in each subregion, estimating  $d = (4, 2, 5, 4) \text{ pc}$  and  $\sigma_{\text{los}} = (1.6, 1.7, 1.6, 1.6) \text{ km s}^{-1}$  in the (North, Central, South, L1641N) subregions respectively.

The mechanical luminosity of a shell  $\dot{E}_{\text{shell}}$  can be simply estimated by dividing the shell energy by the expansion time of the shell  $t_{\text{exp}}$ . Assuming the shell has expanded at a constant rate,  $t_{\text{exp}} = R / v_{\text{exp}}$ . For the purposes of this calculation, we use the best-fit radius and expansion velocity for each shell reported in Table 2.1. The mechanical luminosity of each shell is reported in Table 4.2 and the total mechanical luminosity of the shells is reported in Table 2.4.

In the North, the mechanical luminosity of shells is twice the turbulent dissipation rate and a factor of five lower than the outflow injection rate. In the Central subregion, the shells contain 70% the power of turbulent dissipation and contribute a small fraction of the outflow injection rate which is dominated by the Orion KL explosive outflow. The shells have the most impact in the South, where the total shell luminosity is a factor of nine higher than the turbulent dissipation rate (we found no outflows in the South).<sup>3</sup> In L1641N, the shell luminosity is comparable to the turbulent dissipation rate and a factor of a few lower than the outflow injection rate. The shells contain enough power to counteract the turbulent dissipation rate in all but perhaps the Central subregion. A similar result was found for the shells in Perseus by Arce et al. (2011). In Taurus, Li et al. (2015) found that shells inject energy at about 2–10× the turbulent dissipation rate.

### Momentum Injection and Dissipation

Because shells and outflows are momentum-driven, Nakamura & Li (2014) compare the outflow momentum injection rate to the momentum dissipation rate in several clouds. We find the momentum dissipation rate of the cloud regions using Equation 4 in Nakamura & Li (2014):

---

<sup>3</sup>The South is dominated by two outliers: Shell 19 and 23. These are two of the largest shells in the catalog, with high expansion velocities. The physical quantities for these shells are likely to be more contaminated by unrelated emission compared to the other shells. Removing the contribution from Shell 19 and 23 reduces the shell luminosity in the South to about 30% higher than the turbulent energy dissipation rate. See Table 2.4 for more details.

$$\frac{dP_{\text{turb}}}{dt} = 6.4 \times 10^{-4} M_{\odot} \text{ km s}^{-1} \text{ yr}^{-1} \times \\ \left( \frac{M_{\text{cl}}}{500 M_{\odot}} \right) \times \left( \frac{R_{\text{cl}}}{0.5 \text{ pc}} \right)^{-1} \times \left( \frac{\sigma_{\text{los}}}{\text{km s}^{-1}} \right)^2 \quad (2.6)$$

$M_{\text{cl}}$  is the mass of the cloud subregion,  $R_{\text{cl}}$  is the radius of the cloud subregion, and  $\sigma_{\text{los}}$  is the line-of-sight velocity dispersion of the cloud subregion. We use the same estimates as the energy dissipation calculation,  $R_{\text{cl}} = (2, 1, 2.5, 2)$  pc and  $\sigma_{\text{los}} = (1.6, 1.7, 1.6, 1.6)$  km s<sup>-1</sup>, and find  $M_{\text{cl}} = (4048, 3736, 5001, 5196) M_{\odot}$  for the North, Central, South, and L1641N subregion, respectively. Because the method of Nakamura & Li (2014) is intended for the clump scale, we do not apply Equation 2.6 to the entire cloud, but only report the momentum dissipation rates of the subregions in Table 2.4.

We compare the momentum dissipation rate of the cloud subregions to the momentum injection rates of the outflows (reported in Section 3.3.2) and shells. As with the mechanical luminosity, we calculate a shell's momentum injection rate by dividing the shell momentum by its expansion time. The momentum injection rate of each shell is reported in Table 4.2 and the total shell momentum injection rate is reported in Table 2.4.

In the North, the shells inject momentum at about three times the rate of outflows and twice the dissipation rate. In the Central subregion, shells inject enough momentum to counteract dissipation but are again dominated by the massive outflows in Orion KL. In the South, shells inject momentum at seven times the dissipation rate.<sup>4</sup> In L1641N, the shell momentum injection rate is twice that of the outflows and twice the dissipation rate.

The shells inject more momentum into the cloud than outflows except in the Central subregion, which is dominated by high velocity outflows. The momentum injection by shells and outflows is greater than the momentum dissipation rate throughout the cloud

---

<sup>4</sup>If the two outliers Shell 19 and 23 are removed, the total shell momentum injection rate in the South is a factor of two higher than the turbulent dissipation rate. See note *d* in Table 2.4 for more details.

and can thus maintain the cloud turbulence.

### 2.5.2 Shell Driving Mechanisms

What powers the shells? Arce et al. (2011) and Offner & Arce (2015) consider protostellar outflows, turbulent voids, and stellar winds. Protostellar outflow cavities are generally collimated but could appear circular if viewed on-axis. Because most outflows are highly collimated, the momentum on the plane of the sky is a small fraction of the total outflow momentum. Offner & Arce (2015) estimate the outflow rates required to drive a typical shell would be several orders of magnitude higher than observed. Wide-angle outflows are sometimes observed around pre-main sequence stars (e.g. Ruíz-Rodríguez et al., 2017; Principe et al., 2018). Such an outflow would not need to be viewed on-axis and may help explain structures like Shell 40 (Section 2.3.2).

Random turbulent voids may masquerade as feedback-driven shells. Offner & Arce (2015) find that CO voids can be created by turbulence in simulated clouds. However, they note that an over-dense rim like those found around many of the observed shells is difficult to explain without a driving mechanism providing the momentum to entrain gas.

Accretion-driven winds provide the most likely driving mechanism for the shells. Offner & Arce (2015) show that a spherical stellar wind with a sufficiently high mass-loss rate can reproduce the shells observed in Perseus by Arce et al. (2011). Below, we compare the winds needed to reproduce the shells in Orion A to winds from intermediate-mass main-sequence stars.

#### Wind mass-loss Rates and Energy Injection Rates

For the following calculations, we assume the shells are driven by winds. Following Arce et al. (2011), we assume that the winds conserve momentum, the wind velocity  $v_w$  is  $200 \text{ km s}^{-1}$ , and the duration of the wind  $t_w$  is 1 Myr. These values are based on the

typical escape velocity of intermediate-mass stars and the approximate age of Class II/III pre-main sequence stars. The wind mass-loss rate that drives a shell with momentum  $P_{\text{shell}}$  is

$$\dot{m}_w = \frac{P_{\text{shell}}}{v_w t_w} = 5 \times 10^{-9} M_{\odot} \text{yr}^{-1} \frac{P_{\text{shell}}}{M_{\odot} \text{km s}^{-1}} \quad (2.7)$$

The wind mass-loss rates of the shells are reported in Table 4.2. The rates range from  $10^{-8}$  to  $8 \times 10^{-6} M_{\odot} \text{yr}^{-1}$ . These rates are similar to those required by Offner & Arce (2015) to simulate the types of shells found in Perseus. As noted by Offner & Arce (2015), these mass-loss rates are 2-3 orders of magnitudes larger than predicted by theoretical models of line-driven winds from main-sequence B stars (e.g. Smith, 2014, Figure 3). The discrepancy between the wind mass-loss rates needed to produce the observed shells and the mass-loss rates predicted for line-driven winds from the B and later-type stars present inside the shells shows more modeling of intermediate-mass stellar winds is needed. Offner & Arce (2015) suggest that periodic wind enhancements due to short term increases in stellar activity or accretion could produce variable mass-loss rates. In this scenario, shells are produced during a short period ( $\approx 0.1$  Myr) of enhanced mass-loss while the stars spend most of their lives at the lower mass-loss rates predicted by models. In such a burst, the mass-loss rate would need to increase by an order of magnitude over that estimated by Equation 2.7.

Following Arce et al. (2011) and Li et al. (2015), we estimate the wind energy injection rate with Equation 3.7 of McKee (1989):

$$\dot{E}_w = \frac{1}{2} \dot{m}_w v_w \sigma_{3D} \quad (2.8)$$

where  $v_w = 200 \text{ km s}^{-1}$  and  $\sigma_{3D} = 2.9 \text{ km s}^{-1}$  (see Section 2.5.1). This calculation assumes that the wind deposits its remaining energy on the cloud after radiative losses when it slows to  $\sigma_{3D}$ . The wind energy injection rate is distinct from the shell luminosities

discussed in Section 2.5.1. The total wind energy injection rate is about 14% of the total mechanical luminosity in the shells. A similar result was found by Li et al. (2015). The power deficit of winds compared to the shells they are driving is likely due to the longer time over which the energy is distributed. The average shell expansion time (from Table 2.1) is 17% of the assumed 1 Myr wind duration time. Without better constraints on  $t_w$  (and  $v_w$ ), the wind mass-loss rates and energy injection rates are approximate.

Based on the above rates (see Table 2.4), wind-blown shells may maintain a significant portion of Orion A’s turbulence, especially in the North, South, and L1641N subregions.

## 2.6 Summary and Conclusions

We identify 42 expanding shells in CO maps of the Orion A giant molecular cloud. The shells range in radius from 0.05 to 0.85 pc and are expanding at 0.8 to 5 km s<sup>-1</sup>. Many of the shells are correlated with dust emission and have candidate driving sources near their centers.

We present all 42 shells in the online journal and detail several in this paper:

- A C-shaped CO shell near the Herbig A2-3e star T Ori. This pre-main sequence star powers a stellar wind within an order of magnitude of the mass-loss rate needed to drive the CO shell.
- Two nested shells around the Herbig B9e star V380 Ori. This star is in a hierarchical quadruple system and is responsible for several Herbig-Haro (HH) objects. The dynamical ages of the HH objects are similar to the expansion time of the shells. The shells and outflows traced by the HH objects may have been launched in an accretion-driven outburst during a dynamical interaction among the multiple stellar components of V380 Ori.
- A shell centered on the B2 pre-main sequence star LP Ori. The mass-loss rate of LP

Ori is 2-3 orders of magnitude lower than the wind necessary to drive the expanding shell.

We compare model shells to the CO position-velocity diagrams to estimate their radius, thickness, expansion velocity, and central velocity. Using the models, we extract the H<sub>2</sub> mass and calculate momentum, energy, mechanical luminosity, and momentum injection rate of the expanding shells.

The total kinetic energy of the Orion A shells is comparable to the total energy in outflows compiled from the literature. The combined kinetic energy from shells and outflows is significant compared to the turbulent energy of the cloud. The mechanical luminosity and momentum injection rate of the shells and outflows are enough to counteract turbulent dissipation, suggesting that feedback from low to intermediate mass stars may help explain the observed turbulence and low star formation efficiencies in clouds.

One of the mysteries raised by the discovery of CO shells around intermediate-mass stars is the driving mechanism. If the shells are driven by stellar winds, we find wind mass-loss rates ranging from  $10^{-8}$  to  $8 \times 10^{-6} M_{\odot} \text{ yr}^{-1}$ . These rates are higher than expected for intermediate-mass line-driven stellar winds by 2-3 orders of magnitude. If shells are driven by winds, they probably represent bursts of mass-loss driven by accretion events rather than a continuous flow. A possible source of additional momentum is the heating and ablation of the molecular cloud by FUV photons. Further study of the powering sources and interiors of these shells is needed to resolve the mechanism that drives them.

Orion A marks the third molecular cloud in which expanding shells have been found after Perseus (Arce et al., 2011) and Taurus (Li et al., 2015). Many of these shells show strong evidence for expansion, correlated infrared nebulosity, and candidate sources. Shells have been found in low-mass (Perseus and Taurus) and high-mass (Orion A) star forming regions around intermediate and low-mass stars and are significant to the energetics of these turbulent molecular clouds. These results strongly suggest that further study

of the driving sources, mass-loss process, and cloud impact is needed for this new stellar feedback mechanism.

The CARMA-NRO Orion Survey (Kong et al., 2018) combines the single-dish data used in this paper with interferometry from the Combined Array for Research in Millimeter-wave Astronomy (CARMA). These combined data provide an unprecedented dynamic range in spatial scale - 0.01 to 10 pc - and offer a factor of 3x better resolution compared to the NRO maps alone. This survey will provide a clearer picture of the impact of feedback on the molecular cloud.

## Acknowledgments

We thank the anonymous referee for valuable suggestions that improved this paper. JRF was funded by NSF grant AST-1311825 to HGA. This project was also partly funded by AST-1140063. We thank Shuri Oyamada, Sachiko K. Okumura, Yumiko Urasawa, Ryohei Nishi, Kazuhito Dobashi, Tomomi Shimoikura, Takeshi Tsukagoshi, Yoshihiro Tanabe, Takashi Tsukagoshi, and Munetake Momose for their valuable contribution to the 45-m observations. We thank Christopher Beaumont for providing the expanding shell model. We thank Maria Jose Maureira, Mario Tafalla, Crystal Brogan, and Tom Megeath for useful discussions that improved this paper. The Nobeyama 45-m radio telescope is operated by Nobeyama Radio Observatory, a branch of National Astronomical Observatory of Japan. This research has made use of observations made with the NASA/ESA Hubble Space Telescope, and obtained from the Hubble Legacy Archive, which is a collaboration between the Space Telescope Science Institute (STScI/NASA), the Space Telescope European Coordinating Facility (ST-ECF/ESA) and the Canadian Astronomy Data Centre (CADC/NRC/CSA). This research has made use of the NASA/IPAC Infrared Science Archive, which is operated by the Jet Propulsion Laboratory, California Institute of Technology, under contract with the National Aeronautics and Space Administration. This

research has made use of the Vizier catalogue access tool (Ochsenbein et al., 2000) and Simbad database (Wenger et al., 2000) operated at CDS, Strasbourg, France.

Table 2.1. Shell Parameters

Shell	Position $\alpha(J2000), \delta(J2000)$	$R^a$ (pc)	$dr^a$ (pc)	$v_{\text{exp}}^a$ (km s $^{-1}$ )	$v_0^a$ (km s $^{-1}$ )	$t_{\text{exp}}^b$ (Myr)
1	$5^{\text{h}}34^{\text{m}}49^{\text{s}}.0/-4^{\circ}51'41''$	0.180 ± 0.020	0.180 ± 0.020	1.30 ± 0.30	10.00 ± 0.30	0.14 ± 0.03
2	$5^{\text{h}}34^{\text{m}}27^{\text{s}}.4/-4^{\circ}52'20''$	0.100 ± 0.010	0.100 ± 0.010	0.80 ± 0.20	11.40 ± 0.20	0.12 ± 0.03
3	$5^{\text{h}}34^{\text{m}}33^{\text{s}}.9/-4^{\circ}54'3''$	0.110 ± 0.030	0.095 ± 0.015	1.10 ± 0.20	11.50 ± 0.20	0.10 ± 0.03
4	$5^{\text{h}}35^{\text{m}}23^{\text{s}}.9/-4^{\circ}55'15''$	0.130 ± 0.020	0.200 ± 0.050	1.50 ± 0.50	11.50 ± 0.50	0.08 ± 0.03
5	$5^{\text{h}}34^{\text{m}}45^{\text{s}}.8/-4^{\circ}55'36''$	0.120 ± 0.020	0.075 ± 0.025	1.15 ± 0.15	11.70 ± 0.20	0.10 ± 0.02
6	$5^{\text{h}}35^{\text{m}}24^{\text{s}}.8/-5^{\circ}2'10''$	0.220 ± 0.020	0.115 ± 0.015	2.00 ± 1.00	8.80 ± 0.80	0.11 ± 0.05
7	$5^{\text{h}}34^{\text{m}}54^{\text{s}}.5/-5^{\circ}4'40''$	0.170 ± 0.010	0.200 ± 0.050	3.00 ± 1.00	14.25 ± 0.75	0.06 ± 0.02
8	$5^{\text{h}}35^{\text{m}}32^{\text{s}}.3/-5^{\circ}6'49''$	0.150 ± 0.050	0.175 ± 0.025	1.75 ± 0.25	13.75 ± 0.25	0.08 ± 0.03
9	$5^{\text{h}}34^{\text{m}}55^{\text{s}}.1/-5^{\circ}11'10''$	0.850 ± 0.050	0.850 ± 0.050	2.30 ± 0.30	8.70 ± 0.30	0.36 ± 0.05
10	$5^{\text{h}}35^{\text{m}}43^{\text{s}}.0/-5^{\circ}27'47''$	0.350 ± 0.020	0.200 ± 0.050	3.00 ± 1.00	11.00 ± 0.50	0.11 ± 0.04
11	$5^{\text{h}}35^{\text{m}}9^{\text{s}}.4/-5^{\circ}27'53''$	0.220 ± 0.040	0.230 ± 0.030	2.00 ± 0.50	13.00 ± 0.50	0.11 ± 0.03
12	$5^{\text{h}}36^{\text{m}}39^{\text{s}}.7/-5^{\circ}28'41''$	0.150 ± 0.050	0.175 ± 0.075	3.50 ± 0.50	7.75 ± 0.25	0.04 ± 0.02
13	$5^{\text{h}}34^{\text{m}}24^{\text{s}}.2/-5^{\circ}29'0''$	0.350 ± 0.050	0.250 ± 0.050	2.00 ± 0.50	6.50 ± 0.50	0.17 ± 0.05
14	$5^{\text{h}}35^{\text{m}}0^{\text{s}}.7/-5^{\circ}29'57''$	0.210 ± 0.040	0.190 ± 0.020	1.40 ± 0.50	13.50 ± 0.50	0.15 ± 0.06
15	$5^{\text{h}}34^{\text{m}}53^{\text{s}}.1/-5^{\circ}30'58''$	0.550 ± 0.050	0.550 ± 0.050	1.50 ± 0.50	7.00 ± 1.00	0.36 ± 0.12
16	$5^{\text{h}}36^{\text{m}}25^{\text{s}}.1/-5^{\circ}33'38''$	0.180 ± 0.020	0.125 ± 0.025	2.00 ± 1.00	7.50 ± 0.50	0.09 ± 0.05
17	$5^{\text{h}}34^{\text{m}}1^{\text{s}}.7/-5^{\circ}36'14''$	0.250 ± 0.050	0.250 ± 0.050	1.35 ± 0.15	7.20 ± 0.20	0.18 ± 0.04
18	$5^{\text{h}}34^{\text{m}}30^{\text{s}}.3/-5^{\circ}37'5''$	0.350 ± 0.050	0.250 ± 0.050	1.75 ± 0.25	9.30 ± 0.30	0.20 ± 0.04
19	$5^{\text{h}}35^{\text{m}}24^{\text{s}}.0/-5^{\circ}45'57''$	0.650 ± 0.050	0.550 ± 0.050	5.00 ± 1.00	6.00 ± 1.00	0.13 ± 0.03

Table 2.1 (cont'd)

Shell	Position $\alpha(J2000), \delta(J2000)$	$R^a$ (pc)	$dr^a$ (pc)	$v_{\text{exp}}^a$ (km s $^{-1}$ )	$v_0^a$ (km s $^{-1}$ )	$t_{\text{exp}}^b$ (Myr)
20	$5^{\text{h}}35^{\text{m}}18^{\text{s}}.2/-5^{\circ}52'48''$	0.145 ± 0.015	0.125 ± 0.025	1.25 ± 0.25	10.00 ± 0.10	0.11 ± 0.03
21	$5^{\text{h}}34^{\text{m}}34^{\text{s}}.4/-5^{\circ}57'22''$	0.500 ± 0.100	0.350 ± 0.050	3.50 ± 0.50	7.00 ± 1.00	0.14 ± 0.03
22	$5^{\text{h}}35^{\text{m}}0^{\text{s}}.1/-5^{\circ}59'17''$	0.550 ± 0.050	0.190 ± 0.040	1.80 ± 0.30	10.10 ± 0.30	0.30 ± 0.06
23	$5^{\text{h}}36^{\text{m}}8^{\text{s}}.2/-6^{\circ}4'25''$	0.650 ± 0.050	0.300 ± 0.100	3.00 ± 1.00	8.75 ± 0.75	0.21 ± 0.07
24	$5^{\text{h}}35^{\text{m}}36^{\text{s}}.0/-6^{\circ}5'14''$	0.235 ± 0.035	0.235 ± 0.035	2.00 ± 1.00	7.00 ± 1.00	0.11 ± 0.06
25	$5^{\text{h}}35^{\text{m}}15^{\text{s}}.7/-6^{\circ}15'22''$	0.275 ± 0.025	0.150 ± 0.050	1.50 ± 0.50	7.55 ± 0.25	0.18 ± 0.06
26	$5^{\text{h}}36^{\text{m}}12^{\text{s}}.7/-6^{\circ}15'34''$	0.175 ± 0.025	0.150 ± 0.050	2.50 ± 0.50	11.00 ± 0.30	0.07 ± 0.02
27	$5^{\text{h}}35^{\text{m}}57^{\text{s}}.9/-6^{\circ}19'52''$	0.300 ± 0.050	0.150 ± 0.050	1.00 ± 0.50	5.75 ± 0.25	0.29 ± 0.15
28	$5^{\text{h}}36^{\text{m}}10^{\text{s}}.2/-6^{\circ}24'7''$	0.300 ± 0.050	0.250 ± 0.050	1.70 ± 0.50	9.50 ± 0.20	0.17 ± 0.06
29	$5^{\text{h}}36^{\text{m}}49^{\text{s}}.6/-6^{\circ}28'6''$	0.170 ± 0.020	0.125 ± 0.025	1.20 ± 0.20	3.75 ± 0.25	0.14 ± 0.03
30	$5^{\text{h}}36^{\text{m}}28^{\text{s}}.9/-6^{\circ}28'10''$	0.335 ± 0.035	0.275 ± 0.025	1.00 ± 0.20	8.50 ± 0.20	0.33 ± 0.07
31	$5^{\text{h}}35^{\text{m}}40^{\text{s}}.0/-6^{\circ}29'51''$	0.300 ± 0.050	0.315 ± 0.035	1.65 ± 0.15	7.75 ± 0.25	0.18 ± 0.03
32	$5^{\text{h}}35^{\text{m}}58^{\text{s}}.0/-6^{\circ}32'34''$	0.260 ± 0.020	0.220 ± 0.020	1.50 ± 0.50	7.70 ± 0.30	0.17 ± 0.06
33	$5^{\text{h}}36^{\text{m}}54^{\text{s}}.3/-6^{\circ}32'55''$	0.150 ± 0.030	0.150 ± 0.050	2.00 ± 0.40	10.70 ± 0.50	0.07 ± 0.02
34	$5^{\text{h}}36^{\text{m}}24^{\text{s}}.4/-6^{\circ}35'0''$	0.290 ± 0.030	0.250 ± 0.050	2.10 ± 0.30	9.60 ± 0.30	0.14 ± 0.02
35	$5^{\text{h}}36^{\text{m}}10^{\text{s}}.7/-6^{\circ}37'37''$	0.250 ± 0.050	0.250 ± 0.050	0.85 ± 0.15	8.00 ± 0.10	0.29 ± 0.08
36	$5^{\text{h}}36^{\text{m}}40^{\text{s}}.4/-6^{\circ}38'11''$	0.550 ± 0.050	0.275 ± 0.025	1.00 ± 0.50	8.00 ± 0.20	0.54 ± 0.27
37	$5^{\text{h}}37^{\text{m}}6^{\text{s}}.5/-6^{\circ}38'20''$	0.350 ± 0.050	0.250 ± 0.050	2.50 ± 0.70	7.50 ± 0.50	0.14 ± 0.04
38	$5^{\text{h}}35^{\text{m}}47^{\text{s}}.7/-6^{\circ}38'43''$	0.280 ± 0.030	0.150 ± 0.050	1.00 ± 0.50	9.00 ± 0.50	0.27 ± 0.14

Table 2.1 (cont'd)

Shell	Position $\alpha(J2000), \delta(J2000)$	$R^a$ (pc)	$dr^a$ (pc)	$v_{\text{exp}}^a$ (km s $^{-1}$ )	$v_0^a$ (km s $^{-1}$ )	$t_{\text{exp}}^b$ (Myr)
39	$5^{\text{h}}36^{\text{m}}21^{\text{s}}.4/-6^{\circ}42'18''$	$0.250 \pm 0.020$	$0.170 \pm 0.030$	$3.00 \pm 1.00$	$12.00 \pm 1.00$	$0.08 \pm 0.03$
40	$5^{\text{h}}36^{\text{m}}23^{\text{s}}.1/-6^{\circ}42'27''$	$0.050 \pm 0.025$	$0.100 \pm 0.025$	$1.50 \pm 0.50$	$11.10 \pm 0.30$	$0.03 \pm 0.02$
41	$5^{\text{h}}36^{\text{m}}4^{\text{s}}.4/-6^{\circ}42'43''$	$0.175 \pm 0.025$	$0.200 \pm 0.050$	$1.75 \pm 0.75$	$10.40 \pm 0.60$	$0.10 \pm 0.04$
42	$5^{\text{h}}38^{\text{m}}24^{\text{s}}.0/-6^{\circ}45'52''$	$0.280 \pm 0.020$	$0.300 \pm 0.050$	$1.00 \pm 0.30$	$7.65 \pm 0.25$	$0.27 \pm 0.08$

<sup>a</sup>The parameter uncertainties are visually estimated by comparing models to shell PV diagrams.

<sup>b</sup> $t_{\text{exp}} = R/v_{\text{exp}}$ . The uncertainty in expansion time is given by error propagation.

Table 2.2. Shell Criteria

Shell	Channel Maps	IR Nebulosity	Circular Structure	PV Diagram	Candidate Source <sup>a</sup>	Score
1	Y ( <sup>12</sup> CO)	Y (3.6/8/24/Dust T)	Y ( <sup>12</sup> CO)	Y ( <sup>12</sup> CO)	Y (Multiple YSO)	5
2	Y ( <sup>12</sup> CO)	N	Y ( <sup>12</sup> CO)	Y ( <sup>12</sup> CO)	N	3
3	Y ( <sup>12</sup> / <sup>13</sup> CO)	N	Y ( <sup>12</sup> / <sup>13</sup> CO)	Y ( <sup>12</sup> CO)	N	3
4	Y ( <sup>12</sup> / <sup>13</sup> CO)	N	Y ( <sup>12</sup> CO)	Y ( <sup>12</sup> CO)	Y (Multiple YSO)	4
5	Y ( <sup>12</sup> / <sup>13</sup> CO)	Y (Dust T)	Y ( <sup>12</sup> CO)	Y ( <sup>12</sup> CO)	Y (Multiple YSO)	5
6	Y ( <sup>12</sup> / <sup>13</sup> CO)	Y (3.6/8/24)	Y ( <sup>12</sup> CO)	Y ( <sup>12</sup> CO)	Y (Multiple YSO)	5
7	Y ( <sup>12</sup> CO)	Y (3.6/8/24)	Y ( <sup>12</sup> CO)	Y ( <sup>12</sup> CO)	Y (BD-05 1309/A0 & Multiple YSO)	5
8	Y ( <sup>12</sup> / <sup>13</sup> CO)	Y (Dust T)	N	Y ( <sup>12</sup> CO)	Y (Multiple YSO)	4
9	Y ( <sup>12</sup> CO)	N	Y ( <sup>12</sup> CO)	Y ( <sup>12</sup> CO)	Y (Brun 193/F9 & Multiple YSO)	3
10	Y ( <sup>12</sup> / <sup>13</sup> CO)	Y (3.6/8)	Y ( <sup>13</sup> CO)	N	Y (T Ori/A3e & Multiple YSO)	4
11	Y ( <sup>12</sup> / <sup>13</sup> CO)	Y (3.6/8/24)	Y ( <sup>12</sup> CO)	Y ( <sup>12</sup> CO)	Y (LP Ori/B2V & Multiple YSO)	5
12	Y ( <sup>12</sup> / <sup>13</sup> CO)	Y (Dust T)	N	N	Y (Brun 1018/B6V)	3
13	Y ( <sup>12</sup> / <sup>13</sup> CO)	Y (Dust T)	Y ( <sup>13</sup> CO)	Y ( <sup>12</sup> CO)	Y (Multiple YSO)	5
14	Y ( <sup>12</sup> / <sup>13</sup> CO)	Y ( <sup>12</sup> CO)	Y ( <sup>12</sup> CO)	Y ( <sup>12</sup> CO)	Y (HD 36939/B7-8II & Multiple YSO)	4
15	Y ( <sup>12</sup> / <sup>13</sup> CO)	Y (Dust T)	N	N	Y (HD 36939/B7-8II & YSO)	3
16	Y ( <sup>12</sup> CO)	Y (Dust T)	Y ( <sup>12</sup> / <sup>13</sup> CO)	N	Y ([MGM2012] 1431/YSO)	4
17	Y ( <sup>12</sup> CO)	N	N	Y ( <sup>12</sup> CO)	Y (HD 36782/F5-6V & Multiple YSO)	3
18	Y ( <sup>13</sup> CO)	N	Y ( <sup>13</sup> CO)	Y ( <sup>13</sup> CO)	Y (Multiple YSO)	4
19	Y ( <sup>12</sup> CO)	N	N	Y ( <sup>12</sup> CO)	Y (BD-05 1322/A6V & Multiple YSO)	3
20	Y ( <sup>12</sup> CO)	Y (Dust T)	Y ( <sup>12</sup> CO)	N	N	3

Table 2.2 (cont'd)

Shell	Channel Maps	IR Nebulosity	Circular Structure	PV Diagram	Candidate Source <sup>a</sup>	Score
21	Y ( <sup>12</sup> / <sup>13</sup> CO)	N	N	N	Y (Multiple YSO)	2
22	Y ( <sup>12</sup> CO)	N	Y ( <sup>12</sup> CO)	N	Y (Brun 508/B9V & Multiple YSO)	3
23	Y ( <sup>12</sup> / <sup>13</sup> CO)	Y (Dust T)	Y ( <sup>13</sup> CO)	N	Y (Multiple YSO)	4
24	Y ( <sup>12</sup> CO)	N	N	N	Y (HD 37078/A2V & Multiple YSO)	2
25	Y ( <sup>12</sup> / <sup>13</sup> CO)	Y (Dust T)	Y ( <sup>13</sup> CO)	Y ( <sup>12</sup> CO)	Y (BD-06 1236/F9 & Multiple YSO)	5
26	Y ( <sup>12</sup> / <sup>13</sup> CO)	N	Y ( <sup>12</sup> CO)	Y	N	3
27	Y ( <sup>12</sup> CO)	Y (3.6/8/24)	N	N	Y ([MGM2012] 969/YSO)	3
28	Y ( <sup>12</sup> / <sup>13</sup> CO)	Y (3.8/8/24)	Y ( <sup>12</sup> CO)	Y ( <sup>12</sup> CO)	Y (BD-06 1251/F5 & Multiple YSO)	5
29	Y ( <sup>12</sup> / <sup>13</sup> CO)	N	N	Y ( <sup>12</sup> CO)	N	2
30	Y ( <sup>13</sup> CO)	Y (3.6/8/24/Dust T)	Y ( <sup>13</sup> CO)	N	Y (V1133 Ori/B9IV/V & Multiple YSO)	4
31	Y ( <sup>12</sup> / <sup>13</sup> CO)	Y (3.6/8/Dust T)	N	Y ( <sup>12</sup> CO)	Y ([MGM2012] 871/YSO)	4
32	Y ( <sup>12</sup> CO)	Y (3.6/8/24/Dust T)	Y (R)	Y ( <sup>13</sup> CO)	Y (Multiple YSO)	5
33	Y ( <sup>12</sup> CO)	Y (Dust T)	N	Y ( <sup>12</sup> CO)	Y (Multiple YSO)	4
34	Y ( <sup>12</sup> CO)	N	N	Y ( <sup>12</sup> CO)	Y (Multiple YSO)	3
35	Y ( <sup>12</sup> / <sup>13</sup> CO)	N	Y ( <sup>13</sup> CO)	Y ( <sup>12</sup> CO)	Y (BD-06 1252/F8)	4
36	Y ( <sup>13</sup> CO)	N	N	N	Y (Multiple YSO)	2
37	Y ( <sup>12</sup> / <sup>13</sup> CO)	Y (Dust T)	Y ( <sup>12</sup> / <sup>13</sup> CO)	Y ( <sup>12</sup> CO)	Y (Multiple YSO)	5
38	Y ( <sup>13</sup> CO)	N	N	N	N	1
39	Y ( <sup>12</sup> CO)	Y (3.6/8/24)	N	Y ( <sup>12</sup> CO)	Y (V380 Ori/B9e & Multiple YSO)	4
40	Y ( <sup>12</sup> / <sup>13</sup> CO)	Y (Dust T/HST)	Y ( <sup>12</sup> CO)	Y ( <sup>12</sup> CO)	Y (V380 Ori/B9e & YSO)	5

Table 2.2 (cont'd)

Shell	Channel Maps	IR Nebulosity	Circular Structure	PV Diagram	Candidate Source <sup>a</sup>	Score
41	Y ( <sup>12/13</sup> CO)	N	Y ( <sup>12</sup> CO)	Y ( <sup>12</sup> CO)	Y (Multiple YSO)	4
42	Y ( <sup>12/13</sup> CO)	Y (3.6/8)	Y ( <sup>12/13</sup> CO)	Y ( <sup>12</sup> CO)	Y ([MGM2012] 765/YSO)	5

Note. — Entries with Y indicate the shells which satisfy the criteria listed in Section 2.2.4. We also list the observations in which the criteria is most clearly satisfied, among the the two CO spectral cubes and the ancillary data. The ancillary data are indicated as 3.6 = IRAC 3.6  $\mu\text{m}$ , 8 = IRAC 8  $\mu\text{m}$ , 24 = MIPS 24  $\mu\text{m}$ , Dust T = *Herschel/Planck* dust temperature map, and HST = *HST WFC2*.

<sup>a</sup>If an OB AF-type star is located inside the projected shell radius, we report it as the candidate source. If not, we report YSOs from the Spitzer Orion Survey of Megeath et al. (2012)[MGM2012]. When multiple OB AF-type stars are inside projected shell radius, we report the one most likely to drive the shell, based on a combination of spectral type, projected distance to the shell center, parallax, and radial velocity if reported in *Simbad*.

Table 2.3. Shell Physics

Shell	$M_{\text{shell}}$ ( $\text{M}_{\odot}$ )	$P_{\text{shell}}$ ( $\text{M}_{\odot} \text{ km s}^{-1}$ )	$E_{\text{shell}}$ ( $10^{44} \text{ erg}$ )	$\dot{E}_{\text{shell}}$ ( $10^{31} \text{ erg s}^{-1}$ )	$\dot{P}_{\text{shell}}$ ( $10^{-4} \text{ M}_{\odot} \text{ km s}^{-1} \text{ yr}^{-1}$ )	$\dot{m}_{\text{w}}$ ( $10^{-7} \text{ M}_{\odot} \text{ yr}^{-1}$ )	$\dot{E}_{\text{w}}$ ( $10^{31} \text{ erg s}^{-1}$ )
1	31 [18, 44]	41 [18, 71]	5 [2, 11]	12 [4, 26]	3 [1, 5]	2 [0.9, 4]	4 [2, 6]
2	16 [10, 22]	13 [6, 22]	1 [0.4, 2]	3 [1, 6]	1 [0.5, 2]	0.6 [0.3, 1]	1 [0.6, 2]
3	21 [13, 31]	23 [12, 40]	3 [1, 5]	8 [4, 17]	2 [1, 4]	1 [0.6, 2]	2 [1, 4]
4	42 [22, 64]	63 [22, 127]	9 [2, 25]	35 [8, 95]	7 [3, 15]	3 [1, 6]	6 [2, 12]
5	15 [9, 24]	18 [9, 31]	2 [0.9, 4]	6 [3, 12]	2 [0.9, 3]	0.9 [0.5, 2]	2 [0.9, 3]
6	46 [9, 120]	92 [9, 361]	18 [0.9, 108]	54 [3, 317]	9 [0.9, 34]	5 [0.5, 18]	8 [0.9, 33]
7	29 [7, 67]	87 [14, 268]	26 [3, 107]	149 [15, 610]	16 [2, 48]	4 [0.7, 13]	8 [1, 25]
8	28 [14, 49]	48 [21, 97]	8 [3, 19]	32 [12, 73]	6 [2, 12]	2 [1, 5]	4 [2, 9]
9	220 [145, 274]	505 [290, 714]	116 [58, 184]	101 [51, 162]	14 [8, 20]	25 [14, 36]	46 [26, 65]
10	125 [81, 169]	374 [162, 677]	112 [32, 269]	310 [90, 748]	33 [14, 59]	19 [8, 34]	34 [15, 62]
11	72 [34, 117]	146 [52, 295]	29 [8, 74]	87 [24, 220]	14 [5, 28]	7 [3, 15]	13 [5, 27]
12	24 [14, 40]	86 [41, 159]	30 [12, 63]	225 [93, 478]	20 [10, 38]	4 [2, 8]	8 [4, 15]
13	31 [9, 71]	62 [14, 177]	12 [2, 44]	23 [4, 81]	4 [0.8, 10]	3 [0.7, 9]	6 [1, 16]
14	15 [6, 26]	20 [6, 49]	3 [0.5, 9]	6 [1, 20]	1 [0.4, 3]	1 [0.3, 2]	2 [0.5, 4]
15	284 [168, 416]	426 [168, 832]	64 [17, 165]	56 [15, 146]	12 [5, 23]	21 [8, 42]	39 [15, 76]
16	10 [5, 14]	19 [5, 43]	4 [0.5, 13]	14 [2, 46]	2 [0.6, 5]	1 [0.3, 2]	2 [0.5, 4]
17	23 [13, 37]	31 [16, 56]	4 [2, 8]	7 [3, 15]	2 [0.9, 3]	2 [0.8, 3]	3 [1, 5]
18	102 [63, 147]	178 [95, 294]	31 [14, 58]	50 [23, 95]	9 [5, 15]	9 [5, 15]	16 [9, 27]
19	299 [179, 429]	1494 [718, 2574]	743 [285, 1535]	1852 [711, 3828]	117 [56, 202]	75 [36, 129]	137 [66, 235]

Table 2.3 (cont'd)

Shell	$M_{\text{shell}}$ ( $\text{M}_{\odot}$ )	$P_{\text{shell}}$ ( $\text{M}_{\odot} \text{ km s}^{-1}$ )	$E_{\text{shell}}$ ( $10^{44} \text{ erg}$ )	$\dot{E}_{\text{shell}}$ ( $10^{31} \text{ erg s}^{-1}$ )	$\dot{P}_{\text{shell}}$ ( $10^{-4} \text{ M}_{\odot} \text{ km s}^{-1} \text{ yr}^{-1}$ )	$\dot{m}_{\text{w}}$ ( $10^{-7} \text{ M}_{\odot} \text{ yr}^{-1}$ )	$\dot{E}_{\text{w}}$ ( $10^{31} \text{ erg s}^{-1}$ )
20	6 [4, 9]	8 [4, 13]	0.9 [0.4, 2]	3 [1, 5]	0.7 [0.3, 1]	0.4 [0.2, 0.7]	0.7 [0.4, 1]
21	24 [10, 58]	83 [31, 232]	29 [9, 92]	66 [21, 209]	6 [2, 17]	4 [2, 12]	8 [3, 21]
22	81 [58, 106]	146 [87, 222]	26 [13, 46]	28 [14, 49]	5 [3, 7]	7 [4, 11]	13 [8, 20]
23	335 [190, 490]	1005 [381, 1959]	300 [76, 779]	448 [113, 1165]	47 [18, 92]	50 [19, 98]	92 [35, 179]
24	101 [47, 172]	202 [47, 517]	40 [5, 154]	111 [13, 425]	18 [4, 45]	10 [2, 26]	18 [4, 47]
25	35 [18, 57]	52 [18, 113]	8 [2, 23]	14 [3, 40]	3 [1, 6]	3 [0.9, 6]	5 [2, 10]
26	36 [34, 63]	89 [68, 190]	22 [14, 57]	102 [63, 262]	13 [10, 28]	4 [3, 9]	8 [6, 17]
27	7 [1, 22]	7 [0.6, 34]	0.7 [0, 5]	0.8 [0, 5]	0.2 [0, 1]	0.4 [0, 2]	0.6 [0.1, 3]
28	101 [46, 173]	173 [55, 380]	29 [7, 83]	54 [12, 152]	10 [3, 22]	9 [3, 19]	16 [5, 35]
29	2 [1, 4]	3 [1, 5]	0.3 [0.1, 0.7]	0.8 [0, 3, 2]	0.2 [0.1, 0.4]	0.1 [0.1, 0.3]	0.3 [0.1, 0.5]
30	56 [36, 82]	56 [29, 99]	6 [2, 12]	5 [2, 11]	2 [0.9, 3]	3 [1, 5]	5 [3, 9]
31	135 [101, 191]	223 [151, 344]	37 [23, 61]	65 [40, 110]	13 [9, 19]	11 [8, 17]	20 [14, 31]
32	109 [67, 149]	163 [67, 299]	24 [7, 59]	45 [13, 111]	10 [4, 18]	8 [3, 15]	15 [6, 27]
33	8 [3, 15]	17 [6, 36]	3 [0.9, 9]	14 [4, 37]	2 [0.8, 5]	0.8 [0.3, 2]	2 [0.5, 3]
34	40 [22, 66]	85 [40, 159]	18 [7, 38]	42 [17, 89]	6 [3, 12]	4 [2, 8]	8 [4, 15]
35	71 [38, 111]	60 [27, 111]	5 [2, 11]	6 [2, 12]	2 [0.9, 4]	3 [1, 6]	5 [2, 10]
36	114 [46, 180]	114 [23, 271]	11 [1, 40]	7 [0.7, 24]	2 [0.4, 5]	6 [1, 14]	10 [2, 25]
37	112 [69, 149]	280 [124, 477]	70 [22, 152]	161 [51, 351]	20 [9, 35]	14 [6, 24]	26 [11, 44]
38	39 [17, 69]	39 [9, 104]	4 [0.4, 15]	4 [0.5, 18]	1 [0.3, 4]	2 [0.4, 5]	4 [0.8, 9]

Table 2.3 (cont'd)

Shell	$M_{\text{shell}}$ ( $\text{M}_{\odot}$ )	$P_{\text{shell}}$ ( $\text{M}_{\odot} \text{ km s}^{-1}$ )	$E_{\text{shell}}$ ( $10^{44} \text{ erg}$ )	$\dot{E}_{\text{shell}}$ ( $10^{31} \text{ erg s}^{-1}$ )	$\dot{P}_{\text{shell}}$ ( $10^{-4} \text{ M}_{\odot} \text{ km s}^{-1} \text{ yr}^{-1}$ )	$\dot{m}_{\text{w}}$ ( $10^{-7} \text{ M}_{\odot} \text{ yr}^{-1}$ )	$\dot{E}_{\text{w}}$ ( $10^{31} \text{ erg s}^{-1}$ )
39	21 [4, 61]	62 [8, 245]	18 [2, 97]	72 [6, 379]	8 [1, 30]	3 [0.4, 12]	6 [0.7, 22]
40	3 [1, 7]	4 [1, 15]	0.6 [0.1, 3]	6 [1, 28]	1 [0.3, 5]	0.2 [0.1, 0.7]	0.4 [0.1, 1]
41	21 [4, 52]	37 [4, 129]	7 [0.4, 32]	21 [1, 104]	4 [0.4, 13]	2 [0.2, 6]	3 [0.4, 12]
42	19 [9, 26]	19 [6, 34]	2 [0.4, 4]	2 [0.5, 5]	0.7 [0.2, 1]	0.9 [0.3, 2]	2 [0.5, 3]

Note. — Best-fit values are reported with lower and upper limits in brackets. Each best-fit value represents the median of an ensemble of models with the best-fit  $R$ ,  $dr$ , and  $v_{\text{exp}}$  over the full range in  $v_0$  given in Table 2.1. The lower and upper limits are also ensemble medians using all lower or upper limits of  $R$ ,  $dr$ , and  $v_{\text{exp}}$ . See Section 2.4.1.

Table 2.4. Impact of Shells and Outflows

Subregion Name	$E_{\text{shells}}^{\text{a}}$ ( $10^{46}$ erg)	$E_{\text{out}}^{\text{b}}$	$E_{\text{turb}}^{\text{c}}$	$\dot{E}_{\text{shells}}^{\text{a}}$ ( $10^{33}$ erg s $^{-1}$ )	$\dot{E}_{\text{w}}^{\text{d}}$	$\dot{E}_{\text{out}}^{\text{b}}$	$\dot{E}_{\text{turb}}^{\text{c}}$	$\dot{P}_{\text{shells}}^{\text{a}}$ ( $10^{-3} M_{\odot} \text{km s}^{-1} \text{yr}^{-1}$ )	$\dot{P}_{\text{out}}^{\text{b}}$	$\dot{P}_{\text{turb}}^{\text{c}}$
North	1.9 [0.7, 4.7]	0.68	7.8	4.0 [1.0, 13.2]	0.8 [0.4, 1.6]	20	2.1	6.0 [1.9, 14.3]	2.0	3.3
Central	2.5 [0.7, 6.4]	15	20	7.2 [2.3, 17.4]	1.0 [0.4, 2.0]	4400	10.6	8.6 [3.6, 16.6]	566	6.9
South <sup>e</sup>	12 [4.2, 28]	—	14	26.8 [9.7, 60.9]	3.0 [1.3, 5.6]	—	2.9	22.1 [10.0, 41.6]	—	3.3
L1641N	2.4 [0.8, 6.2]	1.3	16	5.1 [1.5, 15]	1.2 [0.5, 2.5]	17	4.2	8.2 [3.3, 17.7]	4.6	4.3
Total	19 [6.4, 45]	17	58	43.1 [14.5, 106]	6.1 [2.6, 11.7]	4437	19.8	44.9 [18.9, 90.2]	573	—

<sup>a</sup>Shell quantities are given by summing the best-fit values in Table 4.2 corresponding to the shells centered in each subregion (from Figure 2.1). The lower and upper limits are sums of the lower and upper limits in Table 4.2.

<sup>b</sup>Outflows are compiled in Section 3.3.2.

<sup>c</sup>Turbulent energies are calculated in Section 2.5.1 and injection rates are calculated in Section 2.5.1.

<sup>d</sup>Wind energy injection rates are calculated in Section 2.5.2.

<sup>e</sup>The shell totals in the South subregion are dominated by two outliers: Shell 19 and Shell 23. Without these two shells, the South subregion totals become  $E_{\text{shells}} = 1.6$  [0.6, 4.9],  $\dot{E}_{\text{shells}} = 3.8$  [1.5, 11],  $\dot{E}_{\text{w}} = 0.7$  [0.3, 1.5], and  $P_{\text{shells}} = 5.7$  [2.6, 12.2]. The total impact from all shells becomes  $E_{\text{shells}} = 8.4$  [2.8, 21.6],  $\dot{E}_{\text{shells}} = 20.1$  [6.7, 53.6],  $\dot{E}_{\text{w}} = 3.7$  [1.6, 7.5], and  $\dot{P}_{\text{shells}} = 28.5$  [11.8, 59.2].

# Chapter 3

## The CARMA-NRO Orion Survey: Statistical Signatures of Feedback in the Orion A Molecular Cloud

*Originally published as Feddersen, J. R., Arce, H. G., Kong, S., Ossenkopf-Okada, V.*

*Carpenter, J. M. 2019, Astrophysical Journal, 875, 162.*

### Abstract

We investigate the relationship between turbulence and feedback in the Orion A molecular cloud using maps of  $^{12}\text{CO}(1-0)$ ,  $^{13}\text{CO}(1-0)$  and  $\text{C}^{18}\text{O}(1-0)$  from the CARMA-NRO Orion survey. We compare gas statistics with the impact of feedback in different parts of the cloud to test whether feedback changes the structure and kinematics of molecular gas. We use principal component analysis, the spectral correlation function, and the spatial power spectrum to characterize the cloud. We quantify the impact of feedback with momentum injection rates of protostellar outflows and wind-blown shells as well as the surface density of young stars. We find no correlation between shells or outflows and any of the gas statistics. However, we find a significant anti-correlation between young star surface density and the slope of the  $^{12}\text{CO}$  spectral correlation function, suggesting that feedback may

influence this statistic. While calculating the principal components, we find peaks in the covariance matrix of our molecular line maps offset by  $1\text{-}3 \text{ km s}^{-1}$  toward several regions of the cloud which may be produced by feedback. We compare these results to predictions from molecular cloud simulations.

### 3.1 Introduction

Stars form deep inside giant molecular clouds (GMCs) (McKee & Ostriker, 2007; Heyer & Dame, 2015). Young stars output mechanical and thermal energy, or feedback, into their birth clouds (Krumholz et al., 2014). This feedback may decrease the efficiency of star formation by counteracting gravitational collapse (Federrath, 2015) and help drive and maintain turbulence (Nakamura & Li, 2007; Offner & Liu, 2018).

GMCs are turbulent, with supersonic linewidths that increase with physical size (Zuckerman & Evans, 1974; Larson, 1981; Mac Low & Klessen, 2004). However, turbulence decays rapidly (Mac Low et al., 1998; Stone et al., 1998; Padoan & Nordlund, 1999), and must be maintained by some mechanism. Feedback from young stars may help maintain the turbulence of molecular clouds (Li & Nakamura, 2006; Matzner, 2007; Carroll et al., 2009).

Offner & Liu (2018) proposed a mechanism for translating local feedback into large scale turbulent driving. They used magnetohydrodynamic simulations to show that feedback effects may be propagated through a cloud by magnetic fields. Upon injecting winds into the simulation, they showed that the velocity dispersion outside of the wind-blown shells was increased and the velocity power spectrum flattened. These effects were caused by magnetosonic waves coming from the compressed wind-blown shells. These magnetosonic waves could explain how feedback drives turbulence at larger scales.

Feedback in molecular clouds has mostly been studied by cataloging individual features such as protostellar outflows (e.g., Arce et al., 2010; Plunkett et al., 2015a), photon-

dominated regions (PDRs) with far-UV heating and photoablation (e.g., Bally et al., 2018), and stellar wind-blown shells (e.g., Arce et al., 2011; Nakamura et al., 2012; Li et al., 2015; Feddersen et al., 2018). The physical characteristics of these features can then be measured to estimate the impact of feedback on a molecular cloud. However, visually cataloging feedback features is time-consuming and prone to significant bias and difficulty of separating features from the rest of the cloud.

Recently, several studies have considered the impact of feedback by measuring statistics of molecular gas structure and motions. Nakamura & Li (2007) and Carroll et al. (2009) showed that the presence of outflows modifies the velocity power spectrum of simulated molecular clouds, producing peaks at the scale where outflows inject energy into the cloud. Padoan et al. (2009) investigated the power spectrum of the molecular cloud NGC 1333, finding no evidence for a departure from a power-law near the outflow energy injection scales predicted by the above-mentioned simulations.

Swift & Welch (2008) computed the power spectrum of the red and blue line wings of  $^{13}\text{CO}$  in the L1551 molecular cloud, which hosts several outflows. They found a feature in these power spectra at a scale of about 0.05 pc, indicating a preferential scale of energy injection into the cloud. Sun et al. (2006) compared the CO power spectrum in different regions of the Perseus molecular cloud. They found the most actively star-forming region NGC 1333 had a steeper slope than the quiescent dark cloud L1455. Swift & Welch (2008) also measured a flat linewidth-size relationship in the low-mass molecular cloud L1551, suggesting that turbulent motions originate to a large degree at small-spatial scales. This is contrary to the turbulent cascade that is usually assumed for molecular clouds, where driving happens at large scales and dissipation occurs at the smallest scales via gas viscosity (Mac Low & Klessen, 2004).

Principal component analysis (Heyer & Schloerb, 1997) has also been used to investigate the effect of feedback on molecular clouds. Brunt et al. (2009) showed that the ratio between different-order principal components of a simulated cloud is sensitive to the

driving scale of turbulence. Adding outflows to their simulations did not change this ratio, implying that feedback in the form of outflows was not driving turbulence in their simulated cloud. However, Carroll et al. (2010) showed that this analysis is biased towards the largest scales. The presence of significant smaller-scale turbulent driving from feedback may then be hidden in the principal component analysis.

The spectral correlation function quantifies the similarity of pairs of spectra as a function of their separation. Ballesteros-Paredes et al. (2002) applied the spectral correlation function to 21 cm HI spectra of the North Celestial Pole Loop region. Instead of averaging the spectral correlation function (see Equation 3.2 below) over all pixels, they constructed a map of the local SCF of each pixel. Their map of the SCF highlighted the edge of the expanding supernova remnant HI shell. They suggested using the SCF as a tool for finding shells.

Boyden et al. (2016) (hereafter B16) applied the TurbuStat<sup>1</sup> (Koch et al., 2017) suite of statistical measures to molecular cloud simulations from Offner & Arce (2015). These simulations tested the effect of stellar winds on the structure of a simulated molecular cloud and successfully reproduced the expanding shells found in Perseus by Arce et al. (2011). B16 found statistical measures sensitive to the mass-loss rate of the injected stellar winds. In their simulation with winds, the covariance matrix (see Section 3.4.1) showed peaks of spatially correlated emission separated by  $1\text{-}3 \text{ km s}^{-1}$  and the spectral correlation function (see Section 3.4.2) had a steeper slope compared to simulations without winds. They found the power spectrum was insensitive to stellar winds.

In this paper, we test whether statistical measures of CO in the Orion A GMC trace feedback in the cloud, as predicted by B16. In Section 3.2, we describe the CARMA-NRO Orion observations and split the cloud into subregions. In Section 3.3, we define three ways of quantifying feedback in the cloud. In Section 3.4, we introduce the statistics we use to summarize the CO data. In Section 3.5, we present the results of these statistics

---

<sup>1</sup><http://turbustat.readthedocs.io/en/latest/>

and compare with previous studies. In Section 3.6, we discuss the relationship between the statistics and feedback in the cloud. In Section 4.6, we summarize the conclusions of the paper and suggest future directions for the statistical study of feedback.

## 3.2 Data

### 3.2.1 CARMA-NRO Orion CO Maps

We use the  $^{12}\text{CO}$ (1-0),  $^{13}\text{CO}$ (1-0), and  $\text{C}^{18}\text{O}$ (1-0) spectral-line maps of Orion A from the CARMA-NRO Orion Survey (Kong et al., 2018). These maps were obtained by combining interferometric images from the Combined Array for Millimeter/Submillimeter Astronomy (CARMA) with single-dish maps from the Nobeyama Radio Observatory (NRO) 45m radio telescope. This method preserves the angular resolution of CARMA while also recovering large-scale structure. The combined maps probe physical scales of 0.01 - 10 pc at a distance of 414 pc (Menten et al., 2007).<sup>2</sup> The  $^{12}\text{CO}$  and  $\text{C}^{18}\text{O}$  maps have a beam full-width at half-maximum (FWHM) of  $10'' \times 8''$  and the  $^{13}\text{CO}$  map has a FWHM of  $8'' \times 6''$ . The  $^{12}\text{CO}$  velocity resolution is  $0.25 \text{ km s}^{-1}$  while  $^{13}\text{CO}$  and  $\text{C}^{18}\text{O}$  have a velocity resolution of  $0.22 \text{ km s}^{-1}$ . For more details on the CARMA-NRO Orion data, see Kong et al. (2018).

### 3.2.2 Subregions

To compare the statistics of turbulence with feedback impact, we would ideally like to have a control - a cloud which is identical in every way to Orion A except with no stellar feedback. In this ideal case, any statistical differences between the clouds could be

---

<sup>2</sup>The part of Orion A covered by our survey has been located about 5% closer (at about 380-400 pc) with GAIA Data Release 2 parallaxes (Kounkel et al., 2018; Großschedl et al., 2018; Kuhn et al., 2019). Adopting a distance of 390 pc would decrease the projected distances and the derived physical quantities (momentum injection rates) in this paper by a factor of 0.94. Our conclusions are independent of distance.

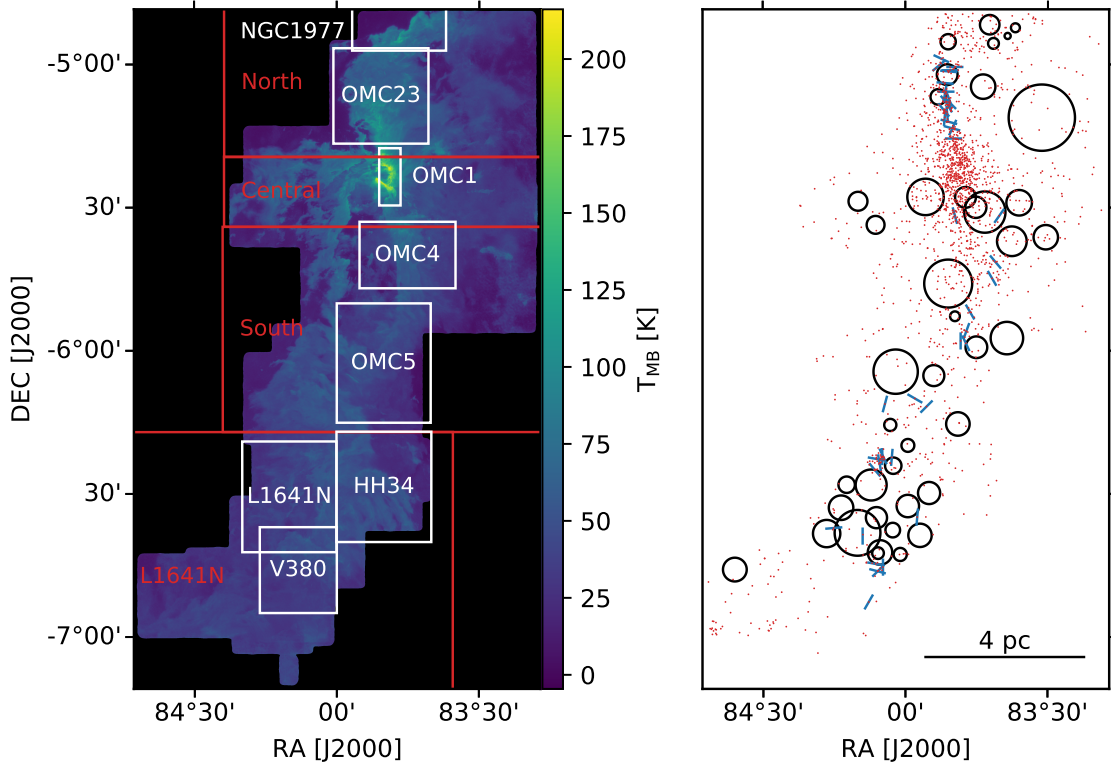


Figure 3.1 Finding charts of subregions and sources of feedback used in this paper. *Left:* Subregions overlaid on the CARMA-NRO Orion  $^{12}\text{CO}$  peak temperature map. The small subregions outlined in white come from Davis et al. (2009) except for OMC1, which comes from Ungerechts et al. (1997). The large subregions outlined in red come from Fedderson et al. (2018). *Right:* The three measures of feedback impact are shown. The *black circles* show the location and radius of the candidate expanding shells from Fedderson et al. (2018). The *blue lines* show the location and orientation of outflows cataloged by Tanabe et al. (2019, in press). The length of the lines is arbitrary and does not indicate outflow length. The *red points* mark all pre-main sequence stars and protostars from the Spitzer Orion catalog of Megeath et al. (2012).

attributed solely to the action of feedback. This ideal scenario was simulated by B16 but no such true control cloud exists for Orion A, though Lada et al. (2009) proposed that the California Molecular Cloud is an Orion A analogue with an order of magnitude lower star formation rate. In this study, we compare different regions of Orion A with different amounts of feedback, assume that this is the only relevant difference, and look for trends in the statistical methods that resemble those found in the simulated clouds of B16. A similar approach is used by Sun et al. (2006) in their comparison of power spectra in different regions of the Perseus molecular cloud.

We divide the Orion maps into several subregions, guided by previous studies. Fedderesen et al. (2018) split Orion A into four subregions - North, Central, South, and L1641N - to compare the impact of expanding shells with protostellar outflows and cloud turbulence. The North subregion includes the NGC 1977 PDR (Peterson & Megeath, 2008), OMC-2/3, and the M43 HII region. The Central subregion covers a wide variety of environments, including the Orion Bar PDR (Goicoechea et al., 2016), OMC-1 (the densest part of the cloud), the explosive Orion BN/KL outflow (Bally et al., 2017), and more diffuse gas to the east and west. The South subregion covers OMC 4/5 and the pillar-shaped PDRs to the east dubbed the dark lane south filament (DLSF) by Shimajiri et al. (2011). The L1641N subregion covers the low-mass cluster L1641-N (Nakamura et al., 2012) and the reflection nebula NGC 1999 (Stanke et al., 2010).

In addition to these regions, we consider several smaller subregions focused on individual parts of the cloud based on the molecular hydrogen outflow survey of Davis et al. (2009). These smaller subregions focus on specific clusters or groups of young stars in the Orion A cloud and all have similar projected areas on the sky of about  $0.1 \text{ deg}^2$  ( $5 \text{ pc}^2$ ). We also add a subregion defined by Ungerechts et al. (1997) which is restricted to the densest core of Orion A - OMC 1, BN-KL, and the Orion Bar. We define these subregions following conventional definitions in Orion A to avoid cherry-picking regions that happen to show the correlations between statistics and feedback that we are looking for. Figure 4.1

shows the subregions on a map of  $^{12}\text{CO}$  peak temperature and Table 3.1 defines the extent of each subregion.

### 3.3 Quantifying Feedback

In order to relate gas statistics to the impact of feedback in the cloud, we attempt to measure this impact. B16 quantified feedback using the mass-loss rate of stellar winds injected into their simulations. Offner & Arce (2015) designed these simulations to reproduce the expanding shells observed by Arce et al. (2011) in the Perseus molecular cloud. Thus, to make the closest comparison to B16, we first consider the expanding shells in Orion A identified by Feddersen et al. (2018).

#### 3.3.1 Expanding Shells

Feddersen et al. (2018) identified 42 expanding shells in Orion A using the CO maps from the NRO 45m telescope. The authors visually identified expanding structures in the CO channel maps and matched many of these structures with low- and intermediate-mass young stars. Similar shells have been found in the Perseus (Arce et al., 2011) and Taurus (Li et al., 2015) molecular clouds. While the origin of such shells is unclear, one explanation is spherical stellar winds from young stars which entrain the cloud material into expanding shells. We show the shells of Feddersen et al. (2018) in Figure 4.1.

The impact of shells on the cloud is summarized by Table 3 in Feddersen et al. (2018). In this study, we quantify a shell’s impact on the cloud by its momentum injection rate ( $\dot{P}_{\text{shell}}$ ). The total shell momentum injection rate in each subregion is the sum of  $\dot{P}_{\text{shell}}$  for each shell centered inside that subregion. The true shell impact is uncertain, as it is difficult to extract shell emission cleanly from the rest of the cloud. Furthermore, most shells are incomplete. They are only detected over a fraction of the expected volume in the spectral cube. Lower and upper limits on  $\dot{P}_{\text{shell}}$  are estimated in Table 3 of Feddersen et al. (2018)

and can span a factor of several above or below the median value. We ignore these lower and upper limits and instead focus on the relative shell impacts between subregions, but the uncertainties mean any results based on the shell momenta are inconclusive. Because of these large uncertainties and the potential for false-positive bias in identifying expanding shells, we use independent methods to quantify feedback.

### 3.3.2 Protostellar Outflows

Young stars that are actively accreting material launch collimated bipolar outflows which impact the surrounding cloud material and may help drive or maintain turbulence (Arce et al., 2007; Frank et al., 2014). In Orion A, outflows have been identified by many authors (e.g. Morgan et al., 1991; Williams et al., 2003; Stanke & Williams, 2007; Takahashi et al., 2008). A comprehensive census of outflows found in our NRO 45m data has been carried out by Tanabe et al. (2019, in press). They have detected about 50% more outflows than previously known. Notably, they identified 11 outflows in the poorly studied OMC 4/5 region where none were previously known. Tanabe et al. (2019, in press) excluded the area around OMC-1 from their search because the YSOs in this region are crowded and the cloud velocity width is too broad to disentangle outflow emission. Therefore, the outflow measurements for our regions around OMC1 are incomplete.

To quantify the impact of outflows on the cloud, we use the momentum injection rates ( $\dot{P}_{\text{out}}$ ) tabulated in Table 6 of Tanabe et al. (2019, in press). Many of the outflows in this table have multiple lobes listed separately. In these cases, we sum the individual lobes of each outflow. We assign outflows to the subregion containing the driving source in Table 3 of Tanabe et al. (2019, in press). The only case where the driving source of an outflow lies in a different subregion from part of the outflow emission is Outflow 19 in Tanabe et al. (2019, in press). A small portion of the emission from this outflow falls south of the OMC23 subregion, where its driving source is located. In every other case, the outflow

emission and its driving source are in the same subregion.

To measure the outflow mass, Tanabe et al. (2019, in press) first integrate the  $^{12}\text{CO}$  emission.  $^{12}\text{CO}$  is often optically thick, which means line intensity is no longer directly proportional to column density and mass. To account for the optical depth of  $^{12}\text{CO}$ , other tracers must be observed. For example, Zhang et al. (2016) use  $^{13}\text{CO}$  and  $\text{C}^{18}\text{O}$  combined with  $^{12}\text{CO}$  to measure outflow masses more accurately. Tanabe et al. (2019, in press) only detect a few outflows in both  $^{12}\text{CO}$  and  $^{13}\text{CO}$ . They calculate the average optical depth of these few outflows and apply this correction factor to every outflow in their catalog, ignoring any variation in optical depth.

After they find the mass of an outflow, Tanabe et al. (2019, in press) they calculate momentum by multiplying this mass by the line-of-sight velocity of the outflow. But if the outflow axis is inclined relative to the line-of-sight, this will underestimate the true momentum.

Variable optical depth and inclination angle both introduce uncertainty in the outflow momentum injection rates. The optical depth of outflows in Orion A is likely not uniform. This fact is evidenced by the different outflow optical depths measured by Tanabe et al. (2019, in press) as well as the variations in the ratio between the integrated intensities of  $^{12}\text{CO}$  and  $^{13}\text{CO}$  throughout the cloud (see Figure 25 in Kong et al., 2018). A variable outflow optical depth will affect our comparisons of outflow impact between subregions.

### 3.3.3 Young Stars

As an independent estimate of feedback we consider the young stars (YSOs) in each subregion. YSOs are more directly a measure of star formation rate than feedback impact. However, YSOs are ultimately responsible for both outflows and shells. Therefore we consider the surface density of YSOs  $n_{\text{YSO}}$  to be a proxy for the relative strength of feedback in different regions.

To measure  $n_{\text{YSO}}$ , we use the Spitzer Orion catalog of YSOs (Megeath et al., 2012). They classified stars as protostars or pre-main sequence stars with disks on the basis of their mid-IR colors. In this classification, 86% of the Spitzer Orion YSOs are pre-main sequence stars and the remaining 14% are protostars. Shells are likely driven by pre-main sequence stars (Arce et al., 2011; Feddersen et al., 2018) while outflows are more likely driven by protostars. Therefore, we calculate  $n_{\text{YSO}}$  using all YSOs in the catalog.

Because the YSO catalog is a mixture of more evolved pre-main sequence stars and younger protostars, this measure traces a wider range of timescales than either shells or outflows alone. As noted in Section 5.2.3 of Arce et al. (2010), the cumulative impact of feedback in a cloud over the course of star formation may be greater than what is traced by the currently active outflows and shells. Thus, if there are YSOs which have ejected outflows or powered shells no longer detectable as coherent structures in the cloud, then  $n_{\text{YSO}}$  may be a better tracer of the potential link between feedback and turbulence than shells or outflows alone.

To compare subregions of different sizes, we calculate the surface density of each feedback measure, dividing by the projected area of each subregion. The Spitzer Orion catalog suffers from incompleteness toward regions with bright IR nebulosity (Megeath et al., 2016). Thus the YSO surface density in the Central and OMC1 subregions is likely higher relative to the surface density in other subregions. From Figure 2 and 3 in Megeath et al. (2016), the typical completeness fraction in the ONC is approximately 0.5. Therefore, the true central YSO surface density may be up to about twice the value reported here. Our three feedback measures are the momentum injection rate surface density of shells/outflows ( $M_{\odot} \text{ km s}^{-1} \text{ yr}^{-1} \text{ deg}^{-2}$ ) and the YSO surface density ( $\text{deg}^{-2}$ ).

## 3.4 Statistical Methods

We use the TurbuStat<sup>3</sup> package, described in detail by Koch et al. (2017), to compute the principal component analysis, spectral correlation function, and spatial power spectrum of the  $^{12}\text{CO}$ ,  $^{13}\text{CO}$ , and  $\text{C}^{18}\text{O}$  data in Orion A. B16 also found several other statistics that were sensitive to wind mass loss rate (see their Table 3). However, Boyden et al. (2018) incorporated astrochemical models into these simulations and found that many of the statistics were also sensitive to the chemical complexity, radiation field, and molecular tracer used. The statistics which are least sensitive to these effects while remaining sensitive to feedback strength were principal component analysis and the spectral correlation function (see Section 5.3 in Boyden et al. 2018). While the spatial power spectrum was not sensitive to feedback in B16, its form has been studied for possible signatures of feedback (e.g. Swift & Welch, 2008) so we include it here. TurbuStat also provides a distance metric for each statistic, which allows comparison of different cubes. We briefly describe these statistical methods below.

### 3.4.1 Principal Component Analysis

Principal component analysis (PCA) is a statistical technique used to reduce the dimensionality of a dataset. Ungerechts et al. (1997) and Heyer & Schloerb (1997) first applied PCA to molecular line maps to study the chemistry and turbulence in molecular clouds.

The method implemented by TurbuStat to compute the PCA of a spectral cube comes from Heyer & Schloerb (1997). A spectral cube with  $n$  pixels can be expressed as a set of  $n$  spectra with a number  $p$  of velocity channels. This can be represented as a matrix  $T(r_i, v_j) \equiv T_{ij}$  with  $n$  rows and  $p$  columns, where  $r_i$  is the position of pixel  $i$  and  $v_j$  is the velocity of channel  $j$ .

---

<sup>3</sup><https://turbustat.readthedocs.io/en/latest>

First, each element of the covariance matrix  $S$  is calculated to be

$$S_{jk} = S(v_j, v_k) = \frac{1}{n} \sum_{i=1}^n T_{ij} T_{ik}. \quad (3.1)$$

This covariance matrix is then diagonalized to find its eigenvalues and eigenvectors. Projecting the spectral cube onto each eigenvector gives a set of eigenimages called principal components. Each eigenvalue correspond to the amount of variance recovered by each principal component.

B16 found the covariance matrix to be sensitive to the injected stellar winds. Their Figure 3 shows peaks at  $1\text{-}3 \text{ km s}^{-1}$  in the covariance matrix of the simulation with winds which are absent in the simulation without winds. We test whether such features appear in the Orion covariance matrices.

To compare their simulated spectral cubes, B16 used the Turbustat PCA distance metric. Each set of eigenvalues for a particular cube is sorted in descending order; then the eigenvalues are normalized by dividing them by their sum. The PCA distance metric between two cubes is then the Euclidean distance between the two normalized sets of eigenvalues, or the square root of the sum of the square differences. B16 found a strong correlation between the PCA distance metric and winds. Boyden et al. (2018) incorporated gas chemistry into these simulations and found that PCA also varied between models with and without chemistry. However, the covariance peaks remained a unique signature of winds. For more details on PCA, see Brunt & Heyer (2002a,b, 2013).

### 3.4.2 Spectral Correlation Function

The spectral correlation function (SCF) was first introduced by Rosolowsky et al. (1999) and refined by Padoan et al. (2001). The SCF measures the similarity of spectra as a function of their spatial separation, or lag. The SCF at a specific lag vector  $\Delta r$  (between

two pixels) is defined to be

$$\text{SCF}(\mathbf{r}, \Delta\mathbf{r}) = 1 - \sqrt{\frac{\sum_v [T(\mathbf{r}, v) - T(\mathbf{r} + \Delta\mathbf{r}, v)]^2}{\sum_v T(\mathbf{r}, v)^2 + \sum_v T(\mathbf{r} + \Delta\mathbf{r}, v)^2}}, \quad (3.2)$$

where  $\mathbf{r}$  is the position of a pixel,  $\Delta\mathbf{r}$  is the lag vector,  $v$  is velocity, and  $T$  is the temperature (or intensity). The SCF is then averaged over all pixels  $\mathbf{r}$ . Repeating this for various lag vectors, a 2D spectral correlation surface can be constructed. An azimuthal average of this surface, or equivalently an average over all rotated lag vectors of the same length, is a 1D spectrum of the SCF as a function of spatial separation. We refer to this 1D spectrum as the SCF in this paper. Padoan et al. (2001) showed that the SCF is well characterized by a power-law in both simulated and observed molecular clouds, over a wide range of physical scales. They also showed that the slope of the SCF is independent of velocity resolution and signal-to-noise.

The SCF distance metric is defined in TurbuStat as the sum of the square differences between the SCF surfaces, weighted by the inverse square distance from the center of the surface. B16 found SCF to be sensitive to the strength of feedback. In their simulations with winds injected, the SCF has a significantly steeper slope than in the wind-free simulations. More recently, Boyden et al. (2018) found that including chemistry in these simulations flattened the SCF slope as opposed to the steepening seen with winds. For more details on SCF, see Rosolowsky et al. (1999) and Padoan et al. (2001).

### 3.4.3 Spatial Power Spectrum

The power spectrum is the Fourier transform of the two-point autocorrelation (or square) of the integrated intensity. We azimuthally average this two-dimensional power spectrum to arrive at a one-dimensional power spectrum which we hereafter refer to as the SPS. See Stutzki et al. (1998) for the general  $n$ -dimensional derivation and Pingel et al. (2018) for a detailed description of the SPS implementation used here.

Because our maps have emission at the edges, the Fourier transform is affected by strong ringing (e.g. Brault & White, 1971; Muller et al., 2004) which can be seen at small spatial scales in the power spectrum. To correct for this ringing, we taper the integrated intensity with a Tukey window where the outer 20% of the map is gradually reduced to zero. This tapering also reduces the noise at the edges of the observed maps. Additionally, the observed beam introduces artificial correlation into the map (e.g. Dickey et al., 2001). To correct for this, we divide the power spectrum of the integrated intensity by the power spectrum of the ellipsoidal Gaussian beam. This introduces a divergence at very small scales but allows us to extend the dynamic range over which the underlying power spectrum is recovered. These corrections are implemented in TurbuStat and described in tutorials included in the package documentation.

B16 found that the SPS was not sensitive to feedback in their simulations of winds, while Boyden et al. (2018) found that temperature variation flattened the slope. However, some studies have suggested that feedback induces a break in the power spectrum. Swift & Welch (2008) reported a “bump” in the  $^{13}\text{CO}$  SPS of L1551 at a scale of about 0.05 pc. They attributed this peak to the energy injection scale of the outflows in the cloud. However, they used the power spectrum of the line wings which may be more sensitive to outflow emission than the full integrated intensity of the cloud. We discuss the line wing power spectra in Section 3.6.2.

## 3.5 Results

### 3.5.1 Principal Component Analysis

B16 showed that the covariance matrix (Equation 3.1), an intermediate product of PCA on spectral cubes, was sensitive to the presence of feedback. In their simulations with winds included, the covariance matrix shows several peaks at  $1 - 3 \text{ km s}^{-1}$  which are not

present in the simulations without winds. In Figure 3.2, we show the covariance matrices of the Orion A  $^{12}\text{CO}$  subregions (the  $^{13}\text{CO}$  and  $\text{C}^{18}\text{O}$  covariance matrices are described in Appendix 3.A). In several regions, most prominently NGC 1977, L1641N, OMC 4, and V380, we find covariance peaks offset from the diagonal axis by  $1 - 3 \text{ km s}^{-1}$  as in the B16 wind simulations. Essentially, these covariance peaks mean there is emission in these subregions which is spatially correlated but separated by a few  $\text{km s}^{-1}$  in velocity. This spatially correlated (but velocity-offset) emission can clearly be seen in the channel maps of these regions (Kong et al., 2018). The source of these features could be feedback, as it is in the B16 simulations, or some other effect.

Nakamura et al. (2012) proposed that the L1641N cluster is located at the intersection of two colliding clouds. This idea is based on the overlapping velocity components in this region. The blue velocity component ( $4\text{-}6 \text{ km s}^{-1}$ ) dominates emission to the southeast of L1641N while the red component ( $7\text{-}12 \text{ km s}^{-1}$ ) extends north of the cluster. Nakamura et al. (2012) noticed these velocity components in channel maps, but these are the same velocity components that appear as peaks in our covariance matrices of the L1641N and V380 regions. It is unclear whether the covariance peaks are the result of this cloud collision scenario or the expansion of wind-blown shells like those simulated by B16 or some combination of the two effects.

In the NGC 1977 region, the molecular cloud is excited by FUV radiation from the H II region to the north (Kutner et al., 1985; Makinen et al., 1985). This FUV may be responsible for photoablation (Ryutov et al., 2003) of the northern edge of the molecular cloud, accelerating it to a few  $\text{km s}^{-1}$  and generating the covariance peaks seen in this region. Well known examples of photoablative flows can be found in the Orion Bar (Goicoechea et al., 2016) and the Horsehead Nebula (Bally et al., 2018). Detailed comparison of the covariance matrix in both simulated and observed molecular clouds is needed to fully understand the mechanisms behind these peaks.

B16 used the PCA distance metric to further show that PCA was sensitive to the winds

in their simulations (see their Figure 16). We find no correlation between any of our feedback measures and the PCA distance metric between subregions. This could be because our feedback measures are not good proxies for the winds simulated by B16, or because another mechanism unrelated to feedback is driving the velocity structure traced by the covariance peaks.

### 3.5.2 Spectral Correlation Function

Figure 3.3 shows the  $^{12}\text{CO}$  SCF and power-law fits of each subregion. The fit slopes are tabulated in Table 3.1. We compute the two-dimensional SCF surface at lags between 0 and 30 pixels (0 to 0.12 pc) in intervals of 3 pixels (0.01 pc). Using a lag interval of 1 pixel does not significantly change the resulting SCF, so we save computational time by only calculating the SCF surface every 3 pixels. We then average the SCF surface in equally-spaced annuli to arrive at the one-dimensional SCF spectrum shown in Figure 3.3. We calculate the SCF over the same range of spatial scales as shown in Figure 6 of B16 for the most direct comparison. Each subregion's SCF follows a power-law closely up to a lag of approximately 20 pixels. We compute a weighted least-squares fit to each SCF between lags of 5 to 17 pixels (approximately 0.02 to 0.07 pc). Unlike in the B16 simulations, the Orion SCF steepens at larger lags. Gaches et al. (2015) also found a steepening SCF in  $^{13}\text{CO}$  maps of Ophiuchus and Perseus. We describe the SCF at scales larger than 0.12 pc in Appendix 3.C.

The SCF slopes in the Orion A subregions range from -0.15 to -0.06. Gaches et al. (2015) calculated the  $^{12}\text{CO}$  SCF of the Perseus and Ophiuchus molecular clouds and found slopes around -2, steeper than in any of our Orion A subregions. However, limited by the angular resolution of their data they fit the SCF at larger scales: 0.1 - 1 pc. Padoan et al. (2003) found  $^{13}\text{CO}$  SCF slopes between -0.1 and -0.5 in various molecular clouds. Most of their SCF spectra are fit at larger scales ( $> 0.1$  pc) than those presented here. But the

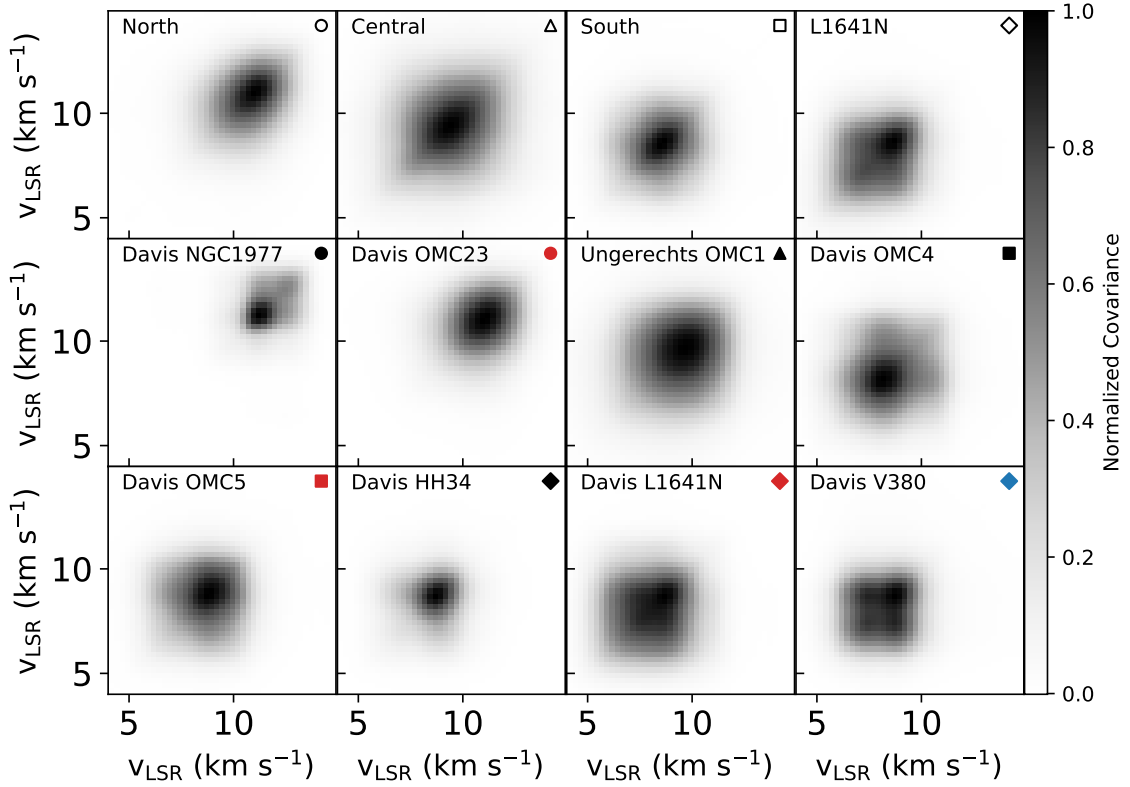


Figure 3.2  $^{12}\text{CO}$  covariance matrices in Orion A subregions. The top row shows the large subregions used by Feddersen et al. (2018), ordered from north to south. The bottom two rows show the smaller subregions defined by Ungerechts et al. (1997) and Davis et al. (2009), ordered from north to south. The symbol in each panel is used in subsequent figures to denote each subregion. The covariance matrix is used for the eigenvalue decomposition that forms the basis of principal component analysis, and is symmetric about the one-to-one axis by construction. Each matrix is normalized by its maximum covariance. Features offset from the one-to-one axis by 1 - 3  $\text{km s}^{-1}$  are seen most prominently in the V380, NGC1977, OMC4, and L1641N subregions and resemble the features B16 noticed in their simulations of winds.

smallest maps in their dataset, L1512 and L134a, have similar spatial resolution to our Orion A maps and also have the shallowest SCF slopes at -0.18 and -0.13, respectively. The simulations in B16 also have steeper SCF slopes compared to our data. The SCF is well known to vary with spatial resolution (Gaches et al., 2015) making comparison between different datasets difficult. B16 found the SCF slope was sensitive to their simulated wind mass loss rate. In Section 3.6.1 we compare the SCF slope between subregions and discuss the relationship between SCF slope and feedback impact.

### 3.5.3 Spatial Power Spectrum

Figure 3.4 shows the  $^{12}\text{CO}$  power spectra and power-law fits for each subregion. The fit slopes are tabulated in Table 3.1. The beam correction described in Section 3.4.3 causes the sharp upturn at scales smaller than about twice the beamwidth. We restrict the power-law fits to spatial scales greater than about five times the beamwidth. We also exclude the largest scale point in each power spectrum from the fits as some of the power spectra show slight deviations at this largest scale. In the fitted regime, the power spectra closely follow a power-law with no evidence of the peaks seen in Swift & Welch (2008).

The power-law fits to the SPS in the Orion A subregions have slopes ranging between about -3 and -4 in  $^{12}\text{CO}$  and  $^{13}\text{CO}$  with somewhat shallower slopes between about -2.2 and -3.4 in  $\text{C}^{18}\text{O}$  (see Appendix 3.A for  $^{13}\text{CO}$  and  $\text{C}^{18}\text{O}$  SPS). The SPS slope of an optically thick medium is predicted to saturate to -3 for a wide range of physical conditions (such as sound speed and magnetic field strength) (Lazarian & Pogosyan, 2004; Burkhart et al., 2013). Previous studies of the  $^{12}\text{CO}$  and  $^{13}\text{CO}$  SPS in molecular clouds have shown slopes close to this optically thick limit of -3 (Stutzki et al., 1998; Padoan et al., 2006; Sun et al., 2006; Pingel et al., 2018, e.g.), shallower than our SPS slopes. However, these studies measure the SPS of entire clouds instead of smaller regions within clouds, averaging over larger areas than our subregions. Sun et al. (2006) reported the power spectrum slope in

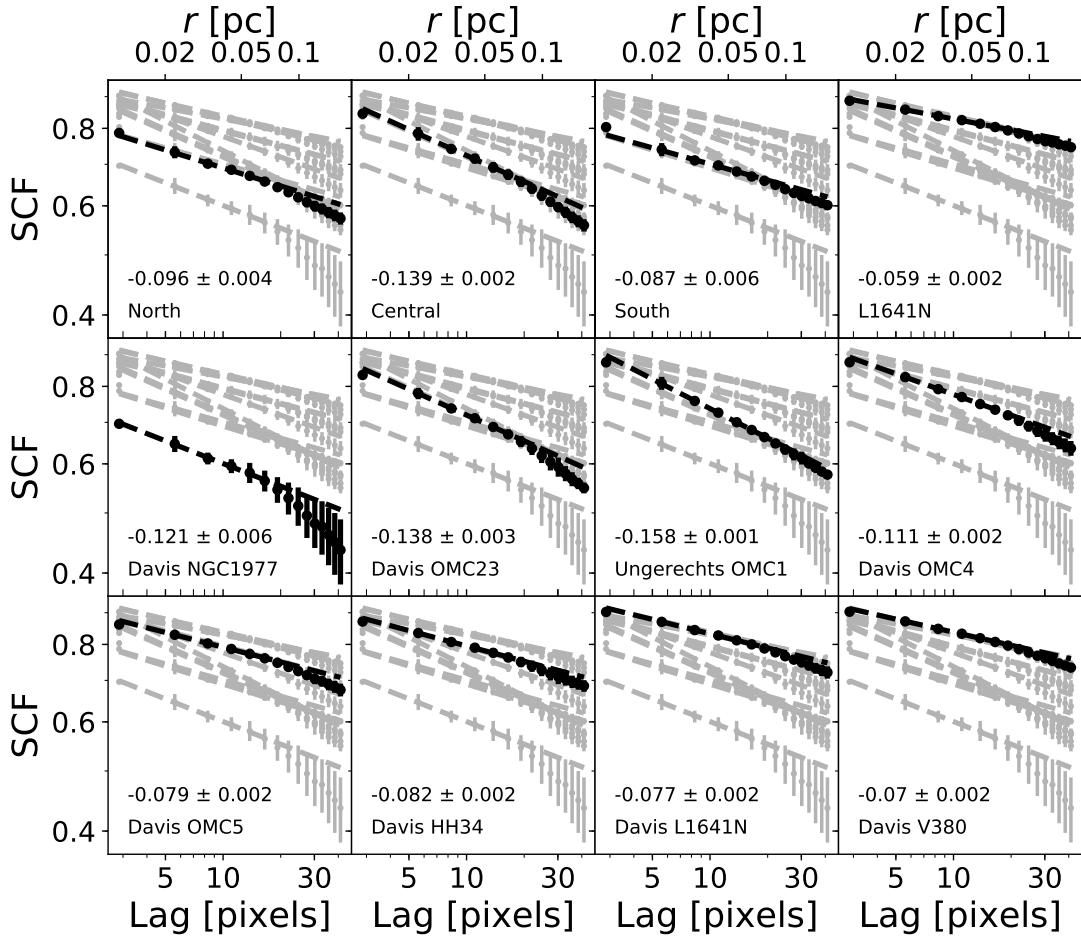


Figure 3.3  $^{12}\text{CO}$  spectral correlation function (SCF) in Orion A subregions. The subregions are ordered in the same way as Figure 3.2. In each panel, the *black points* are the azimuthally averaged values of the SCF surface, with errors given by the standard deviation of the SCF surface in each bin. The *black line* is a weighted least-squares power law fit to these points. The *gray lines and points* show the SCF and fits for all subregions. Each SCF is fit between lags of 5 to 17 pixels. The power law slope and uncertainty are shown in each panel.

several regions within the Perseus Molecular Cloud spanning  $50' \times 50'$ , or  $4.4 \text{ pc} \times 4.4 \text{ pc}$  at a distance of 300 pc (Zucker et al., 2018; Ortiz-León et al., 2018). Most of these regions have SPS slopes steeper than -3, more similar to our subregions than to cloud-wide power spectra. Also, our *largest* subregions have slopes closest to the theoretically predicted value of -3. In Section 3.6.1, we compare the SPS slope to feedback impact in each subregion.

## 3.6 Discussion

### 3.6.1 Spectral Slopes and Feedback Impact

In the simulations of B16, SCF responds strongly to the strength of feedback but is independent of evolutionary time and magnetic field strength. They found that SCF slope steepened with increased wind mass-loss rate. Boyden et al. (2018) showed that SCF is sensitive to gas chemistry, but including chemistry flattens the SCF slope - the opposite impact of feedback. Thus, SCF may still probe the relative strength of feedback in different regions, especially if chemistry is similar between regions.

SPS, on the other hand, has only a weak dependence on feedback in B16 but varies strongly with evolutionary time and magnetic field strength, making SPS a poor diagnostic for feedback. Further, Boyden et al. (2018) showed that SPS is also sensitive to temperature variations in their simulations which include chemistry.

We quantify both SCF and SPS by the slope of their power-law fits which are shown for  $^{12}\text{CO}$  in Figure 3.3 and Figure 3.4. Figures 3.5, 3.6, and 3.7 plot the SCF and SPS slopes in each subregion against the shell momentum injection rate, outflow momentum injection rate, and YSO surface densities, respectively. We look for systematic trends between our feedback impact measures and either statistic.

In our most direct comparison to B16, we find no correlation between the SCF or SPS

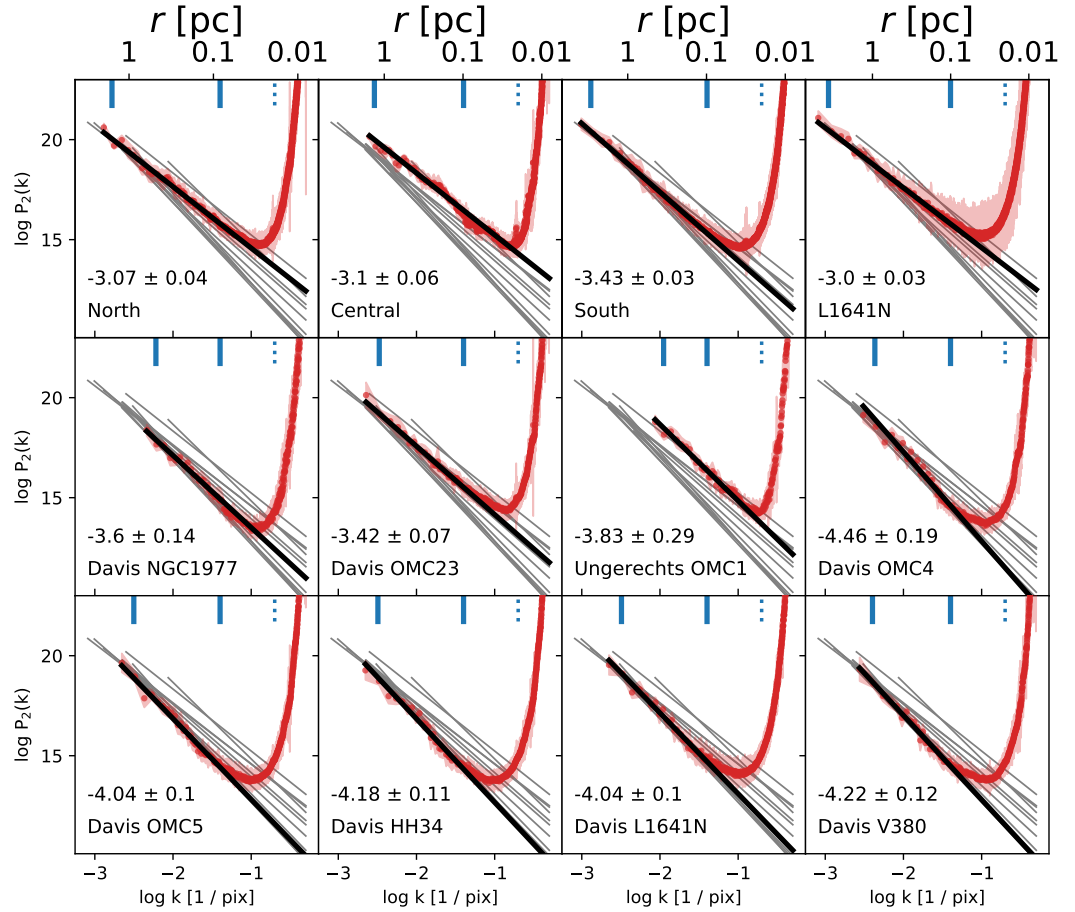


Figure 3.4  $^{12}\text{CO}$  spatial power spectrum (SPS) in Orion A subregions. The subregions are ordered in the same way as Figure 3.2. In each panel, the *red points and red shaded region* are the values and uncertainties of the SPS. The *black line* is a weighted least-squares power law fit to these points. The *solid blue vertical lines* at the top of each panel show the range over which the power law is fit. The *dotted blue vertical line* at the top of each panel shows the FWHM of the beam's major axis. The *gray lines* show the SPS fits for all subregions. Each power spectrum is fit down to a scale of -1.4 (25 pixels), or about five times the beam FWHM. Each fit also excludes the largest scale point in the power spectrum. The power-law slope and its uncertainty is shown in each panel.

slopes and shell momentum injection rate surface density in the Orion A subregions (Figure 3.5). In particular, we do not find the predicted SCF steepening with increased wind feedback. Using only those shells with the highest confidence score (i.e., a score of 5) from Table 2 in Feddersen et al. (2018), there is still no significant trend between shell momentum injection rate and SCF or SPS slope. We also find no correlation between the spectral slopes and the outflow momentum injection rate surface density (Figure 3.6). Because both of these feedback measures are quite uncertain (see Section 3.3), this analysis does not rule out an underlying correlation between the momentum injection rates and the spectral slopes. Using the more objective measure of YSO surface density, we do find a significant correlation with SCF slope.

The  $^{12}\text{CO}$  SCF steepens in subregions with higher YSO surface density (Figure 3.7). While B16 does not model YSO populations, they show that increased feedback strength steepens the  $^{12}\text{CO}$  SCF in their simulations. If the true feedback impact is positively correlated with  $n_{\text{YSO}}$ , then our result is consistent with the SCF prediction by B16. We stress that feedback is not the only possible driver of the relationship between  $n_{\text{YSO}}$  and  $^{12}\text{CO}$  SCF. We tested the effects of column density on these relationships using the Herschel maps from Stutz & Kainulainen (2015). The median column density of a subregion does not affect the trends shown in Figures 3.5 through 3.7. However, some other underlying variable that correlates strongly with stellar density and influences  $^{12}\text{CO}$  emission (e.g., opacity or excitation temperature) may still explain the trend we see between  $n_{\text{YSO}}$  and  $^{12}\text{CO}$  SCF.

We fit the  $^{12}\text{CO}$  SCF slopes with a weighted least-squares regression, shown in the upper left panel of Figure 3.7. The best-fit line is

$$\begin{aligned} \alpha_{\text{SCF}} = & (-0.060 \pm 0.006) \log(n_{\text{YSO}}[\text{deg}^{-2}]) \\ & +(0.090 \pm 0.020) \end{aligned} \quad (3.3)$$

where  $\alpha_{\text{SCF}}$  is the  $^{12}\text{CO}$  SCF slope. This fit has a correlation coefficient of  $r^2 = 0.84$ . If we exclude the OMC-1 subregion, which has an order of magnitude higher  $n_{\text{YSO}}$  than any other subregion, the slope of the best-fit line steepens slightly but the correlation coefficient does not change. Future studies of the SCF in molecular clouds should test this correlation.

We do not find any correlation between SPS slope and  $n_{\text{YSO}}$ , which is also consistent with B16. In  $^{13}\text{CO}$  and  $\text{C}^{18}\text{O}$ , neither SCF nor SPS appear to be correlated with  $n_{\text{YSO}}$ . It is unclear why the  $^{12}\text{CO}$  SCF slope is correlated with  $n_{\text{YSO}}$  while the other CO lines are not.

When measuring the SCF slopes, we fit the SCF up to about 0.12 pc scales. We chose this fitting range to be most consistent with B16. The SCF steepens toward larger scales. However, fitting the SCF at larger scales does not change the relative trends between SCF slope and feedback impact reported in Figures 3.5 through 3.7. In particular, the anticorrelation between  $^{12}\text{CO}$  SCF slope and  $n_{\text{YSO}}$  remains. We show the SCF at larger scales in Appendix 3.C.

Figure 3.8 shows the three feedback measures plotted against each other. There is no significant correlation between any of the three feedback measures among the Orion A subregions. This lack of correlation is unsurprising. As discussed in Section 3.3, shells, outflows, and YSOs each trace different populations of forming stars. For this reason, along with the significant uncertainties in the feedback measures also described in Section 3.3, it is premature to conclude that the feedback mechanisms are not spatially correlated.

### 3.6.2 Line Wing Power Spectrum

The power spectra in Figure 3.4 are calculated using the  $^{12}\text{CO}$  integrated intensity maps. Because outflows are often most prominent in the line wings (channels blueward and redward of the main cloud velocity range), their influence may be largest in power spectra restricted to these velocity ranges.

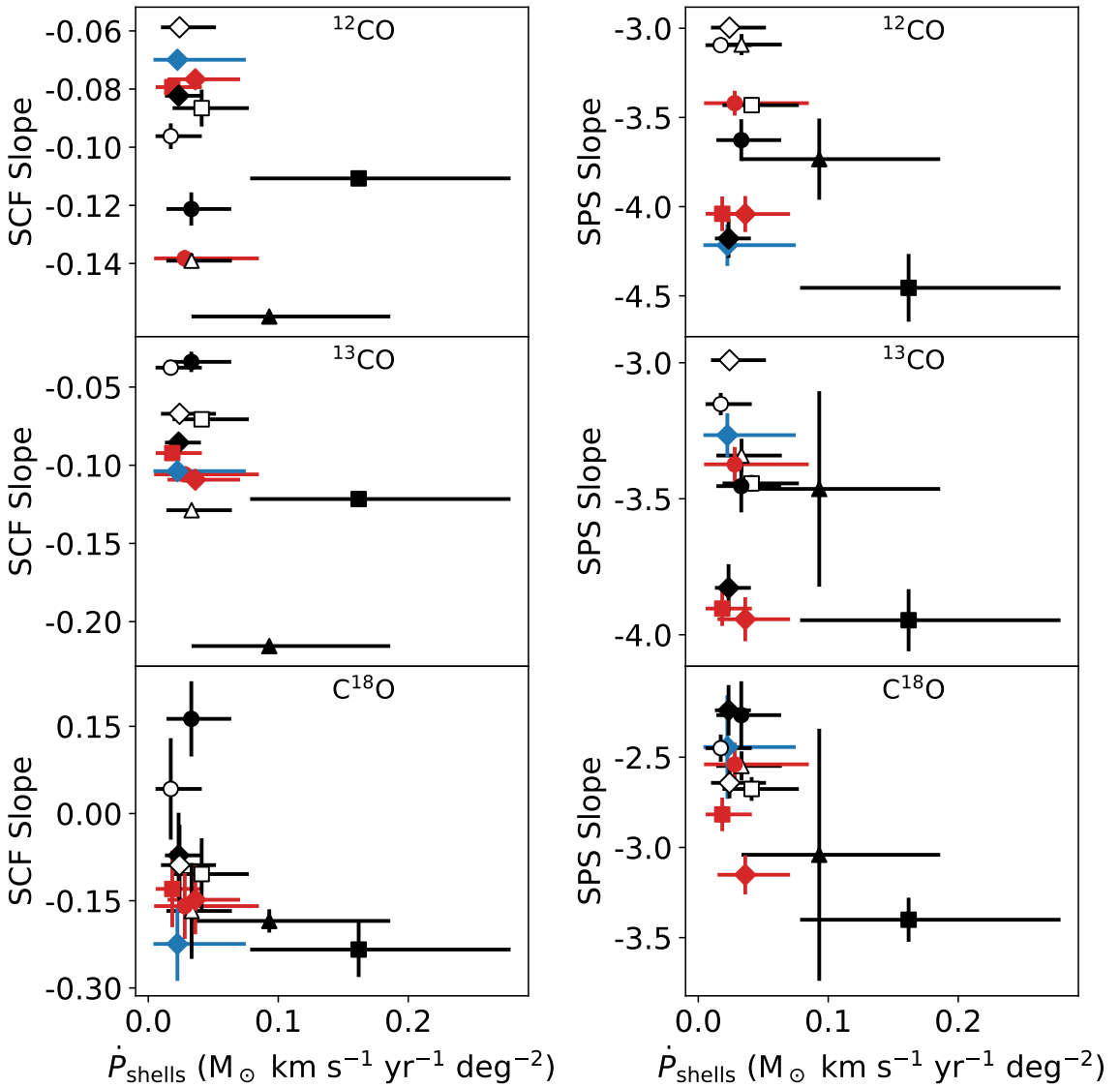


Figure 3.5 The SCF and SPS slopes versus the momentum injection rate surface density of shells in Orion A subregions. Each symbol corresponds to a specific subregion as defined in Figure 3.2. The *filled points* show the smaller subregions from Ungerechts et al. (1997) and Davis et al. (2009). The *open points* show the larger subregions from Feddersen et al. (2018). The horizontal error bars span the cumulative lower and upper limits on  $\dot{P}$  for the shells in each subregion (see Table 3 in Feddersen et al. 2018).

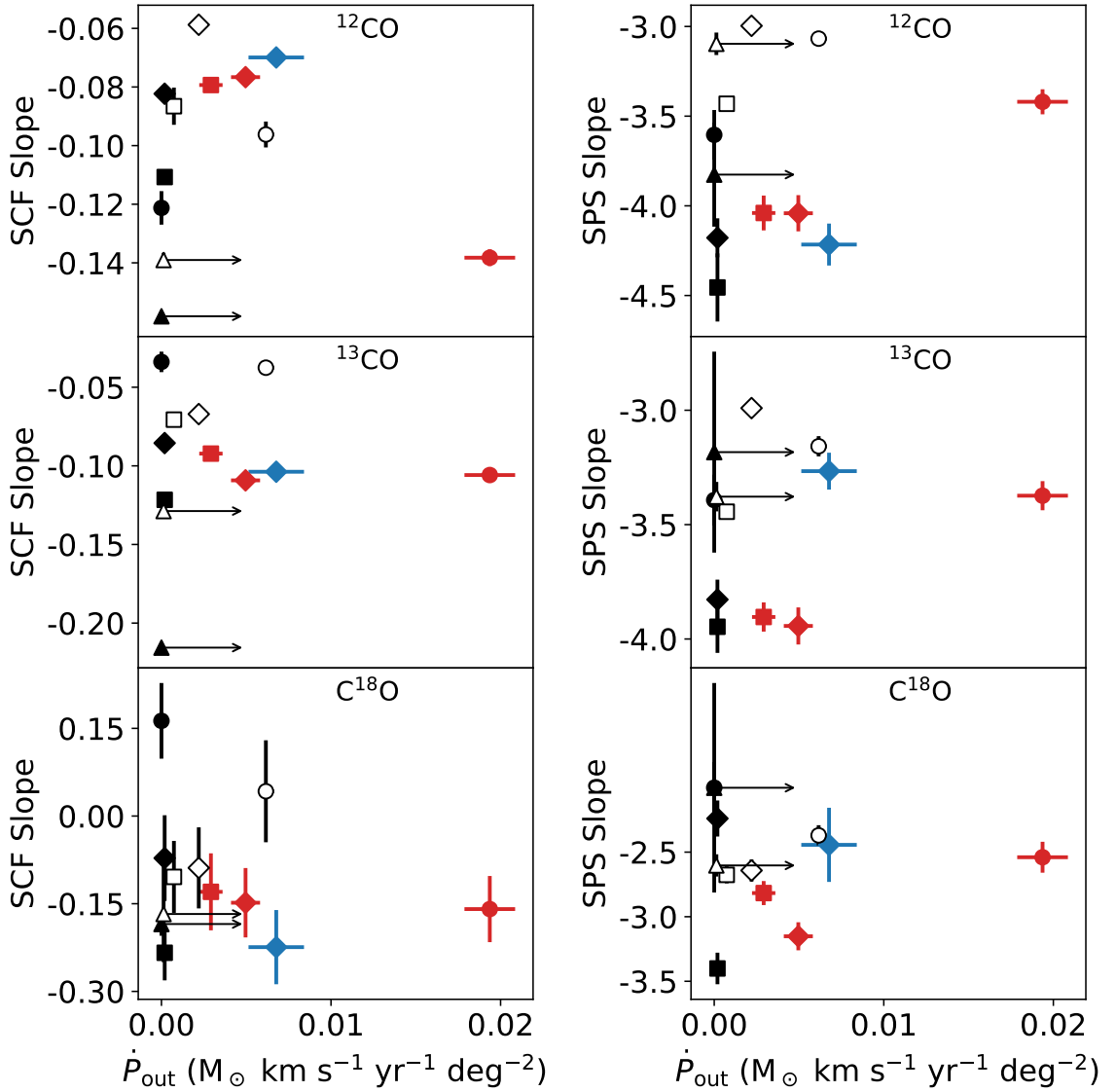


Figure 3.6 The SCF and SPS slopes versus the momentum injection rate surface density of outflows in Orion A subregions. The arrows indicate lower limits in the regions around OMC 1, which was avoided by the outflow search of Tanabe et al. (2019, in press). All other symbols have the same meaning as in Figure 3.5. The horizontal error bars indicate the uncertainty found by adding in quadrature the individual outflow uncertainties (in Table 7 of Tanabe et al. 2019, in press) in each subregion.

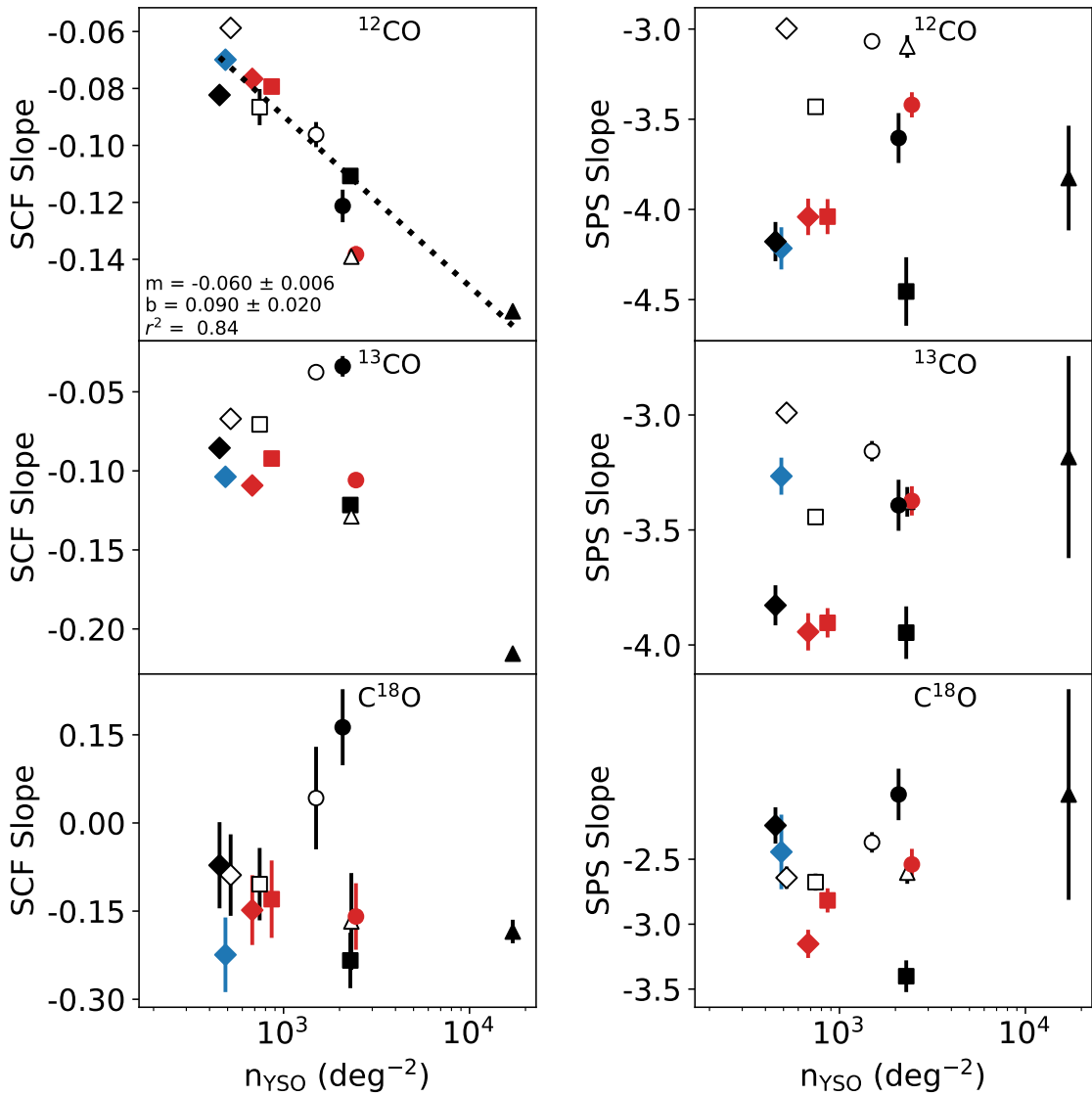


Figure 3.7 The SCF and SPS slopes versus the surface density of YSOs in Orion A sub-regions. The  $^{12}\text{CO}$  SCF slopes (upper left) are fit with a linear least-squares regression (dotted line). The slope  $m$ , intercept  $b$ , and correlation coefficient  $r^2$  are shown. All other symbols have the same meaning as in Figure 3.5.

Swift & Welch (2008) studied the line wing power spectrum of the low-mass star-forming cloud L1551. They found a peak at an angular scale of  $1'$  (0.05 pc) in the power spectrum of  $^{13}\text{CO}$  integrated over the line wings. They attributed this feature to a preferential scale at which protostellar outflows deposit energy into the cloud.

Padoan et al. (2009) showed that the integrated intensity power spectrum in the NGC 1333 molecular cloud is nearly a perfect power law with no features or flattening despite the many outflows present (Plunkett et al., 2013). Padoan et al. (2009) interpret this to mean that all turbulent driving takes place at large scales, presumably by external driving forces, and that outflows do not drive enough momentum into the cloud to affect the turbulent cascade. However, Padoan et al. (2009) focused on the power spectrum of integrated intensity maps, while Swift & Welch (2008) specifically examined the power spectra in the line wings.

To investigate the line wing power spectra in Orion A, we visually define the velocity ranges of the line wings where the main cloud emission disappears. Then, we integrate the emission in these velocity ranges and compare their power spectra. Figure 3.9 shows the  $^{13}\text{CO}$  line wing power spectrum toward the L1641N subregion defined in Feddersen et al. (2018), which contains several outflows. In L1641N, we define the blueshifted line wing as  $4.3$  to  $5.6 \text{ km s}^{-1}$ , the central cloud velocity range as  $6.6$  to  $7.8 \text{ km s}^{-1}$ , and the redshifted line wing as  $10.8$  to  $12.1 \text{ km s}^{-1}$ . We find no sign of peaks in the  $^{12}\text{CO}$  or  $^{13}\text{CO}$  line wing power spectra of any subregion in Orion A.

While the  $^{12}\text{CO}$  and  $^{13}\text{CO}$  power spectra are featureless power-laws, we do find peaks in the  $\text{C}^{18}\text{O}$  power spectrum at  $30\text{-}60''$ . In Appendix 3.B, we show that these peaks are present in the power spectrum of emission-free channels and are therefore artifacts of the data combination process.

We suggest that the peak in the  $^{13}\text{CO}$  line wing power spectra found by Swift & Welch (2008) may be caused by a similar numerical artifact in their data. This peak occurs over angular scales of approximately  $40$  to  $100''$ . Swift & Welch (2008) combined an interfero-

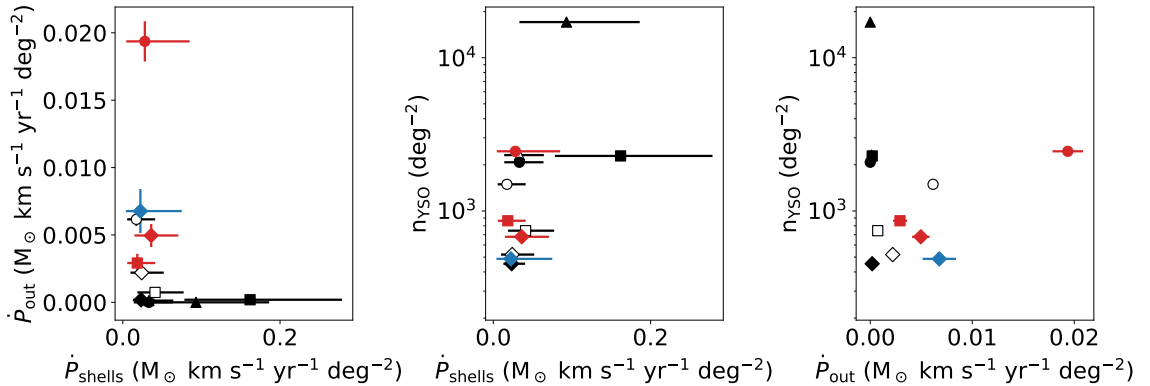


Figure 3.8 The three feedback measures plotted against one another. The symbols have the same meaning as in Figure 3.5. There is no significant correlation between any of the measures.

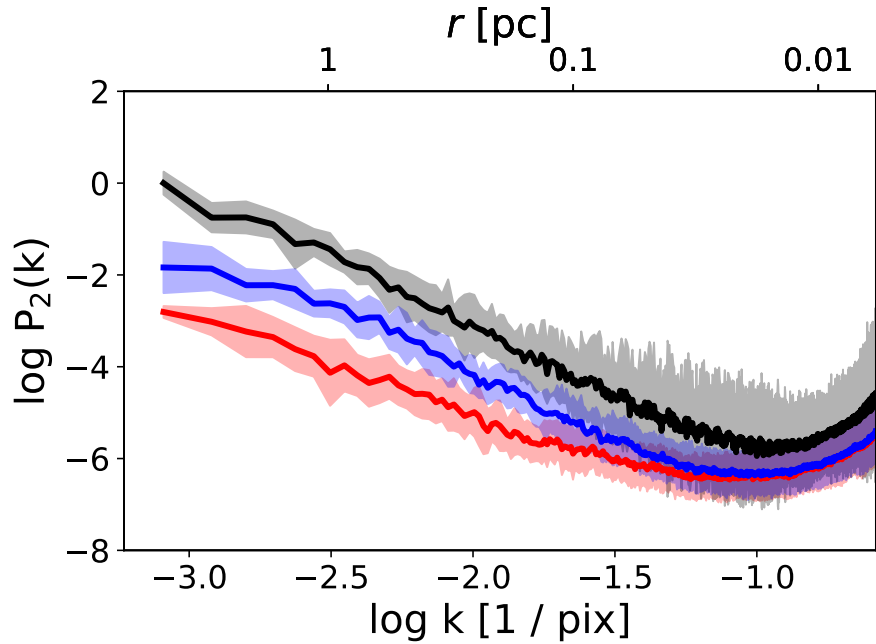


Figure 3.9  $^{13}\text{CO}$  line wing power spectra in L1641N subregion. The *blue line* shows the blue line wing power spectrum of emission integrated from  $4.3$  to  $5.6 \text{ km s}^{-1}$ . The *red line* shows the red line wing power spectrum of emission integrated from  $10.8$  to  $12.1 \text{ km s}^{-1}$ . The *black line* shows the power spectrum at main cloud velocities  $6.6$  to  $7.8 \text{ km s}^{-1}$ . The spectra are divided by the first value of the *black* power spectrum for comparison purposes. Each power spectrum is beam corrected and tapered with a Tukey window. The upturn at  $\log k = -1 \text{ pix}^{-1}$  is a numerical effect caused by the beam correction.

metric mosaic from the Berkeley-Illinois-Maryland Association (BIMA) array with a map from the Arizona Radio Observatory (ARO) 12m telescope. The spacing between BIMA pointings is  $45''$  and the FWHM of the ARO 12m beam is  $55''$ . These angular scales are similar to the scale of the peak in the power spectrum, suggesting that an artifact introduced in the  $^{13}\text{CO}$  data reduction or combination may be responsible for this feature. To test if the peak is real or a data artifact, the power spectrum of emission-free channels should be compared. If the peak appears in this noise power spectrum, it is not intrinsic to the emission and does not indicate a characteristic scale imposed by outflows. We suggest that future studies of molecular cloud power spectra first consider the noise power spectrum before interpreting any deviations from a smooth power-law.

### 3.7 Conclusions

This study is one of the first attempts to quantify the connection between feedback and the statistics of turbulent motion in a molecular cloud. Previous studies of feedback in molecular clouds have focused on cataloging and measuring individual features like outflows and shells.

We find spatially correlated emission at relative velocities of  $1\text{-}3 \text{ km s}^{-1}$  in the covariance matrix toward the NGC 1977, OMC4, L1641N, and V380 regions. These features resemble those found by B16 in their simulations of stellar winds. It is unclear whether winds are responsible for these features in Orion or whether they arise from some other mechanism, such as the cloud-cloud collision proposed for L1641-N by Nakamura et al. (2012). We suggest a detailed comparison of the covariance matrix in simulations that incorporate both feedback and a colliding-cloud model to clarify what mechanism produces these features in Orion A.

Contrary to the predictions of the B16 simulations, we do not find a relationship between the slope of the spectral correlation function in Orion A and the momentum injection

rate of shells or outflows. However, the uncertainties inherent in both shell and, to a lesser extent, outflow momenta mean we cannot rule out an underlying relationship. A better accounting of the impact of these feedback processes is necessary to fully understand their relationship to the statistics of turbulence.

We find, for the first time, a significant trend between the spectral correlation function and the surface density of young stars. Regions with higher YSO surface density have steeper spectral correlation functions in  $^{12}\text{CO}$ . If higher YSO surface density correlates with greater feedback impact, the  $^{12}\text{CO}$  SCF slope may be a useful indicator of the importance of feedback in molecular clouds. Feedback is not the only possible underlying variable in this relationship. Any parameter that correlates strongly with stellar density (such as optical depth or excitation temperature) may contribute to the trend we see with the  $^{12}\text{CO}$  SCF.

We find no significant trend between the power spectrum in Orion A and the momentum injection rate of shells or outflows, in agreement with B16. We find no evidence for features or breaks in the integrated intensity power spectra or line wing power spectra. Thus, we find no evidence in Orion A for a preferential scale imposed by feedback. Future studies of molecular cloud power spectra should first examine the power spectrum of noise before interpreting any deviations from a smooth power-law.

The statistical study of feedback in molecular clouds is still in its infancy. Future simulations of molecular clouds should compare statistical measures of gas structure and kinematics with the *strength* of feedback, beyond merely its presence or absence. To aid this, simulations should explore parameter space more fully (see e.g. Yeremi et al., 2014) to disentangle the impacts of feedback from other factors like chemistry and magnetic fields. Future studies should also differentiate between the statistical effects of protostellar outflows, spherical stellar winds, and other types of feedback.

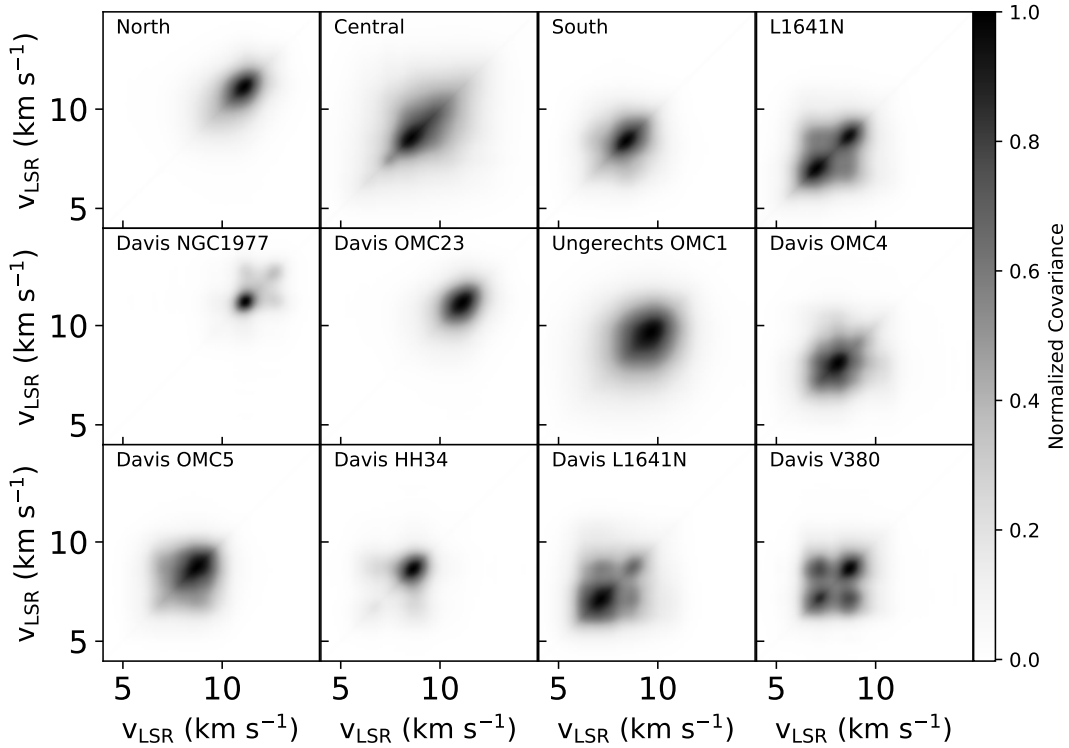
## Acknowledgments

We thank Yoshihiro Tanabe for providing the outflow catalogue. We thank Jens Kauffmann, Jaime Pineda, and the entire CARMA-NRO Orion collaboration for helpful discussion. We thank the referee for thoughtful suggestions that greatly improved the paper. CARMA operations were supported by the California Institute of Technology, the University of California-Berkeley, the University of Illinois at Urbana-Champaign, the University of Maryland College Park, and the University of Chicago. The Nobeyama 45 m telescope is operated by the Nobeyama Radio Observatory, a branch of the National Astronomical Observatory of Japan. This project was supported by the National Science Foundation, award AST-1140063.

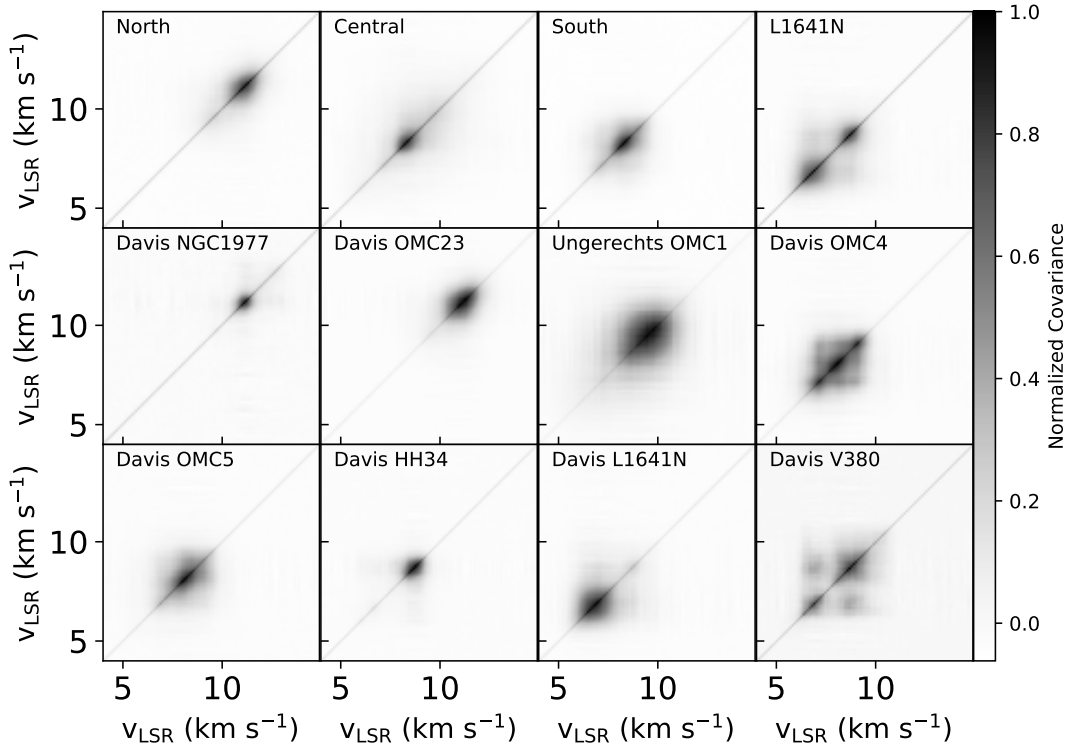
## 3.A Statistics of $^{13}\text{CO}$ and $\text{C}^{18}\text{O}$

### 3.A.1 Covariance Matrix

We show the  $^{13}\text{CO}$  and  $\text{C}^{18}\text{O}$  covariance matrices in Figure 3.10. The off-axis peaks seen in the  $^{12}\text{CO}$  covariance matrices are also present in  $^{13}\text{CO}$  and  $\text{C}^{18}\text{O}$ . Because these features are prominent in both optically thick and thin tracers, they likely result from real velocity structure in the cloud rather than simply from optical depth effects. B16 computed the covariance matrix of their simulated cube before modeling radiative transfer (Figure 21 in B16). This pre-processed cube does not show covariance peaks, implying that excitation and optical depth effects enhance this feature of their winds. The mapping between these pre-processed cubes and observed optically thin CO lines is unclear. We suggest future models incorporate multiple observable transitions to better compare modeled and observed covariance.



(a)



(b)

Figure 3.10 (a)  $^{13}\text{CO}$  and (b)  $\text{C}^{18}\text{O}$  covariance matrices in Orion A subregions.

### 3.A.2 SCF

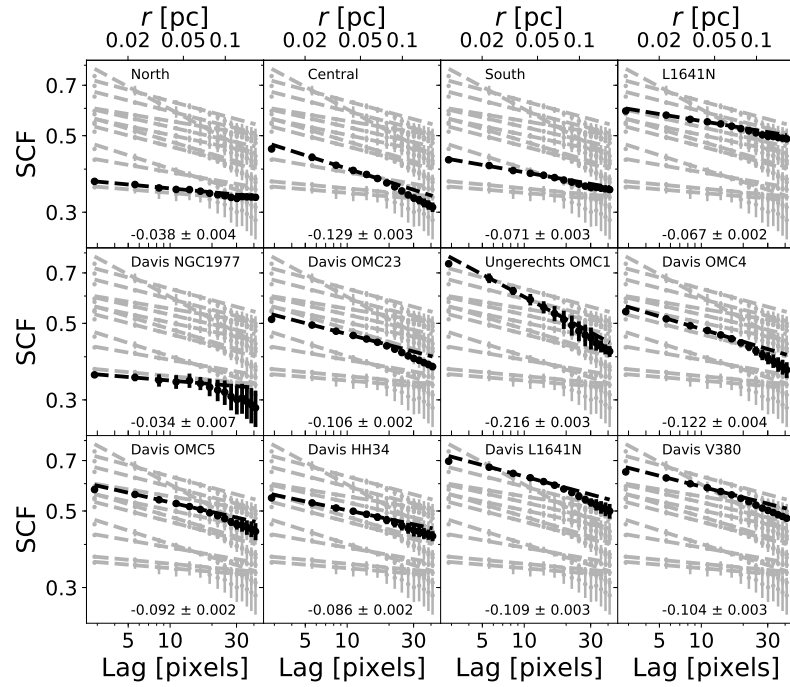
We show the  $^{13}\text{CO}$  and  $\text{C}^{18}\text{O}$  SCF in Figure 3.11 and the  $^{13}\text{CO}$  and  $\text{C}^{18}\text{O}$  SPS in Figure 3.12. The  $^{13}\text{CO}$  SCF spectra have shapes similar to the  $^{12}\text{CO}$  spectra. They follow power-laws up to lags of about 20 pixels ( $40''$  or 0.08 pc), where they steepen toward larger scales.

The  $\text{C}^{18}\text{O}$  SCF spectra look very different. They show a sharp decrease between the shortest lags of 3 and 5 pixels ( $6\text{-}10''$  or 0.01-0.02 pc). Many of the  $\text{C}^{18}\text{O}$  SCF spectra also turn upward at larger scales. An upward sloping SCF means that distantly separated spectra are more similar than close pairs of spectra, an unphysical result. Because the  $\text{C}^{18}\text{O}$  has low signal-to-noise, the upward slopes are more likely to be an artifact of the data reduction process rather than a real signature of the cloud spectra.

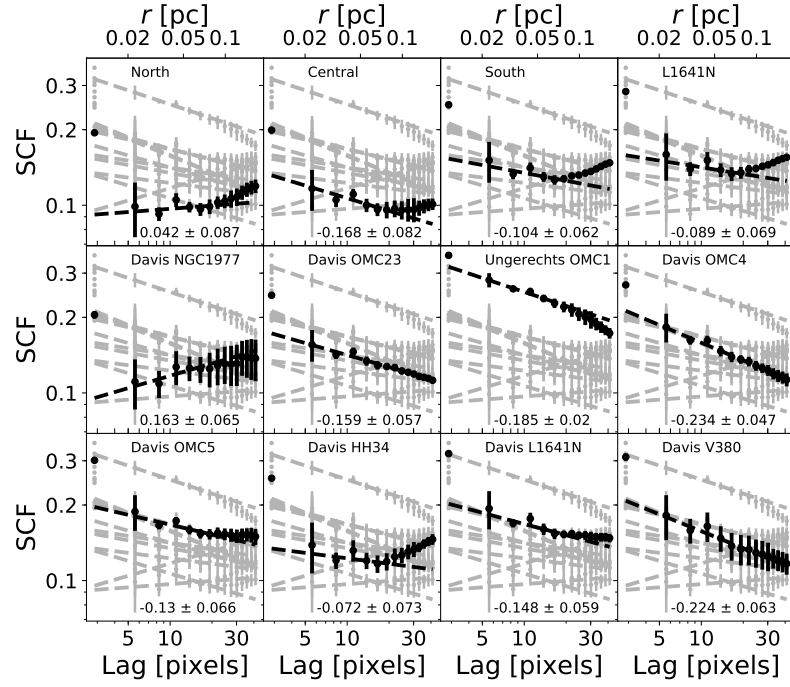
### 3.A.3 SPS

As in  $^{12}\text{CO}$ , the  $^{13}\text{CO}$  SPS (Figure 3.12) closely follows a power-law down to scales of a few beamwidths. The slopes of the  $^{13}\text{CO}$  SPS fits range from -3 to -4. Overall, the  $^{13}\text{CO}$  slopes are slightly shallower than  $^{12}\text{CO}$ , closer to the predicted value of -3 for an optically thick medium and the observational results compiled by Burkhart et al. (2013), although Section 5.2 in Kong et al. (2018) indicates that  $^{13}\text{CO}$  is not very optically thick in Orion A, with only 0.6% of pixels having  $\tau_{^{13}\text{CO}} > 1$ .

The  $\text{C}^{18}\text{O}$  SPS have significantly shallower slopes than  $^{12}\text{CO}$  or  $^{13}\text{CO}$ . However, they show a clear peak near 0.1 pc. This peak remains in the power spectrum of emission-free channels (see Appendix 3.B). Because of the low signal-to-noise of  $\text{C}^{18}\text{O}$ , we do not interpret these power spectra.

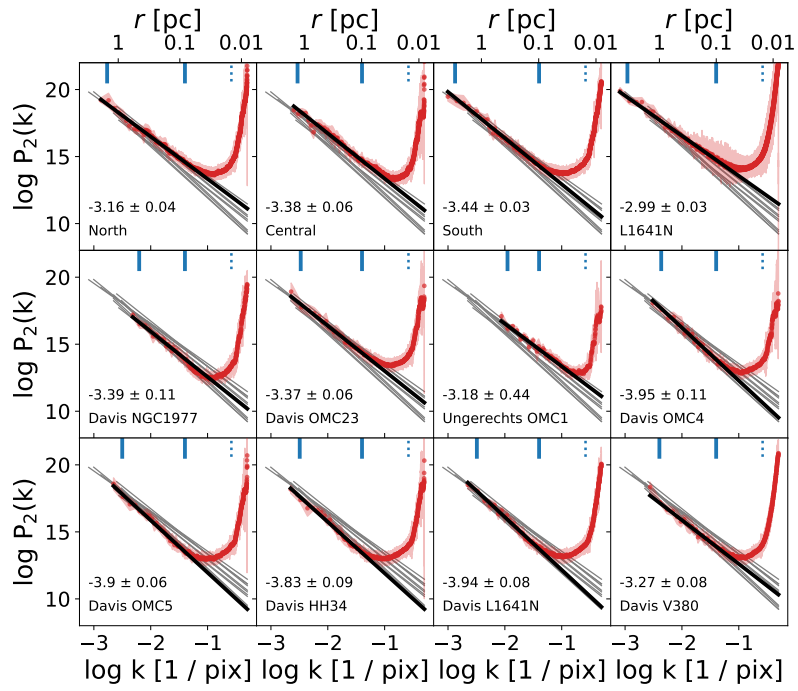


(a)

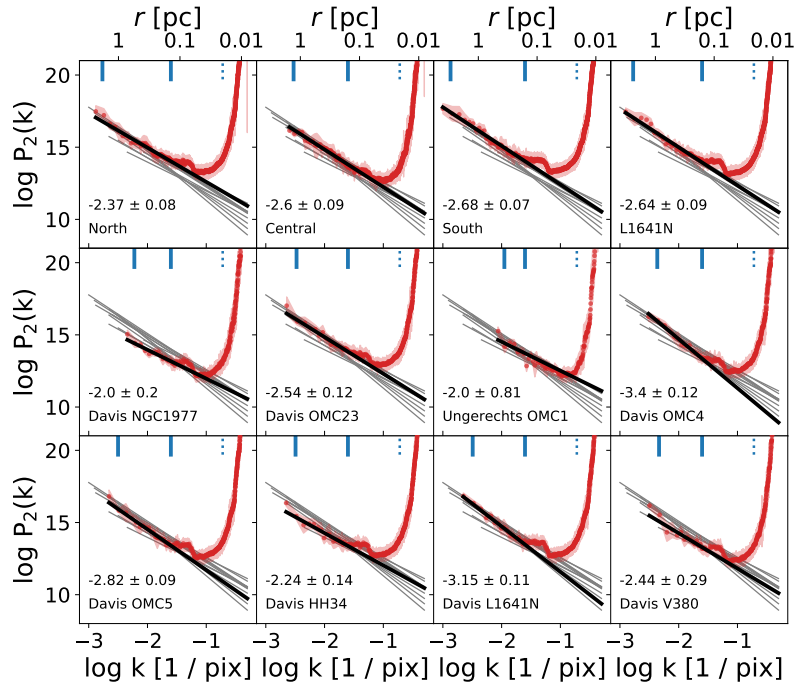


(b)

Figure 3.11 (a)  $^{13}\text{CO}$  and (b)  $\text{C}^{18}\text{O}$  spectral correlation function and power-law fits in Orion A subregions. The symbols and lines have the same meaning as in Figure 3.3.



(a)



(b)

Figure 3.12 (a)  $^{13}\text{CO}$  and (b)  $\text{C}^{18}\text{O}$  spatial power spectrum and power-law fits in Orion A subregions. The symbols and lines have the same meaning as in Figure 3.4. The bump at 0.1 pc in the  $\text{C}^{18}\text{O}$  power spectrum, an artifact of the data, is evident in most panels (see § 3.B)

### 3.B Noise Peak in C<sup>18</sup>O SPS

The C<sup>18</sup>O SPS has a peak near 0.1 pc which is not present in either <sup>12</sup>CO or <sup>13</sup>CO. This feature can also be seen in the integrated C<sup>18</sup>O delta-variance spectra in Figure 3 of Kong et al. (2018), where they speculate it arises from the low signal-to-noise of C<sup>18</sup>O coupled with problems in the map cleaning process. Swift & Welch (2008) found a similar feature in the <sup>13</sup>CO line-wing power spectrum of the L1551 cloud and attributed this SPS feature to feedback (see Section 3.6.2). To rule out the influence of feedback in our C<sup>18</sup>O data, we examine the noise power spectrum. If the feature at 0.1 pc is present in the noise, it is not related to feedback.

To compute the noise power spectrum of C<sup>18</sup>O, we first sum the emission-free channels between 12 and 16 km s<sup>-1</sup>. Then we compute the spatial power spectrum as described in Section 3.4.3, including the beam correction and tapering. We show the power spectrum of noise in the L1641N region C<sup>18</sup>O map in Figure 3.13. The noise shows the 0.1 pc peak. Because the C<sup>18</sup>O map has much lower signal-to-noise than <sup>12</sup>CO and <sup>13</sup>CO, the shape of its noise power spectrum dominates the power spectrum of integrated emission. While the <sup>12</sup>CO and <sup>13</sup>CO noise power spectra also deviate from power-law, their higher signal-to-noise renders the noise power spectrum insignificant. Before interpreting features in the SPS of any new dataset, we suggest calculating the noise power spectrum.

### 3.C SCF at Large Scales

The SCF shown in Figure 3.3 only extends to lags of about 45 pixels, or 0.17 pc, to match the range in physical scales covered by the SCF in B16. However, other observational studies fit the SCF spectra at larger scales (e.g. Padoan et al., 2003; Gaches et al., 2015). In Figure 3.14, we show the <sup>12</sup>CO SCF spectra of the Orion A subregions at scales up to 300 pixels (1.2 pc). The SCF steepens at larger scales, in closer agreement with the SCF

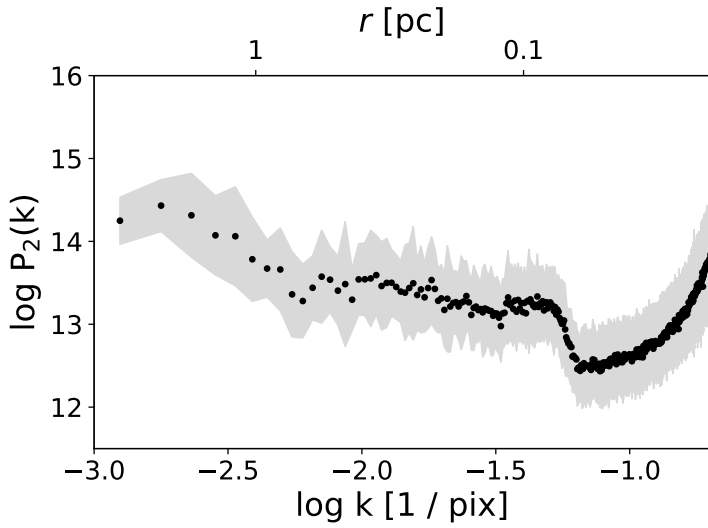


Figure 3.13 The  $\text{C}^{18}\text{O}$  noise power spectrum toward L1641N. The power spectrum is calculated in the emission-free channels between 12 and 16  $\text{km s}^{-1}$ . The bump at 0.1 pc is an artifact of the data combination process and also appears in the  $\text{C}^{18}\text{O}$  delta-variance spectrum shown by Kong et al. (2018).

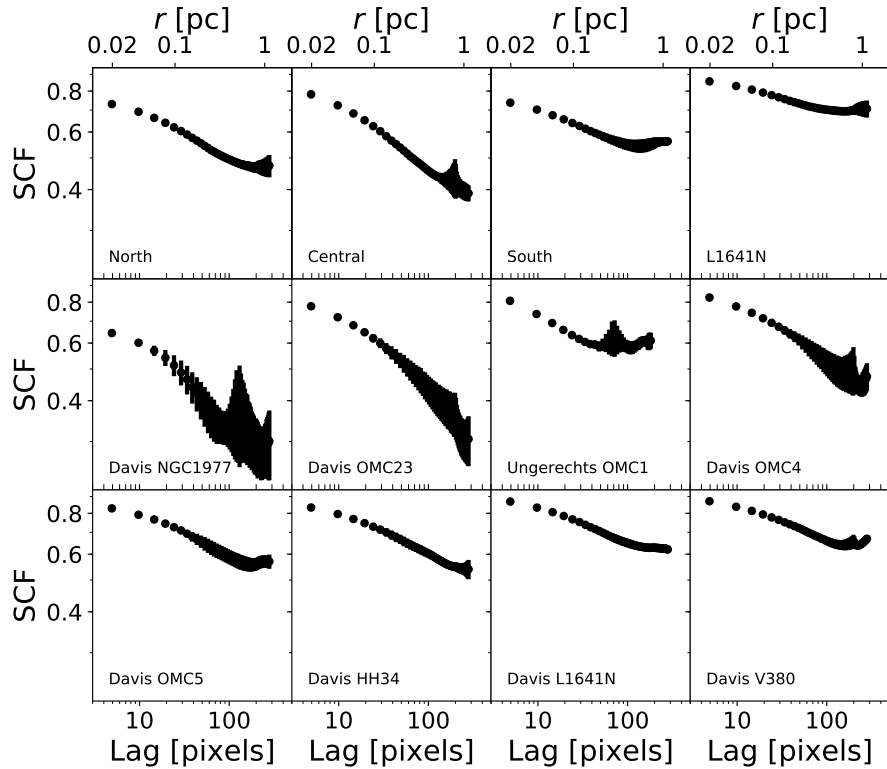


Figure 3.14 The  $^{12}\text{CO}$  large-scale spectral correlation function in Orion A subregions.

measured by Padoan et al. (2003) and Gaches et al. (2015). Each subregion SCF flattens and turns upward at different lags. This shape at large scales is a numerical effect caused by the finite size of the subregions and makes it difficult to compare the SCF at large scales between maps of different sizes. If we fit each subregion SCF with a power-law between 30 and 50 pixels (0.12 to 0.2 pc), which avoids the SCF upturn for all subregions, the relationship between SCF slope and feedback impact remains qualitatively the same as shown in Figures 3.5 through 3.7.

### **3.D Full-Map Statistics**

We show the covariance matrices, SCF, and SPS computed over the entire area covered by the CARMA-NRO Orion maps in Figures 3.15, 3.16, and 3.17, respectively.

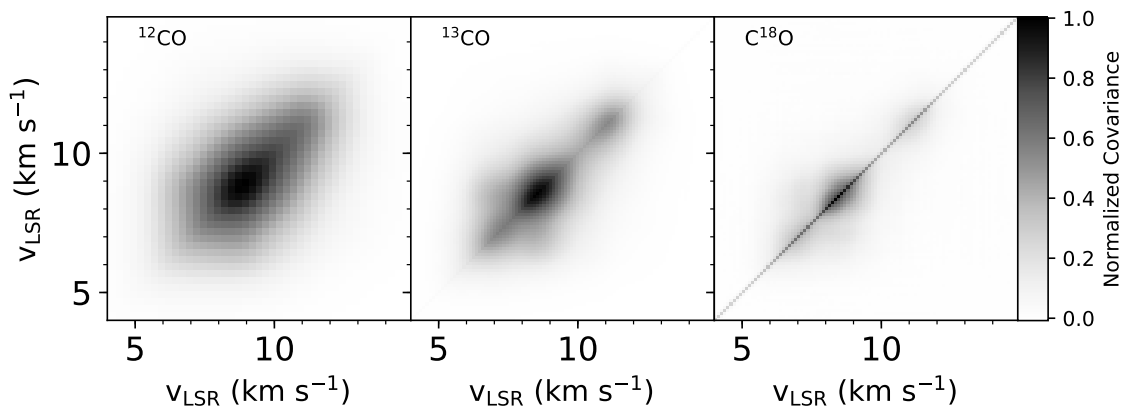


Figure 3.15 The covariance matrices of the full Orion A map.

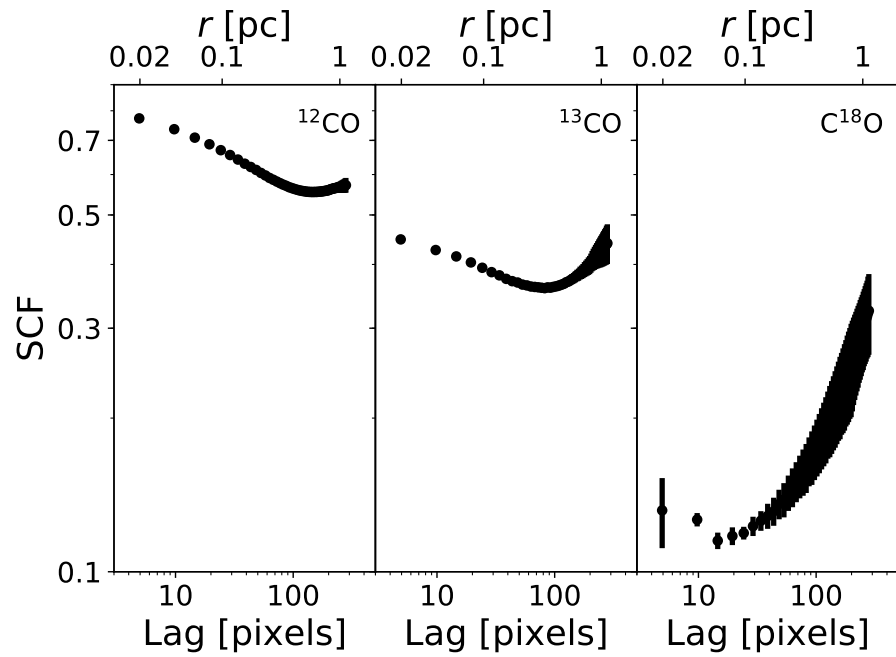


Figure 3.16 The spectral correlation function of the full Orion A map at large scales as in Figure 3.14.

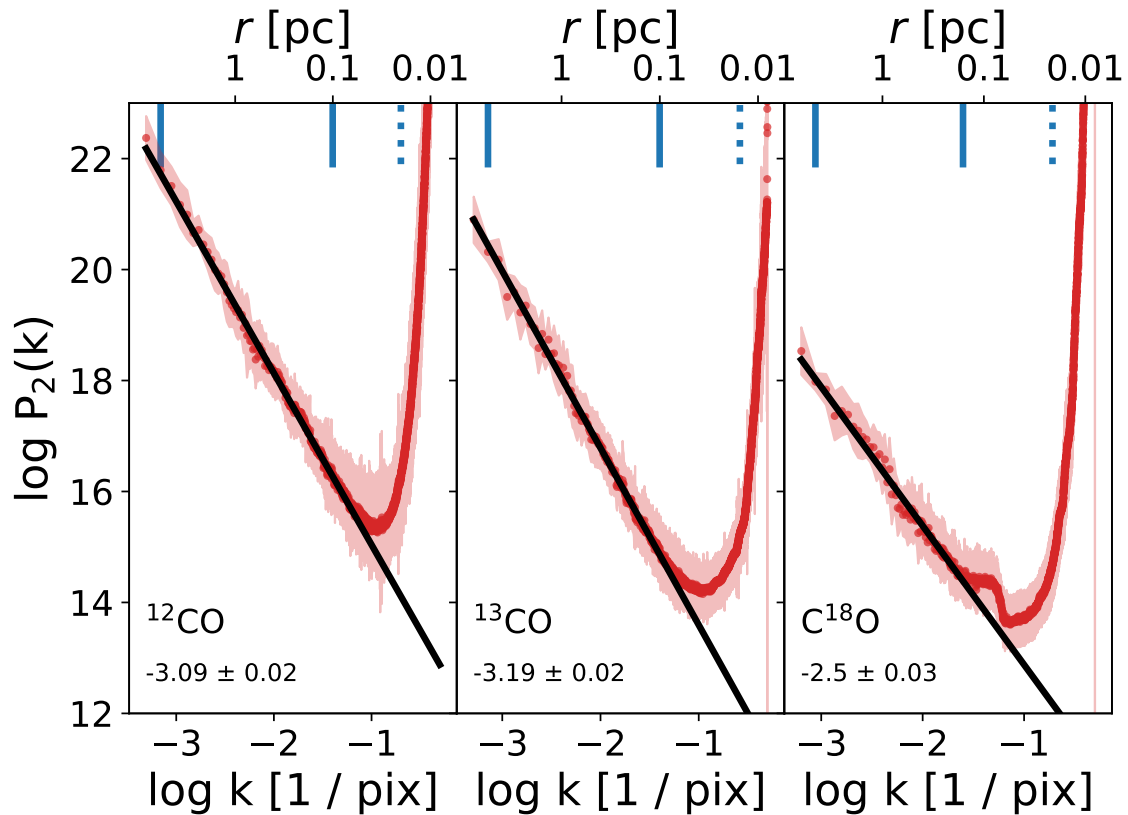


Figure 3.17 The spatial power spectrum and power-law fits of the full Orion A map. All symbols and lines have the same meaning as in Figure 3.4. The bump at 0.1 pc in the  $\text{C}^{18}\text{O}$  power spectrum is an artifact of the data combination process and is also seen in Figure 3.13.

Table 3.1. Subregion Results

Name	Right Ascension (J2000)	Declination (J2000)	$\dot{P}_{\text{shell}}^{\text{d}}$	$\dot{P}_{\text{out}}^{\text{e}}$	$\log_{10} n_{\text{YSO}}^{\text{f}}$	$^{12}\text{CO } \alpha_{\text{SCF}}$	$^{12}\text{CO } \alpha_{\text{SPS}}$
North <sup>a</sup>	5 <sup>h</sup> 37 <sup>m</sup> 35 <sup>s</sup> to 5 <sup>h</sup> 33 <sup>m</sup> 06 <sup>s</sup>	-5°19'26" to -4°48'19"	17 [6, 41]	6.2 ± 0.5	3.2	-0.096 ± 0.004	-3.07 ± 0.04
Central <sup>a</sup>	5 <sup>h</sup> 37 <sup>m</sup> 35 <sup>s</sup> to 5 <sup>h</sup> 33 <sup>m</sup> 06 <sup>s</sup>	-5°34'03" to -5°19'21"	33 [14, 64]	0.13 ± 0.04	3.4	-0.139 ± 0.002	-3.1 ± 0.06
South <sup>a</sup>	5 <sup>h</sup> 37 <sup>m</sup> 36 <sup>s</sup> to 5 <sup>h</sup> 33 <sup>m</sup> 07 <sup>s</sup>	-6°17'03" to -5°34'03"	41 [19, 77]	0.7 ± 0.2	2.9	-0.087 ± 0.006	-3.43 ± 0.03
L164IN <sup>a</sup>	5 <sup>h</sup> 39 <sup>m</sup> 01 <sup>s</sup> to 5 <sup>h</sup> 34 <sup>m</sup> 22 <sup>s</sup>	-7°11'44" to -6°17'03"	24 [10, 52]	2.2 ± 0.3	2.7	-0.059 ± 0.002	-3.0 ± 0.03
NGC1977 <sup>b</sup>	5 <sup>h</sup> 35 <sup>m</sup> 47 <sup>s</sup> to 5 <sup>h</sup> 34 <sup>m</sup> 28 <sup>s</sup>	-4°57'08" to -4°37'23"	33 [14, 64]	0	3.3	-0.121 ± 0.006	-3.6 ± 0.14
OMC23 <sup>b</sup>	5 <sup>h</sup> 36 <sup>m</sup> 03 <sup>s</sup> to 5 <sup>h</sup> 34 <sup>m</sup> 43 <sup>s</sup>	-5°16'37" to -4°56'37"	28 [4, 85]	19 ± 1	3.4	-0.138 ± 0.003	-3.42 ± 0.07
OMC1 <sup>c</sup>	5 <sup>h</sup> 35 <sup>m</sup> 24 <sup>s</sup> to 5 <sup>h</sup> 35 <sup>m</sup> 06 <sup>s</sup>	-5°29'35" to -5°17'35"	93 [33, 186]	0	4.2	-0.158 ± 0.001	-3.83 ± 0.29
OMC4 <sup>b</sup>	5 <sup>h</sup> 35 <sup>m</sup> 41 <sup>s</sup> to 5 <sup>h</sup> 34 <sup>m</sup> 20 <sup>s</sup>	-5°46'56" to -5°33'00"	162 [78, 279]	0.19 ± 0.05	3.4	-0.111 ± 0.002	-4.46 ± 0.19
OMC5 <sup>b</sup>	5 <sup>h</sup> 36 <sup>m</sup> 00 <sup>s</sup> to 5 <sup>h</sup> 34 <sup>m</sup> 41 <sup>s</sup>	-6°15'07" to -5°50'06"	18 [6, 41]	2.9 ± 0.6	2.9	-0.079 ± 0.002	-4.04 ± 0.1
HH34 <sup>b</sup>	5 <sup>h</sup> 36 <sup>m</sup> 00 <sup>s</sup> to 5 <sup>h</sup> 34 <sup>m</sup> 40 <sup>s</sup>	-6°40'07" to -6°17'00"	23 [13, 40]	0.18 ± 0.04	2.7	-0.082 ± 0.002	-4.18 ± 0.11
L164IN <sup>b</sup>	5 <sup>h</sup> 37 <sup>m</sup> 20 <sup>s</sup> to 5 <sup>h</sup> 36 <sup>m</sup> 00 <sup>s</sup>	-6°42'15" to -6°19'02"	36 [15, 71]	5.0 ± 0.9	2.8	-0.077 ± 0.002	-4.04 ± 0.1
V380 <sup>b</sup>	5 <sup>h</sup> 37 <sup>m</sup> 05 <sup>s</sup> to 5 <sup>h</sup> 36 <sup>m</sup> 00 <sup>s</sup>	-6°55'00" to -6°37'00"	22 [4, 75]	7 ± 1	2.7	-0.070 ± 0.002	-4.22 ± 0.12

<sup>a</sup>Subregions from Feddersen et al. (2018)

<sup>b</sup>Subregions from Davis et al. (2009)

<sup>c</sup>Subregion from Ungerichts et al. (1997)

<sup>d</sup>Momentum injection rate surface density of shells. Units are  $10^{-3} M_{\odot} \text{ km s}^{-1} \text{ yr}^{-1} \text{ deg}^{-2}$ . Values in brackets are summed lower and upper limits from Table 3 of Feddersen et al. (2018).

<sup>e</sup>Momentum injection rate surface density of outflows. Units are  $10^{-3} M_{\odot} \text{ km s}^{-1} \text{ yr}^{-1} \text{ deg}^{-2}$ . Uncertainties are calculated by adding in quadrature the individual outflow uncertainties in Table 7 of Tanabe et al. (2019, in press).

<sup>f</sup>Surface density of YSOs. Units are  $\text{deg}^{-2}$ . Because of catalog incompleteness, this is likely an underestimate in the Central and OMC1 regions.

# **Chapter 4**

## **The CARMA-NRO Orion Survey: Protostellar Outflows and Filamentary Alignment**

### **Abstract**

We identify 45 protostellar outflows in CO maps of the Orion A giant molecular cloud from the CARMA-NRO Orion survey. Our sample includes 11 newly detected outflows. We measure the mass and energetics of the outflows, including material at low-velocities by correcting for cloud contributions. The total momentum and kinetic energy injection rates of outflows is comparable to the turbulent dissipation rate of the cloud. We also compare the outflow position angles to the orientation of C<sup>18</sup>O filaments. We find that the full sample of outflows is consistent with being randomly oriented with respect to the filaments. A subsample of the most reliable measurements shows a moderately perpendicular outflow-filament alignment which may reflect accretion of mass across filaments and onto the protostellar cores.

## 4.1 Introduction

Stars form inside the densest parts of giant molecular clouds (GMCs) (McKee & Ostriker, 2007). From newly formed protostars, bipolar high-velocity flows of molecular gas are launched. These structures are so ubiquitous they can be observed even when the protostar itself is unseen (Kong et al., 2019a). While it is unclear how exactly outflows are launched, they likely arise from the interaction of the accretion disk with magnetic fields near the protostar (e.g. Konigl & Pudritz, 2000; Shu et al., 2000; Frank et al., 2014).

Outflows have long been sought as a mechanism for sustaining turbulence and slowing star formation in GMCs (Nakamura & Li, 2007; Carroll et al., 2009; Federrath, 2015). Surveys of outflows have repeatedly shown that they have enough aggregate momentum and kinetic energy to significantly offset the dissipation of turbulence, especially on cluster scales (Arce et al., 2010; Nakamura et al., 2011; Plunkett et al., 2013; Plunkett et al., 2015a; Li et al., 2015). More uncertain is the efficiency with which outflows inject momentum at larger scales in order to maintain the observed turbulence in GMCs (Brunt et al., 2009; Padoan et al., 2009; Carroll et al., 2010). For a comprehensive review of outflows, see Bally (2016).

In many GMCs, most of the star formation takes place in relatively narrow, dense filaments (Arzoumanian et al., 2011; Suri et al., 2019). If the angular momentum of a growing protostar is inherited from the mass accretion onto a filament, the protostellar spin and the filament direction will be correlated (Bodenheimer, 1995; André et al., 2014; Li & Klein, 2019). If, however, the link between mass accretion at filament scales and protostellar scales is disrupted, e.g. by turbulence or interaction with protostellar companions, then the protostellar spin may not be correlated with the filament orientation (Offner et al., 2016; Lee et al., 2017).

To distinguish between these scenarios, several studies have recently considered the

relative orientation of outflows and filaments. Assuming the outflow direction traces the angular momentum of the protostar, a correlation between the outflow and filament direction could mean a connection between scales as small as a few hundred AU, where the outflow is launched, to the 0.1 pc width of a typical filament. Davis et al. (2009) measured the position angle of H<sub>2</sub> outflows in the Orion A GMC and found no correlation with the large-scale integral-shaped-filament (ISF). Stephens et al. (2017) compared CO outflows with filaments extracted from *Herschel* dust maps in the Perseus molecular cloud and likewise found a random outflow-filament alignment. However, Kong et al. (2019a) recently found a preferentially perpendicular outflow-filament alignment in the IRDC G28.37+0.07

The Orion A GMC is an ideal environment for studying protostellar outflows and their connection to filaments. At a distance of 414 pc (Menten et al., 2007),<sup>1</sup> it is one of the closest clouds forming both low- and high-mass stars. Following earlier outflow studies, Tanabe et al. (2019, in press) recently carried out a systematic search of CO outflows in Orion. While our study overlaps with theirs, we use different methods to identify outflows and derive their physical properties. In particular, we correct for velocity-dependent opacity and low-velocity outflow emission to more accurately measure the outflows. We also use the C<sup>18</sup>O filament catalog from Suri et al. (2019) for an entirely new analysis of the outflow-filament connection.

In this paper, we present a study of protostellar outflows in the CARMA-NRO Orion survey. In Section 4.2, we describe the CARMA-NRO Orion CO data and protostar catalogs. In Section 4.3, we describe how we search for outflows in the CO maps and present the outflow catalog. In Section 4.4, we calculate the physical properties of the outflows and discuss their impact on the cloud. In Section 4.5, we discuss the relative orientation of outflows and C<sup>18</sup>O filaments and compare to models for random, parallel, and perpendicular outflow-filament alignment. Finally, in Section 4.6, we summarize our conclusions

---

<sup>1</sup>We adopt a distance of 414 pc throughout this paper to be consistent with Tanabe et al. (2019, in press). Recent parallax measurements from GAIA Data Release 2 place Orion A slightly closer, at 380-400 pc (Kounkel et al., 2018; Großschedl et al., 2018; Kuhn et al., 2019).

and discuss future directions. The entire outflow catalog is presented in the Appendix.

## 4.2 Observations

### 4.2.1 CO Maps

The CARMA-NRO Orion survey combines interferometric observations from the Combined Array for Research in Millimeter-wave Astronomy (CARMA) with single-dish observations from the 45 m telescope at the Nobeyama Radio Observatory (NRO). The combination of interferometric and single-dish observations results in an unprecedented spatial dynamic range of 0.01 - 10 pc in the Orion A molecular cloud.

We use the  $^{12}\text{CO}$ (1-0),  $^{13}\text{CO}$ (1-0), and  $\text{C}^{18}\text{O}$ (1-0) data first presented in Kong et al. (2018). The  $^{12}\text{CO}$  data have a resolution of  $10'' \times 8''$  and velocity resolution of  $0.25 \text{ km s}^{-1}$ . The original  $^{13}\text{CO}$  data have a resolution of  $8'' \times 6''$  and a velocity resolution of  $0.22 \text{ km s}^{-1}$ , but we smooth the  $^{13}\text{CO}$  data to match the resolution of  $^{12}\text{CO}$ . The  $\text{C}^{18}\text{O}$  data have a resolution of  $10'' \times 8''$  and a velocity resolution of  $0.22 \text{ km s}^{-1}$ .

### 4.2.2 Source Catalogs

We primarily use the Herschel Orion Protostar Survey (HOPS; Furlan et al., 2016) to assign driving sources to outflow. The HOPS catalog is the result of *Herschel* PACS 70-160  $\mu\text{m}$  observations of the protostars identified in the *Spitzer* Orion survey by Megeath et al. (2012). Furlan et al. (2016) fit the spectral energy distribution (SED) of these 330 protostars from 1.2-870  $\mu\text{m}$  with models to derive a variety of protostar, disk, and envelope properties.

We also use the study of  $\text{H}_2$  outflows by Davis et al. (2009) to guide our search. Davis et al. (2009) surveyed Orion A using narrow-band images of the ro-vibrational  $\text{H}_2$  2.122  $\mu\text{m}$  line. Their work builds on previous  $\text{H}_2$  mapping by Stanke et al. (2002). We search for

outflows around the 17 sources of H<sub>2</sub> flows that are not in the HOPS catalog. In addition to the driving sources of H<sub>2</sub> outflows, Davis et al. (2009) catalog H<sub>2</sub> features with no obvious driving source. We also search for the CO counterpart to the 29 H<sub>2</sub> flows without an identified source within the CO data footprint. Davis et al. (2009) measure the proper motions of 33 flows. We use the  $H_2$  images and, when available, the proper motions to help assign CO outflows to driving sources.

### 4.2.3 Other Outflow Studies

Orion A has been mapped extensively in CO over the past 30 years (e.g. Bally et al., 1987; Wilson et al., 2005; Shimajiri et al., 2011; Buckle et al., 2012; Ripple et al., 2013; Berné et al., 2014). Several studies have searched for outflows in the cloud using these CO observations. In the northern part of the cloud, previous searches have identified 18 outflows along the OMC 2/3 ridge (Chini et al., 1997; Aso et al., 2000; Williams et al., 2003; Takahashi et al., 2008; Shimajiri et al., 2008, 2009). In the L1641N cluster in the southern part of the cloud, Stanke & Williams (2007) and Nakamura et al. (2012) found six outflows. In the NGC 1999 region further south, previous studies have found five outflows (Morgan et al., 1991; Moro-Martín et al., 1999; Davis et al., 2000; Choi et al., 2017).

Tanabe et al. (2019, in press) have carried out a systematic search for outflows across the Orion A cloud, using the same single-dish NRO observations which are used in our CARMA-NRO Orion survey. They identify a total of 44 outflows across the cloud, including 17 new detections. Eleven of these are in the OMC 4/5 region where no outflows had previously been found. Although we expect our catalog to largely overlap with Tanabe et al. (2019, in press), they use an automated outflow search procedure which may include false positives. The improved resolution of the combined CARMA-NRO Orion data allow us to search for smaller outflows, help us disentangle outflow emission in clustered regions, and help with matching outflows to driving sources. We describe our procedure

for identifying outflows below.

## 4.3 Outflow Identification

We search for CO outflows around every HOPS protostar in Furlan et al. (2016) and every source of an H<sub>2</sub> jet in Davis et al. (2009). We first fit the average <sup>12</sup>CO spectrum within 15'' of the source with a Gaussian. Next, we integrate the <sup>12</sup>CO emission farther than 2 $\sigma$  away from the mean velocity on either side. We inspect the contour maps of the blue-shifted and red-shifted emission to look for collimated structures centered on the source which are detected above 5 $\sigma$  in these integrated blue- and red-shifted intensity maps.

In addition to the <sup>12</sup>CO blue/red contour maps, we use NIR images from the VISTA survey (Meingast et al., 2016) and the H<sub>2</sub> outflows in Davis et al. (2009) to guide our assignment of high-velocity CO to driving sources. These ancillary data are especially useful in areas of overlapping outflows, or where outflow lobes are or where outflow lobes are not detected close to the driving source. When a series of H<sub>2</sub> bow shocks or NIR nebulosity which are clearly associated with a particular source overlap a region of high-velocity CO emission, we can be more confident in the assignment of this CO outflow to its source.

Tanabe et al. (2019, in press) automatically defines any blue or redshifted emission above 5 $\sigma$  near a protostar as an outflow. By restricting our catalog to structures that have the expected morphology, or are correlated with H<sub>2</sub> flows, we limit the risk of false positives. Several of the outflows in Tanabe et al. (2019, in press) are not included here for these reasons (see Table 4.1).

Some regions (e.g. OMC 2/3) contain several overlapping outflows. In these cases, we try to follow previous authors' assignment of the high-velocity emission, unless we strongly disagree with their assessment. In Section 4.4.1, we describe the outflow region extraction.

Once we have identified an outflow, we adjust the velocity range over which we integrate  $^{12}\text{CO}$  to produce contour maps that most clearly separate the blue/red lobes from surrounding cloud emission. Table 4.1 lists these visually determined velocities ( $v_{\text{blue}}$  and  $v_{\text{red}}$ ).

For each outflow, we determine a confidence rating of "Definite" or "Marginal". Definite outflows are clearly associated with their driving source, are clearly distinct from surrounding outflows and cloud emission, and are often clearly correlated with  $\text{H}_2$  outflows. Most definite outflows have been identified previously. Marginal outflows either have an unclear source assignment, are not clearly separated from the cloud or overlapping outflow emission, or are simply very weakly detected. In some cases, we are more confident of either the blue or red outflow lobe, so we assign confidence ratings independently to each. We expect the subset of definite outflows will have more reliable physical properties and position angles (see Section 4.4).

While many studies have identified energetic outflows in the OMC 1 region (e.g. Schmid-Burgk et al., 1990; Zapata et al., 2005; Teixeira et al., 2016; Bally et al., 2017), we avoid this region in our outflow search. Neither Davis et al. (2009) nor Furlan et al. (2016) cover the central part of the Orion Nebula, due to saturation and confusion with the bright nebulosity. Aside from the lack of good source catalogs in this region, the CO velocity dispersion in OMC 1 is as high as  $100 \text{ km s}^{-1}$ , due to the BN/KL "explosion" (Bally et al., 2017), making it hard to define blue/red outflow lobes. Thus, in this study we focus our outflow search outside of OMC 1.

In total, we identify 45 outflows with 67 individual lobes. Of these, 11 were not identified by Tanabe et al. (2019, in press). While we expect all outflows to be bipolar, in several cases we only see one lobe. This could be due to interactions between the outflow and the turbulent environment or obscuration of one of the lobes by intervening dense gas (Offner et al., 2011). We do not detect 10 of the outflows included in Tanabe et al. (2019, in press). Most of these non-detections consist of the most dubious outflows in that study,

which we suspect are spurious due to the automated identification method they use. Of the 67 outflow lobes, we classify 38 as “definite” and 29 as “marginal”. Table 4.1 lists the source, location,  $v_{\text{blue}}$  and  $v_{\text{red}}$ , confidence score, and the corresponding outflow in Tanabe et al. (2019, in press) for our entire catalog. Figure 4.1 shows the outflow catalog on a map of the peak  $^{12}\text{CO}$  temperature.

Figure 4.2 shows an outflow in OMC 2 driven by HOPS 68. This outflow is well-known in the literature (Outflow 12 in Tanabe et al., 2019, in press and FIR 2 in Takahashi et al., 2008). We use this outflow in Figures 4.3-4.9 to demonstrate our methods for calculating outflow properties. We present the entire outflow catalog in Appendix 4.A.

## 4.4 Physical Properties of Outflows

### 4.4.1 Calculating Physical Properties

To calculate the physical properties of outflows, we adapt the methods described by Arce & Goodman (2001), Dunham et al. (2014a), and Zhang et al. (2016).

#### Extracting Outflow Emission

To measure the outflow mass, we must first extract each outflow from the surrounding cloud. This is particularly difficult in Orion, where many outflows are clustered and overlapping. We use a two-step approach to extract each outflow lobe.

First, we integrate the  $^{12}\text{CO}$  cube over the visually estimated velocity range of the outflow lobe (discussed in Section 4.3). We select pixels above  $5\sigma$  in this integrated map of high-velocity emission, excluding insignificant noise from the outflow. Next, we draw a region around each outflow lobe by hand to remove other overlapping outflows or other cloud structures in the area.

To summarize, those pixels above  $5\sigma$  in integrated high-velocity  $^{12}\text{CO}$  and which are

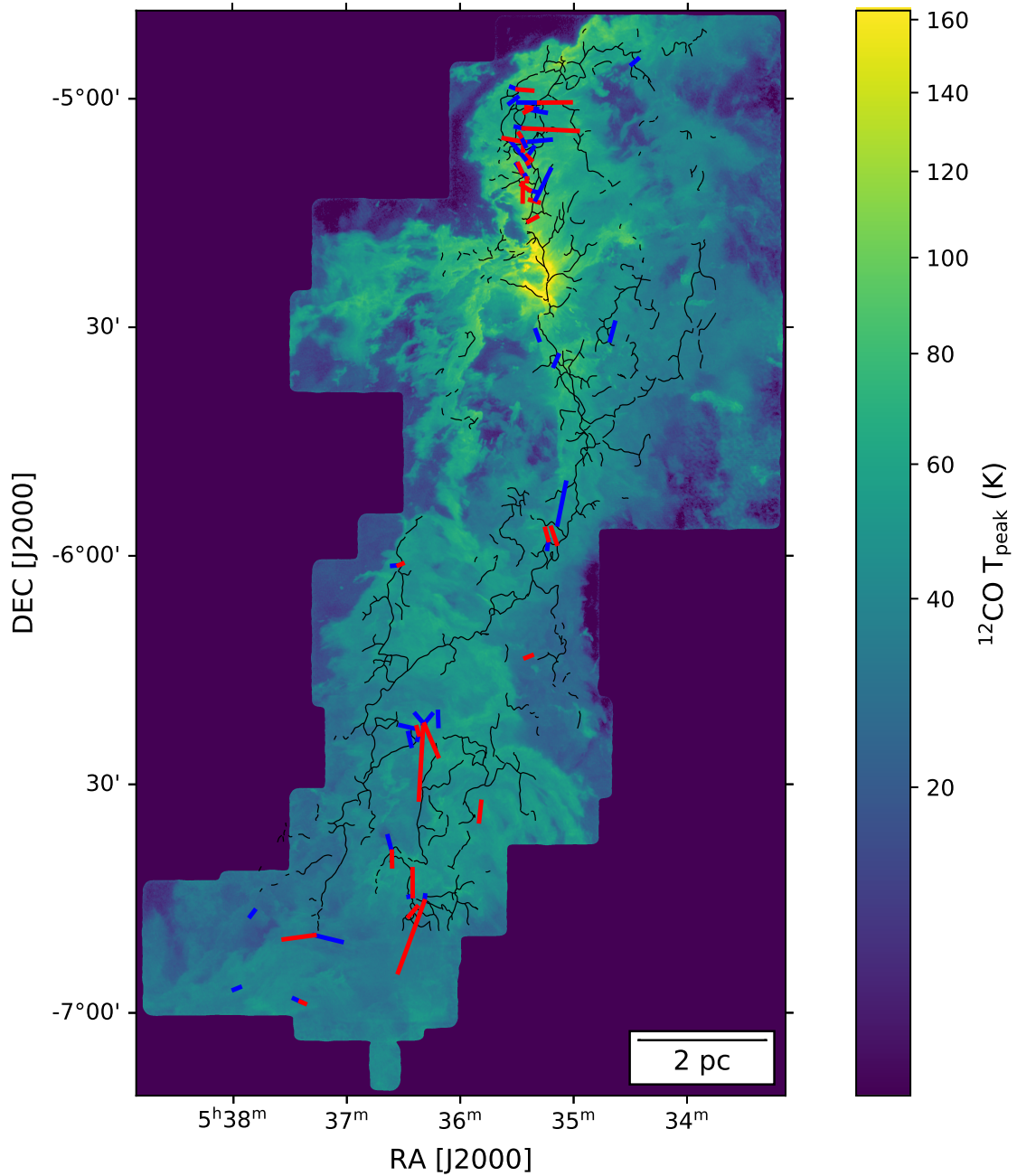


Figure 4.1 Peak  $^{12}\text{CO}$  temperature in Orion A with outflows. The blue (red) lines indicate blue (red) outflow lobes. The length of the lines denote the maximum length of the outflow lobe,  $R_{\max}$  (Section 4.4.1). The orientation of the outflow lobes indicate the measured position angle (Section 4.4.1). The black lines indicate  $\text{C}^{18}\text{O}$  filaments from Suri et al. (2019) (Section 4.5).

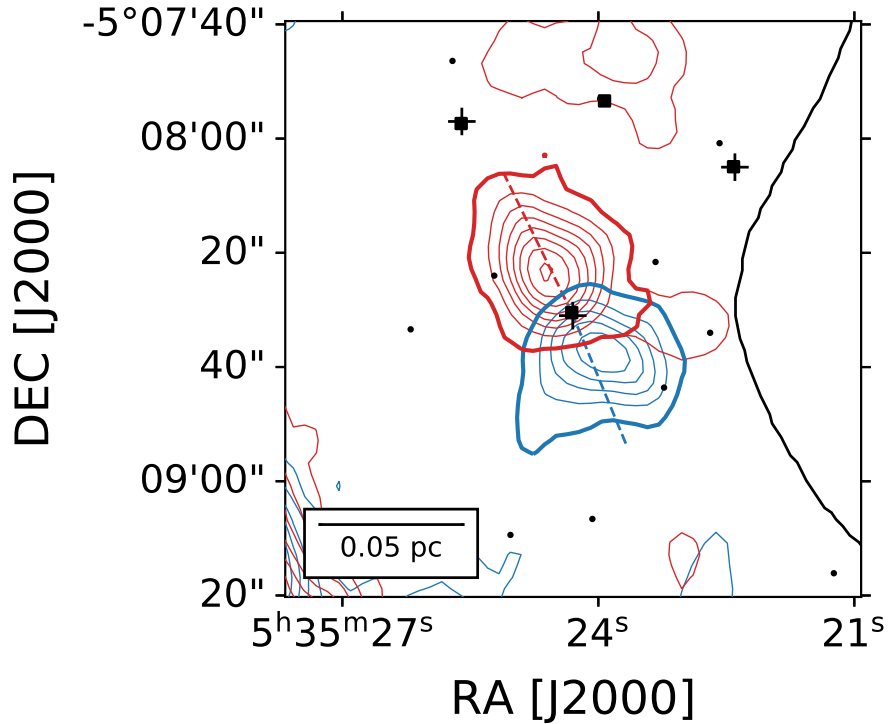


Figure 4.2 Outflow around HOPS 68. The blue (red) *contours* show  $^{12}\text{CO}$  integrated from  $-2 \text{ km s}^{-1}$  to  $v_{\text{blue}}$  ( $v_{\text{blue}}$  to  $20 \text{ km s}^{-1}$ ), where  $v_{\text{blue}}$  and  $v_{\text{red}}$  are given in Table 4.1. Contour levels go from 5 to  $50\sigma$ , in steps of  $5\sigma$  where  $\sigma$  is the RMS error in the integrated map. The *thick contours* show the region we extract for each lobe. The *shaded wedges* show the best-fit position angle and opening angle for the outflow lobes. The *black solid line* shows the closest  $\text{C}^{18}\text{O}$  filament from Suri et al. (2019). *Black squares* indicate HOPS protostars from Furlan et al. (2016), *black crosses* indicate  $\text{H}_2$  outflow sources from Davis et al. (2009), and small *black points* indicate all *Spitzer* YSOs from Megeath et al. (2012).

visually inside the outflow are included in determining the physical properties of the outflow. Figure 4.2 shows the regions extracted for the HOPS 68 outflow. The regions extracted for the other outflows are shown in the Appendix.

## Systemic Velocity

To calculate outflow energetics, we need to know the systemic velocity  $v_{\text{sys}}$  of the outflow source. We use the CARMA-NRO Orion C<sup>18</sup>O data (Kong et al., 2018) for this purpose. We fit a Gaussian model to the average C<sup>18</sup>O spectrum within a 15'' radius around the outflow source and define the mean of this Gaussian to be  $v_{\text{sys}}$ . In most cases, there is only one significant velocity component in the C<sup>18</sup>O spectrum. In the few outflows where multiple velocity components are detected, we use the velocity of the component with the highest peak intensity. Figure 4.3 shows the C<sup>18</sup>O spectrum and fit for the HOPS 68 outflow.

## Excitation Temperature

We estimate the excitation temperature of <sup>12</sup>CO,  $T_{\text{ex}}$ , using the equation from Rohlfs & Wilson (1996), which assumes <sup>12</sup>CO is optically thick in the line core:

$$T_{\text{ex}} = \frac{5.53}{\ln(1 + [5.53/(T_{\text{peak}} + 0.82)])}. \quad (4.1)$$

We define  $T_{\text{peak}}$  for each outflow to be the peak temperature of the average <sup>12</sup>CO spectrum toward the outflow area defined in Section 4.4.1. Figure 4.4 shows the average <sup>12</sup>CO spectrum with  $T_{\text{peak}}$  indicated for the HOPS 68 outflow.

## <sup>12</sup>CO Opacity Correction

In Orion, <sup>12</sup>CO is usually optically thick (Kong et al., 2018). Therefore, if we do not correct for opacity we may miss a substantial amount of outflow mass. By comparing to

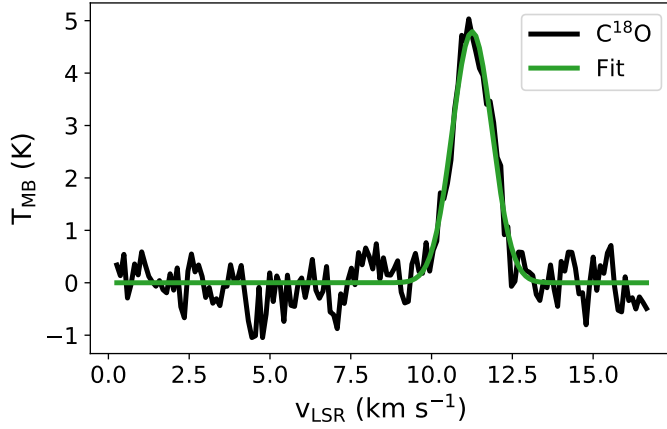


Figure 4.3  $\text{C}^{18}\text{O}$  spectrum of the HOPS 68 outflow. The black line shows the average  $\text{C}^{18}\text{O}$  spectrum within a radius of  $15''$  around HOPS 68. The green line is a Gaussian fit to the spectrum. We define the mean of this fit to be  $v_{\text{sys}}$  (see Section 4.4.1).

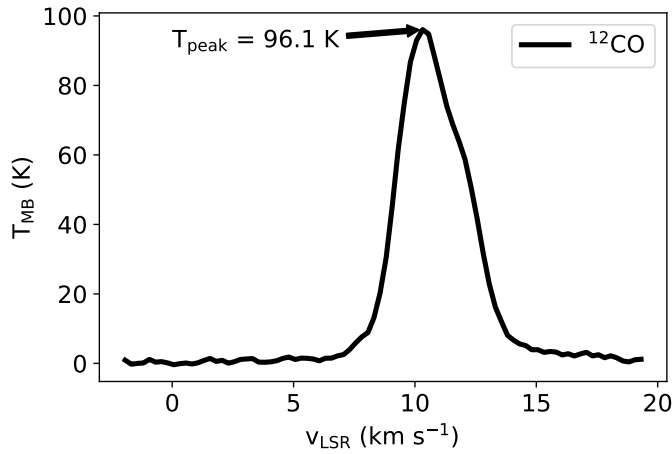


Figure 4.4  $^{12}\text{CO}$  spectrum of the HOPS 68 outflow. The black line shows the average  $^{12}\text{CO}$  spectrum within the outflow mask shown in Figure 4.2. We use the peak of this spectrum,  $T_{\text{peak}}$ , to calculate  $T_{\text{ex}}$  (see Section 4.4.1).

more optically thin tracers, studies have long shown that outflows tend to be optically thick in  $^{12}\text{CO}$ , at least at lower velocities (e.g., Goldsmith et al., 1984; Arce & Goodman, 2001). Dunham et al. (2014a) find that correcting for the optical depth of outflows increases their mass by a factor of 3 on average. Despite this, outflow studies that lack an optically thin tracer often assume that all  $^{12}\text{CO}$  outflow emission is optically thin (e.g. in Orion, Morgan et al., 1991; Takahashi et al., 2008).

Tanabe et al. (2019, in press) adopt an average  $^{12}\text{CO}$  optical depth of 5 for their entire outflow catalog. They apply this constant correction factor to every velocity channel. But Dunham et al. (2014a) show that the optical depth varies with velocity: optical depth decreases with increasing velocity away from the cloud core. We follow Dunham et al. (2014a) and Zhang et al. (2016) and use the ratio of  $^{12}\text{CO} / ^{13}\text{CO}$  to derive a velocity-dependent opacity correction for each outflow.

We assume both  $^{12}\text{CO}$  and  $^{13}\text{CO}$  are in LTE with the same excitation temperature and  $^{13}\text{CO}$  is optically thin. Then the ratio between the two isotopes is

$$\frac{T_{^{12}\text{CO}}}{T_{^{13}\text{CO}}} = \frac{[^{12}\text{CO}]}{[^{13}\text{CO}]} \frac{1 - e^{-\tau_{12}}}{\tau_{12}}, \quad (4.2)$$

where we assume the abundance ratio  $[^{12}\text{CO}]/[^{13}\text{CO}]$  is 62 (Langer & Penzias, 1993) and  $\tau_{12}$  is the optical depth of  $^{12}\text{CO}$ . In each velocity channel, we calculate the average ratio between  $^{12}\text{CO}$  and  $^{13}\text{CO}$  in pixels in the outflow region with both lines detected at  $5\sigma$  or higher.

$^{13}\text{CO}$  is usually too weak to be detected more than 2-3 km s $^{-1}$  away from the line core. Thus we extrapolate the measured ratio spectrum by fitting it with a 2nd-order polynomial, weighting each velocity channel by the standard deviation of the ratio in that channel. For most of the outflows, we use a fitting range of 1.5 km s $^{-1}$  on either side of the minimum ratio. This fitting range is adjusted for the few outflows with multiple velocity components to ensure that the component corresponding to  $v_{\text{sys}}$  is fit. For each velocity, we use the

value of this fit and Equation 4.2 to calculate the correction factor  $\tau_{12}/(1 - e^{-\tau_{12}})$  with which we multiply the observed  $^{12}\text{CO}$ . Because the opacity correction factor cannot be less than unity for any value of  $\tau_{12}$ , the ratio spectrum fit is capped at the value of  $[^{12}\text{CO}]/[^{13}\text{CO}]$  and in this regime we consider  $^{12}\text{CO}$  optically thin. In Figure 4.5, we show an example of the  $^{12}\text{CO}/^{13}\text{CO}$  ratio spectrum and fit for the HOPS 68 outflow.

## Outflow Mass

After correcting for opacity, we use the  $^{12}\text{CO}$  emission to calculate the  $\text{H}_2$  column density in each velocity channel. From Equation A6 in Zhang et al. (2016),

$$\frac{dN}{dv} = \left( \frac{8\pi k \nu_{ul}^2}{hc^3 A_{ul} g_u} \right) Q_{\text{rot}}(T_{\text{ex}}) e^{E_u/k T_{\text{ex}}} \frac{T_R(v)}{f} \quad (4.3)$$

where  $\nu_{ul} = 115.271$  GHz is the frequency of the  $^{12}\text{CO}(1-0)$  transition,  $A_{ul} = 7.203 \times 10^{-8} \text{ s}^{-1}$  is the Einstein A coefficient,  $E_u/k = 5.53$  K is the energy of the upper level,  $g_u = 3$  is the degeneracy of the upper level,  $Q_{\text{rot}}$  is the partition function (calculated to  $j = 100$ ),  $T_{\text{ex}}$  is the excitation temperature defined in Section 4.4.1,  $T_R(v)$  is the opacity-corrected brightness temperature of  $^{12}\text{CO}$ , and  $f$  is the abundance ratio of  $^{12}\text{CO}/\text{H}_2$ . We assume an abundance ratio of  $f = 1 \times 10^{-4}$  (Frerking et al., 1982).

We then calculate the mass in each voxel:

$$M = \mu_{\text{H}_2} m_{\text{H}} A_{\text{pixel}} N_{\text{H}_2}, \quad (4.4)$$

where  $\mu_{\text{H}_2} = 2.8$  is the mean molecular weight of  $\text{H}_2$  (Kauffmann et al., 2008),  $m_{\text{H}} = 1.674 \times 10^{-24} \text{ g}$  is the mass of the hydrogen atom, and  $A_{\text{pixel}} = 1.6 \times 10^{-5} \text{ pc}^2$  is the spatial area subtended by each pixel at the distance of the cloud. In blue (red) outflow lobes we sum the total mass in each velocity channel blueward (redward) of  $v_{\text{sys}}$  and arrive at the outflow mass spectrum  $dM/dv$ . We only consider pixels above  $3\sigma$  and within their

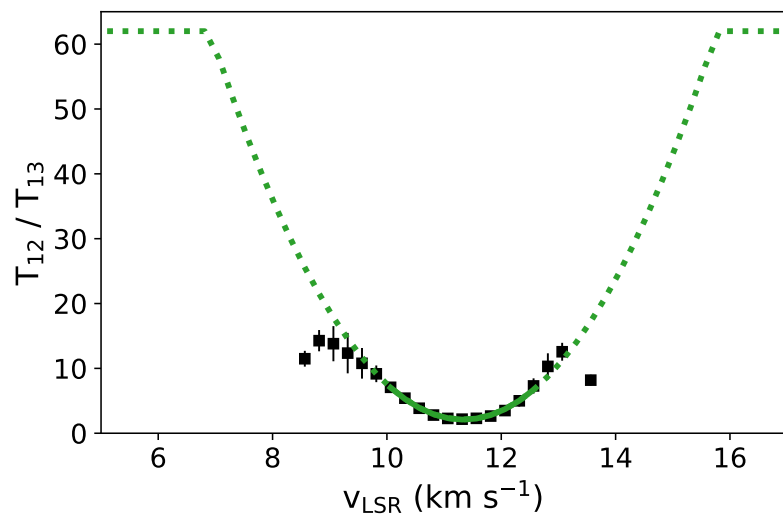


Figure 4.5  $^{12}\text{CO}/^{13}\text{CO}$  ratio of the HOPS 68 outflow. The black points show the average ratio between  $^{12}\text{CO}$  and  $^{13}\text{CO}$  in each velocity channel using only pixels where both lines are detected at  $5\sigma$ . The error bars indicate the standard deviation of the ratio. The green parabola is the weighted least-squares fit to the ratio. The solid line shows the fitting range used, while the dotted line is an extrapolation of this fit. The parabola is capped at the assumed isotopic ratio of 62 (see Section 4.4.1). Note the uncertainty on the ratio at the most extreme velocities is likely underestimated because the only pixels at these velocities lie in a small region with a size similar to the beam. Thus, the standard deviation in these pixels is lower due to the correlation between pixels.

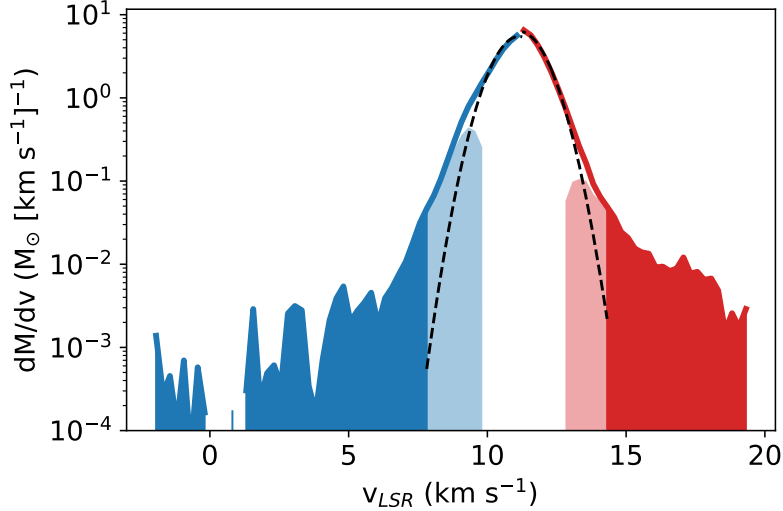


Figure 4.6 Mass spectrum of the HOPS 68 outflow. The blue (red) lines show the opacity-corrected mass spectrum in the blue (red) lobe region. The black dashed lines are Gaussian fits to these mass spectra. The dark blue (dark red) shaded regions indicate the region integrated to get the high-velocity mass. The light blue (light red) shaded regions show the low-velocity mass after subtracting the cloud mass spectrum fit (see Section 4.4.1).

respective outflow lobe region in this mass calculation. Figure 4.6 shows an example mass spectrum for the HOPS 68 outflow.

The total mass of each outflow lobe is obtained by integrating the mass spectrum over the relevant velocity range. For a lower limit on the mass, we consider only the high-velocity component: all velocity channels farther from  $v_{\text{sys}}$  than the minimum visually determined outflow velocity ( $v_{\text{blue}}/v_{\text{red}}$  in Table 4.1). These velocities were chosen to include as much outflow emission as possible while avoiding contamination by the main cloud. However, if we only consider this high-velocity outflow material, we may miss a significant fraction of the total mass.

### Low-Velocity Outflow Emission

Outflows are conspicuous because of their high-velocity emission. But outflows also exist at lower velocities. Dunham et al. (2014a) note that escape velocities from protostars can be as low as  $0.1 \text{ km s}^{-1}$ . As these velocities are much lower than typical cloud CO line-

widths, this low-velocity outflow material is often difficult to disentangle from the CO emission arising from the turbulent host molecular cloud.

The low-velocity contribution to the total outflow mass can be quite significant. Dunham et al. (2014a) found that adding the inferred low-velocity emission increased the mass of outflows by a factor of 7.7 on average, with some outflows increasing by an order of magnitude or more. Outflow momentum and energy increased by factors of 3 to 5, on average. Offner et al. (2011) found that using only high-velocity outflow emission underestimated the total outflow mass by a factor of 5 in synthetic observations of simulated outflows. Clearly, low-velocity emission should be accounted for when assessing the absolute impact of outflows on the cloud. We describe our method, adapted from Dunham et al. (2014a) for recovering this low-velocity outflow mass below.

For each outflow lobe, we fit the opacity-corrected mass spectrum with a Gaussian. For “low” velocities between  $v_{\text{sys}}$  and the visually determined minimum outflow velocity ( $v_{\text{blue}}$  or  $v_{\text{red}}$ ), we subtract this Gaussian fit from the mass spectrum and define any excess mass as low-velocity outflow mass. To reduce the amount of extraneous cloud mass introduced with this method, we exclude all velocity channels within  $1 \text{ km s}^{-1}$  of  $v_{\text{sys}}$ . Figure 4.6 demonstrates this procedure for the HOPS 68 outflow.

Generally, the low-velocity outflow mass is significantly greater than the mass at high velocities. Because this method assumes the cloud mass spectrum is fit well by a Gaussian, we expect that the low-velocity mass will often be contaminated by ambient cloud material. Thus, for each outflow lobe, we consider the high-velocity outflow mass to be a lower limit and the high-velocity plus low-velocity mass to be an upper limit on the total outflow lobe mass. We report these mass ranges for each outflow lobe in Table 4.2.

## Momentum and Kinetic Energy

We define the momentum per velocity channel to be  $dP/dv = (dM/dv)v_{\text{out}}$ , where  $dM/dv$  is the mass spectrum discussed in Section 4.4.1 and  $v_{\text{out}}$  is the velocity relative

to  $v_{\text{sys}}$ . Similarly, the kinetic energy per velocity channel is  $dE/dv = (1/2)(dM/dv)v_{\text{out}}^2$ . We sum the momentum and kinetic energy separately for low velocities, with the ambient cloud corrected mass spectrum, and high velocities. In Table 4.2, we report the momentum and kinetic energy of each outflow lobe.

### Dynamical Time

We use the same method as Curtis et al. (2010) to estimate the dynamical time  $t_{\text{dyn}}$  of each outflow lobe. Assuming the outflow has been expanding uniformly at the same velocity since it was launched,  $t_{\text{dyn}} = R/v_{\text{max}}$ , where  $R$  is the length of the outflow and  $v_{\text{max}}$  is the maximum outflow velocity. We define  $R$  to be the projected distance from the outflow source to the farthest part of the outflow lobe and  $v_{\text{max}}$  as the minimum velocity relative to  $v_{\text{sys}}$  where  $^{12}\text{CO}$  is not detected at  $3\sigma$ . Some outflows are detectable all the way to the limits of the  $^{12}\text{CO}$  spectral coverage (-2 km s $^{-1}$  in the blue, 20 km s $^{-1}$  in the red, relative to the LSR). In these cases,  $v_{\text{max}}$  is a lower limit, as are the mass and mass-derived properties. Figure 4.7 shows our determination of  $v_{\text{max}}$  for the HOPS 68 outflow. We report  $R$ ,  $v_{\text{max}}$ , and  $t_{\text{dyn}}$ , for each outflow lobe in Table 4.2.

We also calculate the mass loss rate, momentum injection rate, and energy injection rate by dividing the outflow mass, momentum, and kinetic energy by  $t_{\text{dyn}}$ . In Section 4.4.2, we use these quantities to compare the impact of outflows to turbulence in the cloud.

### Outflow Position Angle and Opening Angles

Most studies estimate the outflow position angle (PA) by eye (e.g. Morgan et al., 1991; Takahashi et al., 2008; Plunkett et al., 2013; Stephens et al., 2017; Kong et al., 2019a; Tanabe et al., 2019, in press). We adopt a more reproducible and objective method to measure outflow position and opening angles (OA) suggested by M. Dunham (2019, private communication) and modeled after the simulated outflow analysis carried out by Offner et al. (2011).

For each outflow lobe, we make an initial guess of the PA, measured counterclockwise (east) from the north celestial pole by convention. This initial guess is the angle from the outflow source to the peak of the integrated  $^{12}\text{CO}$  over the velocity range of the outflow lobe. Then, we calculate the angle of every pixel in the outflow lobe relative to this initial guess. We fit the distribution of these angles with a Gaussian and define the mean of the Gaussian to be the PA of that outflow lobe. We define the opening angle of the outflow to be the full-width at quarter maximum (FWQM) of the Gaussian, following the definition by Offner et al. (2011). We find this automated method does a suitable job producing a similar PA and OA to a visual determination. Furthermore, when comparing the outflow PA with filament orientation (Section 4.5), we avoid the risk of an artificial correlation produced by unintentional measurement bias. Figure 4.8 shows the distribution of pixel position angles and Gaussian fit for the HOPS 68 outflow. The PA and OA of each outflow lobe, along with their uncertainties from the Gaussian fit, are listed in Table 4.3.

#### 4.4.2 Impact of Outflows on the Cloud

Protostellar outflows may be important in the maintenance of turbulence in clouds, at least at cluster scales (Nakamura & Li, 2007). The efficiency of turbulent driving by outflows is highly uncertain, depending on the transfer of momentum from outflowing gas to the cloud. To be even a plausible source of turbulence, the aggregate impact of outflows must be of a similar magnitude to the observed turbulent dissipation.

The total outflow momentum, kinetic energy, and their injection rates are given in the last row of Table 4.2. We report lower and upper limits on these aggregate values by summing each outflow's high-velocity component and high-velocity + low-velocity components, respectively (see Section 4.4.1).

We compare the aggregate outflow impact with the cloud turbulent statistics summarized in Table 9 of Tanabe et al. (2019, in press). Using methods from Mac Low (1999),

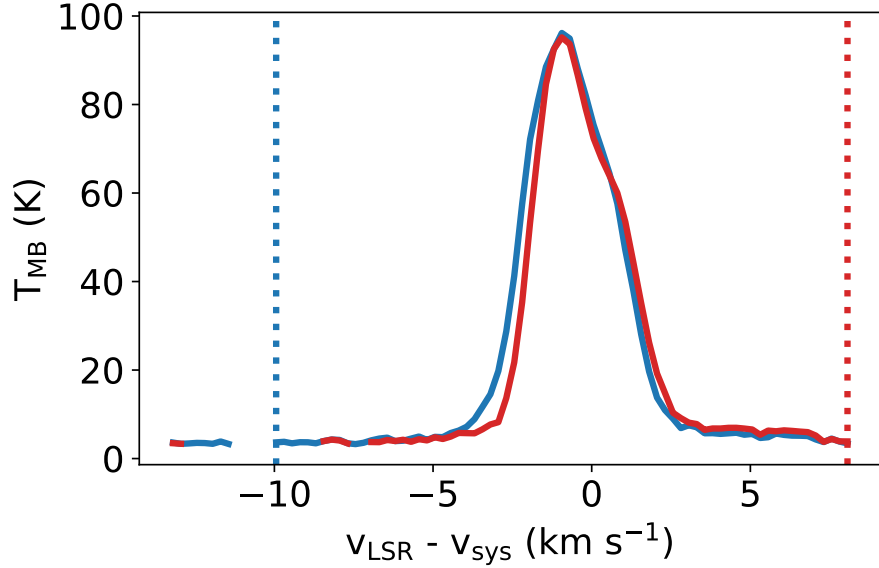


Figure 4.7 Maximum velocity of the HOPS 68 outflow. The blue (red) lines show the mean  $^{12}\text{CO}$  spectrum in the blue (red) lobe regions. The blue (red) dotted line marks the maximum blue (red) outflow velocity, defined as the first channel where  $^{12}\text{CO}$  is not detected at  $3\sigma$  (see Section 4.4.1).

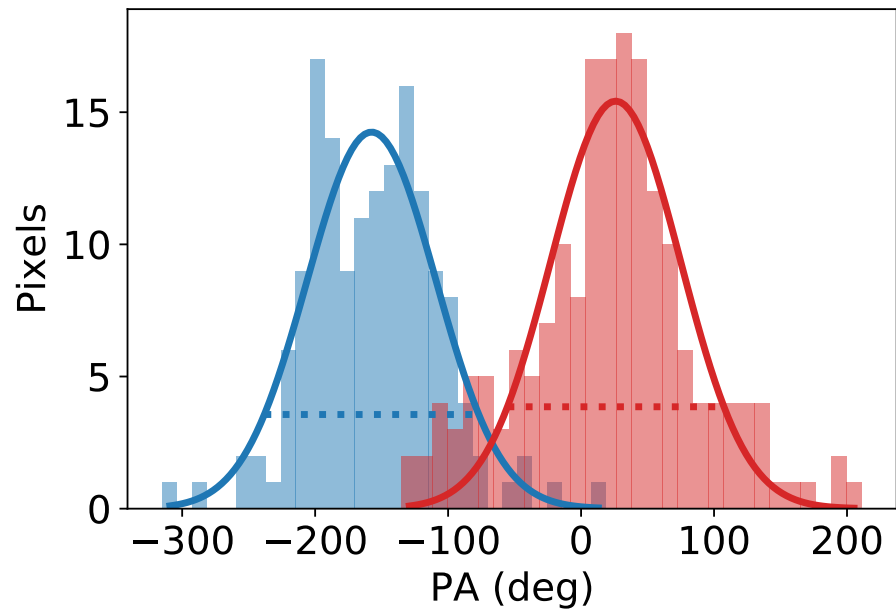


Figure 4.8 Position angle and opening angle of HOPS 68 outflow. The blue (red) histograms show the position angle distribution of all pixels in the blue (red) lobe region. The curves are Gaussian fits to these distributions. We adopt the mean of each lobe as the position angle and the full-width at quarter maximum (dotted lines) as the opening angle (see Section 4.4.1).

McKee & Ostriker (2007), and Li et al. (2015), they estimate the turbulent momentum dissipation rate ( $\dot{P}_{\text{turb}}$ ) and kinetic energy dissipation rate ( $\dot{E}_{\text{turb}}$ ). Excluding the OMC 1 region, they report  $\dot{P}_{\text{turb}} = 2.83 \times 10^{-2} M_{\odot} \text{ km s}^{-1} \text{ yr}^{-1}$  and  $\dot{E}_{\text{turb}} = 1.36 \times 10^{34} \text{ erg s}^{-1}$ .

We compare these turbulent dissipation rates to the aggregate outflow injection rates in Table 4.2  $\dot{P}$  and  $\dot{E}$ . If we only account for the high-velocity outflow components,  $\dot{P}$  is 7% of  $\dot{P}_{\text{turb}}$  and  $\dot{E}$  is 19% of  $\dot{E}_{\text{turb}}$ . If we add the low-velocity outflow emission,  $\dot{P}$  is 25% of  $\dot{P}_{\text{turb}}$  and  $\dot{E}$  is 51% of  $\dot{E}_{\text{turb}}$ .

The outflow physical properties tabulated in Table 4.2 are not corrected for the inclination of outflows to the line-of-sight. Essentially, this means we assume that the radial velocity of outflow emission with respect to the source velocity is equivalent to the actual velocity of the outflowing gas. The closer an outflow is to the plane of the sky, the larger the discrepancy between observed and actual velocities. The outflow length  $R_{\text{max}}$ , which we use to calculate  $t_{\text{dyn}}$  and all the derived injection rates, should also be corrected for the outflow inclination.

Because we do not know the actual inclination of each outflow, we estimate the effect of inclination on the aggregate outflow impact by assuming the same average inclination for every outflow. The average inclination angle, assuming any orientation is equally likely, is  $57.3^\circ$  (where  $0^\circ$  is a pole-on outflow). Dunham et al. (2014a) summarize the inclination dependence of each outflow property in their Table 8. If all of the outflows are inclined  $57.3^\circ$ , the total  $\dot{P}$  ( $\dot{E}$ ) will increase by a factor of 2.9 (5.3). Thus, after correcting for average inclination,  $\dot{P}$  is 20-72% of  $\dot{P}_{\text{turb}}$  and  $\dot{E}$  is 103-281% of  $\dot{E}_{\text{turb}}$  (depending on whether low-velocity emission is included).

We note this inclination correction assumes that all outflow motions are along the axis of the flow, with no transverse motions. Dunham et al. (2014a) caution that the inclination correction factors may be significantly smaller if transverse motions are present, as demonstrated by simulations from Downes & Cabrit (2007). The same simulations show that accounting for *atomic* gas results in additional momentum and energy of about the

same magnitude as the inclination corrections discussed above. While the absolute impact of outflows in Orion A remains highly uncertain, it is safe to say a significant fraction of the turbulent dissipation could be offset if outflows couple efficiently to the cloud.

## 4.5 Outflow-Filament Alignment

Outflows are ejected along the angular momentum axis of the protostar. If mass accretion proceeds hierarchically, from larger scales of the cloud down to the protostellar scale, then the angular momentum axis of the protostar will trace the orientation of mass accretion flows (Bodenheimer, 1995). Protostars tend to form along narrow filaments of dense gas (Arzoumanian et al., 2011), and may accrete mass either along (parallel to) or across (perpendicular to) their host filaments. If protostars predominately accrete mass along filaments, their outflows should be ejected perpendicular to the long axis of the filament. Conversely, if protostars accrete mostly across filaments, their outflows will be ejected parallel to the filament axis.

In simulations, Offner et al. (2016) find that binaries formed via turbulent fragmentation of protostellar cores produce outflows with variable position angles, and they predict a random distribution of outflow orientations under this turbulent fragmentation model. Li et al. (2018) find outflows form preferentially perpendicular to filaments in their simulations of a strongly magnetized cloud.

The alignment between CO outflows and filaments has been studied in the Perseus molecular cloud by Stephens et al. (2017) and in a massive infrared dark cloud (IRDC, Kong et al., 2019a). In Perseus, Stephens et al. (2017) showed that outflows are consistent with being randomly oriented with respect to the filament, neither parallel nor perpendicular. In the IRDC G28.37+0.07, Kong et al. (2019a) showed that outflows are preferentially perpendicular to the filament axis. It remains to be seen whether this discrepancy arises from some meaningful difference between these clouds (e.g. evolutionary state or mag-

netic field strength) or by chance.

In Orion, Davis et al. (2009) showed that H<sub>2</sub> outflows appear randomly oriented on the sky, showing no preferential alignment to the North-South integral-shaped filament. Tanabe et al. (2019, in press) studied the outflows in single-dish CO maps, finding no evidence for alignment between outflows and the large-scale filamentary structure in the cloud. However, the filamentary structure in Orion A is more complex than a single North-South integral-shaped filament. Therefore, we use the C<sup>18</sup>O filaments identified by Suri et al. (2019) in our analysis.

### 4.5.1 C<sup>18</sup>O Filaments

Suri et al. (2019) apply the Discrete Persistent Structures Extractor, DisPerSE (Sousbie, 2011) to extract filaments from the C<sup>18</sup>O spectral cube. DisPerSE connects local maxima and saddle points in the intensity distribution, which are defined as filaments. Suri et al. (2019) identify a total of 625 filaments across the Orion A cloud, each of which are defined by their PPV coordinates, allowing filaments that overlap spatially to be separated in velocity space.

For each outflow source, we search for the closest filament. Because most of the outflow sources are located along lines of sight with a single significant C<sup>18</sup>O velocity component, we ignore the filament velocity information and only consider projected distance on the sky. We use cubic spline interpolation to approximate the discrete filament coordinates with a smooth curve. For this spline interpolation, we used the `splrep` and `splev` functions from the `scipy.interpolate` package. After experimenting with the smoothing parameter  $s$  to find an optimal trade-off between smoothness and goodness-of-fit, we adopt  $s = 0.1 \times d_{\min}$  where  $d_{\min}$  is the minimum distance between the filament and outflow source.

We take the slope of the tangent to the filament curve at the closest point to the outflow

source to be the position angle of the filament, which is constrained to be between  $-180$  and  $180^\circ$ . Figure 4.9 shows an example of the spline interpolation and tangent fitting for the closest filament to the HOPS 68 outflow.

### 4.5.2 Projected Angle Between Outflows and Filaments

We follow Stephens et al. (2017) and Kong et al. (2019a) in our definition of the angular separation between outflow and filament position angles,  $\gamma$ . For each outflow lobe, we define  $\gamma$  to be

$$\gamma = \text{MIN}\{|\text{PA}_{\text{out}} - \text{PA}_{\text{fil}}|, 180^\circ - |\text{PA}_{\text{out}} - \text{PA}_{\text{fil}}|\}, \quad (4.5)$$

where  $\text{PA}_{\text{out}}$  and  $\text{PA}_{\text{fil}}$  are the position angles of the outflow lobe and the closest filament, respectively. The value of  $\gamma$  for each outflow lobe is given in Table 4.3. Figure 4.10 shows the distribution of  $\gamma$ . The full sample of  $\gamma$  shows no obvious clustering at either  $0$  or  $90^\circ$ .

Many of the outflows in our catalog are not as clear as our example outflow driven by HOPS 68. Outflows categorized as "Marginal" in Table 4.1 are likely to have less reliable position angles. In these cases, we either have difficulty disentangling the high-velocity emission near these sources and/or we are unsure of which protostar is driving the outflow. Both of these factors could greatly affect the measured position angle and, by extension,  $\gamma$ . Stephens et al. (2017) argue that the incorrect assignment of driving sources led Anathpindika & Whitworth (2008) to erroneously conclude that outflows and filaments are perpendicular in the Perseus molecular cloud.

To test whether more reliable outflows have a different distribution of  $\gamma$ , we consider a subsample of outflow lobes which we consider "Definite" (Table 4.1). Figure 4.10 shows that these outflows are not distributed significantly differently from the full sample.

Aside from the uncertainties in calculating the outflow position angles discussed above, we consider the difficulty of assigning even a well-known outflow to a particular filament.

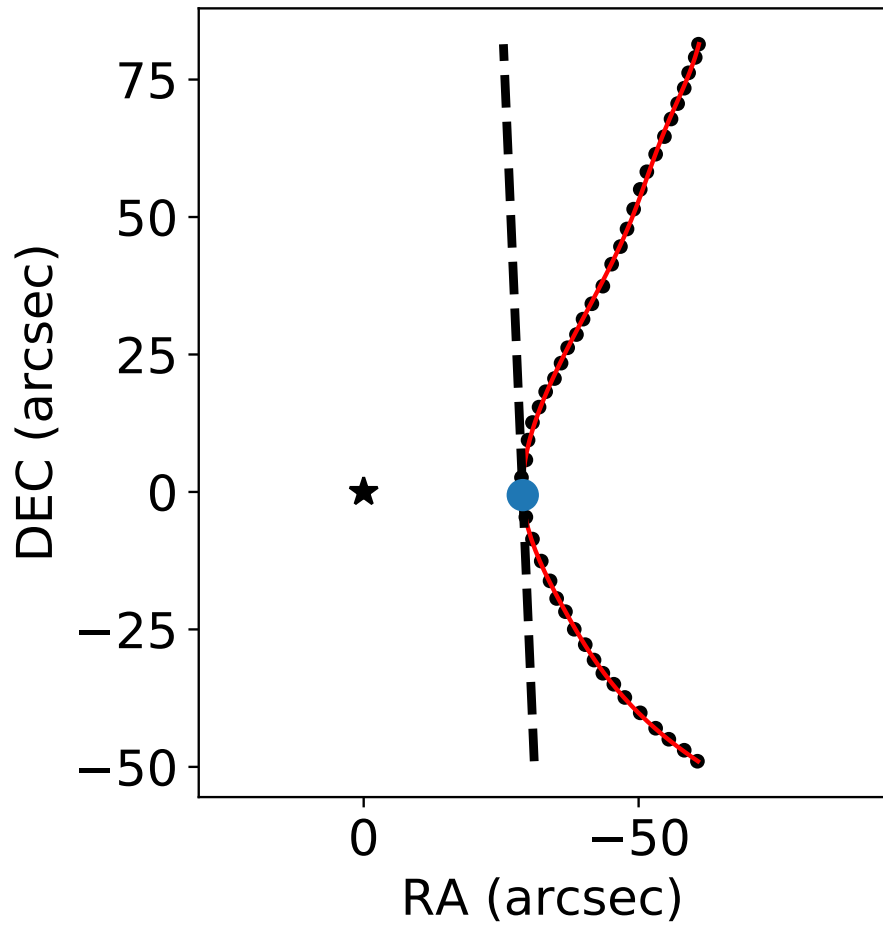


Figure 4.9  $\text{C}^{18}\text{O}$  filament near HOPS 68. The black dots show the filament closes to HOPS 68 from the Suri et al. (2019) catalog. The red curve is a smooth cubic spline interpolation of the filament. The outflow source (HOPS 68) is marked with a black star. The blue circle shows the closest point on the filament to the source. To derive the filament position angle, we find the tangent at this nearest point, shown as a black dashed line (see Section 4.5).

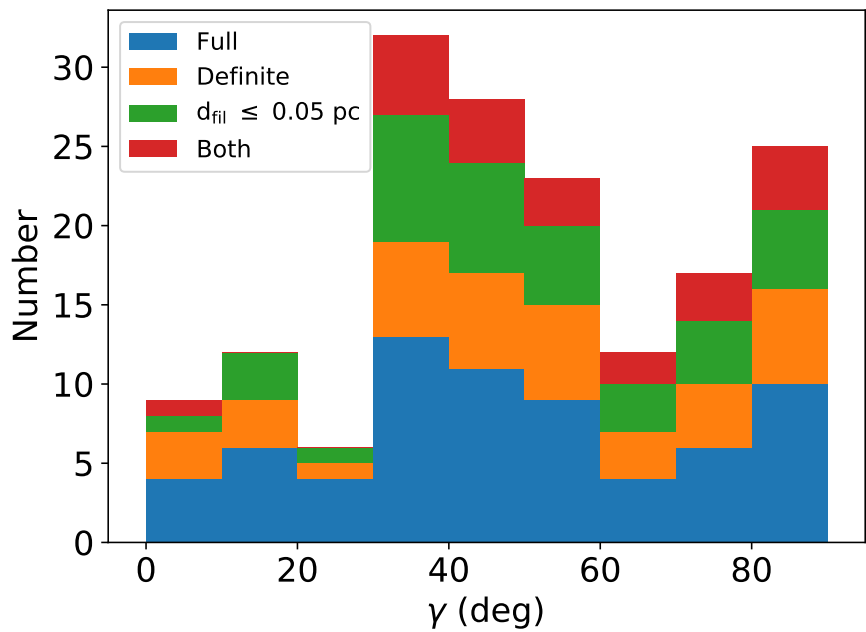


Figure 4.10 Distribution of projected angle between outflows and filaments. The blue histogram shows the distribution of  $\gamma$  in  $10^\circ$  bins for the full sample of 67 outflow lobes. The orange bars show the distribution of  $\gamma$  for the subsample of 38 outflow lobes with a confidence grade of "Definite" (Table 4.1). The green bars show the subsample of 37 outflow lobes whose sources are within 0.05 pc of the nearest filament (Table 4.3). The red bars show the subsample of 22 outflow lobes which satisfy both of these conditions. Note that the total height of the stacked bars does not equal the size of the full sample, since the subsamples are already contained within the full sample shown in blue.

Even though we select for the closest filament to each outflow source, we cannot exclude the possibility that other nearby filaments may be important to the environment of an outflow. In particular, the OMC-4 region contains spatially overlapping filaments which are distinct in velocity space (Suri et al., 2019) similar to the fibers identified by Hacar et al. (2013). The incorrect assignment of outflows to filaments may introduce noise to the distribution of  $\gamma$  and mask an underlying correlation between outflow and filament orientations. To address this concern, we compare the full sample to the closest outflow-filament pairs. We adopt a threshold on the projected outflow-filament distance ( $d_{\text{fil}}$ ) based on the typical filament width.

Suri et al. (2019) found an average filament FWHM of approximately 0.1 pc, similar to the “characteristic” filament width found using *Herschel* dust continuum maps (e.g. Arzoumanian et al., 2011; Koch & Rosolowsky, 2015). However, Suri et al. (2019) find a much larger spread in filament widths (about an order of magnitude around the mean). This is likely due to the fact that they allow the filament width to vary along its length, while most studies average the width over the entire filament. Motivated by the mean filament width, we choose a threshold of  $d_{\text{fil}} \leq 0.05$  pc, which corresponds to an outflow source within the FWHM of an average filament. Figure 4.10 shows the distribution of  $\gamma$  for this subset of outflows.

Figure 4.10 shows that limiting the sample to the closest outflow-filament pairs with the highest confidence reduces the fraction of outflows at projected angles of 0-30° with respect to their filaments. We stress that these angles are projected on the plane of the sky. To determine whether these outflows are preferentially aligned with the filaments, we must consider the underlying distribution of deprojected  $\gamma$ : the outflow-filament alignment in 3D.

### 4.5.3 3D Outflow-Filament Alignment

An outflow-filament pair can appear at various relative orientations on the plane of the sky, depending on the line-of-sight. For example, an outflow observed perpendicular to a nearby filament may actually be parallel in space. Thus, we follow Stephens et al. (2017) and Kong et al. (2019a) and run Monte Carlo simulations<sup>2</sup> of random vector pairs to project different underlying distributions of  $\gamma_{3D}$  onto the plane of the sky.

We first generate  $10^7$  pairs of unit vectors uniformly distributed around the unit sphere. From this random uniform distribution, we draw two samples. In the parallel sample, we keep only those vector pairs separated by 0-20°. In the perpendicular sample, we keep the pairs separated by 70-90°. Then, we project these vectors onto the plane of the sky by setting one coordinate to 0 and calculate the projected angle between them,  $\gamma$ . By comparing the distribution of the observed  $\gamma$  with the random, parallel, and perpendicular models, we investigate which of these underlying scenarios is most likely given the observations.

Figure 4.11 shows the cumulative distribution of  $\gamma$  for the Monte Carlo simulations and each of the outflow-filament samples discussed in Section 4.5.2. Compared to the random distribution of  $\gamma$ , the outflow samples have a deficit of  $\gamma < 40^\circ$ . In particular, the "Both" subsample with the 22 definite outflow lobes closest to their filaments contains only one lobe with  $\gamma < 33^\circ$  (the blue lobe of the SMZ 17 outflow) compared to the  $\sim 8$  which would be expected if  $\gamma$  were distributed randomly.

While Figure 4.11 shows that the "Parallel" scenario is clearly inconsistent with the observed distribution of  $\gamma$ , the "Perpendicular" distribution is more difficult to rule out. We apply the Anderson-Darling (AD) test (Stephens, 1974) to determine if the perpendicular or random distributions can be rejected for each outflow subsample. The AD  $p$ -values listed in Table 4.4 represent the likelihood that the observed outflow-filament  $\gamma$  distribution is drawn from either the random or perpendicular distribution. We do not report the results

---

<sup>2</sup>See Appendix A of Stephens et al. (2017) for a detailed description of the Monte Carlo simulations.

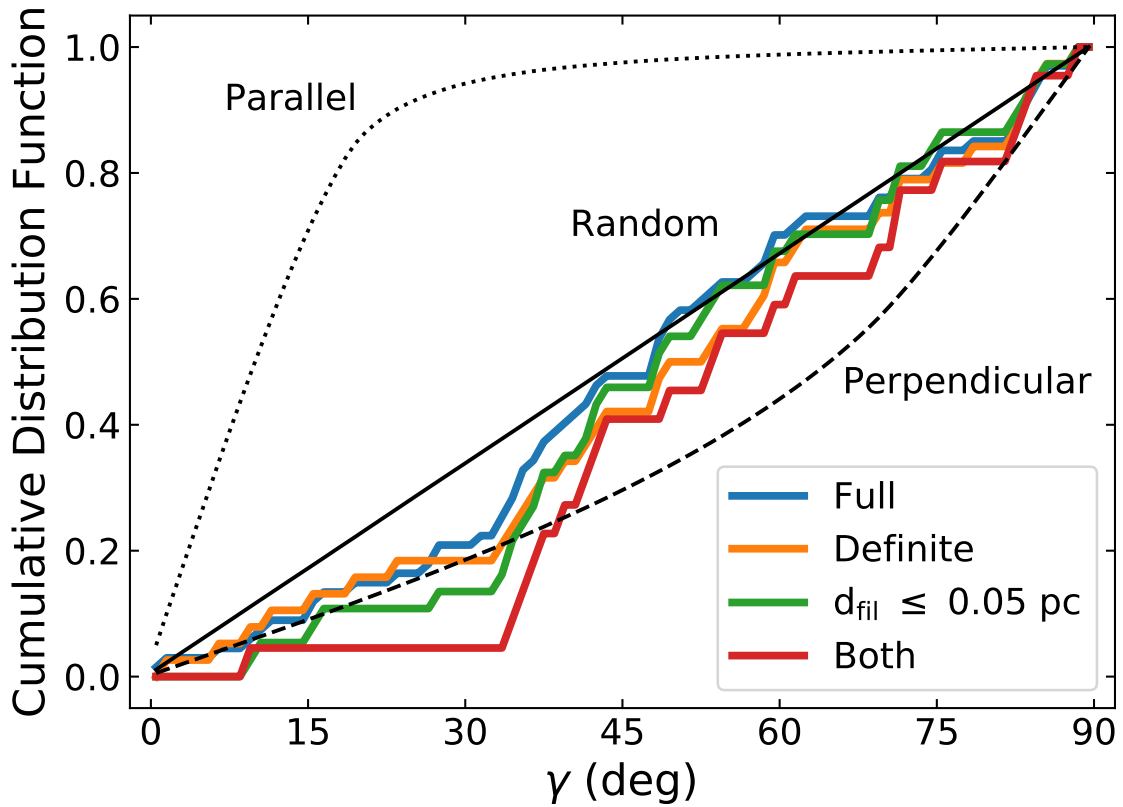


Figure 4.11 Cumulative distribution of projected angle between outflows and filaments. The colored lines show the distribution of  $\gamma$  for different subsets of our outflow catalog. The black lines show the expected distribution given three different model distributions. The parallel case contains only 3D angles between 0 and  $20^\circ$ , the random case contains all 3D angles between 0 and  $90^\circ$ , and the perpendicular case contains 3D angles between  $70$  and  $90^\circ$ . The results of Anderson-Darling tests between the observed and modeled distributions are in Table 4.4 (see Section 4.5.2).

of AD tests for the parallel case; the  $p$ -values for the parallel distribution are all close to zero.

Based on the AD test, we reject the hypothesis that the full outflow sample is drawn from a perpendicular distribution with  $> 99.9\%$  confidence ( $p < 0.001$ ), while the random distribution is not ruled out. For the definite subsample the results are similar, though we can only rule out the perpendicular distribution with 94% confidence ( $p = 0.06$ ). For the  $d_{\text{fil}} \leq 0.05$  pc subsample, we can rule out the perpendicular distribution with 98% confidence ( $p = 0.02$ ). Though these subsamples are unlikely to be drawn from a purely perpendicular distribution, their  $p$ -values are higher than the equivalent in Stephens et al. (2017). We do not test models with a mixture of perpendicular and parallel outflow-filament alignment, but such a bimodal distribution may be a better fit to our data than either random or perpendicular model alone.

If we limit the sample to the definite outflows with  $d_{\text{fil}} \leq 0.05$  pc ("Both"), and compare to the perpendicular model, we calculate an AD  $p$ -value of  $> 0.25$ . While we cannot rule out with better than 94% confidence ( $p = 0.06$ ) that this subsample of outflows is drawn from a random distribution, the perpendicular model more closely matches the angular distribution of these close outflow-filament pairs. We tentatively conclude that the clearest outflow-filament pairs in Orion A are perpendicularly aligned.

In Perseus, Stephens et al. (2017) found a random distribution of outflow-filament angles. This random alignment could reflect processes at large or small scales. At large scales, the orientation of filaments may be irrelevant to the accretion of mass onto them, contradicting simulations of filament formation (e.g. Chen & Ostriker, 2014; Clarke et al., 2017). At core scales, no matter the orientation of mass accretion, the protostellar angular momentum may be randomized by multiplicity or turbulence, as seen in simulations by Offner et al. (2016) and Lee et al. (2017). Our finding of a moderately perpendicular alignment between outflows and filaments in Orion A may mean that filament formation or protostellar mass accretion is different in these two clouds.

In the IRDC G28, Kong et al. (2019a) found a remarkably perpendicular outflow-filament alignment, rejecting a random distribution at high confidence (see Table 4.4). Such a strong perpendicular alignment is predicted in simulations of IRDCs by Li et al. (2018) and Li & Klein (2019) resulting from filament formation perpendicular to a strong magnetic field and continuous mass accretion along the magnetic field lines onto protostellar cores. As IRDCs are generally considered to be in the earliest phase of massive star formation (Rathborne et al., 2006), the outflow-filament alignment may be related to evolutionary stage or magnetic field. A comprehensive study of outflow-filament alignment across many different star forming environments is necessary to answer this question.

While we find some evidence for perpendicular outflow-filament alignment in Orion A, previous studies have concluded that outflows and filaments in this cloud are randomly aligned. Davis et al. (2009) show that the position angles of H<sub>2</sub> jets in Orion A are distributed uniformly and oriented randomly with respect to the ~pc-scale integral shaped filament. Tanabe et al. (2019, in press) conclude the same using their CO outflow catalog. Our study is not directly comparable to these, as we use the C<sup>18</sup>O filaments, which reveal the integral-shaped filament to be made up of many smaller filamentary structures.

The moderately perpendicular outflow-filament alignment may also be a result of observational biases. If we preferentially miss outflows that are parallel to their filaments, this could bias the outflow-filament alignment. An outflow launched parallel to its host filament will encounter more dense gas than a perpendicularly launched outflow. Thus, parallel outflows may be smaller or slower and thus harder to detect. This effect is seen in the simulations of Offner et al. (2011). If this bias is present, we would expect to detect more parallel outflows with higher resolution observations. The physical resolution of the Perseus observations used by Stephens et al. (2017) is about 3.5× better than the CARMA-NRO Orion A survey used here. This could help explain the deficit of parallel outflows seen in Orion relative to Perseus. The Kong et al. (2019a) IRDC observations have a similar physical resolution to our data, so this observational bias cannot explain the

difference between the outflow-filament alignment in the IRDC and Orion.

## 4.6 Conclusions

We have identified 45 outflows in the CARMA-NRO Orion CO maps of Orion A. Eleven of these outflows are new detections. For the previously known outflows, we improve the earlier estimates of their mass by including a correction for low-velocity mass as well as a velocity-dependent opacity correction. Most of the outflows have HOPS protostars associated with them, and many are correlated with H<sub>2</sub> flows. The outflows inject significant momentum and kinetic energy compared to that needed to offset turbulent dissipation in Orion A. If outflows couple efficiently to the cloud, they can maintain cloud turbulence and slow star formation. There is still considerable uncertainty in the outflow impact and a mechanism for transporting momentum from the outflow length scale to the larger cloud is needed (see Offner & Liu, 2018 for an option).

We compare the outflow position angles to the orientation of nearby filaments from the C<sup>18</sup>O catalog of Suri et al. (2019). The full outflow catalog is consistent with random outflow-filament alignment. The most reliable outflows which are closest to their filaments show a moderately perpendicular outflow-filament alignment and a random distribution is ruled out with high confidence.

While we improve the specificity of the outflow-filament comparison compared to previous studies of Orion A by using the C<sup>18</sup>O filament catalog, there is still uncertainty in pairing outflows and filaments. Future work should investigate the outflow-filament alignment over multiple length scales, and take into account the varying filament width.

The outflow-filament alignment may change as protostars evolve. A detailed comparison should be made between this alignment and protostellar properties such as bolometric temperature, multiplicity, and evolutionary stage. A combination of this sample with the studies in other clouds could provide enough statistical power to answer these more spe-

cific questions about outflow-filament alignment and the mass assembly of protostars.

Table 4.1. Outflow Catalog.

Source <sup>a</sup>	R.A. (J2000)	Decl. (J2000)	$v_{\text{blue}}/v_{\text{red}}^{\text{b}}$ (km s $^{-1}$ )	Confidence	Tanabe
SMZ 11	5 <sup>h</sup> 35 <sup>m</sup> 23.30 <sup>s</sup>	-5°07'10.00"	7.5/-	M/-	9
SMZ 17	5 <sup>h</sup> 35 <sup>m</sup> 27.00 <sup>s</sup>	-5°09'54.00"	3/18	D/D	
SMZ 21	5 <sup>h</sup> 35 <sup>m</sup> 26.90 <sup>s</sup>	-5°11'07.00"	-/14	-/M	15
SMZ 30	5 <sup>h</sup> 35 <sup>m</sup> 18.30 <sup>s</sup>	-5°31'42.00"	4.5/-	M/-	20
SMZ 50	5 <sup>h</sup> 36 <sup>m</sup> 11.50 <sup>s</sup>	-6°22'22.00"	4.5/-	M/-	33
HOPS 10	5 <sup>h</sup> 35 <sup>m</sup> 09.00 <sup>s</sup>	-5°58'27.48"	-/12.6	-/D	27
HOPS 11	5 <sup>h</sup> 35 <sup>m</sup> 13.42 <sup>s</sup>	-5°57'57.96"	4.7/12.8	D/D	26
HOPS 12	5 <sup>h</sup> 35 <sup>m</sup> 08.59 <sup>s</sup>	-5°55'54.12"	4.7/-	D/-	25
HOPS 44	5 <sup>h</sup> 35 <sup>m</sup> 10.58 <sup>s</sup>	-5°35'06.36"	4.4/-	M/-	
HOPS 50	5 <sup>h</sup> 34 <sup>m</sup> 40.90 <sup>s</sup>	-5°31'44.40"	5.8/-	M/-	21
HOPS 56	5 <sup>h</sup> 35 <sup>m</sup> 19.46 <sup>s</sup>	-5°15'32.76"	-/14	-/M	19
HOPS 58	5 <sup>h</sup> 35 <sup>m</sup> 18.50 <sup>s</sup>	-5°13'38.28"	-/14	-/M	
HOPS 59	5 <sup>h</sup> 35 <sup>m</sup> 20.14 <sup>s</sup>	-5°13'15.60"	6.9/-	M/-	17
HOPS 60	5 <sup>h</sup> 35 <sup>m</sup> 23.33 <sup>s</sup>	-5°12'03.24"	7.0/14.2	D/D	16
HOPS 68	5 <sup>h</sup> 35 <sup>m</sup> 24.31 <sup>s</sup>	-5°08'30.48"	7.8/14.5	D/D	12
HOPS 70	5 <sup>h</sup> 35 <sup>m</sup> 22.42 <sup>s</sup>	-5°08'04.92"	-/14	-/M	11
HOPS 71	5 <sup>h</sup> 35 <sup>m</sup> 25.61 <sup>s</sup>	-5°07'57.36"	7.5/-	D/-	10
HOPS 75	5 <sup>h</sup> 35 <sup>m</sup> 26.66 <sup>s</sup>	-5°06'10.44"	-/14.3	-/M	8
HOPS 78	5 <sup>h</sup> 35 <sup>m</sup> 25.82 <sup>s</sup>	-5°05'43.80"	6/15	D/D	7
HOPS 81	5 <sup>h</sup> 35 <sup>m</sup> 27.96 <sup>s</sup>	-5°04'58.08"	7.5/13.5	M/M	
HOPS 84	5 <sup>h</sup> 35 <sup>m</sup> 26.57 <sup>s</sup>	-5°03'55.08"	8.5/13.8	D/D	6
HOPS 87	5 <sup>h</sup> 35 <sup>m</sup> 23.47 <sup>s</sup>	-5°01'28.56"	8.6/13.8	M/M	5
HOPS 88	5 <sup>h</sup> 35 <sup>m</sup> 22.44 <sup>s</sup>	-5°01'14.16"	8.1/13.8	D/D	4
HOPS 92	5 <sup>h</sup> 35 <sup>m</sup> 18.31 <sup>s</sup>	-5°00'33.12"	7.6/13.7	D/D	3
HOPS 96	5 <sup>h</sup> 35 <sup>m</sup> 29.71 <sup>s</sup>	-4°58'48.72"	9.8/13.9	D/D	1
HOPS 99	5 <sup>h</sup> 34 <sup>m</sup> 29.50 <sup>s</sup>	-4°55'30.72"	8.3/-	M/-	
HOPS 157	5 <sup>h</sup> 37 <sup>m</sup> 56.57 <sup>s</sup>	-6°56'39.12"	3.5/-	M/-	
HOPS 158	5 <sup>h</sup> 37 <sup>m</sup> 24.46 <sup>s</sup>	-6°58'32.88"	5/9.5	M/M	
HOPS 160	5 <sup>h</sup> 37 <sup>m</sup> 51.05 <sup>s</sup>	-6°47'20.40"	4.7/-	D/-	
HOPS 166	5 <sup>h</sup> 36 <sup>m</sup> 25.13 <sup>s</sup>	-6°44'41.64"	5.5/11.5	M/D	40

Table 4.1 (cont'd)

Source <sup>a</sup>	R.A. (J2000)	Decl. (J2000)	$v_{\text{blue}}/v_{\text{red}}$ <sup>b</sup> (km s <sup>-1</sup> )	Confidence	Tanabe
HOPS 168	5 <sup>h</sup> 36 <sup>m</sup> 18.94 <sup>s</sup>	-6°45'22.68"	4.9/12.1	D/D	41
HOPS 169	5 <sup>h</sup> 36 <sup>m</sup> 36.12 <sup>s</sup>	-6°38'51.72"	4.7/10	D/D	39
HOPS 174	5 <sup>h</sup> 36 <sup>m</sup> 25.85 <sup>s</sup>	-6°24'58.68"	4/-	M/-	36
HOPS 177	5 <sup>h</sup> 35 <sup>m</sup> 50.02 <sup>s</sup>	-6°34'53.40"	-/10.3	-/D	37
HOPS 178	5 <sup>h</sup> 36 <sup>m</sup> 24.60 <sup>s</sup>	-6°22'41.16"	4.3/-	D/-	34
HOPS 179	5 <sup>h</sup> 36 <sup>m</sup> 21.84 <sup>s</sup>	-6°23'29.76"	4.5/11.9	D/M	35
HOPS 181	5 <sup>h</sup> 36 <sup>m</sup> 19.51 <sup>s</sup>	-6°22'12.36"	4/12	D/D	32
HOPS 182	5 <sup>h</sup> 36 <sup>m</sup> 18.84 <sup>s</sup>	-6°22'10.20"	4/11.7	D/D	31
HOPS 192	5 <sup>h</sup> 36 <sup>m</sup> 32.45 <sup>s</sup>	-6°01'16.32"	7.5/10	M/M	
HOPS 198	5 <sup>h</sup> 35 <sup>m</sup> 22.18 <sup>s</sup>	-6°13'06.24"	-/10	-/M	
HOPS 203	5 <sup>h</sup> 36 <sup>m</sup> 22.85 <sup>s</sup>	-6°46'06.24"	-/11.7	-/D	42
HOPS 355	5 <sup>h</sup> 37 <sup>m</sup> 17.09 <sup>s</sup>	-6°49'49.44"	4.3/10.5	M/M	
HOPS 368	5 <sup>h</sup> 35 <sup>m</sup> 24.72 <sup>s</sup>	-5°10'30.36"	7/14	D/D	14
HOPS 370	5 <sup>h</sup> 35 <sup>m</sup> 27.62 <sup>s</sup>	-5°09'33.48"	5/17	M/M	13
HOPS 383	5 <sup>h</sup> 35 <sup>m</sup> 29.81 <sup>s</sup>	-4°59'51.00"	9.6/-	D/-	2

<sup>a</sup>HOPS sources are protostars in the catalog from Furlan et al. (2016). SMZ sources are sources of H<sub>2</sub> outflows in Davis et al. (2009) which are not in the HOPS catalog.

<sup>b</sup>These are the visually determined velocities at which the outflow lobes are most prominent. Entries marked with '-' indicate that one of the outflow lobes is not detected. See Section 4.3 for details.

<sup>c</sup>Each entry has two values, referring to the blue/red lobes separately. Entries marked 'D' for Definite, are clearly outflows. Entries marked 'M' for Marginal are unclear. See Section 4.3 for details.

Table 4.2. Outflow Physical Properties

Source	Lobe	$M^a$ ( $M_\odot$ )	$P$ ( $M_\odot \text{ km s}^{-1}$ )	$E$ ( $10^{43} \text{ erg}$ )	$R_{\max}$ (pc)	$v_{\max}$ ( $\text{km s}^{-1}$ )	$t_{\text{dyn}}$ ( $10^4 \text{ yr}$ )	$\dot{M}$ ( $10^{-6} M_\odot \text{ yr}^{-1}$ )	$\dot{P}$ ( $10^{-6} M_\odot \text{ km s}^{-1} \text{ yr}^{-1}$ )	$\dot{E}$ ( $10^{30} \text{ erg s}^{-1}$ )
SMZ 11	B	0.10 - 1.63	0.47 - 3.94	2.3 - 10.6	0.11	7.1	1.5	6.5 - 105.9	30.8 - 255.9	47.0 - 219.0
SMZ 17	B	0.00 - 0.17	0.01 - 0.52	0.1 - 1.9	0.03	9.0	0.3	0.2 - 50.2	2.2 - 150.2	6.2 - 178.2
-	R	0.01 - 0.24	0.05 - 0.71	0.4 - 2.6	0.05	8.3	0.6	1.2 - 40.9	8.8 - 121.8	20.8 - 140.8
SMZ 21	R	0.11 - 1.33	0.36 - 2.63	1.2 - 5.7	0.29	5.1	5.5	1.9 - 24.1	6.5 - 47.6	7.0 - 32.8
SMZ 30	B	0.65 - 0.99	1.15 - 1.56	2.0 - 2.5	0.16	2.6	6.1	10.7 - 16.3	18.8 - 25.6	10.6 - 13.2
SMZ 50	B	0.08 - 0.23	0.23 - 0.50	0.7 - 1.2	0.22	4.8	4.6	1.8 - 5.0	5.1 - 11.0	4.6 - 8.2
HOPS 10	R	0.08 - 1.57	0.44 - 4.90	2.7 - 16.6	0.27	11.2	2.3	3.3 - 66.9	19.0 - 209.0	36.4 - 224.4
HOPS 11	B	0.13 - 0.19	0.53 - 0.63	2.2 - 2.4	0.14	9.7	1.4	9.5 - 13.2	37.6 - 44.9	50.0 - 54.8
-	R	0.06 - 1.23	0.42 - 3.82	3.0 - 13.5	0.18	11.6	1.6	3.9 - 78.6	26.7 - 244.8	60.9 - 273.9
HOPS 12	B	2.11 - 3.13	8.78 - 10.22	37.6 - 40.1	0.67	10.0	6.6	32.2 - 47.6	134.0 - 156.0	181.0 - 193.1
HOPS 44	B	1.42 - 2.84	5.43 - 9.63	20.9 - 33.4	0.18	9.8	1.8	77.5 - 155.1	296.6 - 526.5	362.0 - 579.0
HOPS 50	B	0.13 - 0.13	0.24 - 0.24	0.5 - 0.5	0.29	5.4	5.2	2.6 - 2.6	4.6 - 4.6	2.9 - 2.9
HOPS 56	R	0.22 - 1.57	0.89 - 3.82	3.7 - 10.4	0.15	7.7	1.9	11.3 - 82.0	46.4 - 199.4	61.7 - 172.7
HOPS 58	R	0.09 - 1.15	0.35 - 2.81	1.4 - 7.3	0.14	6.1	2.3	3.9 - 49.8	15.2 - 121.2	19.3 - 100.6
HOPS 59	B	0.09 - 2.27	0.44 - 4.23	2.2 - 9.3	0.53	8.6	6.0	1.6 - 37.7	7.3 - 70.1	11.5 - 48.9
HOPS 60	B	0.02 - 0.37	0.07 - 0.86	0.3 - 2.2	0.14	6.7	2.1	0.7 - 17.6	3.4 - 40.7	5.2 - 33.2
-	R	0.02 - 0.47	0.06 - 0.79	0.3 - 1.5	0.15	7.8	1.9	0.8 - 24.4	3.3 - 41.1	4.5 - 25.1
HOPS 68	B	0.03 - 0.55	0.16 - 1.25	1.0 - 3.4	0.05	9.9	0.5	6.1 - 109.1	32.1 - 250.4	61.8 - 214.8
-	R	0.05 - 0.19	0.25 - 0.55	1.3 - 2.0	0.06	8.1	0.7	7.9 - 27.5	37.2 - 81.1	59.3 - 91.5
HOPS 70	R	0.13 - 0.39	0.45 - 1.06	1.6 - 3.0	0.10	5.6	1.8	7.2 - 21.6	24.9 - 58.6	27.4 - 52.7
HOPS 71	B	0.19 - 3.95	0.83 - 8.19	3.8 - 19.7	0.35	6.8	5.0	3.7 - 78.4	16.5 - 162.5	23.7 - 123.6
HOPS 75	R	0.03 - 0.27	0.10 - 0.53	0.3 - 1.1	0.08	4.6	1.6	2.0 - 16.5	6.4 - 32.2	6.6 - 21.9
HOPS 78	B	0.34 - 8.42	2.30 - 23.47	16.1 - 76.6	0.41	13.3	3.0	11.2 - 278.3	76.0 - 775.6	168.0 - 802.0
-	R	0.19 - 3.69	0.85 - 7.55	4.0 - 17.9	0.34	8.0	4.2	20.1 - 178.1	29.6 - 134.6	

Table 4.2 (cont'd)

Source	Lobe	$M^a$ ( $M_\odot$ )	$P$ ( $M_\odot$ km s $^{-1}$ )	$E$ ( $10^{43}$ erg)	$R_{\max}$ (pc)	$v_{\max}$ (km s $^{-1}$ )	$t_{\text{dyn}}$ (10 $^4$ yr)	$\dot{M}$ (10 $^{-6}$ $M_\odot$ yr $^{-1}$ )	$\dot{P}$ (10 $^{-6}$ $M_\odot$ km s $^{-1}$ yr $^{-1}$ )	$\dot{E}$ (10 $^{30}$ erg s $^{-1}$ )
HOPS 81	B	0.08 - 1.08	0.38 - 2.51	2.0 - 6.9	0.17	10.1	1.7	4.6 - 64.9	23.0 - 151.0	38.6 - 132.5
-	R	0.02 - 0.09	0.05 - 0.16	0.1 - 0.3	0.05	3.2	1.6	1.2 - 5.7	2.9 - 9.9	2.3 - 5.7
HOPS 84	B	0.02 - 0.13	0.05 - 0.20	0.1 - 0.4	0.13	4.4	2.8	0.7 - 4.5	1.8 - 7.3	1.6 - 4.2
-	R	0.86 - 2.81	3.01 - 7.74	10.6 - 22.3	0.86	8.7	9.7	8.8 - 28.9	30.9 - 79.6	34.6 - 72.6
HOPS 87	B	1.14 - 2.24	3.69 - 6.03	12.4 - 17.4	0.26	7.2	3.6	31.8 - 62.4	103.0 - 168.4	110.0 - 154.6
-	R	0.02 - 0.29	0.06 - 0.48	0.2 - 0.9	0.08	4.6	1.8	1.2 - 16.2	3.4 - 26.6	3.1 - 15.1
HOPS 88	B	0.18 - 1.09	0.75 - 2.63	3.3 - 7.3	0.09	9.1	0.9	19.5 - 115.2	78.7 - 277.7	109.0 - 245.0
-	R	0.05 - 0.11	0.16 - 0.28	0.5 - 0.8	0.08	6.9	1.1	4.5 - 10.0	14.2 - 24.8	14.9 - 21.6
HOPS 92	B	0.40 - 2.61	1.61 - 6.11	6.8 - 16.5	0.33	8.8	3.7	10.9 - 71.5	44.2 - 167.2	59.4 - 142.9
-	R	0.13 - 0.19	0.44 - 0.51	1.5 - 1.6	0.50	6.2	7.9	1.7 - 2.4	5.6 - 6.4	6.0 - 6.3
HOPS 96	B	0.04 - 0.09	0.11 - 0.17	0.3 - 0.4	0.11	4.0	2.6	1.6 - 3.5	4.2 - 6.4	3.9 - 4.6
-	R	0.35 - 1.65	0.73 - 2.61	1.6 - 4.3	0.23	4.7	4.8	7.2 - 34.1	15.1 - 53.9	10.1 - 28.0
HOPS 99	B	0.04 - 0.07	0.07 - 0.10	0.1 - 0.2	0.13	2.6	4.9	0.7 - 1.4	1.3 - 2.1	0.8 - 1.1
HOPS 157	B	0.03 - 0.03	0.08 - 0.08	0.2 - 0.2	0.10	3.4	3.0	1.1 - 1.1	2.6 - 2.6	2.1 - 2.1
HOPS 158	B	0.08 - 0.18	0.22 - 0.39	0.6 - 0.9	0.12	4.1	2.7	3.0 - 6.6	7.9 - 14.4	6.7 - 10.4
-	R	0.03 - 0.04	0.07 - 0.08	0.2 - 0.2	0.08	3.9	1.9	1.4 - 1.9	3.8 - 4.3	3.7 - 3.9
HOPS 160	B	0.07 - 0.07	0.10 - 0.10	0.2 - 0.2	0.11	3.2	3.4	2.0 - 2.0	3.0 - 3.0	1.6 - 1.6
HOPS 166	B	0.03 - 0.50	0.10 - 1.10	0.4 - 2.6	0.07	5.8	1.1	2.4 - 45.1	8.8 - 99.2	10.4 - 73.2
-	R	1.00 - 2.83	3.70 - 7.77	14.6 - 23.8	0.42	10.7	3.9	25.6 - 73.0	95.4 - 200.4	120.0 - 194.7
HOPS 168	B	0.01 - 0.05	0.03 - 0.11	0.2 - 0.3	0.09	6.1	1.5	0.5 - 3.5	2.1 - 7.5	3.4 - 6.5
-	R	1.03 - 7.47	4.61 - 16.30	22.4 - 45.7	1.20	10.4	11.3	9.1 - 66.0	40.7 - 143.7	62.8 - 128.1
HOPS 169	B	0.10 - 0.24	0.49 - 0.71	2.8 - 3.1	0.25	8.9	2.7	3.5 - 8.8	17.9 - 25.7	32.0 - 35.8
-	R	0.14 - 1.18	0.79 - 2.50	5.1 - 8.1	0.23	12.3	1.8	7.7 - 64.2	43.0 - 135.3	88.3 - 139.7
HOPS 174	B	0.07 - 0.16	0.22 - 0.39	0.7 - 1.0	0.21	4.4	4.6	1.6 - 3.4	4.7 - 8.6	4.5 - 7.2

Table 4.2 (cont'd)

Source	Lobe	$M^a$ ( $M_\odot$ )	$P$ ( $M_\odot \text{ km s}^{-1}$ )	$E$ ( $10^{43} \text{ erg}$ )	$R_{\max}$ (pc)	$v_{\max}$ ( $\text{km s}^{-1}$ )	$t_{\text{dyn}}$ ( $10^4 \text{ yr}$ )	$\dot{M}$ ( $10^{-6} M_\odot \text{ yr}^{-1}$ )	$\dot{P}$ ( $10^{-6} M_\odot \text{ km s}^{-1} \text{ yr}^{-1}$ )	$\dot{E}$ ( $10^{30} \text{ erg s}^{-1}$ )
HOPS 177	R	0.77 - 1.06	1.52 - 1.87	3.2 - 3.6	0.31	7.3	4.2	18.5 - 25.5	36.3 - 44.7	24.5 - 27.7
HOPS 178	B	0.19 - 0.55	0.62 - 1.42	2.0 - 3.8	0.21	8.9	2.4	8.2 - 23.4	26.3 - 60.1	27.2 - 51.3
HOPS 179	B	0.06 - 0.06	0.16 - 0.16	0.4 - 0.4	0.09	4.6	1.8	3.3 - 3.3	8.7 - 8.7	7.4 - 7.4
-	R	0.04 - 0.90	0.24 - 3.13	1.6 - 11.8	0.12	12.4	1.0	4.0 - 93.7	25.1 - 326.9	51.2 - 391.2
HOPS 181	B	0.51 - 0.98	2.08 - 3.39	8.9 - 12.6	0.21	9.1	2.3	22.1 - 42.3	90.2 - 147.2	122.0 - 173.0
-	R	0.26 - 10.68	1.57 - 26.51	9.7 - 77.1	1.18	12.1	9.5	2.8 - 111.8	16.4 - 277.8	32.3 - 256.3
HOPS 182	B	0.31 - 0.55	1.34 - 2.01	6.1 - 8.0	0.22	9.1	2.4	13.3 - 23.5	57.0 - 85.4	82.1 - 107.2
-	R	0.11 - 1.35	0.66 - 4.52	4.1 - 16.5	0.55	11.1	4.8	2.3 - 28.2	13.8 - 94.0	27.1 - 109.0
HOPS 192	B	0.78 - 0.78	0.98 - 0.98	1.4 - 1.4	0.10	4.1	2.5	31.2 - 31.2	39.3 - 39.3	18.2 - 18.2
-	R	0.03 - 0.08	0.05 - 0.14	0.1 - 0.2	0.07	3.7	1.8	1.4 - 4.8	3.0 - 7.8	2.2 - 4.4
HOPS 198	R	0.01 - 0.20	0.03 - 0.51	0.1 - 1.4	0.11	6.0	1.8	0.3 - 11.6	1.5 - 28.9	2.2 - 25.9
HOPS 203	R	0.45 - 0.45	0.98 - 0.98	2.3 - 2.3	0.20	5.7	3.4	13.0 - 13.0	28.6 - 28.6	21.0 - 21.0
HOPS 355	B	0.40 - 0.47	1.40 - 1.48	5.0 - 5.1	0.45	8.9	4.9	8.2 - 9.6	28.6 - 30.2	32.7 - 33.3
-	R	0.03 - 0.21	0.13 - 0.55	0.5 - 1.5	0.49	7.8	6.2	0.5 - 3.5	2.1 - 8.8	2.8 - 7.7
HOPS 368	B	0.03 - 0.54	0.13 - 1.37	0.6 - 3.8	0.06	6.7	0.9	3.1 - 62.0	14.4 - 158.4	21.8 - 139.8
-	R	0.02 - 0.05	0.09 - 0.16	0.4 - 0.5	0.04	6.3	0.6	3.8 - 8.3	14.2 - 24.9	17.6 - 25.7
HOPS 370	B	0.05 - 0.35	0.40 - 1.40	3.5 - 7.2	0.14	13.1	1.0	4.7 - 34.3	39.5 - 136.5	109.0 - 222.0
-	R	0.02 - 0.60	0.11 - 1.35	0.8 - 3.9	0.13	8.1	1.5	1.1 - 39.2	7.5 - 88.7	16.0 - 80.4
HOPS 383	B	0.29 - 0.37	0.74 - 0.88	2.0 - 2.2	0.16	5.4	2.8	10.2 - 12.9	25.9 - 30.7	22.0 - 24.8
Total <sup>b</sup>		16.5 - 82.4	59.6 - 206.3	249 - 614		516 - 2710		1920 - 7063		2640 - 6900

<sup>a</sup>Mass and all properties derived from mass are given as lower and upper limits. The lower limit refers to the high-velocity component of the outflow only. The upper limit refers to the sum of the high-velocity and low-velocity components. See Section 4.4.1 for details.

<sup>b</sup>The total of the lower-limits and upper-limits for each column are given. The physical properties in this table are not corrected for inclination angle. See Section 4.4.2 for a discussion of the inclination correction.

Table 4.3. Outflow Angles and Filament Comparison.

Source	Position Angle <sup>a</sup> (°)	Opening Angle (°)	$\gamma^b$ (°)	$d_{\text{fil}}^c$ (pc)
SMZ 11	-35 ± 3.1/-	157 ± 10/-	27/-	0.066
SMZ 17	-118 ± 11/34 ± 3.1	193 ± 38/79 ± 10	10/38	0.01
SMZ 21	-/179 ± 0.5	-/35 ± 2	-/43	0.016
SMZ 30	20 ± 20/-	120 ± 120/-	35/-	0.11
SMZ 50	2 ± 1.4/-	77 ± 8.8/-	36/-	0.19
HOPS 10	-/19 ± 2	-/58 ± 6.8	-/71	0.003
HOPS 11	172 ± 1.2/16 ± 1.7	92 ± 4.1/68 ± 5.6	62/86	0.052
HOPS 12	-11 ± 0.1/-	39 ± 0.4/-	54/-	0.032
HOPS 44	-24 ± 2.4/-	120 ± 8.9/-	70/-	0.013
HOPS 50	-15 ± 0.4/-	42 ± 1.3/-	16/-	0.005
HOPS 56	-/119 ± 6	-/191 ± 23	-/33	0.048
HOPS 58	-/74 ± 0.6	-/44 ± 1.9	-/88	0.058
HOPS 59	-26 ± 0.2/-	15 ± 0.7/-	38/-	0.054
HOPS 60	-104 ± 0.3/57 ± 0.3	22 ± 1.1/24 ± 0.9	78/83	0.057
HOPS 68	-158 ± 3.8/26 ± 3.7	161 ± 13/163 ± 12	20/24	0.058
HOPS 70	-/48 ± 2	-/83 ± 7.5	-/74	0.015
HOPS 71	39 ± 0.6/-	35 ± 2.3/-	59/-	0.11
HOPS 75	-/175 ± 1.6	-/95 ± 5.5	-/17	0.003
HOPS 78	-85 ± 0.5/80 ± 0.2	41 ± 1.5/37 ± 0.8	59/43	0.046
HOPS 81	-154 ± 0.6/34 ± 3.1	51 ± 2/83 ± 12	40/32	0.067
HOPS 84	78 ± 0.7/-93 ± 0.2	38 ± 2.4/18 ± 0.6	58/49	0.056
HOPS 87	-100 ± 0.3/118 ± 1.2	49 ± 1.2/47 ± 4.5	27/11	0.008
HOPS 88	-100 ± 3.5/82 ± 1.7	210 ± 12/99 ± 6.1	36/35	0.023
HOPS 92	89 ± 0.3/-89 ± 0.2	33 ± 1.2/24 ± 0.4	43/41	0.019
HOPS 96	69 ± 0.8/-95 ± 5	46 ± 2.8/142 ± 19	55/71	0.007
HOPS 99	-49 ± 1.3/-	64 ± 4.8/-	48/-	0.003
HOPS 157	112 ± 1.4/-	66 ± 4.8/-	84/-	1.5
HOPS 158	66 ± 1.4/-114 ± 2.7	84 ± 4.7/113 ± 9.1	50/50	1.2
HOPS 160	-38 ± 1.1/-	68 ± 3.6/-	2/-	0.43
HOPS 166	99 ± 4.9/0 ± 1.1	239 ± 17/80 ± 3.7	59/40	0.036

Table 4.3 (cont'd)

Source	Position Angle <sup>a</sup> (°)	Opening Angle (°)	$\gamma^b$ (°)	$d_{\text{fil}}^c$ (pc)
HOPS 168	$-7 \pm 3.2/160 \pm 0.2$	$101 \pm 11/33 \pm 0.6$	83/69	0.001
HOPS 169	$15 \pm 0.5/-179 \pm 0.9$	$46 \pm 1.7/62 \pm 2.9$	49/35	0.004
HOPS 174	$13 \pm 0.4/-$	$35 \pm 1.3/-$	85/-	0.004
HOPS 177	$-/-6 \pm 0.7$	$-/54 \pm 2.4$	-/6	0.095
HOPS 178	$77 \pm 2/-$	$94 \pm 6.7/-$	76/-	0.042
HOPS 179	$164 \pm 1.1/16 \pm 0.8$	$60 \pm 3.6/71 \pm 2.6$	60/28	0.091
HOPS 181	$-40 \pm 2/177 \pm 0.4$	$131 \pm 7.8/24 \pm 1.2$	48/12	0.2
HOPS 182	$41 \pm 2.5/-157 \pm 0.1$	$77 \pm 8.2/9 \pm 0.3$	33/16	0.23
HOPS 192	$95 \pm 2.8/-67 \pm 1.6$	$104 \pm 9.3/105 \pm 5.3$	53/34	0.045
HOPS 198	$-/112 \pm 4.2$	$-/64 \pm 14$	-/0	0.12
HOPS 203	$-/139 \pm 4.5$	$-/60 \pm 15$	-/85	0.011
HOPS 355	$-104 \pm 0.4/98 \pm 0.1$	$45 \pm 1.3/8 \pm 0.3$	75/84	0.099
HOPS 368	$30 \pm 12/175 \pm 4.5$	$289 \pm 44/135 \pm 15$	61/84	0.034
HOPS 370	$36 \pm 1.3/24 \pm 0.5$	$66 \pm 4.8/40 \pm 1.9$	37/48	0.044
HOPS 383	$128 \pm 0.5/-$	$49 \pm 1.7/-$	88/-	0.019

<sup>a</sup>Columns with two entries refer to the blue/red outflow lobes separately.  
Entries marked '-' refer to lobes that are not detected.

<sup>b</sup> $\gamma$  is the projected angle between the outflow and filament. See Section 4.5 for details.

<sup>c</sup> $d_{\text{fil}}$  is the minimum distance between the outflow source and filament.

Table 4.4. Anderson-Darling  $p$ -values.

Sample	Random	Perpendicular
Full	0.23	< 0.001
Definite	> 0.25	0.06
$d_{\text{fl}} \leq 0.05$ pc	0.13	0.02
Both	0.06	> 0.25
Stephens et al. (2017) <sup>a</sup>	0.20	0.0045
Kong et al. (2019a) <sup>b</sup>	$6.5 \times 10^{-5}$	0.53

<sup>a</sup>Perseus outflows;  $\gamma_F$  in their Table 3.

<sup>b</sup>IRDC G28 outflows

## **4.A All Outflows in CARMA-NRO Orion**

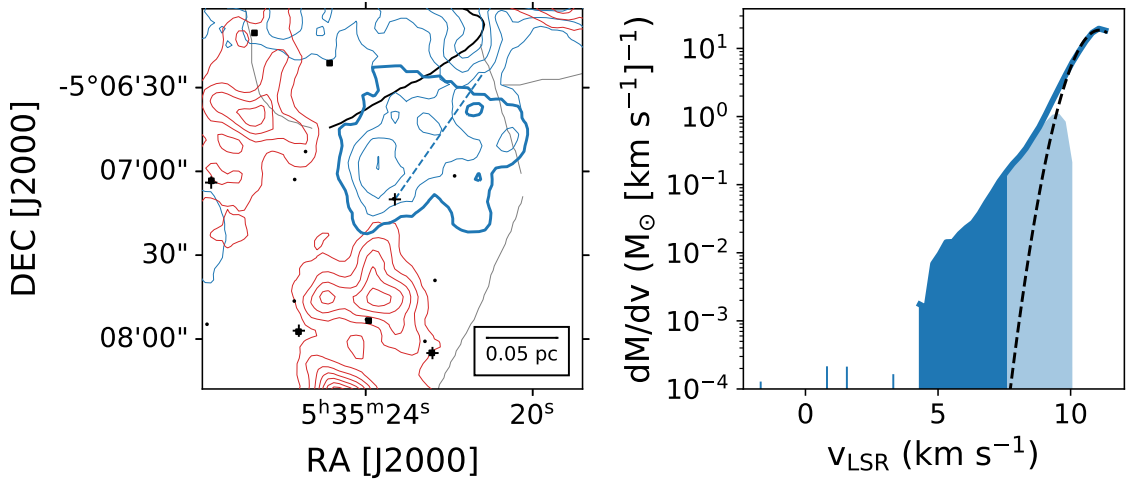


Figure 4.12 SMZ 11 outflow. The left panel shows the outflow, position angle, nearby sources, and filaments. The velocity range of integration is given by  $v_{\text{blue}}/v_{\text{red}}$  in Table 4.1 and the contours go from 5 to  $50\sigma$  in steps of  $5\sigma$ . Symbols are the same as Figure 4.2. The right panel shows the mass spectrum with fit. Symbols are the same as Figure 4.6.

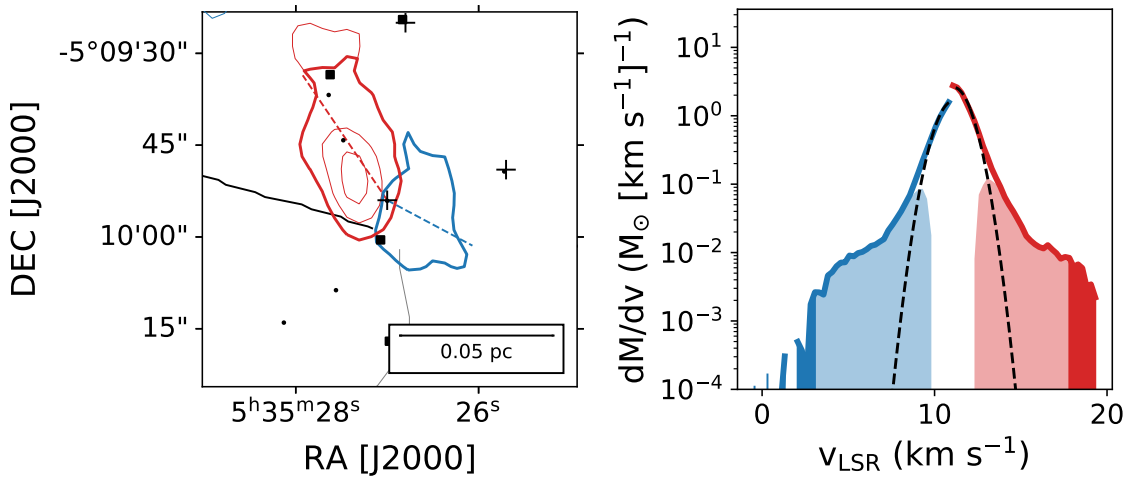


Figure 4.12 SMZ 17 outflow. The left panel shows the outflow, position angle, nearby sources, and filaments. The velocity range of integration is given by  $v_{\text{blue}}/v_{\text{red}}$  in Table 4.1 and the contours go from 5 to  $50\sigma$  in steps of  $5\sigma$ . Symbols are the same as Figure 4.2. The right panel shows the mass spectrum with fit. Symbols are the same as Figure 4.6.

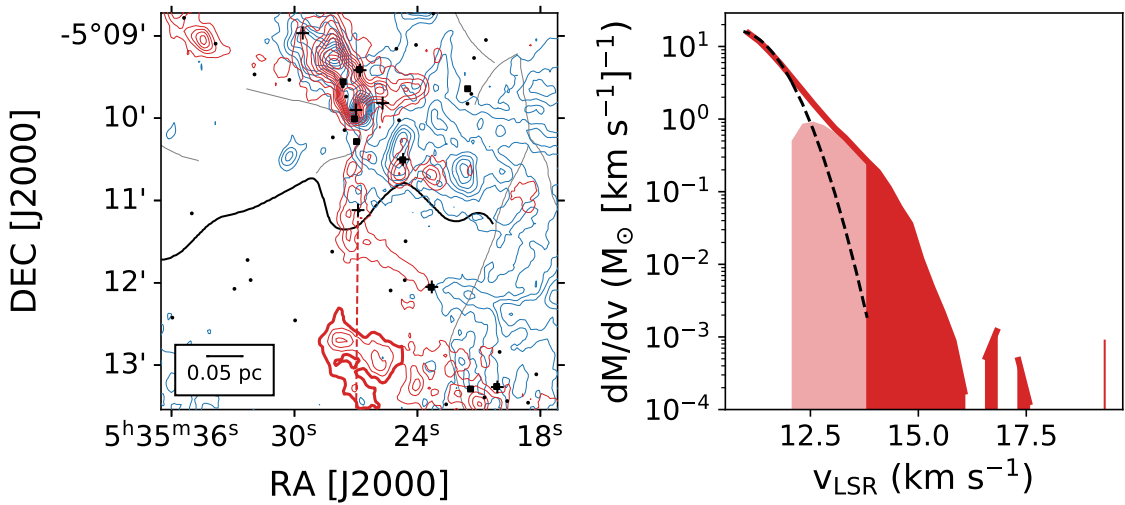


Figure 4.12 SMZ 21 outflow. The left panel shows the outflow, position angle, nearby sources, and filaments. The velocity range of integration is given by  $v_{\text{blue}}/v_{\text{red}}$  in Table 4.1 and the contours go from 5 to  $50\sigma$  in steps of  $5\sigma$ . Symbols are the same as Figure 4.2. The right panel shows the mass spectrum with fit. Symbols are the same as Figure 4.6.

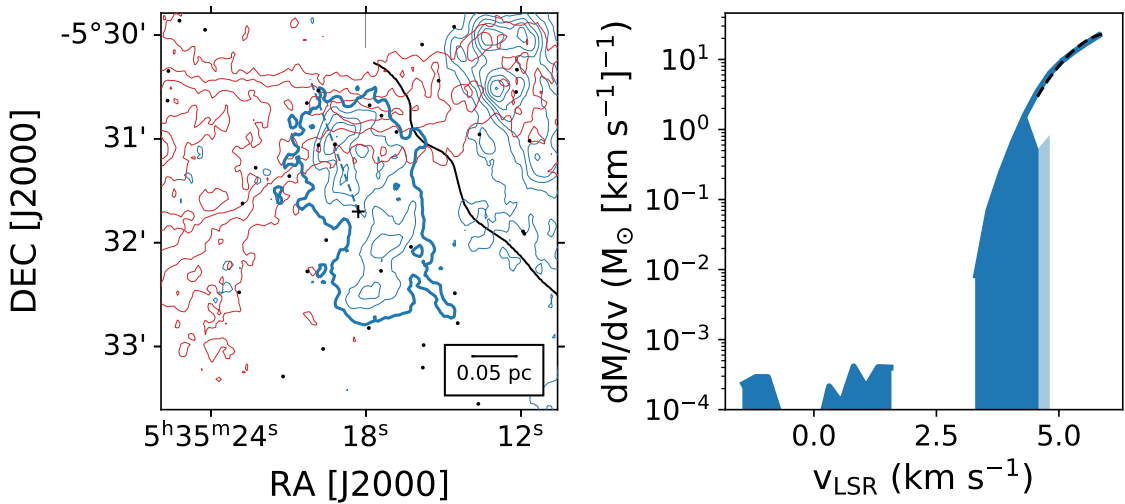


Figure 4.12 SMZ 30 outflow. The left panel shows the outflow, position angle, nearby sources, and filaments. The velocity range of integration is given by  $v_{\text{blue}}/v_{\text{red}}$  in Table 4.1 and the contours go from 5 to  $50\sigma$  in steps of  $5\sigma$ . Symbols are the same as Figure 4.2. The right panel shows the mass spectrum with fit. Symbols are the same as Figure 4.6.

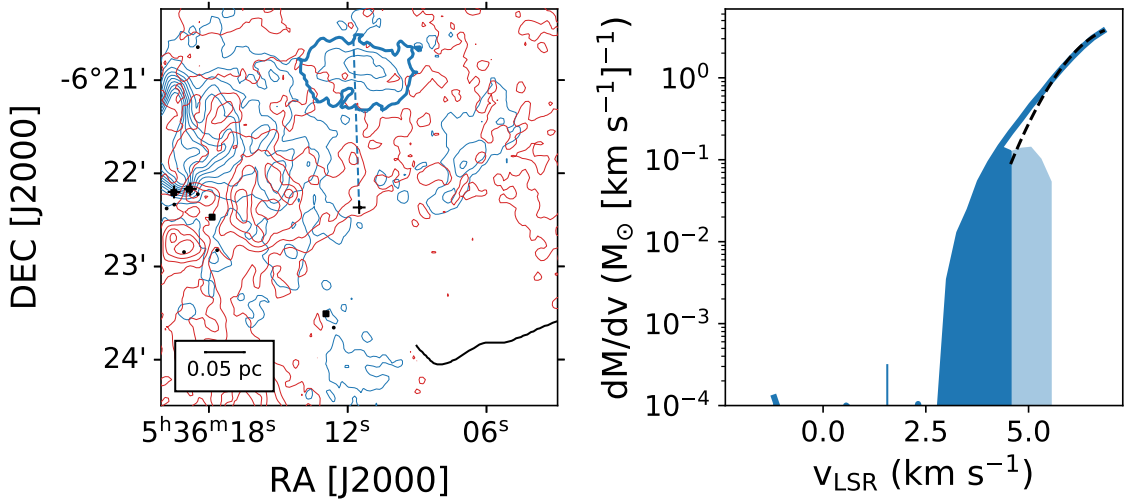


Figure 4.12 SMZ 50 outflow. The left panel shows the outflow, position angle, nearby sources, and filaments. The velocity range of integration is given by  $v_{\text{blue}}/v_{\text{red}}$  in Table 4.1 and the contours go from 5 to  $50\sigma$  in steps of  $5\sigma$ . Symbols are the same as Figure 4.2. The right panel shows the mass spectrum with fit. Symbols are the same as Figure 4.6.

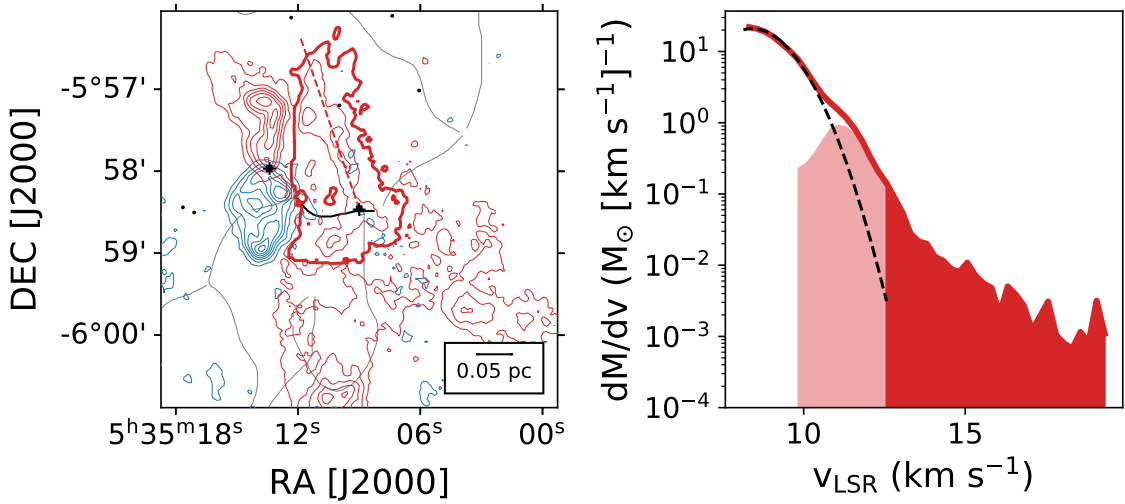


Figure 4.12 HOPS 10 outflow. The left panel shows the outflow, position angle, nearby sources, and filaments. The velocity range of integration is given by  $v_{\text{blue}}/v_{\text{red}}$  in Table 4.1 and the contours go from 5 to  $50\sigma$  in steps of  $5\sigma$ . Symbols are the same as Figure 4.2. The right panel shows the mass spectrum with fit. Symbols are the same as Figure 4.6.

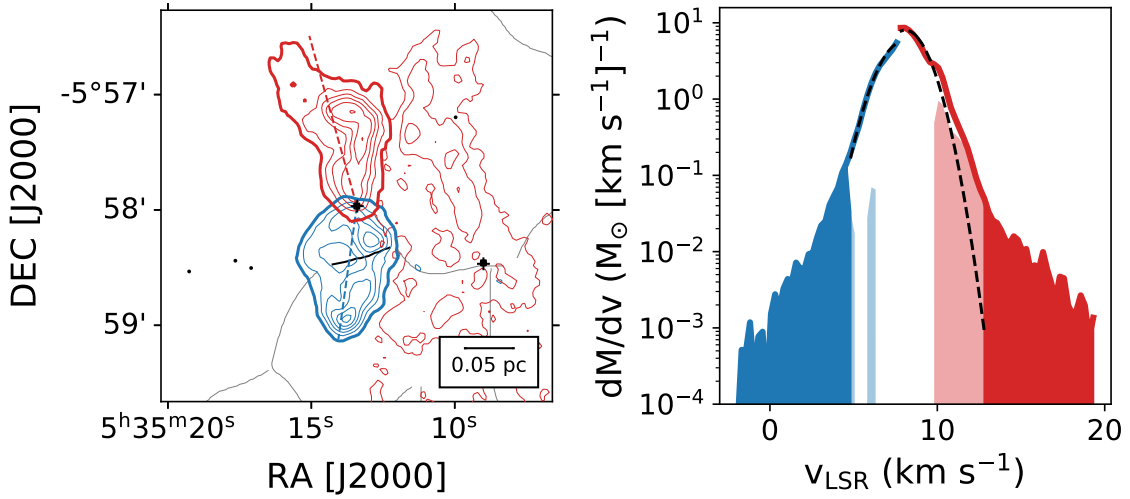


Figure 4.12 HOPS 11 outflow. The left panel shows the outflow, position angle, nearby sources, and filaments. The velocity range of integration is given by  $v_{\text{blue}}/v_{\text{red}}$  in Table 4.1 and the contours go from 5 to  $50\sigma$  in steps of  $5\sigma$ . Symbols are the same as Figure 4.2. The right panel shows the mass spectrum with fit. Symbols are the same as Figure 4.6.

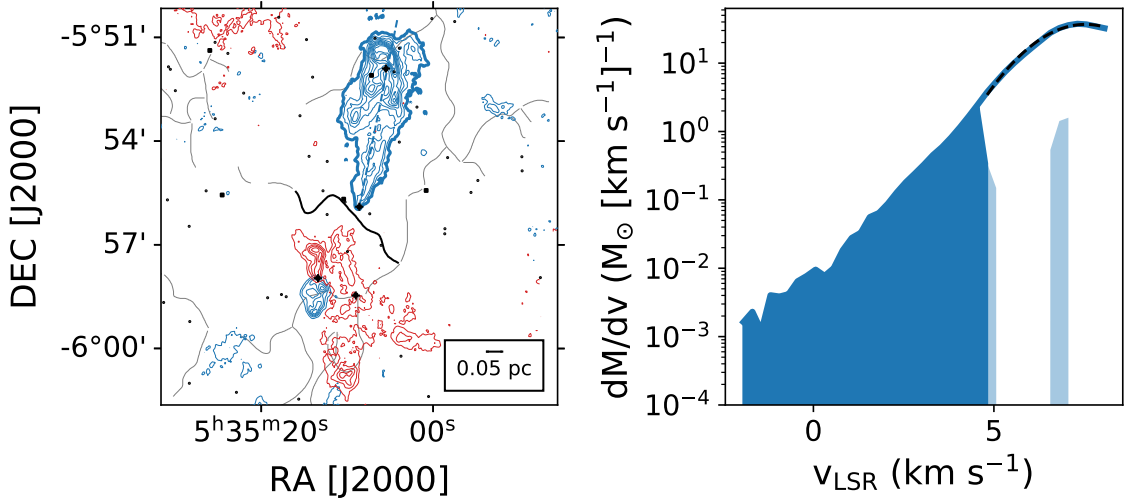


Figure 4.12 HOPS 12 outflow. The left panel shows the outflow, position angle, nearby sources, and filaments. The velocity range of integration is given by  $v_{\text{blue}}/v_{\text{red}}$  in Table 4.1 and the contours go from 5 to  $50\sigma$  in steps of  $5\sigma$ . Symbols are the same as Figure 4.2. The right panel shows the mass spectrum with fit. Symbols are the same as Figure 4.6.

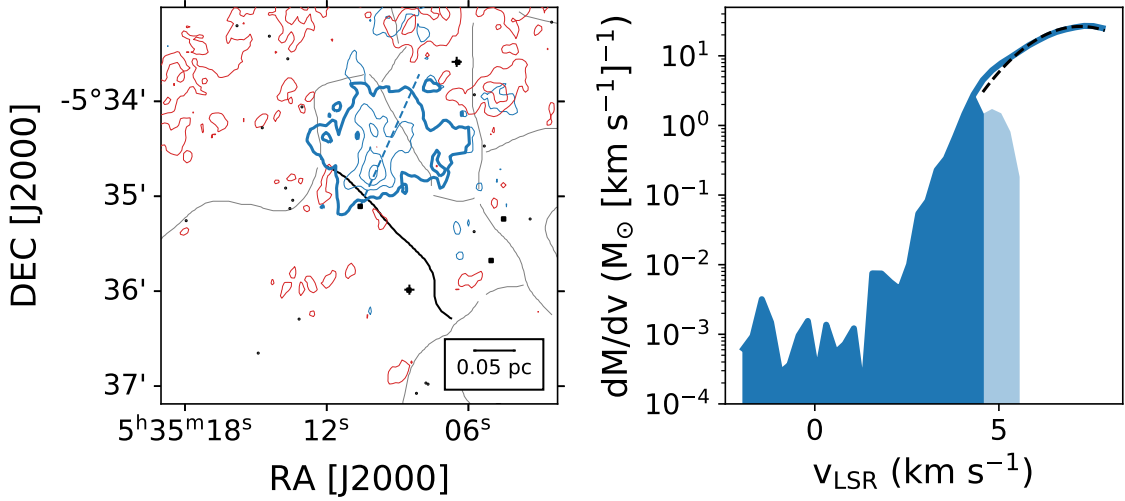


Figure 4.12 HOPS 44 outflow. The left panel shows the outflow, position angle, nearby sources, and filaments. The velocity range of integration is given by  $v_{\text{blue}}/v_{\text{red}}$  in Table 4.1 and the contours go from 5 to  $50\sigma$  in steps of  $5\sigma$ . Symbols are the same as Figure 4.2. The right panel shows the mass spectrum with fit. Symbols are the same as Figure 4.6.

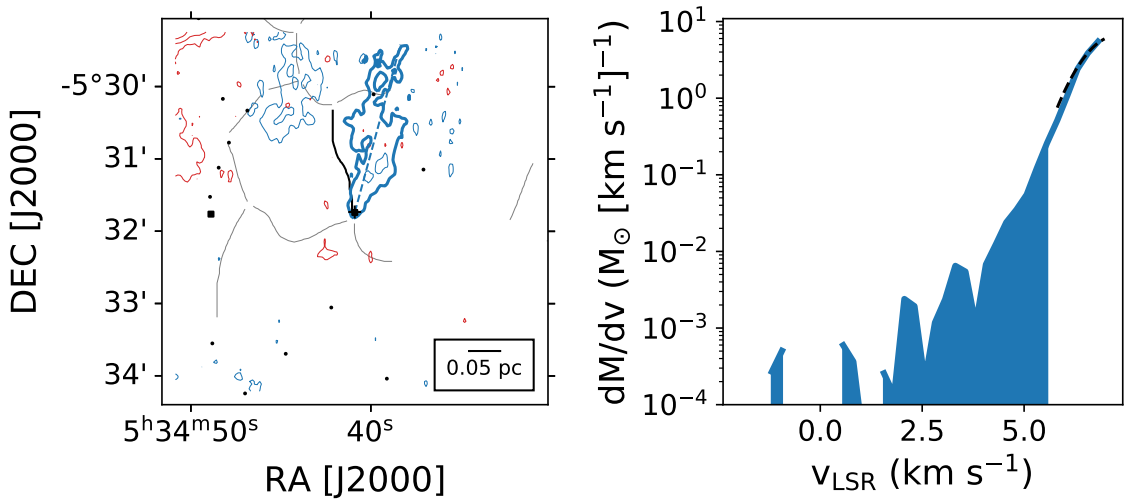


Figure 4.12 HOPS 50 outflow. The left panel shows the outflow, position angle, nearby sources, and filaments. The velocity range of integration is given by  $v_{\text{blue}}/v_{\text{red}}$  in Table 4.1 and the contours go from 5 to  $50\sigma$  in steps of  $5\sigma$ . Symbols are the same as Figure 4.2. The right panel shows the mass spectrum with fit. Symbols are the same as Figure 4.6.

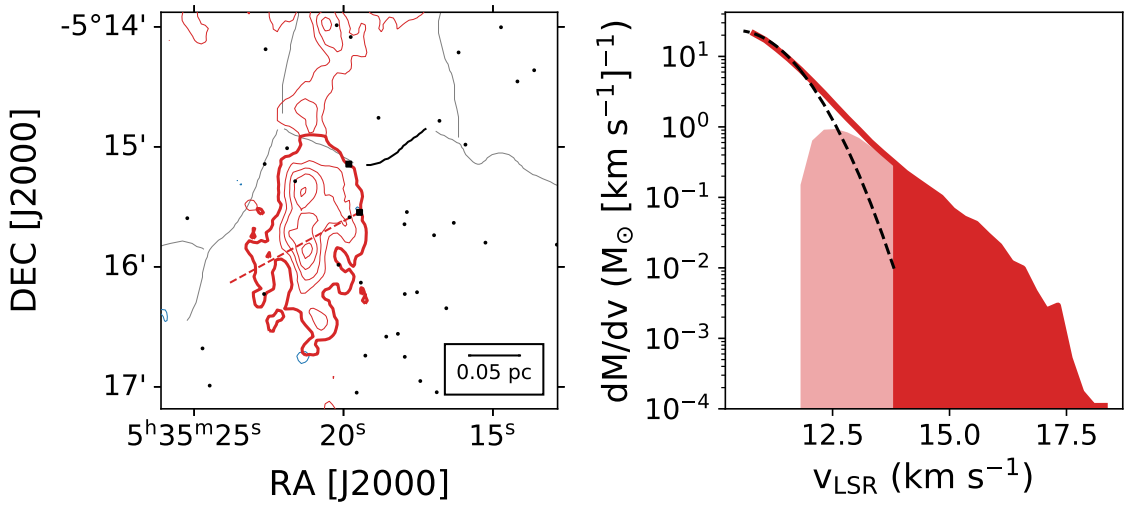


Figure 4.12 HOPS 56 outflow. The left panel shows the outflow, position angle, nearby sources, and filaments. The velocity range of integration is given by  $v_{\text{blue}}/v_{\text{red}}$  in Table 4.1 and the contours go from 5 to  $50\sigma$  in steps of  $5\sigma$ . Symbols are the same as Figure 4.2. The right panel shows the mass spectrum with fit. Symbols are the same as Figure 4.6.

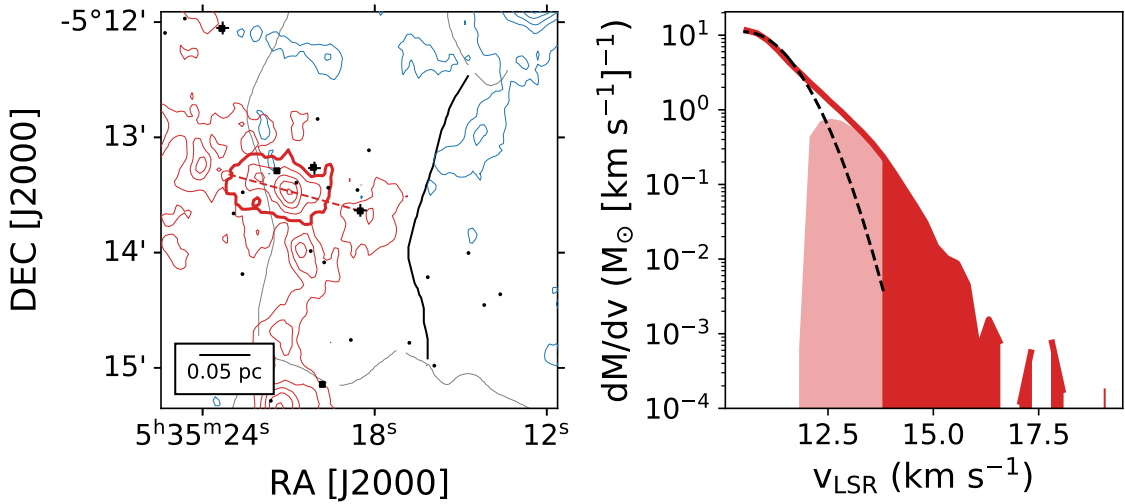


Figure 4.12 HOPS 58 outflow. The left panel shows the outflow, position angle, nearby sources, and filaments. The velocity range of integration is given by  $v_{\text{blue}}/v_{\text{red}}$  in Table 4.1 and the contours go from 5 to  $50\sigma$  in steps of  $5\sigma$ . Symbols are the same as Figure 4.2. The right panel shows the mass spectrum with fit. Symbols are the same as Figure 4.6.

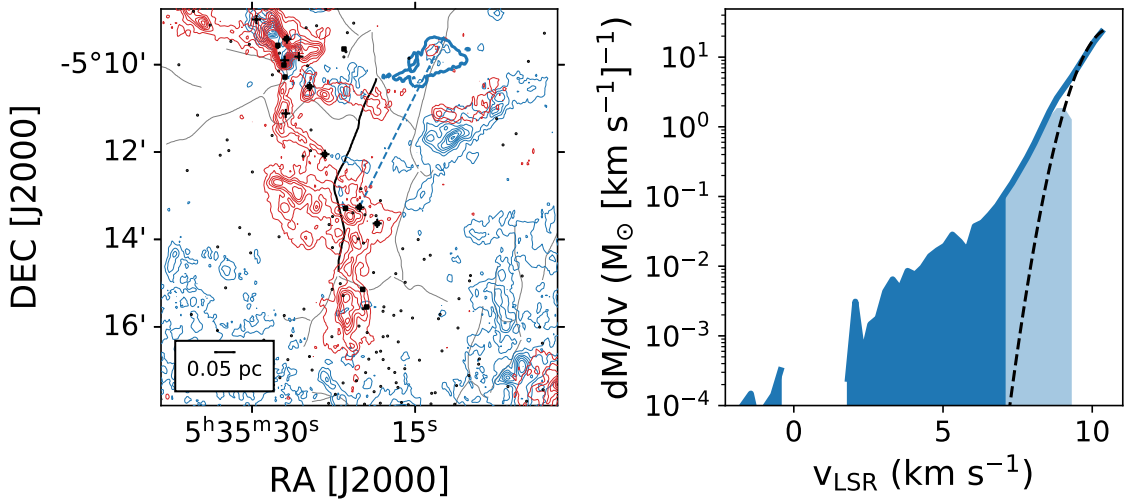


Figure 4.12 HOPS 59 outflow. The left panel shows the outflow, position angle, nearby sources, and filaments. The velocity range of integration is given by  $v_{\text{blue}}/v_{\text{red}}$  in Table 4.1 and the contours go from 5 to  $50\sigma$  in steps of  $5\sigma$ . Symbols are the same as Figure 4.2. The right panel shows the mass spectrum with fit. Symbols are the same as Figure 4.6.

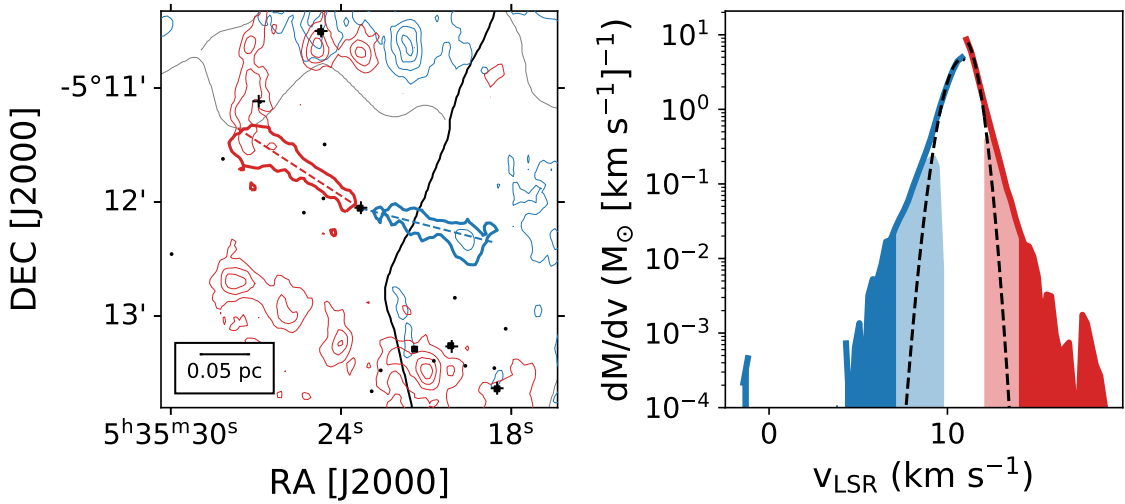


Figure 4.12 HOPS 60 outflow. The left panel shows the outflow, position angle, nearby sources, and filaments. The velocity range of integration is given by  $v_{\text{blue}}/v_{\text{red}}$  in Table 4.1 and the contours go from 5 to  $50\sigma$  in steps of  $5\sigma$ . Symbols are the same as Figure 4.2. The right panel shows the mass spectrum with fit. Symbols are the same as Figure 4.6.

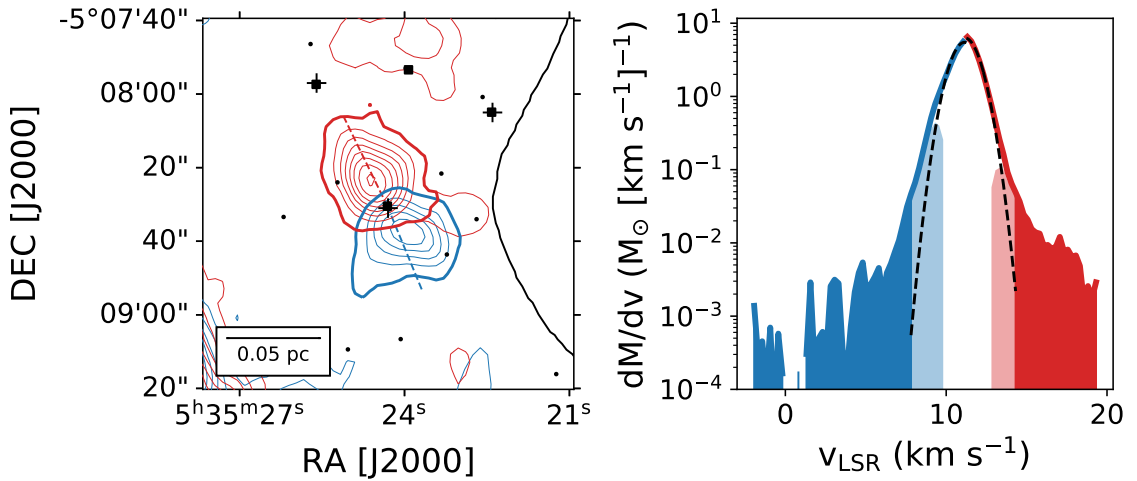


Figure 4.12 HOPS 68 outflow. The left panel shows the outflow, position angle, nearby sources, and filaments. The velocity range of integration is given by  $v_{\text{blue}}/v_{\text{red}}$  in Table 4.1 and the contours go from 5 to  $50\sigma$  in steps of  $5\sigma$ . Symbols are the same as Figure 4.2. The right panel shows the mass spectrum with fit. Symbols are the same as Figure 4.6.

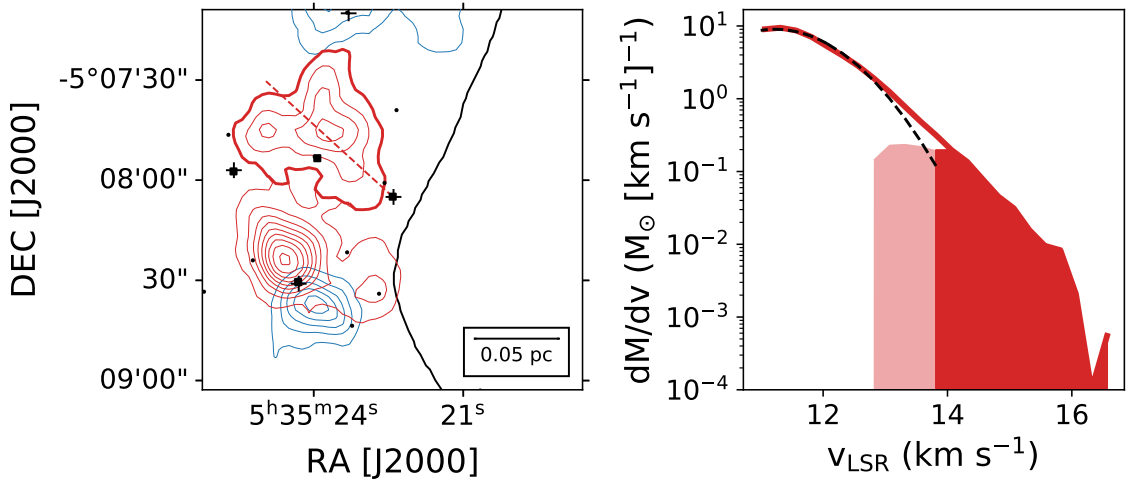


Figure 4.12 HOPS 70 outflow. The left panel shows the outflow, position angle, nearby sources, and filaments. The velocity range of integration is given by  $v_{\text{blue}}/v_{\text{red}}$  in Table 4.1 and the contours go from 5 to  $50\sigma$  in steps of  $5\sigma$ . Symbols are the same as Figure 4.2. The right panel shows the mass spectrum with fit. Symbols are the same as Figure 4.6.

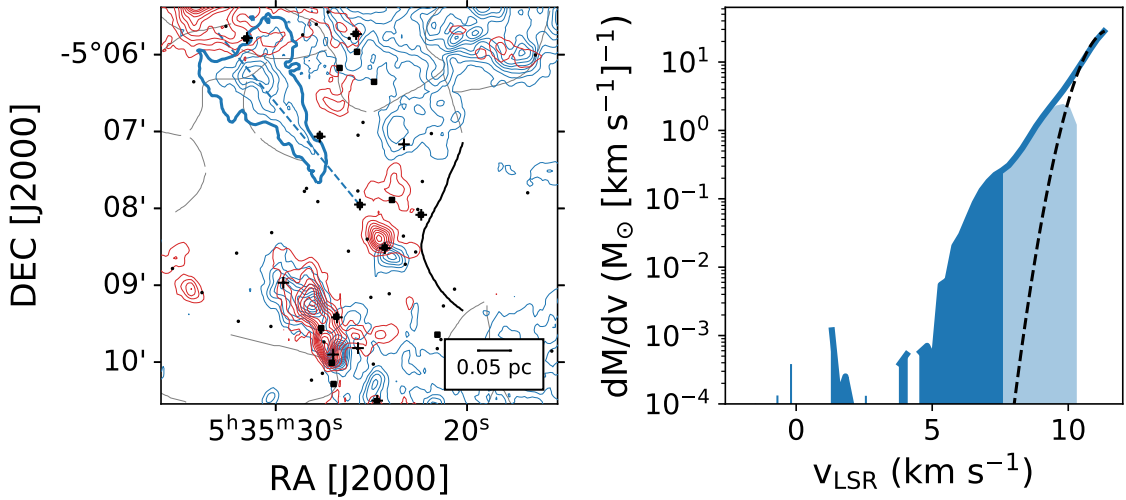


Figure 4.12 HOPS 71 outflow. The left panel shows the outflow, position angle, nearby sources, and filaments. The velocity range of integration is given by  $v_{\text{blue}}/v_{\text{red}}$  in Table 4.1 and the contours go from 5 to  $50\sigma$  in steps of  $5\sigma$ . Symbols are the same as Figure 4.2. The right panel shows the mass spectrum with fit. Symbols are the same as Figure 4.6.

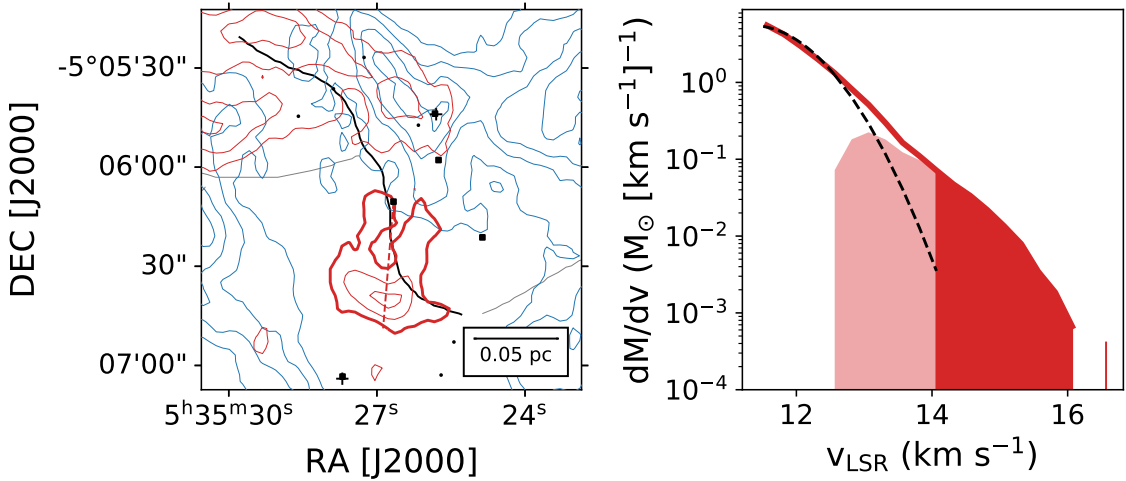


Figure 4.12 HOPS 75 outflow. The left panel shows the outflow, position angle, nearby sources, and filaments. The velocity range of integration is given by  $v_{\text{blue}}/v_{\text{red}}$  in Table 4.1 and the contours go from 5 to  $50\sigma$  in steps of  $5\sigma$ . Symbols are the same as Figure 4.2. The right panel shows the mass spectrum with fit. Symbols are the same as Figure 4.6.

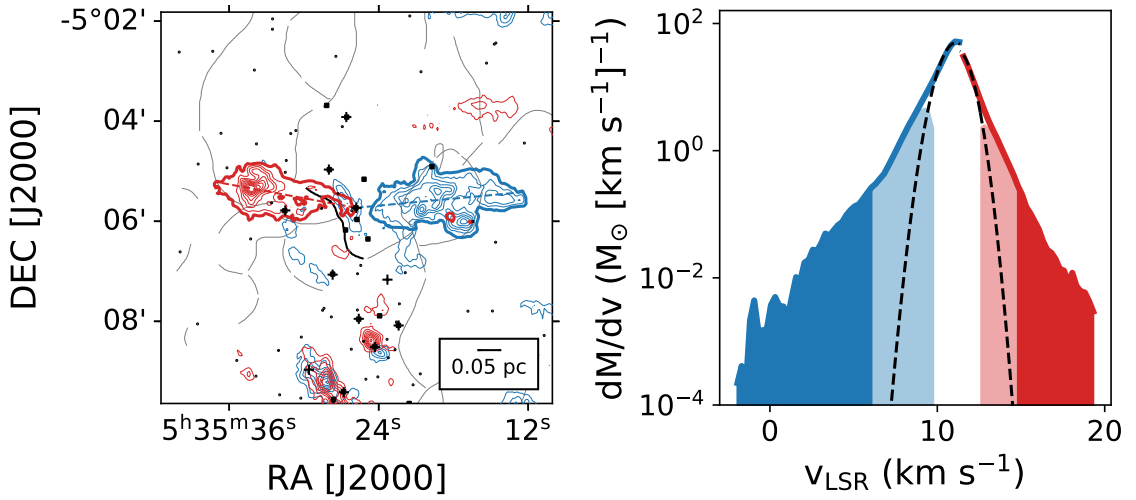


Figure 4.12 HOPS 78 outflow. The left panel shows the outflow, position angle, nearby sources, and filaments. The velocity range of integration is given by  $v_{\text{blue}}/v_{\text{red}}$  in Table 4.1 and the contours go from 5 to  $50\sigma$  in steps of  $5\sigma$ . Symbols are the same as Figure 4.2. The right panel shows the mass spectrum with fit. Symbols are the same as Figure 4.6.

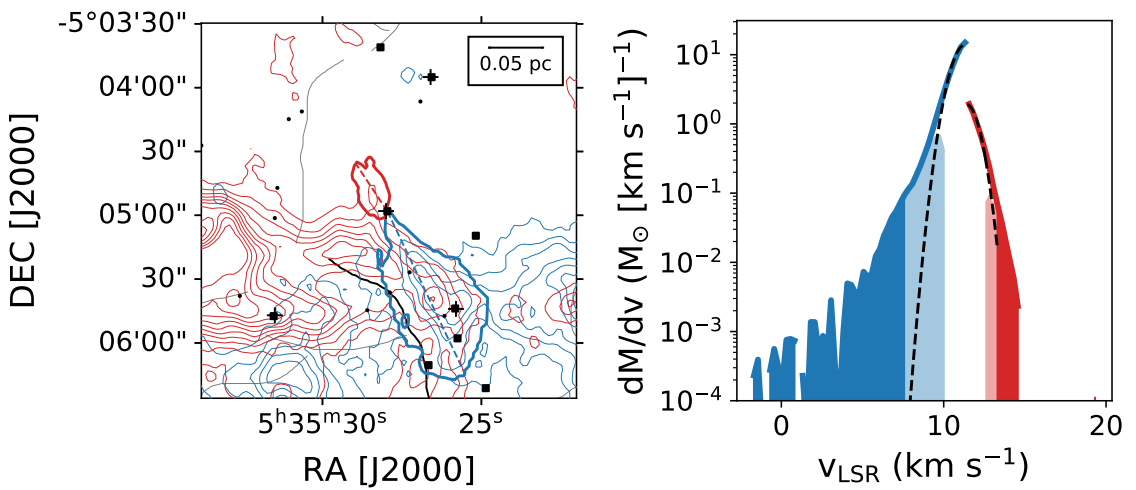


Figure 4.12 HOPS 81 outflow. The left panel shows the outflow, position angle, nearby sources, and filaments. The velocity range of integration is given by  $v_{\text{blue}}/v_{\text{red}}$  in Table 4.1 and the contours go from 5 to  $50\sigma$  in steps of  $5\sigma$ . Symbols are the same as Figure 4.2. The right panel shows the mass spectrum with fit. Symbols are the same as Figure 4.6.

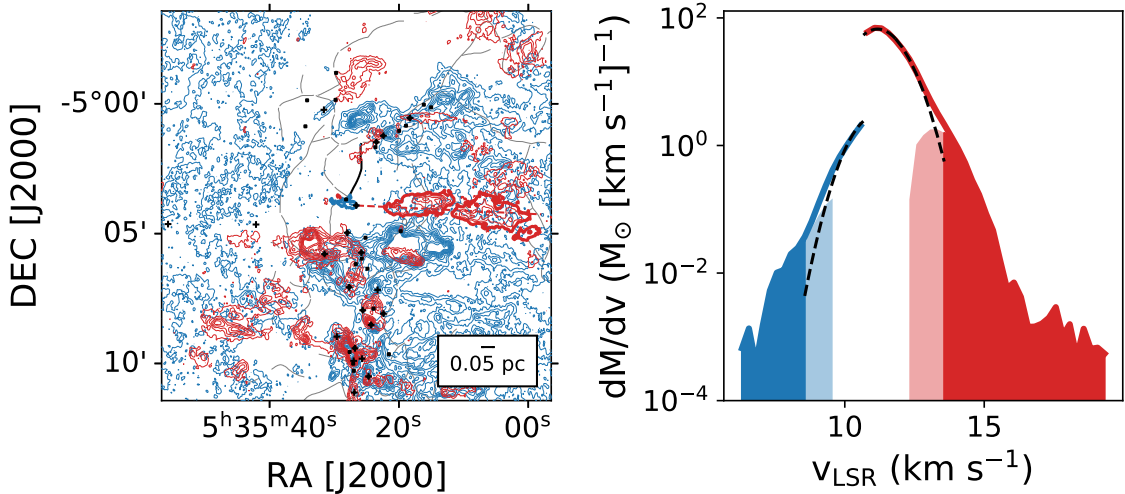


Figure 4.12 HOPS 84 outflow. The left panel shows the outflow, position angle, nearby sources, and filaments. The velocity range of integration is given by  $v_{\text{blue}}/v_{\text{red}}$  in Table 4.1 and the contours go from 5 to  $50\sigma$  in steps of  $5\sigma$ . Symbols are the same as Figure 4.2. The right panel shows the mass spectrum with fit. Symbols are the same as Figure 4.6.

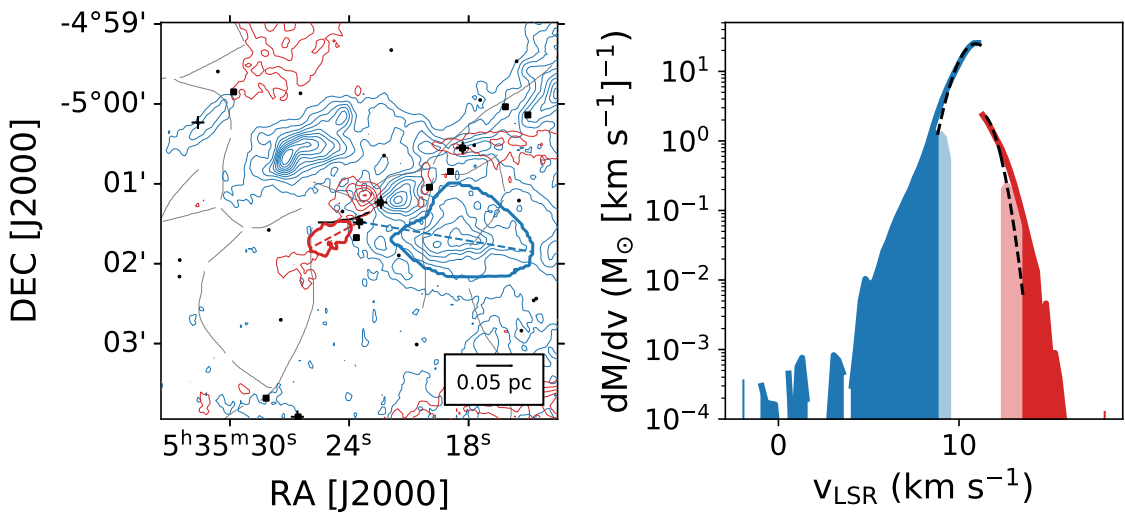


Figure 4.12 HOPS 87 outflow. The left panel shows the outflow, position angle, nearby sources, and filaments. The velocity range of integration is given by  $v_{\text{blue}}/v_{\text{red}}$  in Table 4.1 and the contours go from 5 to  $50\sigma$  in steps of  $5\sigma$ . Symbols are the same as Figure 4.2. The right panel shows the mass spectrum with fit. Symbols are the same as Figure 4.6.

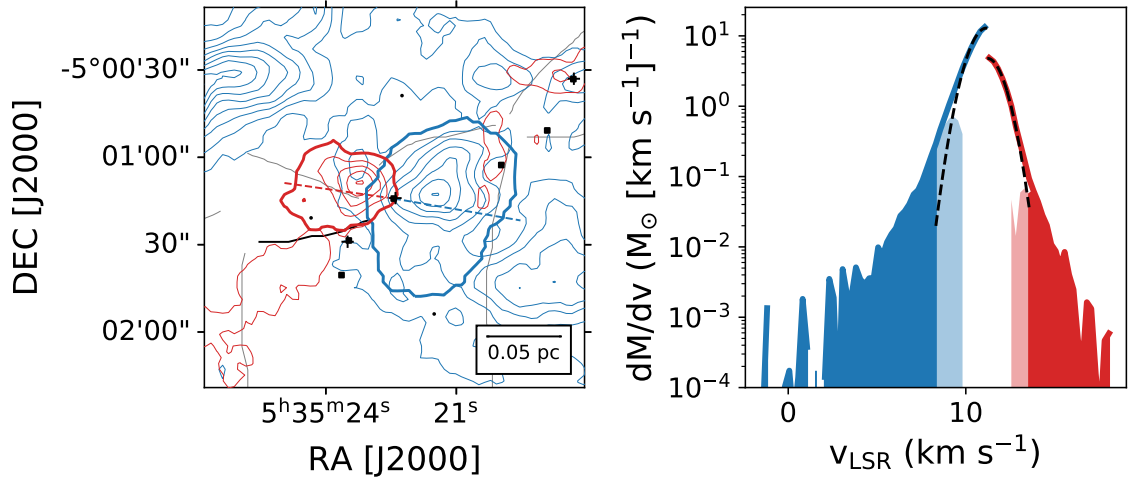


Figure 4.12 HOPS 88 outflow. The left panel shows the outflow, position angle, nearby sources, and filaments. The velocity range of integration is given by  $v_{\text{blue}}/v_{\text{red}}$  in Table 4.1 and the contours go from 5 to  $50\sigma$  in steps of  $5\sigma$ . Symbols are the same as Figure 4.2. The right panel shows the mass spectrum with fit. Symbols are the same as Figure 4.6.

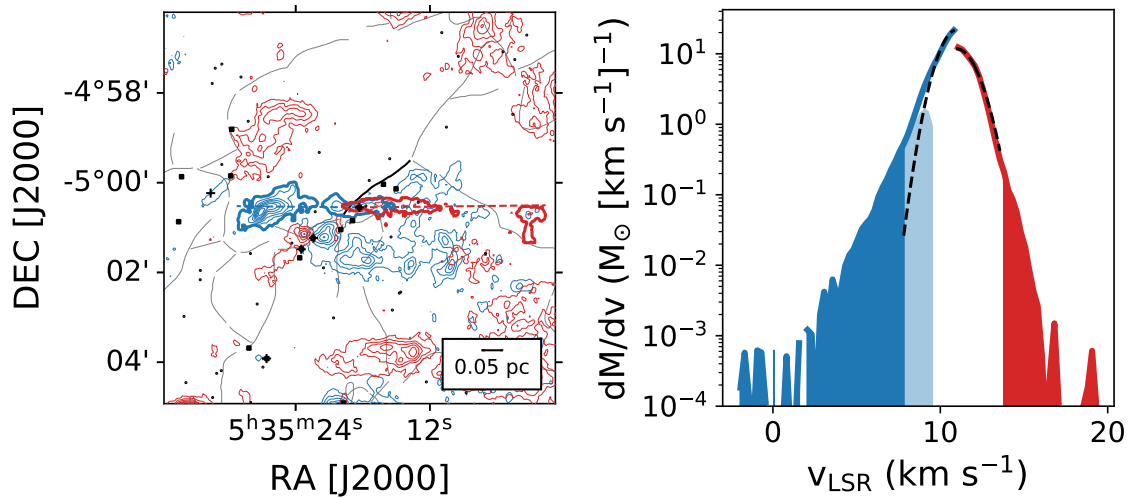


Figure 4.12 HOPS 92 outflow. The left panel shows the outflow, position angle, nearby sources, and filaments. The velocity range of integration is given by  $v_{\text{blue}}/v_{\text{red}}$  in Table 4.1 and the contours go from 5 to  $50\sigma$  in steps of  $5\sigma$ . Symbols are the same as Figure 4.2. The right panel shows the mass spectrum with fit. Symbols are the same as Figure 4.6.

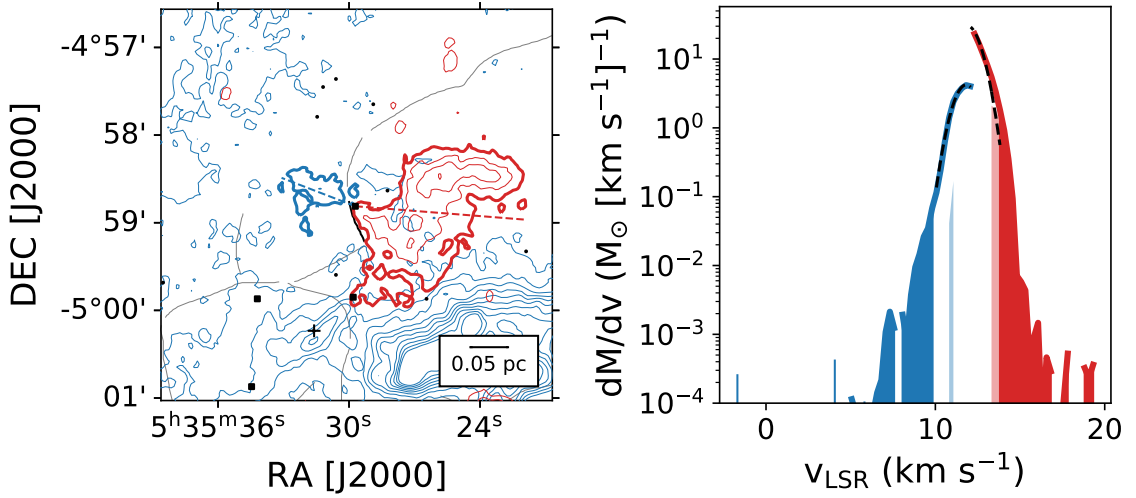


Figure 4.12 HOPS 96 outflow. The left panel shows the outflow, position angle, nearby sources, and filaments. The velocity range of integration is given by  $v_{\text{blue}}/v_{\text{red}}$  in Table 4.1 and the contours go from 5 to  $50\sigma$  in steps of  $5\sigma$ . Symbols are the same as Figure 4.2. The right panel shows the mass spectrum with fit. Symbols are the same as Figure 4.6.

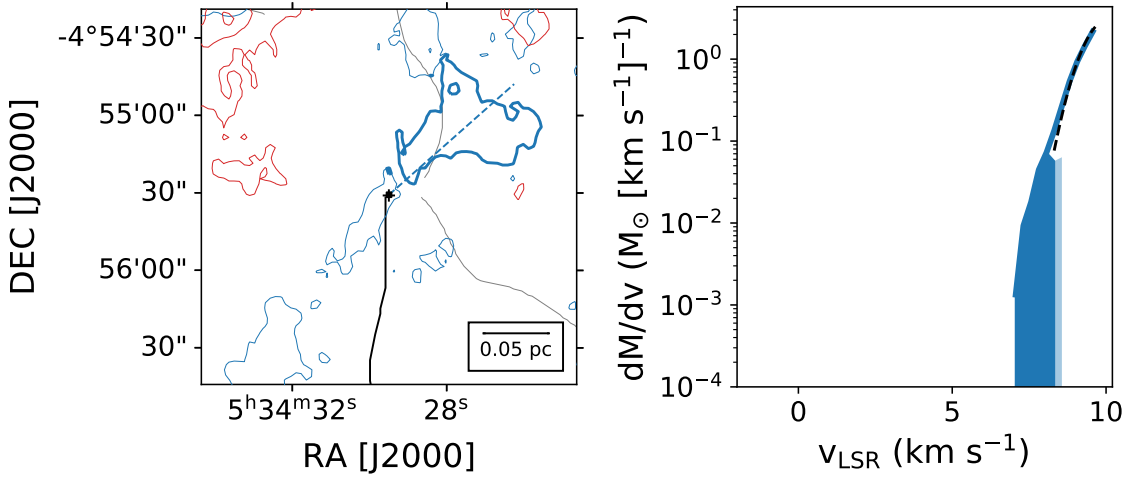


Figure 4.12 HOPS 99 outflow. The left panel shows the outflow, position angle, nearby sources, and filaments. The velocity range of integration is given by  $v_{\text{blue}}/v_{\text{red}}$  in Table 4.1 and the contours go from 5 to  $50\sigma$  in steps of  $5\sigma$ . Symbols are the same as Figure 4.2. The right panel shows the mass spectrum with fit. Symbols are the same as Figure 4.6.

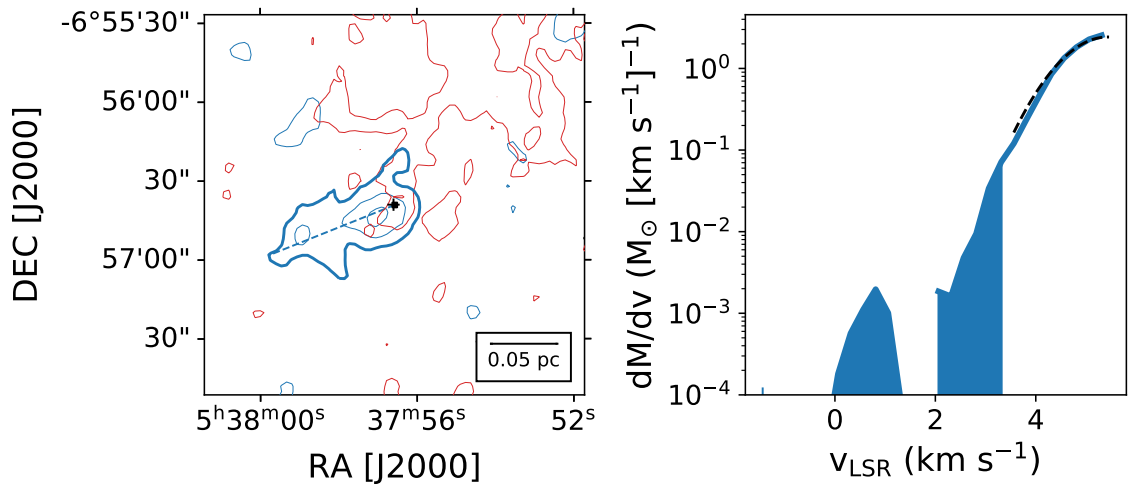


Figure 4.12 HOPS 157 outflow. The left panel shows the outflow, position angle, nearby sources, and filaments. The velocity range of integration is given by  $v_{\text{blue}}/v_{\text{red}}$  in Table 4.1 and the contours go from 5 to  $50\sigma$  in steps of  $5\sigma$ . Symbols are the same as Figure 4.2. The right panel shows the mass spectrum with fit. Symbols are the same as Figure 4.6.

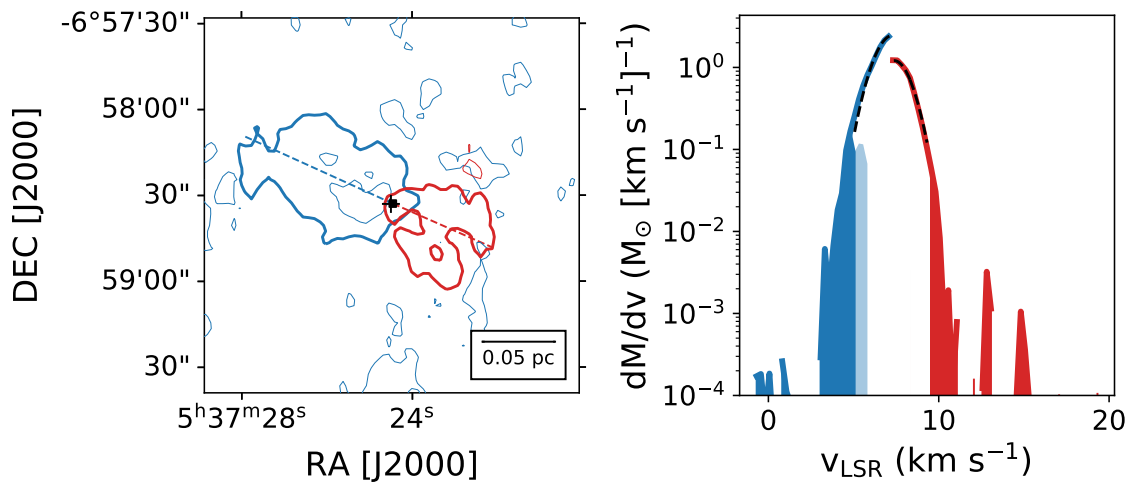


Figure 4.12 HOPS 158 outflow. The left panel shows the outflow, position angle, nearby sources, and filaments. The velocity range of integration is given by  $v_{\text{blue}}/v_{\text{red}}$  in Table 4.1 and the contours go from 5 to  $50\sigma$  in steps of  $5\sigma$ . Symbols are the same as Figure 4.2. The right panel shows the mass spectrum with fit. Symbols are the same as Figure 4.6.

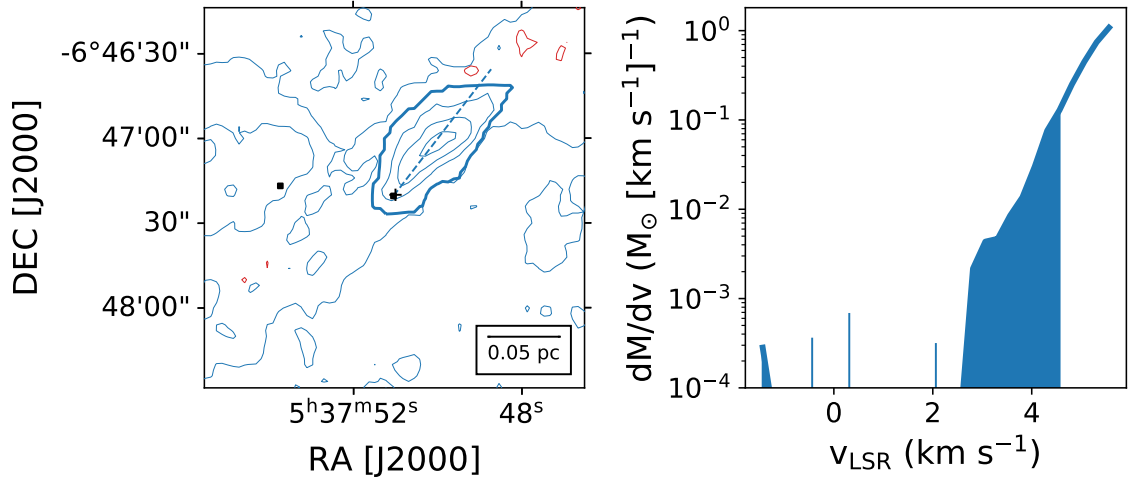


Figure 4.12 HOPS 160 outflow. The left panel shows the outflow, position angle, nearby sources, and filaments. The velocity range of integration is given by  $v_{\text{blue}}/v_{\text{red}}$  in Table 4.1 and the contours go from 5 to  $50\sigma$  in steps of  $5\sigma$ . Symbols are the same as Figure 4.2. The right panel shows the mass spectrum with fit. Symbols are the same as Figure 4.6.

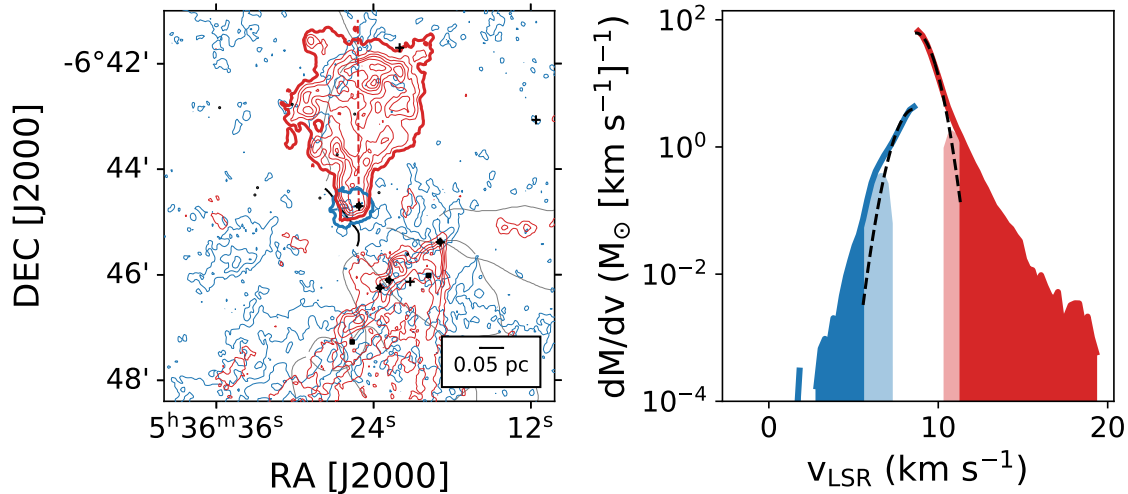


Figure 4.12 HOPS 166 outflow. The left panel shows the outflow, position angle, nearby sources, and filaments. The velocity range of integration is given by  $v_{\text{blue}}/v_{\text{red}}$  in Table 4.1 and the contours go from 5 to  $50\sigma$  in steps of  $5\sigma$ . Symbols are the same as Figure 4.2. The right panel shows the mass spectrum with fit. Symbols are the same as Figure 4.6.

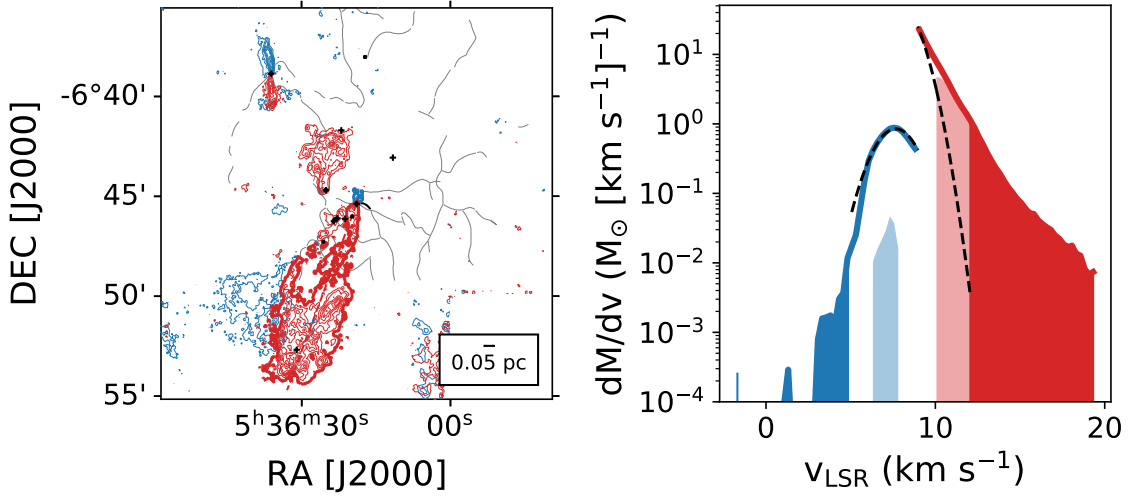


Figure 4.12 HOPS 168 outflow. The left panel shows the outflow, position angle, nearby sources, and filaments. The velocity range of integration is given by  $v_{\text{blue}}/v_{\text{red}}$  in Table 4.1 and the contours go from 5 to  $50\sigma$  in steps of  $5\sigma$ . Symbols are the same as Figure 4.2. The right panel shows the mass spectrum with fit. Symbols are the same as Figure 4.6.

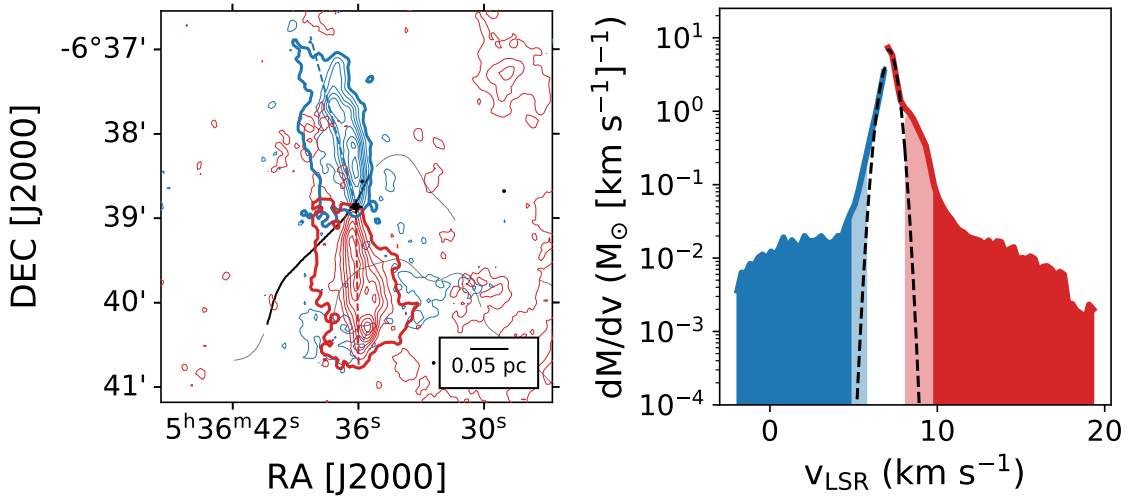


Figure 4.12 HOPS 169 outflow. The left panel shows the outflow, position angle, nearby sources, and filaments. The velocity range of integration is given by  $v_{\text{blue}}/v_{\text{red}}$  in Table 4.1 and the contours go from 5 to  $50\sigma$  in steps of  $5\sigma$ . Symbols are the same as Figure 4.2. The right panel shows the mass spectrum with fit. Symbols are the same as Figure 4.6.

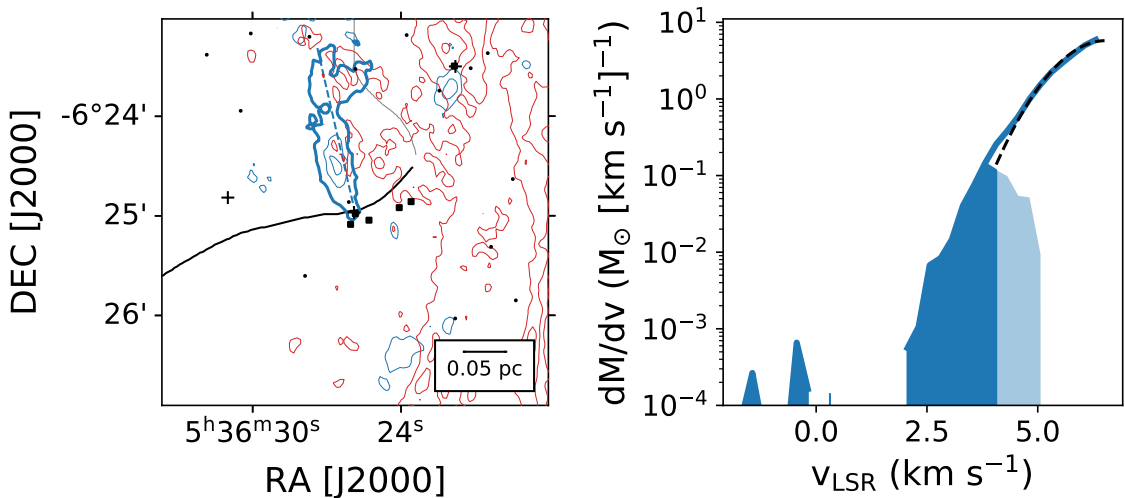


Figure 4.12 HOPS 174 outflow. The left panel shows the outflow, position angle, nearby sources, and filaments. The velocity range of integration is given by  $v_{\text{blue}}/v_{\text{red}}$  in Table 4.1 and the contours go from 5 to  $50\sigma$  in steps of  $5\sigma$ . Symbols are the same as Figure 4.2. The right panel shows the mass spectrum with fit. Symbols are the same as Figure 4.6.

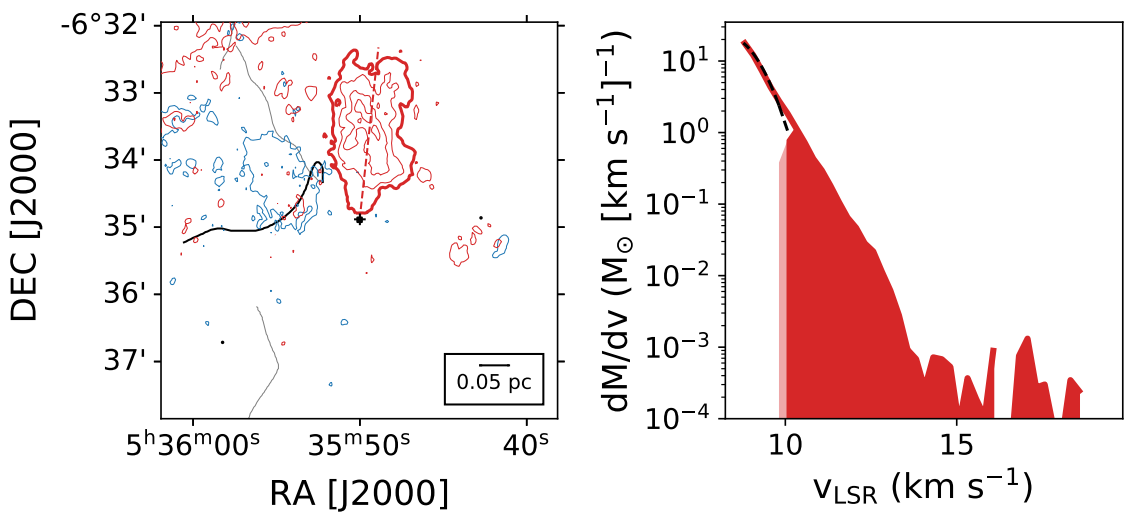


Figure 4.12 HOPS 177 outflow. The left panel shows the outflow, position angle, nearby sources, and filaments. The velocity range of integration is given by  $v_{\text{blue}}/v_{\text{red}}$  in Table 4.1 and the contours go from 5 to  $50\sigma$  in steps of  $5\sigma$ . Symbols are the same as Figure 4.2. The right panel shows the mass spectrum with fit. Symbols are the same as Figure 4.6.

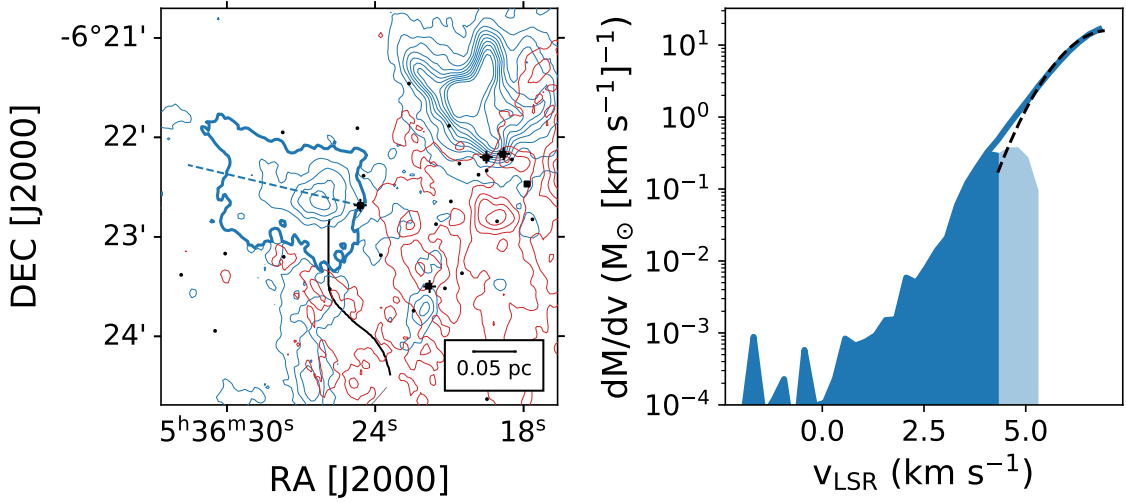


Figure 4.12 HOPS 178 outflow. The left panel shows the outflow, position angle, nearby sources, and filaments. The velocity range of integration is given by  $v_{\text{blue}}/v_{\text{red}}$  in Table 4.1 and the contours go from 5 to  $50\sigma$  in steps of  $5\sigma$ . Symbols are the same as Figure 4.2. The right panel shows the mass spectrum with fit. Symbols are the same as Figure 4.6.

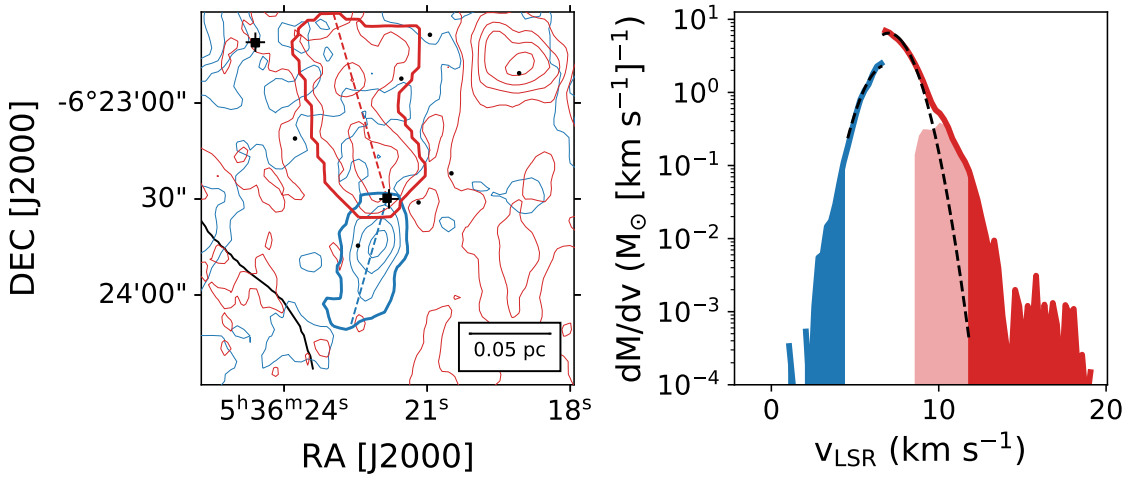


Figure 4.12 HOPS 179 outflow. The left panel shows the outflow, position angle, nearby sources, and filaments. The velocity range of integration is given by  $v_{\text{blue}}/v_{\text{red}}$  in Table 4.1 and the contours go from 5 to  $50\sigma$  in steps of  $5\sigma$ . Symbols are the same as Figure 4.2. The right panel shows the mass spectrum with fit. Symbols are the same as Figure 4.6.

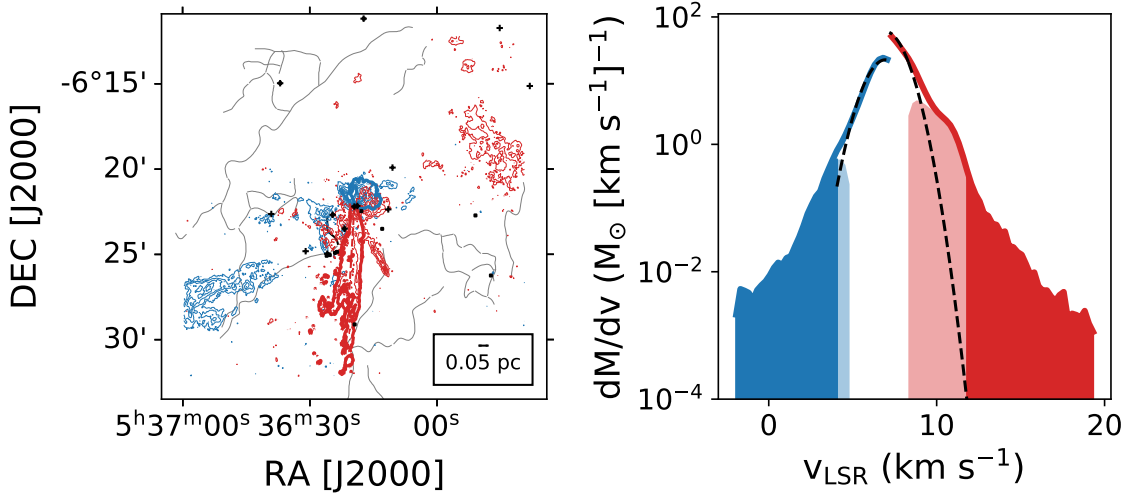


Figure 4.12 HOPS 181 outflow. The left panel shows the outflow, position angle, nearby sources, and filaments. The velocity range of integration is given by  $v_{\text{blue}}/v_{\text{red}}$  in Table 4.1 and the contours go from 5 to  $50\sigma$  in steps of  $5\sigma$ . Symbols are the same as Figure 4.2. The right panel shows the mass spectrum with fit. Symbols are the same as Figure 4.6.

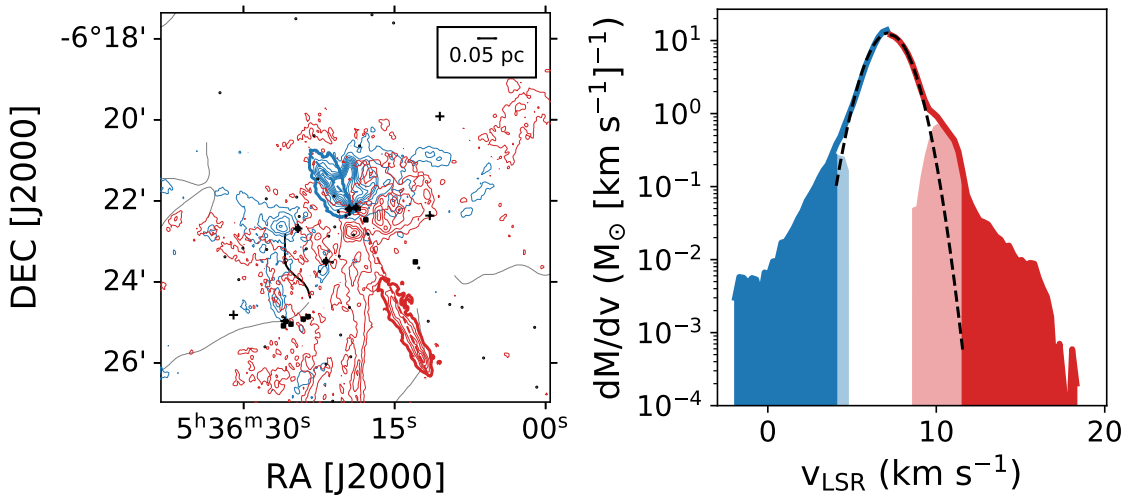


Figure 4.12 HOPS 182 outflow. The left panel shows the outflow, position angle, nearby sources, and filaments. The velocity range of integration is given by  $v_{\text{blue}}/v_{\text{red}}$  in Table 4.1 and the contours go from 5 to  $50\sigma$  in steps of  $5\sigma$ . Symbols are the same as Figure 4.2. The right panel shows the mass spectrum with fit. Symbols are the same as Figure 4.6.

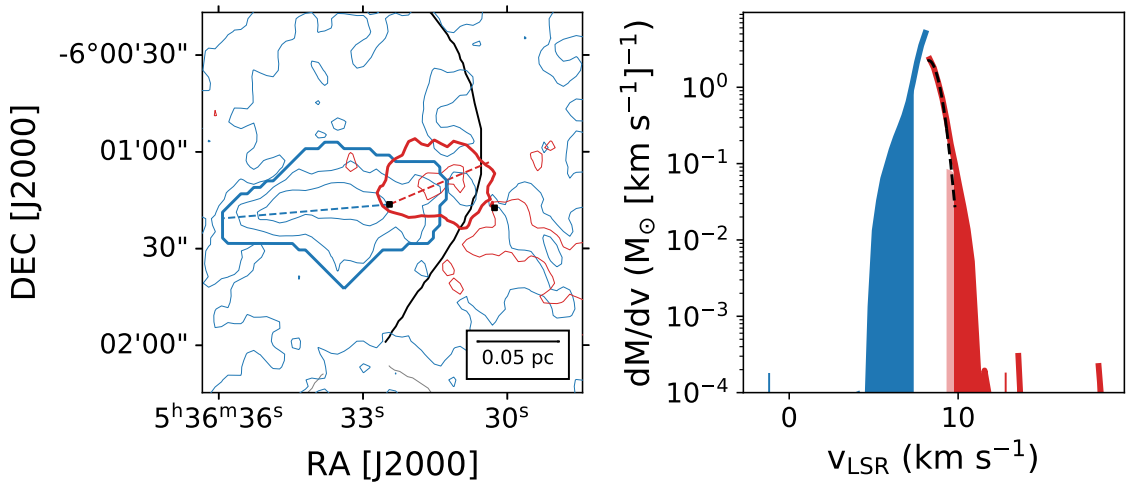


Figure 4.12 HOPS 192 outflow. The left panel shows the outflow, position angle, nearby sources, and filaments. The velocity range of integration is given by  $v_{\text{blue}}/v_{\text{red}}$  in Table 4.1 and the contours go from 5 to  $50\sigma$  in steps of  $5\sigma$ . Symbols are the same as Figure 4.2. The right panel shows the mass spectrum with fit. Symbols are the same as Figure 4.6.

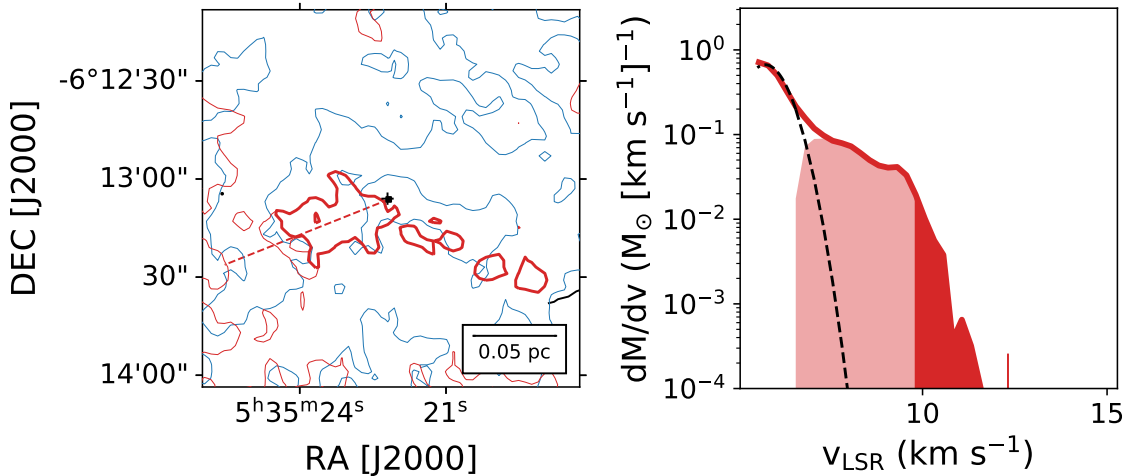


Figure 4.12 HOPS 198 outflow. The left panel shows the outflow, position angle, nearby sources, and filaments. The velocity range of integration is given by  $v_{\text{blue}}/v_{\text{red}}$  in Table 4.1 and the contours go from 5 to  $50\sigma$  in steps of  $5\sigma$ . Symbols are the same as Figure 4.2. The right panel shows the mass spectrum with fit. Symbols are the same as Figure 4.6.

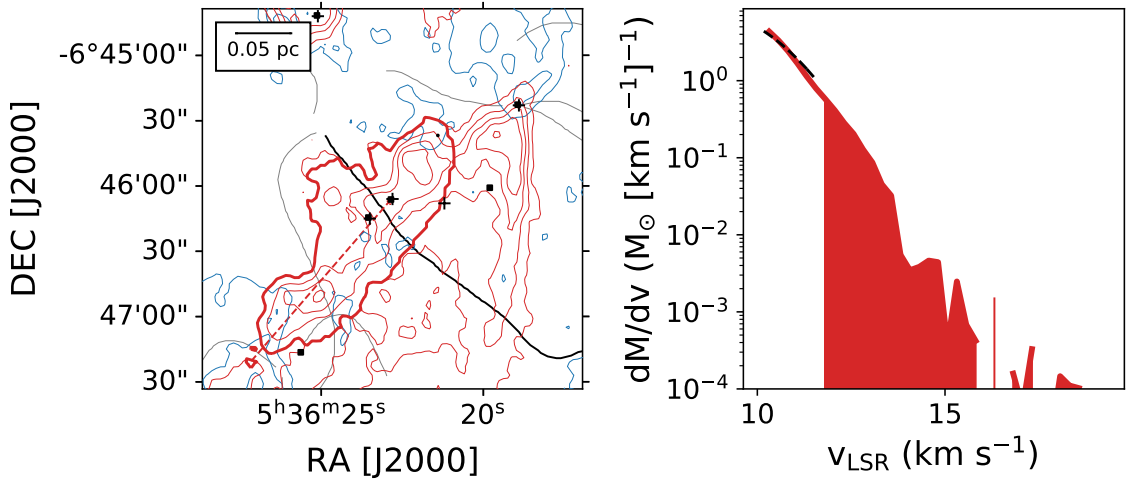


Figure 4.12 HOPS 203 outflow. The left panel shows the outflow, position angle, nearby sources, and filaments. The velocity range of integration is given by  $v_{\text{blue}}/v_{\text{red}}$  in Table 4.1 and the contours go from 5 to  $50\sigma$  in steps of  $5\sigma$ . Symbols are the same as Figure 4.2. The right panel shows the mass spectrum with fit. Symbols are the same as Figure 4.6.

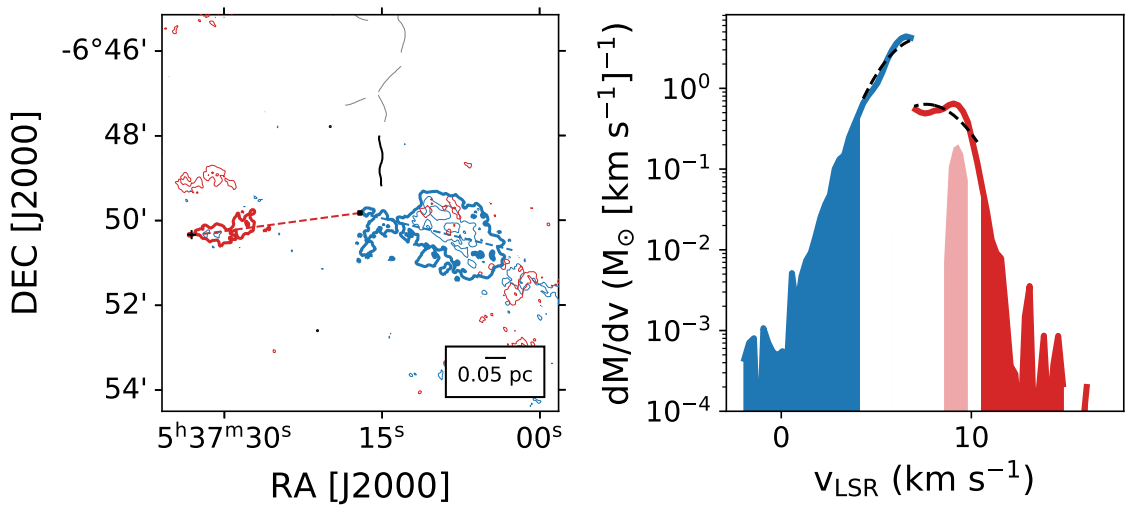


Figure 4.12 HOPS 355 outflow. The left panel shows the outflow, position angle, nearby sources, and filaments. The velocity range of integration is given by  $v_{\text{blue}}/v_{\text{red}}$  in Table 4.1 and the contours go from 5 to  $50\sigma$  in steps of  $5\sigma$ . Symbols are the same as Figure 4.2. The right panel shows the mass spectrum with fit. Symbols are the same as Figure 4.6.

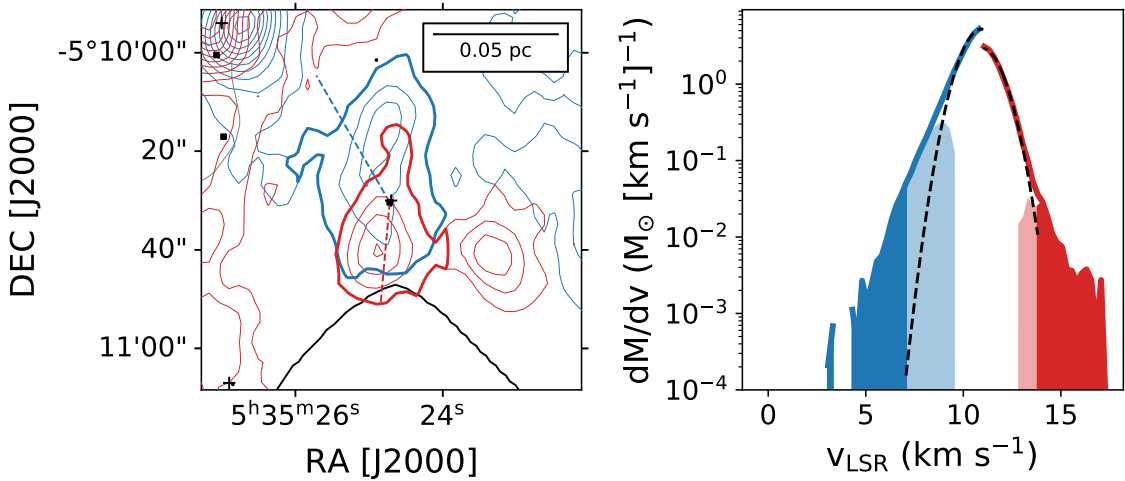


Figure 4.12 HOPS 368 outflow. The left panel shows the outflow, position angle, nearby sources, and filaments. The velocity range of integration is given by  $v_{\text{blue}}/v_{\text{red}}$  in Table 4.1 and the contours go from 5 to  $50\sigma$  in steps of  $5\sigma$ . Symbols are the same as Figure 4.2. The right panel shows the mass spectrum with fit. Symbols are the same as Figure 4.6.

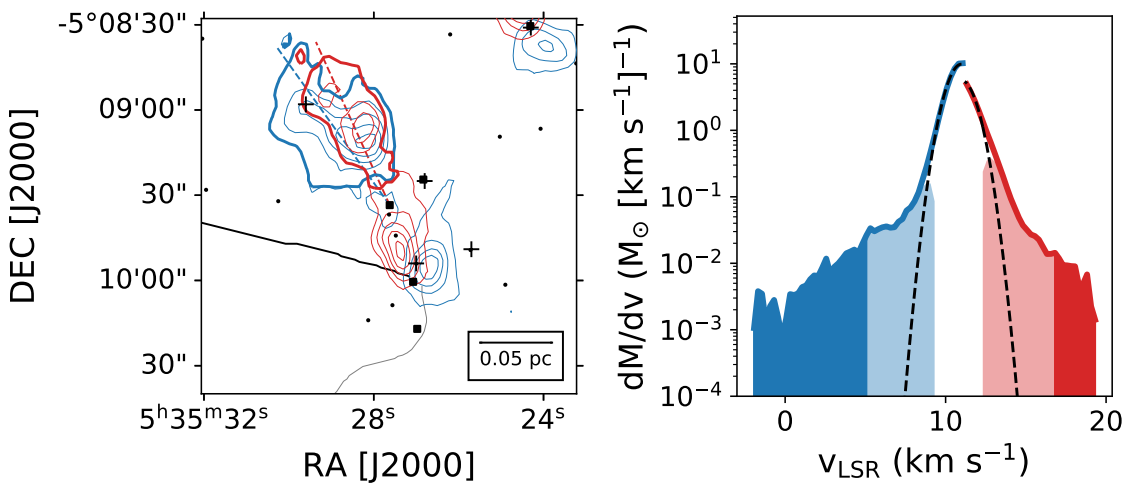


Figure 4.12 HOPS 370 outflow. The left panel shows the outflow, position angle, nearby sources, and filaments. The velocity range of integration is given by  $v_{\text{blue}}/v_{\text{red}}$  in Table 4.1 and the contours go from 5 to  $50\sigma$  in steps of  $5\sigma$ . Symbols are the same as Figure 4.2. The right panel shows the mass spectrum with fit. Symbols are the same as Figure 4.6.

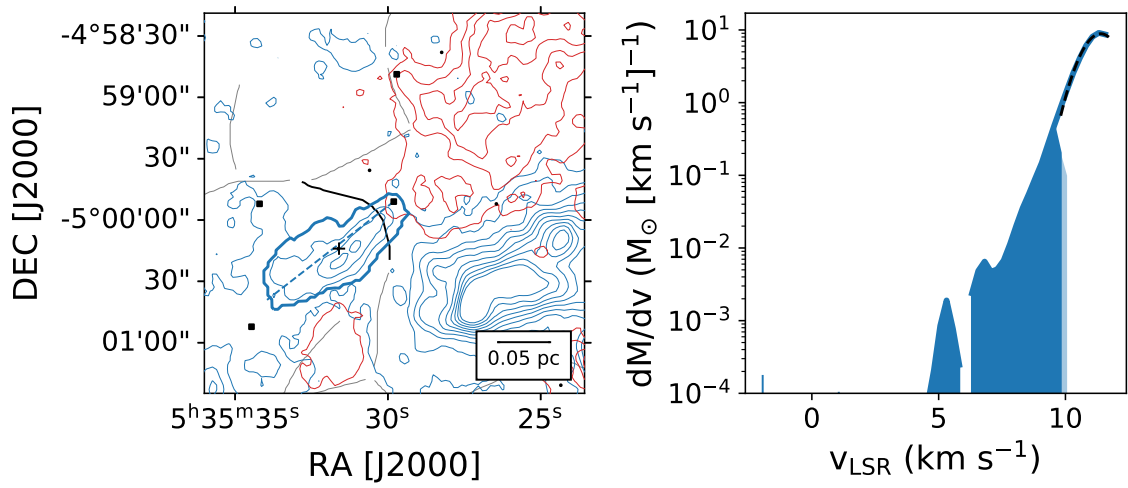


Figure 4.12 HOPS 383 outflow. The left panel shows the outflow, position angle, nearby sources, and filaments. The velocity range of integration is given by  $v_{\text{blue}}/v_{\text{red}}$  in Table 4.1 and the contours go from 5 to  $50\sigma$  in steps of  $5\sigma$ . Symbols are the same as Figure 4.2. The right panel shows the mass spectrum with fit. Symbols are the same as Figure 4.6.

# Chapter 5

## Conclusion

Feedback has a significant impact inside the Orion A molecular cloud. Shells and outflows stir the cloud and can help maintain turbulence, thereby reducing the efficiency with which gravity converts the cloud into stars. The main results of this thesis are summarized below.

In Chapter 2, I identified 42 expanding shell candidates in Orion A. Shells inject enough momentum into the cloud over time to counteract turbulent dissipation. The stellar-wind mass-loss rates necessary to produce the shells in Orion A are 2-3 orders of magnitude higher than predicted by wind models. Orion A is the third molecular cloud where shells have been found, after Perseus and Taurus.

In Chapter 3, I investigated the correlation in Orion A between feedback impact and several statistics of turbulence, compared to predictions from simulations. The CO covariance matrix shows correlations at relative velocities of  $1\text{-}3 \text{ km s}^{-1}$  toward several regions in Orion A. These features resemble those found in simulations of stellar winds, but it is unclear whether winds or some other mechanism generate the covariance features in Orion A. I discovered a new trend between the spectral correlation slope and the surface density of young stars. Regions in Orion A with more young stars have a steeper spectral correlation function slope.

In Chapter 4, I found 45 outflows in Orion A, including 11 new detections. I improved outflow mass estimates by accounting for low-velocity outflow material and incorporating a velocity-dependent opacity correction. Outflows inject enough momentum and kinetic energy to significantly offset turbulent dissipation in the cloud. The outflows in Orion A show a moderately perpendicular alignment with the filamentary structure in the cloud.

## 5.1 Next Steps

Much more work is needed to fully understand the impacts of feedback in molecular clouds. Expanding shells have now been found in three GMCs: Perseus, Taurus, and Orion A. This newly discovered stellar feedback mechanism is still poorly understood. Future studies should investigate the driving sources powering these shells to understand the discrepancy between the mass-loss rates necessary to explain the shells and those predicted by stellar wind models. The expanding shells should also be followed up with observational tracers of FUV heating, such as [C II] or [O I], to elucidate the impact of embedded FUV-luminous sources on the cloud chemistry and kinematics (e.g. Gaches & Offner, 2018).

To further the study of the statistical signatures of feedback, future simulations should incorporate multiple feedback mechanisms and test for correlations between the strength of feedback and statistical metrics like the spectral correlation function, while controlling for other factors like chemistry and magnetic fields. Further study in other clouds of the correlation between spectral correlation function slope and young star surface density is also needed to confirm and explain this relationship.

Methods for measuring protostellar outflow mass vary widely in the literature. Future outflow studies should follow Dunham et al. (2014a) in correcting for velocity-dependent opacity and low-velocity outflow material. The alignment, or lack thereof, between outflows and filaments is a promising avenue for testing models of mass accretion within and

onto cores. The outflow-filament alignment should be investigated in other clouds and in simulations.

A major remaining question is the efficiency with which feedback couples to the cloud. Offner & Liu (2018) suggest a mechanism, magnetosonic waves, by which expanding shells, and presumably outflows as well, could transport momentum to the farthest reaches of molecular clouds. It remains to be seen whether this mechanism could be observed, but a study of the immediate vicinity of such feedback features compared to a quiescent control region could provide clues.

The study of stellar feedback in molecular clouds has a bright future. The Atacama Large Millimeter/Submillimeter Array (ALMA) is now capable of mapping GMCs with 10-100× the resolution of the CARMA-NRO Orion survey. While observing entire nearby GMCs like Orion with ALMA is not practical, this telescope opens up more distant star forming environments to study. In the near future, it will be possible to compare the results of this thesis directly with GMCs in the galactic center (e.g. Barnes et al., 2019; Murchikova et al., 2019) or the Large Magellanic Cloud (e.g. Sawada et al., 2018; Fukui et al., 2018). With such observations, we will be able to compare the impact of feedback in drastically different environments.

## 5.2 Final Thoughts

”To find yourself in the infinite, you must distinguish and then combine.” Goethe wrote these words in 1827 as an ode to Luke Howard, the British chemist and pioneer of the study of clouds: the sort that obscure the night sky and force astronomers to play pool instead of observe. While Goethe is most famous as a novelist and father of the Romantic movement in literature, he was also a connoisseur of science. When Goethe learned that Luke Howard had classified the clouds into a taxonomy, the same we use to this day, he was captivated. Goethe understood that scientific and humanistic pursuits aim at the same

fundamental goal: to know the unknown.

This goal has kept me going these past six years. I have been lucky to find myself in the infinite, if only for a little while.

# Bibliography

- Alecian, E., Villebrun, F., Grunhut, J., et al. 2017, ArXiv e-prints. <https://arxiv.org/abs/1705.10650> 41
- Alecian, E., Wade, G. A., Catala, C., et al. 2009, MNRAS, 400, 354 32
- . 2013, MNRAS, 429, 1001 41
- Allen, L. E., & Davis, C. J. 2008, Low Mass Star Formation in the Lynds 1641 Molecular Cloud, ed. B. Reipurth, Vol. 4 (ASP Monograph Publications), 621 10
- Alves, J., Lombardi, M., & Lada, C. J. 2017, A&A, 606, L2 16
- Anathpindika, S., & Whitworth, A. P. 2008, A&A, 487, 605 136
- André, P., Di Francesco, J., Ward-Thompson, D., et al. 2014, in Protostars and Planets VI, ed. H. Beuther, R. S. Klessen, C. P. Dullemond, & T. Henning, 27 8, 114
- Arce, H. G., Borkin, M. A., Goodman, A. A., Pineda, J. E., & Beaumont, C. N. 2011, ApJ, 742, 105 8, 17, 19, 21, 41, 45, 51, 52, 54, 55, 57, 72, 73, 77, 80
- Arce, H. G., Borkin, M. A., Goodman, A. A., Pineda, J. E., & Halle, M. W. 2010, ApJ, 715, 1170 6, 41, 71, 80, 114
- Arce, H. G., & Goodman, A. A. 2001, ApJL, 551, L171 41, 120, 125
- Arce, H. G., Shepherd, D., Gueth, F., et al. 2007, Protostars and Planets V, 245 16, 78
- Arzoumanian, D., André, P., Didelon, P., et al. 2011, A&A, 529, L6 6, 114, 134, 139
- Aso, Y., Tatematsu, K., Sekimoto, Y., et al. 2000, ApJS, 131, 465 117
- Ballesteros-Paredes, J., Vázquez-Semadeni, E., & Goodman, A. A. 2002, ApJ, 571, 334 73
- Bally, J. 2008, Overview of the Orion Complex, ed. B. Reipurth, Vol. 1 (ASP Monograph Publications), 459 10, 11, 17

- Bally, J. 2011, in IAU Symposium, Vol. 270, Computational Star Formation, ed. J. Alves, B. G. Elmegreen, J. M. Girart, & V. Trimble, 247–254 9, 16
- . 2016, *ARA&A*, 54, 491 6, 16, 114
- Bally, J., Chambers, E., Guzman, V., et al. 2018, *AJ*, 155, 80 9, 72, 85
- Bally, J., Ginsburg, A., Arce, H., et al. 2017, *ApJ*, 837, 60 11, 45, 49, 76, 119
- Bally, J., Langer, W. D., Stark, A. A., & Wilson, R. W. 1987, *ApJL*, 312, L45 10, 12, 17, 117
- Barnes, A. T., Longmore, S. N., Avison, A., et al. 2019, *MNRAS*, 486, 283 180
- Beaumont, C. N., Goodman, A. A., Kendrew, S., Williams, J. P., & Simpson, R. 2014, *ApJS*, 214, 3 8, 17
- Beaumont, C. N., & Williams, J. P. 2010, *ApJ*, 709, 791 17
- Bergin, E. A., & Tafalla, M. 2007, *ARA&A*, 45, 339 1
- Berné, O., Marcelino, N., & Cernicharo, J. 2014, *ApJ*, 795, 13 12, 17, 50, 117
- Bodenheimer, P. 1995, *ARA&A*, 33, 199 114, 134
- Boyden, R. D., Koch, E. W., Rosolowsky, E. W., & Offner, S. S. R. 2016, *ApJ*, 833, 233 4, 73, 76, 77, 81, 82, 83, 84, 85, 86, 87, 88, 90, 92, 93, 99, 100, 101, 106
- Boyden, R. D., Offner, S. S. R., Koch, E. W., & Rosolowsky, E. W. 2018, *ApJ*, 860, 157 81, 82, 83, 84, 90
- Brault, J. W., & White, O. R. 1971, *A&A*, 13, 169 84
- Brown, A. G. A., de Geus, E. J., & de Zeeuw, P. T. 1994, *A&A*, 289, 101 11
- Brun, A. 1935, *Publications of the Observatoire de Lyon*, 1, 12 11
- Brunt, C. M., & Heyer, M. H. 2002a, *ApJ*, 566, 276 82
- . 2002b, *ApJ*, 566, 289 82
- . 2013, *MNRAS*, 433, 117 82
- Brunt, C. M., Heyer, M. H., & Mac Low, M. M. 2009, *A&A*, 504, 883 4, 72, 114
- Buckle, J. V., Davis, C. J., Francesco, J. D., et al. 2012, *MNRAS*, 422, 521 12, 45, 50, 117
- Burkhart, B., Lazarian, A., Ossenkopf, V., & Stutzki, J. 2013, *ApJ*, 771, 123 88, 103
- Carroll, J. J., Frank, A., & Blackman, E. G. 2010, *ApJ*, 722, 145 4, 6, 73, 114

- Carroll, J. J., Frank, A., Blackman, E. G., Cunningham, A. J., & Quillen, A. C. 2009, ApJ, 695, 1376 3, 71, 72, 114
- Castor, J. I., Abbott, D. C., & Klein, R. I. 1975, ApJ, 195, 157 8, 16
- Chen, C.-Y., & Ostriker, E. C. 2014, ApJ, 785, 69 142
- Chini, R., Reipurth, B., Ward-Thompson, D., et al. 1997, ApJL, 474, L135 117
- Choi, M., Kang, M., Lee, J.-E., et al. 2017, ApJS, 232, 24 6, 117
- Churchwell, E., Povich, M. S., Allen, D., et al. 2006, ApJ, 649, 759 8, 17
- Churchwell, E., Watson, D. F., Povich, M. S., et al. 2007, ApJ, 670, 428 17
- Clarke, S. D., Whitworth, A. P., Duarte-Cabral, A., & Hubber, D. A. 2017, MNRAS, 468, 2489 142
- Coffey, D., Bacciotti, F., Ray, T. P., Eisloffel, J., & Woitas, J. 2007, ApJ, 663, 350 6
- Cohen, M., & Kuhi, L. V. 1979, ApJS, 41, 743 11
- Corcoran, D., & Ray, T. P. 1995, A&A, 301, 729 38
- Crutcher, R. M. 2012, ARA&A, 50, 29 2, 16
- Cunningham, A. J., Frank, A., Carroll, J., Blackman, E. G., & Quillen, A. C. 2009, ApJ, 692, 816 6
- Curtis, E. I., Richer, J. S., Swift, J. J., & Williams, J. P. 2010, MNRAS, 408, 1516 130
- Dale, J. E., Haworth, T. J., & Bressert, E. 2015, MNRAS, 450, 1199 4
- Davis, C. J., Dent, W. R. F., Matthews, H. E., Coulson, I. M., & McCaughrean, M. J. 2000, MNRAS, 318, 952 117
- Davis, C. J., Froebrich, D., Stanke, T., et al. 2009, A&A, 496, 153 45, 75, 76, 87, 94, 112, 115, 116, 117, 118, 119, 122, 135, 143, 147
- Deharveng, L., Schuller, F., Anderson, L. D., et al. 2010, A&A, 523, A6 17
- Dickey, J. M., McClure-Griffiths, N. M., Stanimirović, S., Gaensler, B. M., & Green, A. J. 2001, ApJ, 561, 264 84
- Dobbs, C. L., & Pringle, J. E. 2013, MNRAS, 432, 653 2, 3, 16
- Downes, T. P., & Cabrit, S. 2007, A&A, 471, 873 133
- Draine, B. T. 2011, Physics of the Interstellar and Intergalactic Medium (Princeton University Press) 1

- Dunham, M. M., Arce, H. G., Mardones, D., et al. 2014a, ApJ, 783, 29 6, 16, 41, 120, 125, 128, 129, 133, 179
- Dunham, M. M., Stutz, A. M., Allen, L. E., et al. 2014b, Protostars and Planets VI, 195 1, 2
- Feddersen, J. R., Arce, H. G., Kong, S., et al. 2018, ApJ, 862, 121 72, 75, 76, 77, 80, 87, 92, 94, 97, 112
- Federrath, C. 2015, MNRAS, 450, 4035 3, 5, 16, 71, 114
- Frank, A., Ray, T. P., Cabrit, S., et al. 2014, Protostars and Planets VI, 451 4, 6, 7, 16, 78, 114
- Frerking, M. A., Langer, W. D., & Wilson, R. W. 1982, ApJ, 262, 590 44, 126
- Fuente, A., Martín-Pintado, J., Bachiller, R., Rodríguez-Franco, A., & Palla, F. 2002, A&A, 387, 977 27
- Fukui, Y., Tokuda, K., Saigo, K., et al. 2018, arXiv e-prints, arXiv:1811.00812. <https://arxiv.org/abs/1811.00812> 180
- Furlan, E., Fischer, W. J., Ali, B., et al. 2016, ApJS, 224, 5 11, 116, 118, 119, 122, 147
- Gaches, B. A. L., & Offner, S. S. R. 2018, ApJ, 854, 156 179
- Gaches, B. A. L., Offner, S. S. R., Rosolowsky, E. W., & Bisbas, T. G. 2015, ApJ, 799, 235 86, 88, 106, 108
- Goicoechea, J. R., Pety, J., Cuadrado, S., et al. 2016, Nature, 537, 207 9, 45, 76, 85
- Goldsmith, P. F., Snell, R. L., Hemeon-Heyer, M., & Langer, W. D. 1984, ApJ, 286, 599 125
- Großschedl, J. E., Alves, J., Meingast, S., et al. 2018, A&A, 619, A106 10, 74, 115
- Großschedl, J. E., Alves, J., Teixeira, P. S., et al. 2019, A&A, 622, A149 11
- Hacar, A., Tafalla, M., Kauffmann, J., & Kovács, A. 2013, A&A, 554, A55 139
- Hartmann, L. 2002, ApJ, 578, 914 20
- Haworth, T. J., & Harries, T. J. 2012, MNRAS, 420, 562 4
- Herbig, G. H., & Bell, K. R. 1988, Third Catalog of Emission-Line Stars of the Orion Population : 3 : 1988 11
- Heyer, M., & Dame, T. M. 2015, ARA&A, 53, 583 71
- Heyer, M. H., Morgan, J., Schloerb, F. P., Snell, R. L., & Goldsmith, P. F. 1992, ApJL, 395, L99 17, 24, 38

- Heyer, M. H., & Schloerb, F. P. 1997, *ApJ*, 475, 173 72, 81
- Hillenbrand, L. A. 1997, *AJ*, 113, 1733 11
- Hillenbrand, L. A., Hoffer, A. S., & Herczeg, G. J. 2013, *AJ*, 146, 85 41
- Hillenbrand, L. A., Strom, S. E., Vrba, F. J., & Keene, J. 1992, *ApJ*, 397, 613 27
- Hollenbach, D. J., & Tielens, A. G. G. M. 1997, *ARA&A*, 35, 179 9
- Johnstone, D., & Bally, J. 2006, *ApJ*, 653, 383 45
- Kauffmann, J., Bertoldi, F., Bourke, T. L., Evans, N. J., I., & Lee, C. W. 2008, *A&A*, 487, 993 126
- Koch, E. W., & Rosolowsky, E. W. 2015, *MNRAS*, 452, 3435 139
- Koch, E. W., Ward, C. G., Offner, S., Loewry, J. L., & Rosolowsky, E. W. 2017, *MNRAS*, 471, 1506 73, 81
- Kong, S., Arce, H. G., José Maureira, M., et al. 2019a, *ApJ*, 874, 104 8, 114, 115, 130, 134, 136, 140, 143, 153
- Kong, S., Arce, H. G., Feddersen, J. R., et al. 2018, *ApJS*, 236, 25 12, 13, 18, 58, 74, 79, 85, 103, 106, 107, 116, 123
- Kong, S., Arce, H. G., Sargent, A. I., et al. 2019b, arXiv e-prints, arXiv:1908.04488. <https://arxiv.org/abs/1908.04488> 12
- Konigl, A., & Pudritz, R. E. 2000, in *Protostars and Planets IV*, ed. V. Mannings, A. P. Boss, & S. S. Russell, 759 114
- Kounkel, M., Covey, K., Suárez, G., et al. 2018, *AJ*, 156, 84 10, 74, 115
- Krumholz, M. R., Bate, M. R., Arce, H. G., et al. 2014, in *Protostars and Planets VI*, ed. H. Beuther, R. S. Klessen, C. P. Dullemond, & T. Henning, 243 2, 4, 71
- Kuhn, M. A., Hillenbrand, L. A., Sills, A., Feigelson, E. D., & Getman, K. V. 2019, *ApJ*, 870, 32 10, 74, 115
- Kutner, M. L., Machnik, D. E., Mead, K. N., & Evans, II, N. J. 1985, *ApJ*, 299, 351 85
- Kutner, M. L., Tucker, K. D., Chin, G., & Thaddeus, P. 1977, *ApJ*, 215, 521 12
- Kwan, J., & Scoville, N. 1976, *ApJL*, 210, L39 49
- Lada, C. J., Lombardi, M., & Alves, J. F. 2009, *ApJ*, 703, 52 76
- Langer, W. D., & Penzias, A. A. 1993, *ApJ*, 408, 539 43, 125
- Larson, R. B. 1981, *MNRAS*, 194, 809 3, 16, 71

- . 2010, Reports on Progress in Physics, 73, 014901 6
- Lazarian, A., & Pogosyan, D. 2004, ApJ, 616, 943 88
- Lee, J. W. Y., Hull, C. L. H., & Offner, S. S. R. 2017, ApJ, 834, 201 114, 142
- Leinert, C., Henry, T., Glindemann, A., & McCarthy, Jr., D. W. 1997, A&A, 325, 159 32
- Li, H., Li, D., Qian, L., et al. 2015, ApJS, 219, 20 6, 8, 17, 51, 52, 55, 56, 57, 72, 77, 114, 133
- Li, P. S., & Klein, R. I. 2019, MNRAS, 485, 4509 114, 143
- Li, P. S., Klein, R. I., & McKee, C. F. 2018, MNRAS, 473, 4220 134, 143
- Li, Z.-Y., & Nakamura, F. 2006, ApJ, 640, L187 71
- Liu, T., Zhang, H., Wu, Y., Qin, S.-L., & Miller, M. 2011, ApJ, 734, 22 27, 37
- Lombardi, M., Bouy, H., Alves, J., & Lada, C. J. 2014, A&A, 566, A45 18
- Loren, R. B. 1979, ApJL, 234, L207 24, 38
- Mac Low, M.-M. 1999, ApJ, 524, 169 51, 131
- Mac Low, M.-M., & Klessen, R. S. 2004, RvMP, 76, 125 3, 16, 71, 72
- Mac Low, M.-M., Klessen, R. S., Burkert, A., & Smith, M. D. 1998, PhRvL, 80, 2754 3, 16, 71
- Makinen, P., Harvey, P. M., Wilking, B. A., & Evans, II, N. J. 1985, ApJ, 299, 341 85
- Manoj, P., Maheswar, G., & Bhatt, H. C. 2002, MNRAS, 334, 419 28, 41
- Matzner, C. D. 2007, ApJ, 659, 1394 71
- McCaughrean, M. J., & Stauffer, J. R. 1994, AJ, 108, 1382 11
- McKee, C. F. 1989, ApJ, 345, 782 55
- McKee, C. F., & Ostriker, E. C. 2007, ARA&A, 45, 565 1, 2, 16, 51, 71, 114, 133
- Megeath, S. T., Gutermuth, R., Muzerolle, J., et al. 2012, AJ, 144, 192 2, 11, 19, 28, 65, 75, 80, 116, 122
- . 2016, AJ, 151, 5 80
- Meingast, S., Alves, J., Mardones, D., et al. 2016, A&A, 587, A153 118
- Menten, K. M., Reid, M. J., Forbrich, J., & Brunthaler, A. 2007, A&A, 474, 515 10, 17, 44, 74, 115

- Mestel, L., & Spitzer, Jr., L. 1956, MNRAS, 116, 503 2, 16
- Mohanty, S., & Shu, F. H. 2008, ApJ, 687, 1323 27, 37
- Morgan, J. A., Schloerb, F. P., Snell, R. L., & Bally, J. 1991, ApJ, 376, 618 28, 50, 78, 117, 125, 130
- Moro-Martín, A., Cernicharo, J., Noriega-Crespo, A., & Martín-Pintado, J. 1999, ApJL, 520, L111 11, 28, 117
- Muench, A., Getman, K., Hillenbrand, L., & Preibisch, T. 2008, Star Formation in the Orion Nebula I: Stellar Content, ed. B. Reipurth, Vol. 4 (ASP Monograph Publications), 483 10
- Muller, E., Stanimirović, S., Rosolowsky, E., & Staveley-Smith, L. 2004, ApJ, 616, 845 84
- Murchikova, E. M., Phinney, E. S., Pancoast, A., & Blandford, R. D. 2019, Nature, 570, 83 180
- Murray, N. 2011, ApJ, 729, 133 2, 16
- Nakamura, F., & Li, Z.-Y. 2007, ApJ, 662, 395 3, 16, 71, 72, 114, 131
- . 2014, ApJ, 783, 115 52, 53
- Nakamura, F., Kamada, Y., Kamazaki, T., et al. 2011, ApJ, 726, 46 6, 114
- Nakamura, F., Miura, T., Kitamura, Y., et al. 2012, ApJ, 746, 25 8, 11, 17, 18, 19, 45, 50, 72, 76, 85, 99, 117
- Nazé, Y., Petit, V., Rinbrand, M., et al. 2014, ApJS, 215, 10 41
- Ochsenbein, F., Bauer, P., & Marcout, J. 2000, A&AS, 143, 23 59
- O'dell, C. R., & Wong, K. 1996, AJ, 111, 846 11
- Offner, S. S. R., & Arce, H. G. 2015, ApJ, 811, 146 9, 17, 37, 54, 55, 73, 77
- Offner, S. S. R., Dunham, M. M., Lee, K. I., Arce, H. G., & Fielding, D. B. 2016, ApJL, 827, L11 114, 134, 142
- Offner, S. S. R., Lee, E. J., Goodman, A. A., & Arce, H. 2011, ApJ, 743, 91 119, 129, 130, 131, 143
- Offner, S. S. R., & Liu, Y. 2018, NatAs, 2, 896 6, 71, 144, 180
- Ortiz-León, G. N., Loinard, L., Dzib, S. A., et al. 2018, ApJ, 865, 73 90
- Pabst, C., Higgins, R., Goicoechea, J. R., et al. 2019, Nature, 565, 618 9

- Padoan, P., Goodman, A. A., & Juvela, M. 2003, *ApJ*, 588, 881 86, 106, 108
- Padoan, P., Juvela, M., Krutsuk, A., & Norman, M. L. 2006, *ApJL*, 653, L125 88
- . 2009, *ApJ*, 707, L153 4, 72, 97, 114
- Padoan, P., & Nordlund, Å. 1999, *ApJ*, 526, 279 16, 71
- Padoan, P., Rosolowsky, E. W., & Goodman, A. A. 2001, *ApJ*, 547, 862 82, 83
- Parenago, P. P. 1954, Trudy Gosudarstvennogo Astronomicheskogo Instituta, 25, 3 11
- Peterson, D. E., & Megeath, S. T. 2008, in Handbook of Star Forming Regions, Volume I: The Northern Sky, ed. B. Reipurth, Vol. 4 (ASP Monograph Publications), 590 10, 45, 76
- Petit, V., Wade, G. A., Drissen, L., Montmerle, T., & Alecian, E. 2008, *MNRAS*, 387, L23 41
- Pingel, N. M., Lee, M.-Y., Burkhardt, B., & Stanimirović, S. 2018, *ApJ*, 856, 136 83, 88
- Plunkett, A. L., Arce, H. G., Corder, S. A., et al. 2015a, *ApJ*, 803, 22 6, 71, 114
- Plunkett, A. L., Arce, H. G., Corder, S. A., et al. 2013, *ApJ*, 774, 22 97, 114, 130
- Plunkett, A. L., Arce, H. G., Mardones, D., et al. 2015b, *Nature*, 527, 70 EP 6
- Principe, D. A., Cieza, L., Hales, A., et al. 2018, *MNRAS*, 473, 879 38, 54
- Pudritz, R. E., Ouyed, R., Fendt, C., & Brandenburg, A. 2007, Protostars and Planets V, 277 4, 27, 37
- Rathborne, J. M., Jackson, J. M., & Simon, R. 2006, *ApJ*, 641, 389 143
- Reipurth, B., Bally, J., Aspin, C., et al. 2013, *AJ*, 146, 118 32, 37
- Ripple, F., Heyer, M. H., Gutermuth, R., Snell, R. L., & Brunt, C. M. 2013, *MNRAS*, 431, 1296 12, 17, 117
- Rodríguez, L. F., Yam, J. O., Carrasco-González, C., Anglada, G., & Trejo, A. 2016, *AJ*, 152, 101 32
- Rodríguez-Franco, A., Martín-Pintado, J., & Wilson, T. L. 1999, *A&A*, 351, 1103 49
- Rohlfs, K., & Wilson, T. L. 1996, Tools of Radio Astronomy (Springer-Verlag Berlin Heidelberg New York), 127 44, 123
- Rosolowsky, E. W., Goodman, A. A., Wilner, D. J., & Williams, J. P. 1999, *ApJ*, 524, 887 82, 83
- Ruiz-Rodríguez, D., Cieza, L. A., Williams, J. P., et al. 2017, *MNRAS*, 468, 3266 38, 54

- Ryutov, D. D., Kane, J. O., Pound, M. W., & Remington, B. A. 2003, PPCF, 45, 769 85
- Sawada, T., Koda, J., & Hasegawa, T. 2018, ApJ, 867, 166 180
- Schmid-Burgk, J., Guesten, R., Mauersberger, R., Schulz, A., & Wilson, T. L. 1990, ApJL, 362, L25 119
- Shimajiri, Y., Takahashi, S., Takakuwa, S., Saito, M., & Kawabe, R. 2008, ApJ, 683, 255 117
- . 2009, PASJ, 61, 1055 117
- Shimajiri, Y., Kawabe, R., Takakuwa, S., et al. 2011, PASJ, 63, 105 17, 18, 27, 28, 76, 117
- Shimajiri, Y., Sakai, T., Tsukagoshi, T., et al. 2013, ApJL, 774, L20 27, 28
- Shimajiri, Y., Kitamura, Y., Saito, M., et al. 2014, A&A, 564, A68 18
- Shu, F. H. 1983, ApJ, 273, 202 2, 16
- Shu, F. H., Najita, J. R., Shang, H., & Li, Z. Y. 2000, in Protostars and Planets IV, ed. V. Mannings, A. P. Boss, & S. S. Russell, 789–814 4, 114
- Simpson, R. J., Povich, M. S., Kendrew, S., et al. 2012, MNRAS, 424, 2442 8
- Skinner, S. L. 1994, in Astronomical Society of the Pacific Conference Series, Vol. 62, The Nature and Evolutionary Status of Herbig Ae/Be Stars, ed. P. S. The, M. R. Perez, & E. P. J. van den Heuvel, 143 27
- Smith, N. 2014, ARA&A, 52, 487 8, 9, 55
- Snell, R. L., Scoville, N. Z., Sanders, D. B., & Erickson, N. R. 1984, ApJ, 284, 176 49
- Sousbie, T. 2011, MNRAS, 414, 350 135
- Stanke, T., McCaughrean, M. J., & Zinnecker, H. 2002, A&A, 392, 239 38, 116
- Stanke, T., & Williams, J. P. 2007, AJ, 133, 1307 50, 78, 117
- Stanke, T., Stutz, A. M., Tobin, J. J., et al. 2010, A&A, 518, L94 11, 28, 37, 76
- Stelzer, B., Flaccomio, E., Montmerle, T., et al. 2005, ApJS, 160, 557 28
- Stephens, I. W., Dunham, M. M., Myers, P. C., et al. 2017, ApJ, 846, 16 8, 115, 130, 134, 136, 140, 142, 143, 153
- Stephens, M. A. 1974, Journal of the American Statistical Association, 69, 730 140
- Stone, J. M., Ostriker, E. C., & Gammie, C. F. 1998, ApJL, 508, L99 16, 71

- Strömgren, B. 1939, ApJ, 89, 526 8
- Stutz, A. M., & Kainulainen, J. 2015, A&A, 577, L6 92
- Stutzki, J., Bensch, F., Heithausen, A., Ossenkopf, V., & Zielinsky, M. 1998, A&A, 336, 697 83, 88
- Sun, K., Kramer, C., Ossenkopf, V., et al. 2006, A&A, 451, 539 72, 76, 88
- Suri, S., Sánchez-Monge, Á., Schilke, P., et al. 2019, A&A, 623, A142 12, 114, 115, 121, 122, 135, 137, 139, 144
- Swift, J. J., & Welch, W. J. 2008, ApJS, 174, 202 72, 81, 84, 88, 93, 97, 106
- Takahashi, S., Saito, M., Ohashi, N., et al. 2008, ApJ, 688, 344 11, 49, 78, 117, 120, 125, 130
- Tanabe, Y., Nakamura, F., Tsukagoshi, T., et al. 2019, in press, PASJ 75, 78, 79, 95, 112, 115, 117, 118, 119, 120, 125, 130, 131, 135, 143
- Teixeira, P. S., Takahashi, S., Zapata, L. A., & Ho, P. T. P. 2016, A&A, 587, A47 119
- The, P. S., de Winter, D., & Perez, M. R. 1994, A&AS, 104, 315 28
- Tobin, J. J., Hartmann, L., Furesz, G., Mateo, M., & Megeath, S. T. 2009, ApJ, 697, 1103 20
- Ungerechts, H., Bergin, E. A., Goldsmith, P. F., et al. 1997, ApJ, 482, 245 75, 76, 81, 87, 94, 112
- Vazquez-Semadeni, E. 1994, ApJ, 423, 681 16
- Vink, J. S., de Koter, A., & Lamers, H. J. G. L. M. 2000, A&A, 362, 295 16, 41  
—. 2001, A&A, 369, 574 8
- Vorobyov, E. I., Elbakyan, V. G., Plunkett, A. L., et al. 2018, A&A, 613, A18 6
- Walker, M. F. 1969, ApJ, 155, 447 11
- Weaver, R., McCray, R., Castor, J., Shapiro, P., & Moore, R. 1977, ApJ, 218, 377 8
- Wenger, M., Ochsenbein, F., Egret, D., et al. 2000, A&AS, 143, 9 59
- Williams, J. P., Plambeck, R. L., & Heyer, M. H. 2003, ApJ, 591, 1025 49, 78, 117
- Wilson, B. A., Dame, T. M., Masheder, M. R. W., & Thaddeus, P. 2005, A&A, 430, 523 17, 117
- Yeremi, M., Flynn, M., Offner, S., Loeppky, J., & Rosolowsky, E. 2014, ApJ, 783, 93 100

- Zapata, L. A., Rodríguez, L. F., Ho, P. T. P., et al. 2005, ApJL, 630, L85 49, 119
- Zhang, Y., Arce, H. G., Mardones, D., et al. 2016, ApJ, 832, 158 43, 79, 120, 125, 126
- Zucker, C., Schlafly, E. F., Speagle, J. S., et al. 2018, ApJ, 869, 83 90
- Zuckerman, B., & Evans, II, N. J. 1974, ApJL, 192, L149 71